Development of Highly Anisotropic Nanomaterials for Fabrication, Detection and Theranostic Applications

By
MAIREYEE BHATTACHARYA
CHEM05201504001

Saha Institute of Nuclear Physics, Kolkata

A thesis submitted to the
Board of Studies in Chemical Sciences

In partial fulfillment of requirements
for the Degree of
DOCTOR OF PHILOSOPHY
of
HOMI BHABHA NATIONAL INSTITUTE

November, 2018

Homi Bhabha National Institute

Recommendations of the Viva Voce Committee

As members of the Viva Voce Committee, we certify that we have read the dissertation prepared by **Maireyee Bhattacharya** entitled "**Development of Highly Aniostropic Nanomaterials for Fabrication, Detection and Theranostic Applications**" and recommend that it may be accepted as fulfilling the thesis requirement for the award of Degree of Doctor of Philosophy.

Chairman : Prof. Samita Basu	Samitabasu	**Date:** 25.01.19
Guide / Convener : Dr. Dulal Senapati		**Date:** 25.01.19
Co-guide - (if any) : None		**Date:**
Examiner : Dr. Kanishka Biswas	Kanishka Biswas	**Date:** 25/1/19
Member 1 : Dr. Padmaja P Mishra		**Date:** 25/1/19
Member 2 : Dr. Manabendra Chandra		**Date:** 25/1/19

Final approval and acceptance of this thesis is contingent upon the candidate's submission of the final copies of the thesis to HBNI.

I hereby certify that I have read this thesis prepared under my direction and recommend that it may be accepted as fulfilling the thesis requirement.

Date: 25.1.2019

Place: Kolkata

Dulal Senapati
Guide

Version approved during the meeting of Standing Committee of Deans held during 29-30 Nov 2013

STATEMENT BY AUTHOR

This dissertation has been submitted in partial fulfillment of requirements for an advanced degree at Homi Bhabha National Institute (HBNI) and is deposited in the Library to be made available to borrowers under rules of the HBNI.

Brief quotations from this dissertation are allowable without special permission, provided that accurate acknowledgement of source is made. Requests for permission for extended quotation from or reproduction of this manuscript in whole or in part may be granted by the Competent Authority of HBNI when in his or her judgment the proposed use of the material is in the interests of scholarship. In all other instances, however, permission must be obtained from the author.

Maireyee Bhattacharya

Maireyee Bhattacharya

List of Publications arising from the thesis

Journal

1.“Decoupled *in-plane* dipole resonance modulated colorimetric assay-based optical ruler for ultra-trace Gold (Au) detection”, A. Mandal[#], M. Bhattacharya[#], D. V. Kuznetsov, T. Ghosh, S. Das Chakraborty, B. Satpati, V. Mazov and D. Senapati*, *Sci. Rep.*, **2018**, *8*, 868-878 ([#]*contributed equally*).

2. “Exploiting Le Chatelier's principle for a one-pot synthesis of nontoxic HHogGNPs with the sharpest nanoscopic features suitable for tunable plasmon spectroscopy and high throughput SERS sensing”, M. Bhattacharya, V. Mazov, B. Satpati, P. Jena, S. Das Chakraborty, S. Kumar, B. Pathak, D. V. Kuznetsov and D. Senapati*, *Chem. Commun.*, **2017**, *53*, 10402-10405.

3. “Direct experimental observation of salt induced aspect ratio tunable PFPT silver-nanowire formation: SERS-based *ppt* level Hg^{2+} sensing from ground water”, M. Bhattacharya, A. R. Mandal, S. Das Chakraborty, A. Maiti, A. Maity, D. V. Kuznetsov, P. Mondal and D. Senapati*, *RSC Adv.*, **2016**, *6*, 45279-45289.

4. M. Bhattacharya**,** V. Mazov, A. A. Markova, A. A. Shtil, P. Jena, G. Bhattacharjee, S. K. De, D. V. Kuznetsov and D. Senapati*, Depletion stabilized HHogGNPs find side-effect free theranostic applications in physiological saline condition; ***communicated.***

Chapters in books and lectures notes: None

Conferences

1. Presented a **Talk** in the 255th ACS National Meeting and Exposition: Nexus of Food, Energy & Water - 18th -22nd March, **2018**, New Orleans, Louisiana, USA.
2. Presented a **Poster** in the 5th International Symposium on Advanced Biological Inorganic Chemistry (SABIC) 7th-11th January, **2017**, IACS, Kolkata, India.

List of Publications arising from the thesis

Journal

1."Decoupled *in-plane* dipole resonance modulated colorimetric assay-based optical ruler for ultra-trace Gold (Au) detection", A. Mandal[#], M. Bhattacharya[#], D. V. Kuznetsov, T. Ghosh, S. Das Chakraborty, B. Satpati, V. Mazov and D. Senapati*, *Sci. Rep.*, **2018**, *8*, 868-878 (*[#]contributed equally*).

2. "Exploiting Le Chatelier's principle for a one-pot synthesis of nontoxic HHogGNPs with the sharpest nanoscopic features suitable for tunable plasmon spectroscopy and high throughput SERS sensing", M. Bhattacharya, V. Mazov, B. Satpati, P. Jena, S. Das Chakraborty, S. Kumar, B. Pathak, D. V. Kuznetsov and D. Senapati*, *Chem. Commun.*, **2017**, *53*, 10402-10405.

3. "Direct experimental observation of salt induced aspect ratio tunable PFPT silver-nanowire formation: SERS-based *ppt* level Hg^{2+} sensing from ground water", M. Bhattacharya, A. R. Mandal, S. Das Chakraborty, A. Maiti, A. Maity, D. V. Kuznetsov, P. Mondal and D. Senapati*, *RSC Adv.*, **2016**, *6*, 45279-45289.

4. M. Bhattacharya**,** V. Mazov, A. A. Markova, A. A. Shtil, P. Jena, G. Bhattacharjee, S. K. De, D. V. Kuznetsov and D. Senapati*, Depletion stabilized HHogGNPs find side-effect free theranostic applications in physiological saline condition; ***communicated***.

Chapters in books and lectures notes: None

Conferences

1. Presented a **Talk** in the 255th ACS National Meeting and Exposition: Nexus of Food, Energy & Water - 18th -22nd March, **2018**, New Orleans, Louisiana, USA.
2. Presented a **Poster** in the 5th International Symposium on Advanced Biological Inorganic Chemistry (SABIC) 7th-11th January, **2017**, IACS, Kolkata, India.

3. Presented a **Poster** in the International Conference of Optics Within Life Sciences (OWLS) 16th-19th March, **2016**, TIFR, Mumbai, India.

Others

1. Attended a **Workshop** on AFM organized by Bruker and Forevision Instruments on 1st -2nd December, 2017.

Maireyee Bhattacharya

Maireyee Bhattacharya

ACKNOWLEDGEMENTS

Firstly, I would like to express my sincere gratitude to my supervisor Dr. Dulal Senapati for his continuous support, encouragement and motivation throughout the Ph.D. tenure. He guided me in every way pursuing this study by sharing his ideas, experience and knowledge. He has introduced me to this field of research, starting from planning of experiments to writing a paper. This thesis mostly owes to him. I would like to thank Prof. Samita Basu, the HOD of our Chemical Sciences Division (CSD) for her constant support. I convey my thanks to Dr. Padmaja Prasad Mishra, Dr. Manabendra Chandra, Prof. Munna Sarkar, Prof. Montu K. Hazra, Dr. Mrinmay K. Mukhopadhyay, Dr. Biswarup Satpati, Prof. Tapas Chini, Dr. Pulak Ray, Dr. Biswarup Pathak and all our external collaborators for their insightful suggestions and kind assistance. I would like to thank my mentors, Dr. Munmun Bardhan, Dr. Ajoy Mandal and Dr. Prajna Jena and also Sudeshna, Sandip, Subratada, Sourav, Tapas, Abhishek, Gourab, Abhijit, Tapas, Tanmayda, Achyut, Arpan, Subhasda, Kallolda, Chaitralidi, Arnabda, Uttamda, Pritiranjan, Maheswaree, Shuvajit and Sougata. I would like to thank Sudipta Barman, Avijit Das, Sushanta Debnath, C. Palanivel and Ajay Patra for their help. I would like to thank all the staffs of CSD, workshop, library and canteen of SINP. Many people in SINP have enriched me in the last five years. Thanks to Debdatto, Debasish, Dibyasree, Arpita, Bankim, Siddhi, Anisha, Sukannya, Shramana, Susmita, Saswati, Sourav, Shameek, Rome, Aminulda, Sourav and Chandrima. I feel blissful to have a friend like Rajani in my life. Lastly and most importantly, my family is the core source of my peace, strength and inspiration. They all have been there with me in this journey so far and will be so forever.

CONTENTS

SYNOPSIS 1
LIST OF FIGURES 10
LIST OF TABLES 12
CHAPTER 1 INTRODUCTION 13
  1.1 Introduction 14
  1.2 Characteristics of Nanoscale Materials 16
    1.2.1 High values of Dispersion and Surface to Volume ratio 16
    1.2.2 Melting Point Depression 17
    1.2.3 Lattice parameters 18
    1.2.4 Catalysis 19
    1.2.5 Color and Localized Surface Plasmon Resonance 20
    1.2.6. Electronic Properties 24
    1.2.7 Mechanical Properties 25
    1.2.8 Thermal Properties 26
    1.2.9 Magnetism 27
    1.2.10 Cytotoxicity 28
  1.3 Common Synthetic Approaches 29
  1.4 Isotropic and Anisotropic nanostructures 30
    1.4.1 Parameters influencing Anisotropic Growth 31
  1.5 Why noble metals? 36
  1.6 Common Synthetic Approaches for Anisotropic Nanomaterials 38
  1.7 Selected Applications Relevant to Current Study 45
    1.7.1 Sensing 45
    1.7.2 Diagnostics 47
    1.7.3 Therapeutics - Photothermal Treatment 49
    1.7.4 Superlattice 52
CHAPTER 2 EXPERIMENTAL METHODS, INSTRUMENTS, AND MATERIALS 55
  2.1 Characterization Techniques 56
    2.1.1 UV-Vis-NIR Absorption Spectroscopy 56
      2.1.1.1 Working Principle 56
      2.1.1.2 Instrument and Operating Parameters 58
    2.1.2 Scanning Electron Microscopy 58
      2.1.2.1 Working Principle 58
      2.1.2.2 Instrument Details and Operating Parameters 59
    2.1.3 Transmission Electron Microscopy 60
      2.1.3.1 Working Principle 60
      2.1.3.2 Instrument and Operating Parameters 62
    2.1.4 Surface Enhanced Raman Scattering (SERS) 62
      2.1.4.1 Working Principle 62
        2.1.4.1.1 Electromagnetic Enhancement Theory 65

2.1.4.1.2 Chemical Enhancement Theory..67
2.1.4.1.3 Other Mechanisms..68
2.1.4.2 Instrument and Operating Parameters 70
2.1.5 Inductively Coupled Plasma-Optical Emission Spectrometry (ICP-OES) .71
2.1.5.1 Working Principle 71
2.1.5.2 Instrument and Operating Parameters 72
2.1.6 Dynamic light scattering (DLS) and Zeta potential measurement.............73
2.1.6.1 Basic Principle for Dynamic Light Scattering 73
2.1.6.2 Basic Principle for Zeta Potential...74
2.1.6.3 Instrument and Operating Parameters 77
2.1.7 Ultrasonic treatment or Sonication...77
2.1.7.1 Working Principle 77
2.1.7.2 Instrument Details 78
2.1.8 Grazing Incidence Small Angle X-ray Scattering......................................78
2.1.8.1 Working Principle 78
2.1.8.2 Instrument Details and Operating Parameters......................................80
2.2 Methodologies...80
2.2.1 Washing for Synthesis...80
2.3 Materials..81
CHAPTER 3 ASPECT RATIO TUNABLE SILVER-NANOWIRES IN SERS-BASED *ppt* LEVEL Hg^{2+} SENSING 82
3.1 Introduction...83
3.2 Preparation of Silver Nanocubes..86
3.3 Preparation of Silver Nanowires 86
3.4 Preparation of Silver tubular nanocages...90
3.5 SERS 90
3.6 Result and Discussion 91
3.6.1 Role of common salt for the generation of silver nanowires 92
3.6.2 Purification, networking, leaching, and preservation of synthesized silver nanowires 101
3.6.3 Highly specific and ultrasensitive Hg (II) detection by silver nanowires .105
3.7 Conclusions...114
CHAPTER 4 ULTRA-TRACE GOLD (Au) DETECTION BY A COLORIMETRY BASED OPTICAL RULER...116
4.1 Introduction...117
4.2 Growth Solution Preparation..120
4.3 Synthesis of Silver Nanoparticles (AgNPs) 120
4.4 Extraction of Gold as Gold Ion from the Ore...121
4.5 Results and Discussion..122
4.5.1 In-plane and Out-of-plane Surface Plasmon Modes and their Decoupling 123
4.5.2 Analytical Study illustrating Plasmon Shifting with Stress 127
4.5.3 Control Experiments 130
4.5.4 Plausible Role of Au in Ag Nanoparticle Formation 135

4.5.5 Selectivity of Sensing 138
4.5.6 Optical Ruler and its Sensitivity 140
4.5.6.1 Construction of Optical Ruler 140
4.5.6.2 Calculation of Average Error and Comparative Study for Sensitivity Analysis 142
4.5.6.3 Detection of Gold from Real Ore Sample 143
4.6 Conclusion 145
CHAPTER 5 HEDGEHOG GOLD NANOPARTICLES SYNTHESIZED BY APPLYING LE CHATELIER'S PRINCIPLE OFFER TUNABLE PLASMONICS AND HIGH SERS SIGNAL 147
5.1 Introduction 148
5.2 Synthesis of HHogGNPs 150
5.3 Results and Discussion 153
5.3.1 Alteration of Structural Parameters with NaCl Variation 153
5.3.2 Theoretical Correlation from Discrete Dipole Scattering (DDSCAT) approximation 159
5.3.3 Growth Governed by Le Chatelier's Principle 161
5.3.4 Tunable Plasmon Spectroscopy 166
5.3.5 SERS Measurement 168
5.3.6 Toxicity test of HHogGNPs by MTT assay in dark 170
5.3.6.1 MTT Assay protocol 170
5.3.6.2 Result of MTT-based cell viability assay in dark 170
5.4 Conclusion 172
CHAPTER 6 DEPLETION STABILIZED HEDGEHOG GOLD NANOPARTICLES IN THERANOSTICS 173
6.1 Introduction 174
6.2 Preparation of depletion force stabilised HHogGNPs 176
6.3 Results and Discussion 177
6.3.1 Depletion stabilization of HHogGNPs 177
6.3.2 Depletion stabilized HHogGNPs under different external conditions 185
6.3.2.1 pH response of Depletion stabilized HHogGNPs 185
6.3.2.2 Thermal response of Depletion stabilized HHogGNPs 187
6.3.2.3 Photo-stability of Depletion stabilized HHogGNPs 188
6.3.2.4 Depletion Stabilized HHogGNPs under Ultrasonic Wave 189
6.3.3 Surface Properties retained by depletion stabilized HHogGNPs 190
6.3.4 Photothermal Lysis Efficiency of Depletion Stabilized HHogGNPs 194
6.3.4.1 Protocols followed for Cell culture, Photothermal Therapy and MTT assay 194
6.3.4.2 Results of Photothermal treatment and MTT assay 195
6.3.5 Analytical Calculation of the Local Temperature generated at tips of HHogGNPs 200
6.4 Conclusion 203
CHAPTER 7 FUTURE DIRECTION AND CONCLUSION 204
7.1 Introduction 205
7.2 Synthesis of Superlattice 207

7.2.1 Superlattice of monometallic nanoparticle units 207
7.2.2 Superlattice of bimetallic nanoparticle units 208
7.3 Results and Discussion 208
7.4 A General Conclusion 218
REFERENCES 219

SYNOPSIS

Nanoparticles have offered extensive scope of research in last few decades to play with their unique physicochemical properties as a function of size, shape, composition and crystallization. Among them, anisotropic noble metal nanoparticles show promising applications in technological (e.g., photonics, electronics, imaging, sensing, etc.)[1–4] as well as medicinal (e.g. as photothermal agents, contrasting agents, drug delivery carriers, in theranostics, etc.)[5–7] fields. Multidirectional application of nanomaterials stem from their unusual optical, mechanical, electrical and magnetic properties[8] along with their photo-chemical stability, negligible toxicity, easy synthesis, and standard protocol of surface modification.[9,10] However, origin of anisotropy depends on several factors that vary from one system to other and thus requires thorough understanding and systematic study[11–13]. The present treatise deals with designing anisotropic nanomaterials that can execute desired functions. It records the strategies that we have formulated for bottom-up synthesis of such materials, plausible explanation for their growth based on experimental results, and their use in fabrication, sensing and biomedical applications. With controlled tuning of aspect ratio of anisotropic nanostructures, it is possible to alter their properties as required and that is the underlying principle we followed throughout the study.

The First Chapter of the thesis introduces the nanomaterials from a chemist’s point of view. Nanoscale, nanomaterials, their properties, uniqueness of noble metal nanomaterials, classification, synthetic strategies, methods of characterization, and some selected applications relevant to the study are discussed in this chapter by emphasizing the context of anisotropic noble metal nanoparticles.

The Second Chapter briefs information about the methodologies, instrumentation and precursors that are necessary for fabrication. Details of the characterization tools, instruments, specific techniques routinely practiced for sample preparation, any special measures taken during nanoscale synthesis and specification of the chemicals have been listed and elaborated in this section. Some of the factors that are unimportant in the bulk synthesis but are responsible for different issues like non-reproducibility, polydispersity, low yield, etc. in case of nanomaterial synthesis, are also mentioned here. With this, we move to the specific case studies on anisotropic noble metal synthesis and their applications in the following chapters.

Polyol synthesis method is a well-studied method where the polyol works as the solvent as well as the reducing agent depending on the reaction temperature to give rise to high-yield metallic nanomaterials[14]. It was noticed that the use of sodium sulfide leads to the formation of silver nanocubes whereas the use of sodium halides (NaCl, NaBr) produces silver nanowires (AgNWs) other reaction parameters remaining constant. Also, with increasing the amount of these halides the length of the synthesized wires could be tuned from ~500 nm to 60 μm. A plausible explanation based on real-time experimental observation has been put forward to explain how aspect ratio can be tuned as a function of the type and concentration of common salts (e.g., NaCl, NaBr, NaI, etc.). Here Pentagonal Faceted Pyramidal Tipped (PFPT) AgNWs are synthesized and the growth mechanism has been understood largely by considering the combined effects of (i) solubility product of the *in situ* generated silver halides, (ii) binding affinity of the added halides at the {111} facets on the growing front, and (iii) the free energy associated with the crystallographic planes (obtained from HRTEM study). The course of development of these pentagonal faceted wires from seeds has been investigated by freezing the intermediate-nanostructure in every step as the color of the mother solution changes. We have altered the blocking agents in the medium as AgF, AgCl, AgBr, and AgI by introducing NaF, NaCl, NaBr, and NaI respectively as the common salt to check the effect of the solubility product of the Ag-halides at the reaction temperature on the growth dynamics. Galvanic replacement reaction under two different conditions, i) in ethylene glycol at room temperature and ii) in boiling water, elucidated that the former procedure generates spiky and uneven leaching whereas the latter gave uniformly leached smooth nanotubes. Network structure of cross-linked AgNWs was achieved when dithiothreitol ($HS–CH_2–CH(OH)–CH(OH)–CH_2–SH$) was used as the tethering agent in the reaction mixture. The synthesized AgNWs show aspect ratio dependent Raman activity by using 4-mercaptobenzoic acid (4-MBA) as the Raman tag. Obtained Raman signal from surface adsorbed 4-MBA is completely quenched when we add 10^{-2} M Hg^{2+} into the nanocomposite solution due to the preferential binding of Hg^{2+} on the pyramidal tip of the silver-nanowire [i.e., {111} facet] and thereby dissolving the nanowire to reduce the active SERS surface area to its minimum level. Though at higher concentration other metal ions (Pb^{2+}, Cu^{2+}, As^{3+}, and Cr^{3+}) show considerable interference, below 50 *ppb* the Hg^{2+} shows selective Raman quenching. Controlled leaching of the nanowires offers the best-possible Raman platform for the ultrasensitive detection of Hg^{2+} contamination from ground water. The detection limit of Hg^{2+} by using our AgNW assay is up to 50 *ppt*, which is 40 times lower in concentration than the EPA (Environmental Protection Agency, USA) approved upper limit of Hg^{2+} in drinking water. The Third Chapter, therefore, addresses the mechanism of AgNW formation, their salt-induced aspect ratio variation and the application of AgNWs composite in SERS-based *ppt* level detection of Hg^{2+}.

In the Fourth Chapter I have described the construction of decoupled *in-plane* dipole resonance modulated colorimetric assay-based optical ruler for ultra-trace gold (Au) detection. Decoupling of different plasmon resonance modes (*in-plane*, and *out-of-plane* dipole and quadrupole resonances) by tuning nanoparticle's size and shape offers a new field of plasmonics as colorimetric assay-based optical-ruler for ultra-trace sensing. Driven by its low cost, easy to perform and efficient way to measure trace level (up to 30 *ppt* in presence of common mining elements in natural gold ore) abundance, this study develops a highly selective and ultrasensitive turn-on colorimetric sensor to detect gold-ion from environmental samples. Different level of gold-ion tracer makes size variable spherical- and disc-shaped silver nanoparticles when added to a 'growth solution' which results decoupling of *in-plane* dipole resonance from *in-plane* quadrupole and *out-of-plane* dipole resonances with a wide range of *in-plane* dipole plasmon tunability to generate different colors. This color-coded sensing of gold-ion shows high selectivity and ultrasensitivity over other metal ions in the *ppt* level with an impurity aberration limit of 1*ppm*. A plausible explanation elucidates the possible role of catalytic gold-ion to initiate unfavorable silver ion (Ag^{+}) reduction by ascorbic acid to generate silver nanoparticles. Proposed technology has been applied in real mining sample (Bugunda Gold Deposit, Tajikistan) to detect gold concentration from ores to find potential application in mining technology. By considering low cost, non-toxicity, and simplicity to perform a sensing experiment, our turn-on colorimetric sensor offers a robust analytical assay for accurate gold (Au) concentration measurement suitable for field applications both in mining industry as well as in forensic science.

In the Fifth Chapter we have introduced a highly anisotropic gold nanoparticle (GNP) resembling ‘Hedgehog’. Though the literature is rich in reports producing branched nanostructures, the inherent toxicity of the commonly used surfactants[15] [e.g., Cetyltrimethylammoniumbromide (CTAB), Cetyltrimethylammoniumchloride (CTAB), etc.] makes their applicability limited. In this study, we have demonstrated a one-pot synthetic strategy that does not require seed or surfactant. Instead, the anisotropy can be controlled simply by the variation of salt (NaCl) concentration and the whole reaction takes place in water medium and at room temperature. Here trisodium citrate (TSC) is employed as a particle stabilizing agent and ascorbic acid (AA) as mild reducing agent. In the presence of $AgNO_3$, AgCl is formed *in situ* which is insoluble at reaction temperature and is deposited preferentially onto specific high-energy-crystal facets over the others. This has been considered as the driving force for efficient facet blocking condition to generate highly anisotropic ‘Hedgehog gold nanoparticles’, HHogGNPs, with sharp spikes. With the increase in NaCl concentration in the medium, production of insoluble AgCl becomes more, which is induced by common ion effect imparted by Cl^- following Le Chatelier’s principle. To track the effect of Cl^- concentration on the nanostructures in course of growth, different structural parameters have been accounted. Synthesized HHogGNPs show broad-band plasmon tunability which covers the physiological NIR window and huge surface enhanced Raman scattering (SERS) efficiency. A plausible explanation has been put forward to explain their highly anisotropic nature and superlative SERS activity as a function of ‘common ion’ concentration in the mother solution.

Theoretical calculation using Discrete Dipole Approximation for scattering (DDSCAT) has been used to understand the plasmonic and scattering properties of HHogGNPs as a function of their tip size. To the best of our knowledge this is the first report where we successfully used the Le Chatelier's principle to generate highly anisotropic nanomaterials with regulated exposed surface area, variable tip curvature, and improved aspect ratio without employing any templating ligand or seed. MTT-based dark-toxicity test with RAW 264.7 mouse macrophage cell lines show that these HHogGNPs are nontoxic in the absence of light. So, these are the substrates showing excellent plasmonic tunability and strong SERS signal, easy to synthesize and tunable with respect to size, biocompatible in dark, stable in high salt environment and optimum pH mimicking physiological condition to show all the positive characteristics to be a potential candidate for theranostic application.

The Sixth Chapter focuses on the biomedical application of previously synthesized (Chapter 5) HHogGNPs, their modification, experimental results in the direction of theranostics, possibilities and limitations. It is known that high salt concentration is responsible for aggregation of nanoparticles both *in vivo* and *in vitro*. Therefore, stabilization and retention in physiological saline condition is highly desirable for intravenous treatment of any nanoparticle. Aggregation directly affects the size, shape, optical properties and stability of the particles. As already mentioned in the previous chapter, the synthesized HHogGNPs are stable at high salt condition but for applying in nanomedicine their structures need to be intact throughout circulation in the body saline. In other words, they must have longer retention time. For this, we have modified the dispersion of our HHogGNPs without altering the nano-surface by introducing a low-dose high-molecular mass polymer in the system.

Dispersed HHogGNPs experience a depletion of London attraction force and they do not allow any ion to come within the excluded volume zone. Thus the charge induced aggregation is inhibited. Formulated depletion stabilized HHogGNPs show enhanced stability against broad-band pH change, hyperthermic treatment, photochemical excitation, and mechanical disturbance in the form of ultrasonic wave to qualify as a robust candidate for theranostic application. In addition, depletion stabilized HHogGNPs shows negligible toxicity in absence of light and they still produce substantial SERS signal. To estimate the extent of local heat generation by the HHogGNPs we have adopted an analytical calculation by considering Coulomb potential outside the particle under uniform-temperature approximation. Application of these depletion stabilized HHogGNPs on HCT-116 colon carcinoma cells followed by photoexcitation in the biological window under physiological condition causes considerable local cell death. The type of cell death (necrotic or apoptotic) and the selectivity in terms of cell specificity, however, are under investigation to confirm their applicability.

We have then moved towards making ordered assembly of nanoparticles. In the Seventh Chapter, the synthesis, TEM and SAX-based characterization of 2D and 3D plasmonic superlattice applicable in photoelectric devices are described. Periodic assembly of nanoscale building blocks is an ideal system to explore novel chemical and physical properties arising out of the interactions between the constituent particles. In a way, they offer a pathway to fundamental research finding similarity with atoms tailored to nanomaterials. More importantly, they find applications in the storage of mass and energy and also in optical devices. Regularity in shape and size of nanoparticles (NPs) is a prerequisite for their arrangement on a Bravais lattice termed as ‘Superlattice’. Following digestive ripening method, it is possible to synthesize highly monodisperse NPs of very narrow size distributions ($\sigma < 5\%$). We have followed a two-step growth method to achieve low dimensional (5-10 nm) gold nanoparticles in organic medium and allowed them to self-assemble that eventually leads to two-dimensional (2D) array to three-dimensional (3D) superlattices if controlled with time. AuNPs of each step are analyzed by transmission electron microscopy (TEM) and UV-visible Spectroscopy, SAXS measurements to evaluate the mode of aggregation in dried and colloidal bulk phases, respectively. We have tracked the growth of superlattice formation with time by measuring the X-ray diffraction (XRD) patterns. Currently we are designing a temperature variable GISAXS measurement mount that can be useful for tracking the crystal growth with temperature alteration and to determine the reversibility of superlattice formation. Last section of this chapter briefs the progress of our investigation to investigate the origin and control of anisotropy in the course of solution phase growth for different noble metal nanostructures and their application in fabrication, optics, SERS-based-assays, sensing, therapy, diagnosis, pathogen killing, etc. If the silver nanowires are considered as one-dimensional nanostructure (due to very high aspect ratio), silver nanodiscs as two-dimensional nanostructure and hedgehog gold nanoparticle as a three-dimensional nanostructure, then the study records how the growth of anisotropic nanomaterials of different dimension is controlled by reaction parameters and how this anisotropy affects their physical and chemical properties. The conclusions of all the preceding chapters have been summarized here. The challenges towards attaining a regular assembly of nanoscopic units and its utility have been emphasized in more details as a future direction of my research. This chapter finally ends up with few more unresolved queries where there is scope for further investigation.

LIST OF FIGURES

Figure 1.1: Close-packing of atoms in *hcp* and *fcc* lattices. 16
Figure 1.2: Variation of melting point with particle size. 18
Figure 1.3: Localized Surface Plasmon Resonance. 21
Figure 1.4: Multipolar modes of plasmon excitation. 22
Figure 1.5: Surface plasmon resonance modes for a nanosphere and a nanorod. 23
Figure 1.6: Change of density of states of matter with decrease in size. 24
Figure 1.7: The openness of different facets of an *fcc* lattice. 32
Figure 1.8: Underpotential deposition of silver on gold nanorods. 33
Figure 1.9: Pathways to different anisotropic *fcc* metal nanocrystals. 35
Figure 1.10: Surfactant-directed metal nanorod growth. 41
Figure 1.11: Illustration of the mechanism of photothermal therapy. 51
Figure 2.1: Different components of a spectrophotometer. 57
Figure 2.2: Visible light microscope and transmission electron microscope. 61
Figure 2.3: Chemical enhancement and capacitive coupling in SERS. 69
Figure 2.4: Home-made Raman setup used for SERS experiments. 71
Figure 2.5: Illustration of Zeta potential. 75
Figure 3.1: TEM-images of silver nanowires with NaCl variation. 88
Figure 3.2: SEM-images of silver nanowires with NaCl variation. 88
Figure 3.3: Quantification of aspect ratio of the synthesized nanowires. 89
Figure 3.4: SEM images of the silver nanowires with pentagonally twinned face and pyramidal tipped structure. 94
Figure 3.5: TEM images of the silver nanocubes at different magnifications. 94
Figure 3.6: Absorption spectra of NaCl induced nanowires. 95
Figure 3.7: Real-time growth steps from silver seeds to nanowires. 96
Figure 3.8: HRTEM images of the silver seeds along with the silver nanowires. 97
Figure 3.9: "String with several knots"– TEM image of arrangement of seeds. 98
Figure 3.10: Effect of different halides on the formation of silver nanowires. 99
Figure 3.11: Purification of nanowires by sonication and fractional centrifugation. 102
Figure 3.12: Controlled generation of hollow nanotubes. 103
Figure 3.13: The effect of dithiothreitol addition in the reaction mixture. 104
Figure 3.14: The UV-Vis absorption spectra of silver nanowires synthesized in absence and presence of dithiothreitol 104
Figure 3.15: SERS shown by 4-MBA on different aspect ratio silver nanowires. 106
Figure 3.16: Comparison of silver nanowire leaching by gold and mercury ions. 110
Figure 3.17: Hg(II) sensing by NaCl-induced silver nanowires. 111
Figure 3.18: Raman quenching efficiency of Hg(II) with respect to other ions. 113
Figure 4.1: Stepwise Synthesis of Au-ion catalyzed silver nanoparticles and their UV-vis spectra for different concentrations of Au-ions. 121
Figure 4.2: Out-of-plane quadrupole resonance from the 'growth solution'. 123
Figure 4.3: Kinetics of morphology transition different concentration of Au-ion. 126
Figure 4.4: TEM images of thickness mapping of silver nanodiscs. 127
Figure 4.5: Relative stress between disc and sphere. 128
Figure 4.6: Different sets of control experiments. 132
Figure 4.7: 'Growth solution' prepared with higher Au-ion concentration. 135
Figure 4.8: EDX spectra of the in situ generated silver nanodiscs. 136

Figure 4.9: Effect of Au-ion on differential reduction potential of ascorbic acid. 137
Figure 4.10: Selectivity of Au-ion sensing by the ‘growth solution’. 139
Figure 4.11: Variation of in-plane dipole resonance with the concentration of added Au-ion. 140
Figure 4.12: Comparison between Au-ion detection by our colorimetric assay-based optical ruler with respect to the ICP-OES as standard. 143
Figure 4.13: Colorimetric detection of gold ion from oxidized ore samples. 145
Figure 5.1: Structural similarity of a ‘hedgehog’ to Hedgehog gold nanoparticles. 149
Figure 5.2: Synthetic schemes by varying different reaction parameters. 150
Figure 5.3: Structural evolution of gold nanomaterials varying TSC concentration. 151
Figure 5.4: Gold nanostars obtained by the reduction with ascorbic acid only. 153
Figure 5.5: TEM images of HHogGNPs synthesized using different concentrations of NaCl 154
Figure 5.6: Large area TEM and SEM image of HHogGNPs. 155
Figure 5.7: Number of tips in HHogGNPs formed at different NaCl concentration. 156
Figure 5.8: Theoretical interpretation of molar extinction coefficient and SPR maxima for different tip-to-tip distances of HHogGNPs. 160
Figure 5.9: HRTEM of HHogGNPs. 162, 163
Figure 5.10: Structural change of HHogGNPs with increase in NaCl concentration 165
Figure 5.11: TEM images of stepwise transition from seed to HHogGNPs. 165
Figure 5.12: UV-vis-NIR absorption spectra of HHogGNPs obtained by varying different reaction parameters. 166
Figure 5.13: Recorded SERS for Rh6G with different NaCl-induced HHogGNPs. 169
Figure 5.14: Probable factors of high Raman cross section of HHogGNPs. 170
Figure 5.15: MTT assay results of HHogGNPs on RAW 264.7 cell lines in dark. 171
Figure 6.1: Absorption spectra of synthesized HHogGNPs with NaCl variation. 178
Figure 6.2: Optimization of PVP required for depletion stabilization of HHogGNPs in 0.9% NaCl. 180
Figure 6.3: TEM pictures and absorption spectra of HHogGNPs, before and after PVP addition. 182
Figure 6.4: Structure and probable distribution of PVP around the nanoparticles. 183
Figure 6.5: EDX spectra and elemental mapping of PVP-HHogGNPs. 184
Figure 6.6: Stability of PVP-HHogGNPs under pH variation. 186
Figure 6.7: Effect of constant and high temperature on PVP-HHogGNPs. 187
Figure 6.8: PVP-HHogGNPs upon laser irradiation. 189
Figure 6.9: PVP-HHogGNPs under sonication. 190
Figure 6.10: Plasmon tuning of PVP-HHogGNPs. 191
Figure 6.11: SERS activity of PVP-HHogGNPs. 193
Figure 6.12: Effect of photothermal therapy on HCT-116 cells. 198
Figure 6.13: Cell viability results of HCT-116 cells with PVP-HHogGNPs. 200
Figure 7.1: Absorption spectra of only Au and AuAg samples. 209
Figure 7.2: TEM images of only Au samples collected at different stages. 210
Figure 7.3: I(q) vs. qz plot of the only Au sample. 212
Figure 7.4: Relation between unit length and lattice parameters in an *fcc* lattice. 212
Figure 7.5: TEM image and chemical mapping of the AuAg sample before reflux. 213
Figure 7.6: TEM images and EDX spectra of Au-Ag samples after reflux 214
Figure 7.7: Small angle electron diffraction patterns obtained for AuAg sample 215
Figure 7.8: Design of the temperature variable GISAXS measurement mount 217

LIST OF TABLES

Table 2.1: The operating parameters in ICP-OES measurement for Au-ion tracer. 73
Table 2.2: List of reagents with the specifications and company names. 81
Table 3.1: Detection of Hg^{2+} from different source of water samples. 114
Table 4.1: Calculation of error in colorimetric and optical assay with respect to the standard ICP-OES method. 142
Table 5.1: Detailed structural statistics of synthesized HHogGNPs. 158
Table 5.2: The calculated properties for modelled HHog nanoparticles. 161
Table 5.3: Results of MTT-based dark toxicity. 171
Table 6.1: Calculated average temperature change per tip for HHogGNPs. 202

CHAPTER 1

INTRODUCTION

OUTLINE: What does the chapter brief?

- Introduction to Nanoscale, Nanomaterials and their classification
- Uniqueness of noble metal nanomaterials
- Synthetic strategies of anisotropic nanomaterials
- Selected applications relevant to the study

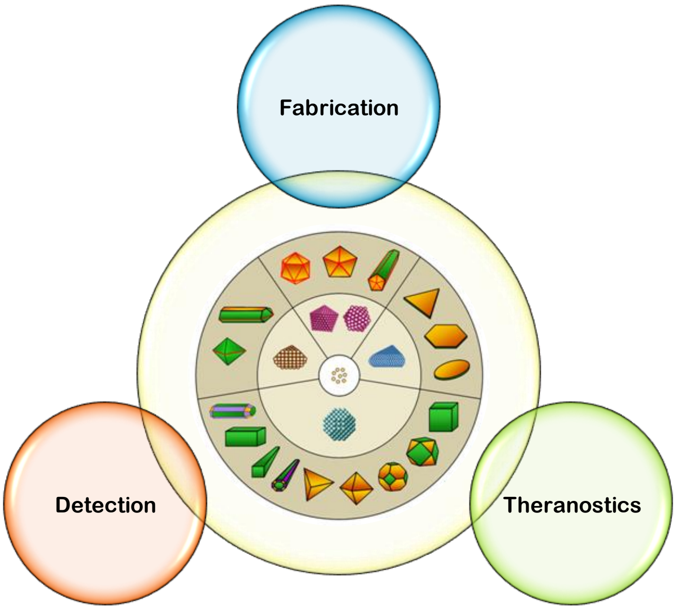

1.1 Introduction

The smallest chemical entity of any matter is known as atom. When more than one atom combines together, they form a molecule with specific molecular properties generally different from individual atoms. Atom has its dimensions in Angstrom (Å or 10^{-10} m) order. Chemists have discovered the properties of atoms and molecules elaborately. The dimension they focus is, therefore, below 1 nm. On the other hand, condensed matter physicists look upon infinite arrays of bound atoms beyond submicron range eventually forming a bulk material. The regime falling in between, dealing with particles of 1 nm-100 nm, represents a collection of a few (about 10 to 10^6) atoms or molecules per particle[16], and can be considered to be a link between atoms and the bulk. Neither the laws of quantum chemistry, nor those of surface physics can explain all the properties independently.

Among strongly bonded atoms, delocalization of electrons can take place. The extent of delocalization can vary with the size and shape of the system, which again depends on the size of the constituent atoms and their electronic configuration. Thus for different structures of same or different combination of elements, new physical and chemical properties are expected to evolve. In reality, indeed it has been observed that these materials possess many unique properties which are absent in case of an individual atom as well as in case of the bulk and are tunable as a function of their size and shape. Controlling several factors, they can be further fabricated for performing desired functions. This is why extensive amount of research work concentric to nanoscale has flourished in the last few decades. Nanomaterials are typically defined as materials having at least one external dimension in the range between 1 nm to 100 nm[17]. However, along with its expansion appearance of several subdivisions have been introduced with specified terminologies[16]. For example,

(1) A ‘Cluster’ is a collection of up to about 50 units of atoms or molecules. Cluster compounds are stable, isolable and soluble moieties surrounded by ligand shell.

(2) ‘Colloid’ is a stable liquid phase composed of 1-1000 nm (1 μm) sized particles each of which are known as ‘Colloidal’ particles.

(3) ‘Nanoparticles’, similar to ‘Nanomaterials’, are characterized to have dimensions in the nanometer range, e.g. 1-1000 nm. They are solid particles, may be noncrystalline, a single crystallite or an aggregate of crystallites[16].

(4) ‘Nanocrystal’ refers to a solid particle that is a single crystal in the nanometer regime.

(5) ‘Nanostructured or Nanophase or Nanoscale materials’ are any solid material having at least one dimension in nanometer range. If the material has all three dimensions in nanometer range, it is a 3D nanoparticle e.g. nanocube, nanoflower, nanosphere, etc, if it has two nano-dimensions, it is a 2D nanoparticle e.g., nanoplate, nanofilm, etc and with only one active nano-dimension, it is a 1D nanoparticle e.g., nanowire, nanofibre, etc.

(6) ‘Quantum dot’ is a particle showing a size quantization effect in at least one dimension.

The current treatise deals with developing methodologies to produce nanomaterials with specific features designed for different applications. To get the essence of its aim and scope, it is necessary to first introduce the unique nanoscale properties along with the factors they are likely to stem from.

1.2 Characteristics of Nanoscale Materials

1.2.1 High values of Dispersion and Surface to Volume ratio

When a material is subdivided into parts, the cumulative surface area of these parts is larger than that of the matter. Also the ratio of the number of atoms exposed at the surface to those in the bulk increases as the size of the material decreases. This ratio of number of atoms at the surface to total number of atoms present in the particle is called 'Dispersion', F. If we consider full shell clusters, they are majorly built up by hexagonal close-packed (*hcp*) or cubic close-packed (*ccp*) structures (**Figure 1.1A**) where the coordination number of the central atom of an unit cell is 12[16]. In contrary, atoms lying at a face reduce their coordination number to 9 or less depending on their locations (2D-plane, edge or corner and also which face) (**Figure1.1B**).

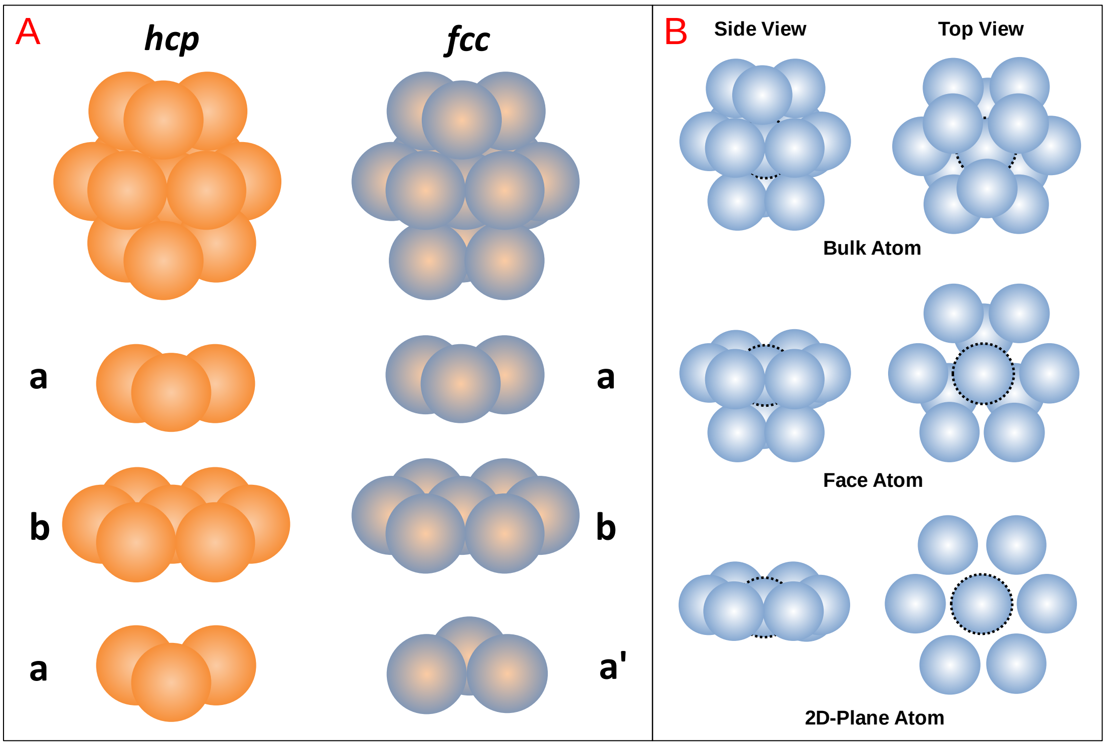

Figure 1.1: (A) Two forms of close-packing of spheres, hexagonal close-packed (*hcp*) or face-centered cubic (*fcc*) with exploded view of the lattices, showing that *hcp* involves alternating layer patterns a and b, while *fcc* comprises triplets of layer

patterns a and b, while *fcc* comprises triplets of layer patterns, a, b, and a′, where a′ is a 180° horizontal rotation of a. (B) Schematic view of atoms constructing an *fcc* lattice where the central atom represents a bulk atom which is coordinatively saturated with 12 surrounding atoms. In comparison, if we consider an atom lying at faces has coordination number 9 and that reduces to 6 for a 2D-plane atom and so on.

Thus the smallest crystal is made of 13 atoms with the central atom is surrounded by 12 atoms which gives, $\boldsymbol{F = (12/13) \times 100\% = 92\%}$. The fraction F scales with surface area divided by volume, i.e. 'surface to volume ratio', S/V. For a spherical particle of radius R, S/V is inversely proportional to R [$\boldsymbol{S/V = 4\pi R^2/(4\pi R^3/3) = 3/R}$]. With higher S/V ratio, the relative number of atoms exposed over the surface with respect to the bulk increases and the surface energy of the nanoparticle also increases. As a result the nanoparticles become more reactive and many other surface-related properties are altered. For example, application of nanomaterials for pollution control[18], fabrication of highly efficient catalytic materials[19] or tailored materials for drug delivery[20].

1.2.2 Melting Point Depression

The atoms lying at the surface are coordinatively unsaturated. Being a part of the rigid bond structure in the solid phase, they are under strain due to this unsaturation. A phase transition to liquid helps in releasing this strain. In liquids, the surface atoms are in dynamic equilibrium. They are allowed to move and exchange positions to minimize the surface area and energy. The overall surface energy is thus reduced by melting. Smaller the size of the solid (nanocrystal), number of surface atoms is more, the contribution made by the surface energy to the overall energy of the system is then larger. Therefore the crystal is more prone to melt for surface stabilization. Again, the bonds shared by surface atoms are more dangling in nature due to unsaturation. So, it is easier to disrupt them first to initiate melting at lower temperature and this is the reason melting starts from the surface. In other words, there is a depression in melting point with decrease in particle size, and for particles with dimension below 3-4 nm[16], there is a dramatic fall as shown in **Figure 1.2**.

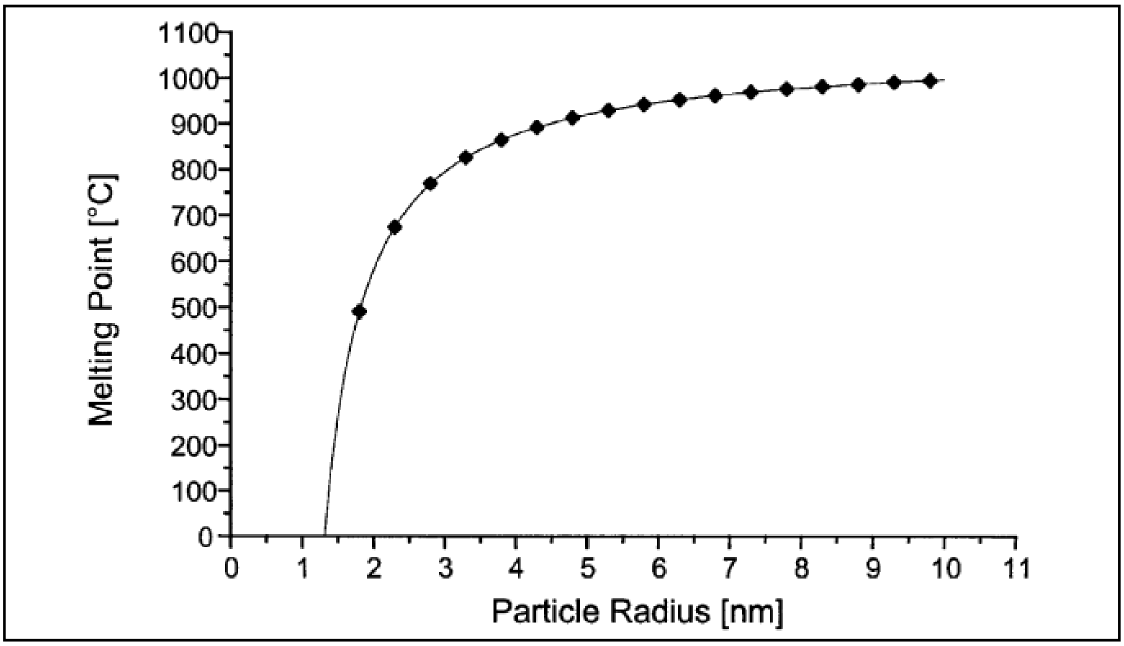

Figure 1.2: Relation between particle size and melting point of gold particles synthesized by the condensation of gold vapor on a thin amorphous carbon film mounted on a gold mesh of the type used for electron microscopy[21](adapted with permission from ref.16, copyright 2001Wiley-Interscience).

1.2.3 Lattice parameters

Size-dependent lattice expansion is observed for nanoparticles of many ionic compounds, including metal oxides, while lattice contraction prevails for pure metals[22]. The increase in the surface energy by lattice expansion induces a stress that alters the lattice parameters by elastic contraction. Vermaak *et al.*[23,24] have explained the reduction of lattice parameter in terms of the surface stress caused by the reduction in the particle dimension. Qi *et al.*[25,26] have introduced a shape factor to their previous spherical model of nanoparticles to calculate the lattice parameter of metal nanoparticles based on the shape dependence by considering a minimized sum of the surface energy and the elasticity energy. Lattice surface energy itself plays a determining role on the direction of growth for a nanostructure.

1.2.4 Catalysis

Many properties those are significantly different or even absent in the bulk, arise in nano-regime, e.g. gold is no more noble at nano-dimension and can act as an excellent catalyst for the oxidation of carbon monoxide[27,28]. In general, nanoparticles serve as good catalysts having high surface area, lower work function, and unique electronic structure both for homogenous catalysis in solution or heterogeneous catalysis on a solid support. Along with these, if they possess mismatched facet boundaries and defect sites with additional strain, then they are more apt to adsorb reactant molecules to reduce their surface energy and in that way indirectly helps in catalysis[29]. This is one of the reasons for the application of bi- and multi-metallic nanoparticles as attractive catalytic material in this field[30,31]. The other two factors attributed for the enhanced performance of a bimetallic catalytic material over each monometallic counterparts are ensemble (structural) effects and electronic (ligand) effects[32]. Again, while adsorption, the reactant molecules may be adsorbed either on to the surface of the nanoparticle by surfactant-reactant electrostatic interaction or to the core of the nanoparticle by metal-reactant covalent bonding (like, Au-S bonding by click chemistry). To do so, shape of the particle, accessibility (surfactant free surface) and surface energy of different active facets, surface charge as well as size of the particle are few most important factors among several others which we will describe in details during discussion.

1.2.5 Color and Localized Surface Plasmon Resonance

It is now well known that unlike bulk materials, nanomaterials show a dramatic variation in properties as they change in size, shape, and surface chemistry. Out of several different properties the most prominent and interesting one for noble metal nanomaterials is their spectroscopic and colorimetric property. For example, bulk noble metals are glossy and reflective with a **fixed** color to find heavy applications in jewelry, on the nanoscale same metals exhibit the ability to confine and guide light, results these materials to appear with **different** beautiful and vibrant colours[33]. Magnificent optical property of noble metal nanomaterials bears their signature in Lycurgus Cup (a 4th century Roman glass cup made of a dichroic glass) which contains both gold and silver nanoparticles and transmit vibrant ruby red and reflects emerald green light[34] or the creation of Medieval time stained glass window in cathedrals[35]. The striking appearance of noble metal nanoparticles originates from the extraordinarily efficient interaction between nanoscale metal particles and incident light, termed as the localized surface Plasmon resonance (LSPR)[36].

When a small spherical metallic nanoparticle is irradiated by light, the oscillating electric field causes the conduction electrons to oscillate coherently. This is schematically pictured in **Figure 1.3.** When the electron cloud is displaced relative to the nuclei, a restoring force arises from Coulomb attraction between electrons and nuclei that results in oscillation of the electron cloud relative to the nuclear framework.

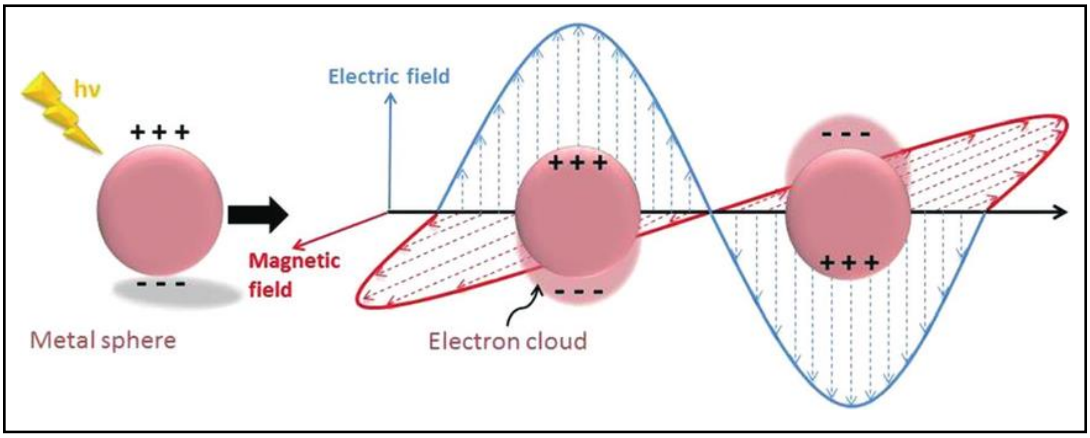

Figure 1.3: Schematic illustration of Localized Surface Plasmon Resonance upon irradiating a metallic nanoparticle (adapted with permission from ref. 37, copyright 2015 The Royal Society of Chemistry).

Coherent collective oscillations of the conduction electrons (quantized plasma oscillation) against the background of ionic metal core are called Surface Plasmons Resonance. This oscillation frequency is determined by four factors: the density of electrons, the effective electron mass, and the shape and size of the charge distribution. The collective oscillation of the electrons is called the dipole Plasmon resonance of the particle (sometimes denoted “dipole particle plasmon resonance” to distinguish from plasmon excitation that can occur in bulk metal or metal surfaces). Higher modes of plasmon excitation can occur, such as the quadrupole mode (or even hexapole and octupole) where half of the electron cloud moves parallel to the applied field and half moves antiparallel[36] (**Figure 1.4**).

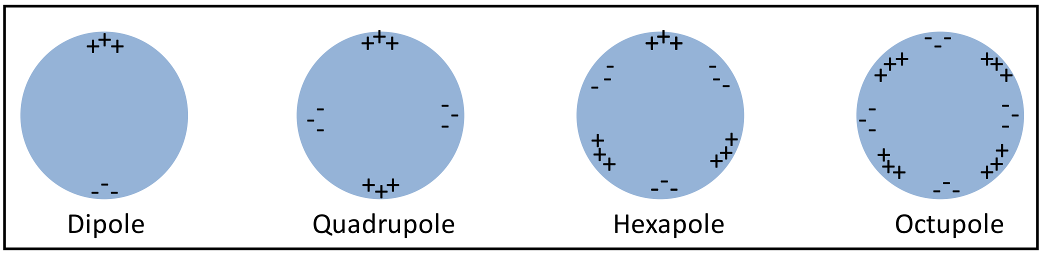

Figure 1.4: Distribution of electron cloud under different probable modes of plasmon excitation.

Since the density of electrons and the effective electron mass depends on the atomic property of the material and hence indirectly on the composition of the materials, similar sized and shaped nanoparticles made from different metals (for metallic particles) shows different plasmon signature. On the other hand the shape and size of the charge distribution depend on the structural properties of the tailored material as a whole and hence a change in size and shape of the nanoparticle leads them to absorb at different wavelengths and show different colors as complementary wavelength. In fact, the optical properties of the nanoparticles are most explored as they show size, shape and composition dependent variation of absorption in the vis-NIR range. Most of the typical metallic properties arise from the fact that the electrons in the metal are free to travel through the material. The mean free path for the d-electrons in gold and silver is ~50 nm[8], therefore in particles smaller than this, no scattering should be observed from the bulk and all interactions are expected to be with the surface only. In principle, when the wavelength of light is much larger than the size of the nanoparticle, it can set up a standing resonance conditions (oscillation of particle electron density in resonance with the frequency of the incident light by considering the frozen particle motion compared to the electromagnetic wave) with the surface plasmon oscillation of the nanoparticle with a measurable broadening defined as Plasmon band.

Since the resonance condition depends on the profile of electron distribution, observed Plasmon band can offer an idea about their physical appearance or shape. For example, a nanosphere has only a single mode of Plasmon oscillation (**Figure 1.5A**) whereas a nanorod has two different modes of plasmon oscillation, one along its length, which is called the Longitudinal mode and another along the diameter which is the Transverse mode (**Figure1.5B**). Both the longitudinal and transverse Plasmon mode peak position heavily depends on the resultant aspect ratio (AR) of the nanoparticle where AR can be mathematically defined as:

$$AR = \left(\frac{Length\ of\ the\ material\ of\ any\ specific\ feature\ of\ the\ material}{Diameter\ of\ the\ material\ of\ that\ specific\ feature\ of\ the\ material}\right) \qquad (1.1)$$

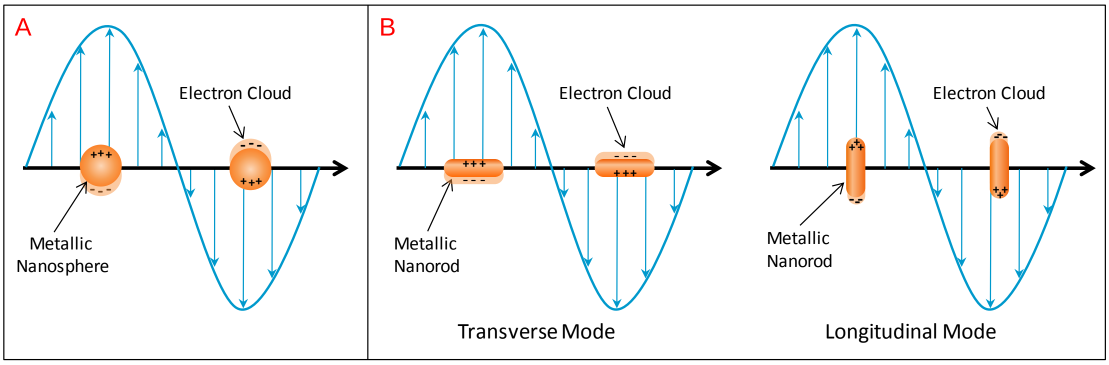

Figure 1.5: The mode(s) of surface plasmon resonance in case of (A) a metallic nanosphere and (B) a metallic nanorod.

As the shape and size of the nanoparticles changes, the change in surface geometry causes a shift in the electric field density over the surface. This leads to a change in the oscillation frequency of the electrons, generating different cross-sections for the optical properties including absorption and scattering. The oscillation frequency is usually in the visible region for gold, silver and copper giving rise to the strong surface plasmon resonance.

1.2.6. Electronic Properties

It is well known that the electrical conductivity of a solid is determined by its electronic structure. An important threshold of electrical conductance is reached when the gap between the highest occupied and the lowest unoccupied state (called the Kubo gap, δ) equals thermal energy *k*T (**Figure 1.6**).

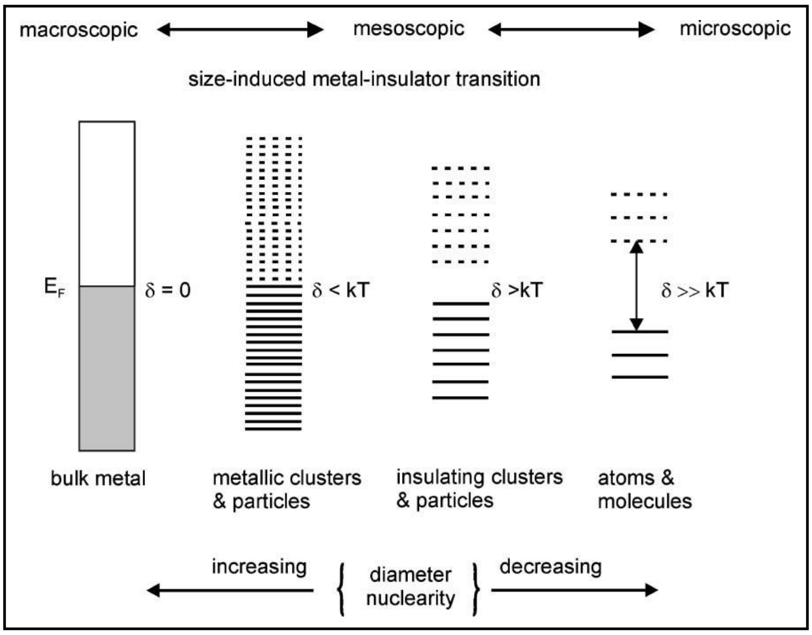

Figure 1.6: Change of the Kubo gap δ with respect to *k*T and the density of states as the size i.e. number of atoms constituting a system decreases (from left to right) (adapted with permission from ref.38, Copyright 2006 Royal Society of Chemistry).

Generally in solids, the valence band is completely filled by electrons and separated from the empty conduction band with the energy gap of E_g (band gap). For metals, since δ=0, the mixing of the valence and conduction bands is allowed. In the case of semiconductors, the value of δ is quite small. The electrons can be excited from the valence band to the conduction band simply by using heat, light, etc. which results in partial conductivity. In case of insulators, the δ is high enough to restrict electrical conductivity simply by applying physical forces like heat or light. The conducting nature of the solids is affected by various factors like, temperature and particle size[37].

For bulk metal due to their infinite array of atoms there is literally no band gap or Kubo gap between the valance and conduction band to show their easy conductivity. Compared to bulk metals, any metallic structures with much smaller in dimension (micron to nanometer) electrons start confined them in discrete quantized state to lose their band structure and results a measurable Kubo gap δ to decrease their conductivity. In case of metal nanoparticles with dimension in the range of nanometers, the density of states in the conduction and valence bands are reduced again to increase the Kubo gap further which changes the electronic properties drastically, i.e., the quasi-continuous density of states is replaced by quantized levels with a size dependent spacing to reduce the conductivity further. In this situation, the metal does not exhibit bulk metallic or semiconducting behavior. This size quantization effect may be regarded as the start of transition between metal to nonmetal. The size at which the transition occurs depends on the nature of the metal[37].

1.2.7 Mechanical Properties

Mechanical properties of solids depend on the chemical composition, the arrangement of the atoms and the overall size of the solid in one, two or three dimensions. Due to the nanometer size, many of the mechanical properties of the nanomaterials are different from the bulk materials including their hardness, elastic modulus, fracture toughness, adhesion and friction, scratch resistance, fatigue strength etc.[38] The elastic constants of nanocrystalline materials have been found to be reduced by 30% or less. These results were attributed to the large free volume of the interfacial component resulting from the increased average interatomic spacings in the boundary regions. The reduction in Young's modulus values was interpreted to be due to the porosity and cracks in the samples[39]. The parameter, strain, also determines the mechanical stability of the nanoparticles. The presence of large number of interfaces in a nanomaterial leads to the incorporation of intrinsic strain in nanosized particles. Apart from the intrinsic strain, the method of preparation may induce an extrinsic strain in these materials. Generally, the hardness increases with a decrease in grain size. But at very small grain sizes, the hardness decreases with decrease in grain size known as 'Inverse Hall-Petch relationship'. The critical grain size at which this reversal takes place is dependent on the material[40].

1.2.8 Thermal Properties

For bulk material, the thermal conductivity is believed to be an intensive property which should be independent of the size and shape of the material. According to Fourier's law, heat flux through a homogeneous material is proportional to the temperature gradient along the path of heat flow, as $J = -\kappa.\nabla T$, where κ is thermal conductivity. The macroscopic bulk systems have been observed to follow it. However, low dimensional lattices are found to violate the Fourier's law. For them, the thermal conductivity diverges with the system size L, as $\kappa \propto L^{\beta}$, where the value of β varies from 0.33 to 0.44[41]. Nanomaterials serve as the model to explore the fundamental thermal transport theory in low-dimensional system. In case of nanomaterials, the thermal energy is mainly carried by 'phonons', 'smallest packet of lattice vibration', which have a wide variation in frequency and the mean free paths (mfp). The heat capacity of the nanomaterials which is related to this phonon vibration, increases with the reduction in size, increasing order of asymmetry and defectiveness of nanoclusters[42]. But it is difficult to measure and control the transport of heat at nanoscale dimension experimentally. Atomic force microscope (AFM) has been used to measure the thermal transport of nanostructures with the help of nanometer-scale high spatial resolution probe. On the other hand the numerical solutions of Fourier's law or computational calculation based on Boltzmann transport equation and Molecular-dynamics (MD) simulation are the common theoretical approaches for simulations and analysis of thermal transport in nanostructures with certain limitations[43].

1.2.9 Magnetism

Materials those are nonmagnetic in bulk phase may exhibit considerable magnetism at nanoscale owing to several unpaired electron spins per entire particle and a ferromagnetic material may show paramagnetic behavior in colloidal state. When the particle size of ferromagnetic materials is reduced to sizes of the order of microns, the particles become single domains. As the particle size reduced further, with removal of external magnetic field, the magnetic moments of individual atoms are free to reorient to finally cancel out the net magnetization and there will be no remnant moment. Therefore, instead of the ferromagnetic property, paramagnetic property is exhibited, and this phenomenon this called 'superparamagnetism' having higher order magnetic susceptibility[44] typically 10^3-10^4 μ_B. The materials become superparamagnetic, at temperature below Curie point. They retain very high permeability and lose their magnetism or polarization when the external field is removed. At these conditions they do not exhibit any hysteresis effects. The magnetization of the superparamagnetic material is higher than that of paramagnetic material and lower than the ferromagnetic material and their coercivity or remanence exhibits an on-off characteristics in presence and absence of the external magnetic field, respectively. The critical size, below which the particles are single domain, depends on the material. In case of spherical particles, the typical values are 128 nm for Fe_3O_4, 70 nm for Co, 14 nm for

Fe[45]. Again, nanoparticles comprising several hundred atoms of Au, Pd and Pt embedded in a polymer revealed magnetic moments corresponding to several unpaired electron spins per entire particle where incompletely filled degenerate HOMO will lead to magnetism[46].

1.2.10 Cytotoxicity

One of the most important aspects in the study of nanoscience and nanotechnology is to assess the biocompatibility of nanoparticles in living systems. In the last two decades nanoparticles find enormous applications in various biological field ranging from sensing to therapy. In the fields of bio-diagnostics, therapeutics, drug delivery, bioimaging, immunostaining and biosensing, they have been proved to have great potential. Thus, it becomes very important to consider the short and long term effects of these nanoparticles on the bioavailability, uptake, subcellular distribution, cellular metabolism and degradation. This in turn depends on the shape, size and surface-functional groups of these different nanostructures and of course on the materials (element(s) that composes it). Issues of cytotoxicity of carbon nanostructures[47], CdSe quantum dots[48], silver nanoparticles[49] and gold nanoparticles[10,50]and the associated studies have been reported in the literature and measures have been undertaken to address these. Gold nanoparticles have specially been studied to check their cytotoxicity effects because it has been extensively used for various applications in the field of biomedical science as a noble metal.

The origins of unique properties on the nanoscale are different for metal nanoparticles and semiconductor nanoparticles. In semiconductors, as the particle size decreases below the Bohr radius of the material used, the electron becomes more confined in the particle leading to an increase in the band gap energy. Also, instead of a continuum, the valence and conduction bands split into quantized energy levels. Thus, minor change in size can alter the optical properties of the CdSe semiconductor nanoparticles[8]. But for metal nanoparticles, optical properties change only slightly with enlargement of size. However, with the introduction of anisotropy in the structure, considerable amount of shift can be observed. Thus the extent of Plasmon tunability with size variation is greater in case of gold nanorods than in gold nanospheres.

1.3 Common Synthetic Approaches

Among the different synthetic approaches developed, two general strategies are often undertaken for nanoparticle synthesis: i) Top down method where bulk materials are pruned down to nanoscale materials by mechanical means and ii) Bottom up method where metal ions are reduced to atoms and the atoms join up to form nanostructures. In the former method, the bulk material is sliced down successively to nanoscale by removing undesired mass. Therefore, it involves loss of materials. Common top down techniques include ball milling, photolithography and electron beam lithography. On the other hand, bottom up method has issues of lack of monodispersity or reproducibility. The essential step of every metal nanomaterial synthesis in solution is the reduction of metal precursor to initiate the nucleation process by constituent metal atoms. The growth of nanoparticles is mainly driven either thermodynamically or kinetically. Often, the intrinsic crystal stabilization and external physical or chemical parameters controls their building atom-by-atom to evolve into nanoscale materials. However, the final shape depends on several growth controlling factors. It is worth to mention that beyond a certain limit of size (above 2 nm)[51] atoms in a nanoparticle try to arrange in a particular fashion to limit their boundary by certain crystal facets along with their extent of surface exposure. Below 2 nm length scale, metal atoms in a particle are not in a position to generate defined crystal facets and are usually very unstable against any external force which could be optical, mechanical, electrical or magnetic forces. In case of noble metal nanoparticles we generally use metal salts as building blocks along with organics or biomaterials as templates or stabilizing agents to develop different size and shaped nanoparticles.

1.4 Isotropic and Anisotropic nanostructures

Size and shape dependent variation of properties of nanomaterials has extended the scope of cutting-edge research hugely in the last two decades. Motion of electrons, phonons and plasmons over the surface area is restricted and also highly dependent on nanoparticle size, shape and aspect ratio. For anisotropic materials, these effects are manifested the most. In the case of an isotropic particle, the confinement of particles, quasiparticles, energy field is to the same extent in all the three dimensions. So, the resultant properties do not vary with directions. But anisotropic material can exhibit measurable direction and dimension dependent parameters related to their physical and chemical properties upon tuning their aspect ratio (which is always 1 for an isotropic material, sphere). Most importantly, the surface plasmon resonance (SPR) in metal nanoparticles results from the collective oscillation of the conduction band electrons over the surface remains in resonance with certain frequencies of radiation. In any given sample of metal nanoparticles, the SPR manifests itself as an extinction spectrum of light passing through the sample. The spectral position of the SPR is highly dependent on nanoparticle size, shape and aspect ratio, as well as the refractive index of the metal and the surrounding medium as we have mentioned in the previous section. Anisotropic shapes have plasmon resonance absorptions that are even stronger, leading to increased detection sensitivity. Though the field density over isotropic nanoparticle is equal everywhere, structures with projected outgrowths or uneven surface area, the field density per area varies enormously depending on their relative curvature[52]. Anisotropy can originate from shape (morphological), composition (chemical), surface chemistry or their combinations[12].

1.4.1 Parameters influencing Anisotropic Growth

Preferred growth along a particular direction or facets over the other may arise from several factors–

A. Difference in surface energy of the growing facets: The surface energies associated with the different crystal faces of a particular crystal structure can differ due to the different degrees of "openness" in each face. The facet-lying-atoms with lesser coordination sites or more unsaturation are under unbalanced force, and hence more surface strain. For example, in the *fcc* crystal structure if we consider the coordination number of individual face atoms, (cyan colored atoms surrounding the central red atom in **Figure 1.7**), the {111} face is expected to be the most stable due to the close-packed nature of the atoms in the layer with the coordination number, CN = 9. The {100} face, which consists of one side of the *fcc* unit cell, has a more open arrangement of atoms (CN = 8). The {110} face is even more open (CN = 7) and so this face is expected to be the most unstable. The more unstable crystal face has the higher surface energy. They are more reactive as they are more in need of stabilization through adsorption of chemical species. Therefore, growth along the most unstable facet precedes over the other.

Facet (*fcc*)	111	100	110
Bulk atom	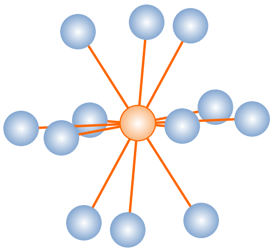 CN = 12	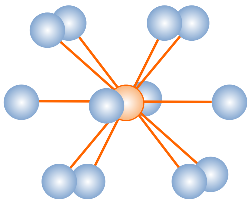 CN = 12	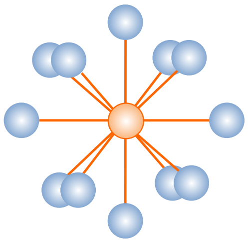 CN = 12
Face atom	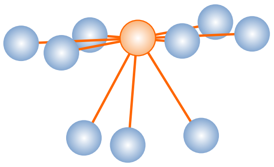 CN = 9	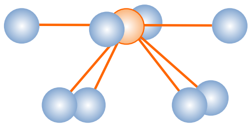 CN = 8	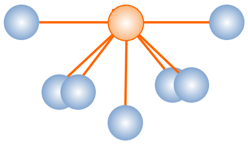 CN = 7

Figure 1.7: The modes of coordination in {111}, {100} and {110} facets of an *fcc* lattice. When present in the bulk, the central atom fulfills its maximum attainable coordination number (CN) of 12 for each facet. But if we assume that the central atoms are located at faces, then they are relatively more open. Then the CN reduces to 9 for {111} facet, 8 for {100} facet, and 7 for {110} facet.

B. Selective Blocking of facets: In an *fcc* lattice, the surface atoms in {100} and {110} crystal faces are relatively unstable than {111} having higher surface energies. If these high energy facets bind to some element or compound (salt, organic molecules, surfactants, polymer etc.) by adsorption (physisorption or chemisorption) or direct deposition then the unsaturation in coordination reduces and they are stabilized. Then only the low energy facet is available to grow. The interaction energy between a coordinating organic species and a {111} face would probably not be hugely different than the interaction energy between the organic species and a less stable {100} or {110} face, at least compared to kT[53]. Therefore, for selective binding to occur it is necessary to amplify this difference in interaction energy through cooperation between the interacting organic species. Generally this is achieved through linking the organic species together in a continuous chain, *i.e.* a polymer, or utilizing coordinating species, such as surfactants, that interact strongly with each other to form layered assemblies. The high energy facets can also be blocked by inorganic species (bromide, iodide ion)[54,55]. Silver and salts of silver having low solubility are often used to break the symmetry in gold nanostructures where selective blocking of the crystal facets is achieved via underpotential deposition (UPD) and silver halide mechanisms respectively[56]. Figure 1.8 illustrates the proposed role Ag in gold nanorod formation. The selective binding of a species is a thermodynamically driven process that leads to kinetic control over the direction of growth.

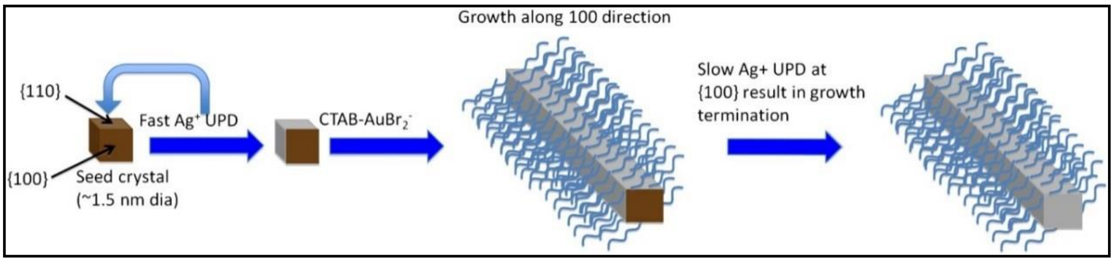

Figure 1.8: One of the proposed mechanisms elucidating the role of silver in the silver-assisted, seed-mediated method of gold nanorod synthesis. Underpotential deposition of silver occurs preferentially at the high energy {110} facets of gold, leading to relatively quick growth of other facets until the slower deposition of silver on the end of the rods eventually terminates growth (adapted with permission from ref. 58 Copyright 2011 Elsevier Ltd.).

C. Slow Kinetics: It is well established that if the reduction process is very fast, nucleation process in general is less influenced by the stabilizing agents or other factors and this leads to the deposition of atoms isotropically on the nucleation site to generate spherically symmetric nanoparticles in a bottom up technique. On the other hand, if the reduction process is slow then the system gets enough time to deposit metal atoms on the nucleation site in a facet specific way controlled by stabilizing organic ligands to provide anisotropic nature in the nanomaterials. As a thumb rule, fast reduction methods in room temperature without any physical and chemical restriction generally produce isotropic nanoparticles whereas slow reduction method of metal precursor with restriction offered by the physical and chemical parameters used during synthesis produces anisotropic nanoparticles. This slowing down of reaction can be achieved by several means which include decreasing the temperature of the reaction medium, applying low (200-300 rpm) stirring speed, using mild reducing agent or increasing the viscosity of the medium by using long chain surfactants in high concentration. These factors restrict the speed of the generation, diffusion and deposition of the atoms.

D. Seed Morphology: It is a well-established fact that the final geometry of the nanostructure is often controlled by the seed morphology as shown in the flow chart of **Figure 1.9**. First, a precursor is reduced or decomposed to form the nuclei which are small clusters composed of a collection of atoms. Once the nuclei have grown past a certain size, they become seeds of single-crystal, singly twinned, or multiply twinned structure. If stacking faults are introduced, then plate-like seeds will be formed. Sometimes anisotropic seeds are introduced into the reaction medium so that they can govern the growth as templates. Depending on the underlying crystal structure of the seed with already induced anisotropy, growth takes place to yield nanostructure of similar shape as that of the seed but with bigger dimension (e.g. from small nanorod seeds to big nanorods).

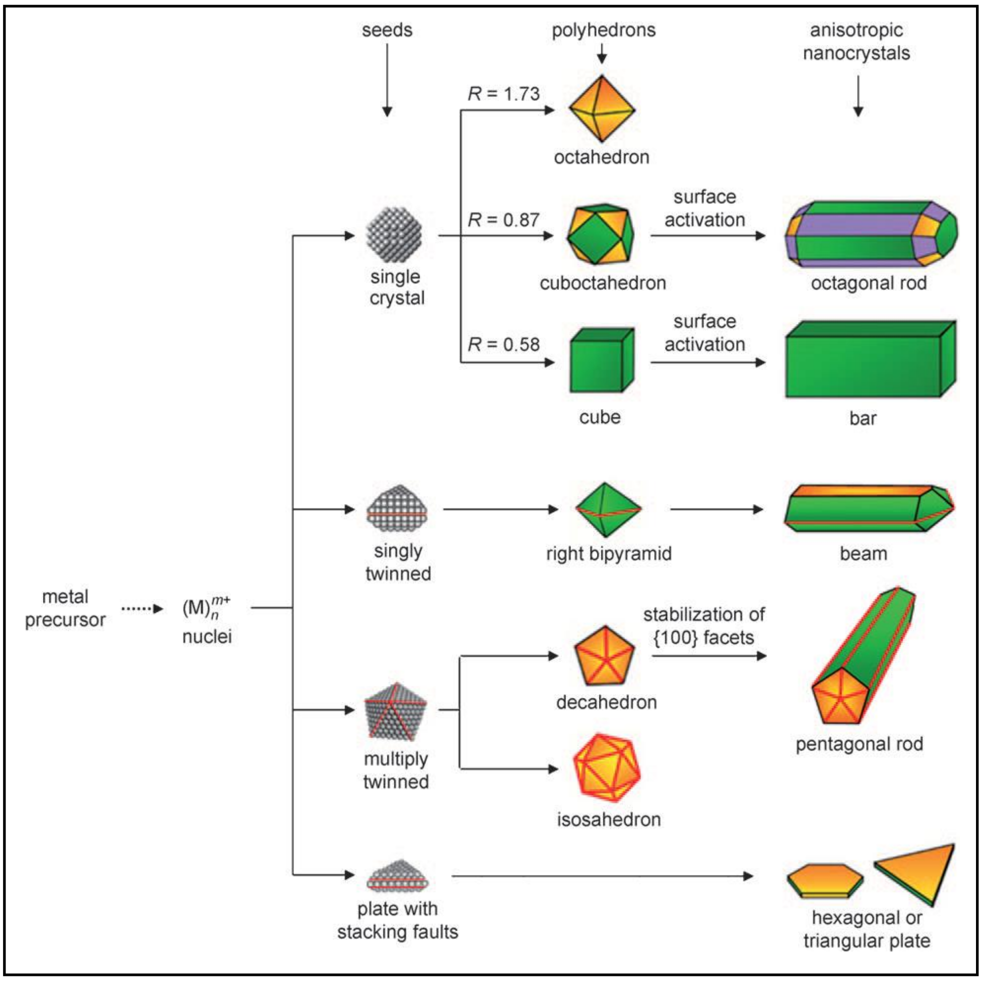

Figure 1.9: Reaction pathways that lead to *fcc* metal nanocrystals of different shapes. The green, orange, and purple colors represent the {100}, {111}, and {110} facets, respectively. Twin planes are delineated in the drawing with red lines. The parameter R is defined as the ratio between the growth rates along the <100> and <111> directions (adapted with permission from ref.11, copyright 2009 Wiley-VCH Verlag GmbH & Co. KGaA, Weinheim)

Though a diverse spectrum of anisotropic nanoparticles (ANPs) are reported in the literature, only Au and Ag based ANPs are widely used in biological applications. The possible reason for this is their high stability (e.g., gold), higher extinction coefficients, sharper extinction bands and higher photothermal heating effect.

1.5 Why noble metals?

The noble metals gained attention from the time immemorial owing to their resistance to corrosion and to the oxidation in moist air. Current literature is very rich to document nanoscale materials by most of the metals including noble metals and extends its range to pure organic nanomaterials too. Out of all these nanomaterials, noble metal nanomaterials have been treated as a special class of nanomaterials due to their striking properties which made them remarkably different from rest of the nanomaterials. These extraordinary properties include:

(i) Very high absorption coefficient and extraordinary Raman cross section

The color of noble metal nanoparticles is due to the previously mentioned SPR (**section 1.2.5**). For gold (Au), silver (Ag), and copper (Cu), incident radiation in visible region can satisfy the surface plasmon resonance condition[57]. The plasmon resonance absorption has an absorption coefficient orders of magnitude higher than strongly absorbing dyes. Specially in case of gold and silver the resonance is strong, hence huge local electric enhancement of the surface electric field takes place on the nanoparticles surface, useful for optics and plasmonics study. Due to the large optical polarization associated with the SPR, noble metal nanoparticles also show very high scattering at the SPR frequency[58].

(ii) Facile synthetic routes

Generally, the s, p block metals are too reactive to give rise to stable nanoparticles. Even, some metal precursors are highly explosive and needed to be handled with precaution. The transition metal nanoparticles, on the other hand, are often prone to oxidation and they generally form oxides and require special synthetic measures like inert atmosphere and further maintenance. The f-block elements also form oxides and the rare earth metal precursors are often too costly. Compared to them, the noble metals offer easier synthetic routes leading to stable nanoparticles.

(iii) Size and shape variation

Noble metal nanomaterials have provided immense scope to play with the sizes and shapes as surface conjugation to a variety of chemical and biomolecular ligands is possible for them.

(iv) Plasmon (absorption band) tunability

The SPR frequency depends not only on the metal, but also on the size and shape of the nanoparticle, the dielectric properties of the surrounding medium, and inter-nanoparticle coupling interactions, thus imparting a unique tunability to the nanoparticle optical properties[9,58–60]. As the shape or size of the nanoparticle changes, the surface geometry also changes causing a shift in the electric field density on the surface. This causes a change in the oscillation frequency of the electrons, generating different cross-sections for the optical properties including absorption and scattering.

(v) Biocompatibility

Apart from their unique photophysical attributes, several other factors have motivated us for the biomedicinal use of noble metal, especially Au nanoparticles. Toxicity is the most important attribute to be considered in this case. Owing to high chemical and photo-stability and biocompatibility, noble metal nanoparticles have been believed to own great potential in novel optical technologies for biology and biomedicine for long[61]. Intricate study on *in vitro* and *in vivo* cell toxicity, however, reveals the fact that the effect of noble metal nanoparticle intake depends on the dose, type of cell, capping agent used for surface modification etc.[15] There is no such unique formula for designing a nanomaterial universally "nontoxic" to all living cells and all organisms.

But there are some important findings that can be applied for reducing cytotoxic effects. In a nutshell, using the lowest dose of nanoparticle made of benign element and capping agent to get the desired response for the shortest period of time seems to promote biocompatibility.[62]

(vi) Easy Surface Modification

Due to the presence of more exposed surface area with atoms having labile d orbitals, attachment of foreign molecules to noble metal nanoparticles' surface is often easier by known organometallic chemistry. Thiolation (Thiol-click chemistry), amination, PEGylation are some commonly used methods of surface modifications with diverse applications[63]. Immobilization of thiolated and aminated nanoparticles on silicon surface allows designing handy and portable chips for sensing and removal or separation of a selected component from mixture[64]. Nanoparticles tethered with fluorescent dye or Raman probe are very important in bioimaging, biosensing, single molecule FRET etc.[65] As a drug delivery agent, internalization of drug (where molecules are embedded into hollow nanoparticles like nanocages) or externally carrying drug molecules attached to surface and then selectively discharging them under appropriate environment also depend on binding ability of these nanoparticles to them.[66] Nanoparticles can be easily functionalized with biological molecules for targeting cancer cells (**Section 1.8.2**). Gold nanorods conjugated to antibodies have been utilized for biological applications.[67]

1.6 Common Synthetic Approaches for Anisotropic Nanomaterials

In nanomaterial synthesis, type and concentration of each of the ingredients like metal precursors, reducing agents, stabilizing agents, blocking agents, nanoseeds, solvent as well as the dielectric constants, pH, temperature of the reaction medium, light exposure, stirring speed, presence of external salts or any impurity, reaction time - all of these reaction parameters play a significant role in determining the final size and shape of the nanoproduct and inducing anisotropy. The priority among these parameters and exact mechanism vary from reaction to reaction.

In the following section, some specialized strategies that are adopted for designing anisotropic noble metal nanoparticles, are discussed. The common methodologies are:

(i) Seed mediated synthesis

In seed mediated synthesis, either smaller nanocrystals are formed *in situ* or they are previously prepared are added in the course of the reaction as seed particles. After reduction the newly formed metal atoms place themselves gradually over the seed that induces aggregation of metal atoms into small clusters (i.e., nuclei) with time via self-nucleation when metal atom concentration is greater than supersaturation concentration[12]. The seed grows finally to a bigger structure until an equilibrium state is reached between the atoms on the surface of the nanocrystal. Growth per nucleation center decreases if number of nucleation center is increased. This can be achieved by raising the concentration of seed. Again, the shape is governed by the seed morphology (as described in section **1.4.1D**) along with other factors.

(ii) Adsorbate directed Synthesis

When molecules such as surfactants, polymers, biomolecules, small organic molecules, metal ions or atoms selectively adsorb onto certain crystal planes to lower their surface energy and thereby prevent the growth at those planes, anisotropic growth is induced. Adsorbate directed synthesis may take place in two different ways: (a) directed growth, and (b) oriented aggregation[68]. In a directed growth mechanism, metal atoms are added at specific planes where there is no or weak binding of adsorbate molecules allowing the crystal to grow along that plane. Addition of metal atoms is restricted over other planes that are strongly bound by adsorbate molecules. However, adsorbate molecules can also bind strongly to specific planes of preformed seed crystals and these crystals may further undergo oriented attachment along the crystal planes where there is no or weak binding, following growth in oriented aggregation pathway[69].

(iii) Template Assisted Synthesis

Template assisted synthesis is a widely used method specially for the preparation of 1D nanostructures, in which spatially and dimensionally constrained 1D nanostructures similar or complementary to those of the template shape are obtained. Hence, this method possesses precise control over both physical dimensions of nanostructures and their periodicity[70,71].

(iv) Surfactant Directed Synthesis

Depending upon the concentration used, surfactants show great control over the shape and size evolution in case of anisotropic noble metal nanomaterials synthesis. They adsorb selectively over a growing surface, capture metallic nuclei via bilayer formation, give mechanical support, direct the growth and stabilize them from agglomeration through charge separation. For example, above the critical micelle concentration, cmc, CTAB (cmc of CTAB is 0.92 to 1.0 mM)[72,73] forms lamellar self-assembly leading to two surfactant leaflets - one interacts with gold surface through the quaternary ammonium head groups at core, whereas the other end has surfactant head groups extending towards aqueous media and in between the hydrophobic tail parts of both the layers resides (**Figure 1.10**). It has been reported that the aspect ratio of the Au nano rod increases with increasing the length of this tail.

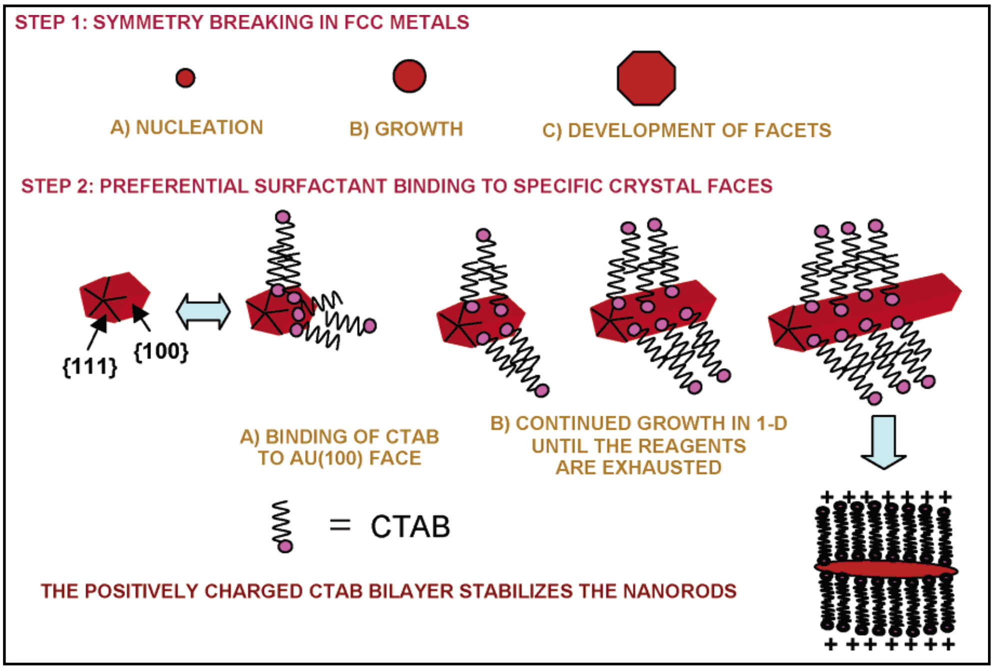

Figure 1.10: Schematic diagram showing the proposed mechanism of surfactant-directed metal nanorod growth. The single crystalline seed particles have facets that are differentially blocked by bilayer of the surfactant (or an initial halide layer that then electrostatically attracts the cationic surfactant). Subsequent addition of metal ions leads to metallic growth at the unblocked, exposed particle faces (modified with permission from ref. 71, copyright 2005 American Chemical Society).

Precisely, along with the concentration, the head groups of the surfactant, the counter ion, the alkyl chain length, presence of any double bond in the chain and its configuration (cis- or trans-) - every such aspect of the surfactant molecule has been found to have a direct effect on the morphology of a nanostructure[56,74,75]. Even trace amount of impurity in a particular surfactant can trigger unexpected change in mechanism[76,77]. Synthetic advantages applying more than one surfactant have also been investigated.[78]

(v) Biological Synthesis

In recent years, number of methods has been reported to make nanoparticles with the help of biological ingredients, such as polypeptides, enzymes, microorganisms, fungi, extract or broth from different plant parts (fruit, flower, leaf, pollen, bark etc.), live plants as well as animal body parts[79,80]. Most of them involve simple addition of metal precursor to biomaterial which is cost effective. The main advantage of such synthetic approaches is, it produces greener nanoparticles suitable for direct biological application without any further modifications[68]. Reports are there to produce different morphological samples - spherical, triangular, hexagonal, pentagonal, squares, rectangular, etc. However, a lot of time it is tedious and complicated to find out the mechanistic pathway and the actual bio-organic or inorganic substance involved in the reduction process. For the same reason, tunability with control over shape and size cannot be achieved in many cases. Generally, these methods give particles of spherical or quasi-spherical or a mixture of shapes with a wide size distribution.

(vi) Sonochemical Synthesis

Nanoparticles can be formed by treating the reaction mixture by ultrasonic wave (typically at 20 kHz). Ultrasound energy causes acoustic cavitation - the formation, growth and implosive collapse of bubbles of very small dimensions on nanosecond timescales[81]. This leads to the formation of local hot spots of very high temperature in the range of 5000 K with pressures of 1000 bar and heating and cooling rates of $>10^{10}$ Ks^{-1}. This extraordinary condition can give rise to variety of unusual nanostructures otherwise inaccessible under normal reaction space. The reactant like an organometallic precursor species gets trapped in this cavity and is decomposed at this temperature. The products are then instantaneously quenched by the surrounding solvent medium, resulting in the formation of amorphous NPs. It is possible to make a variety of transition metal NPs using this strategy.[82,83]

(vii) Solvothermal Synthesis

In solvothermal synthesis method the reaction occurs in a pressure vessel under moderate to high pressure and temperature that allows normal solvents such as water or alcohols to be heated to temperatures far in excess of their normal boiling points[84,85]. In addition, the morphology (sphere (3D), rod (2D), or wire (1D)) of the crystals formed can be controlled by manipulating the solvent super saturation, concentration of the chemical of interest, and kinetic control. The solvothermal reduction route is used widely to prepare high quality crystallized and monodispersed nanocrystals including quantum dots, metal oxides, nitrides, and novel semiconductor materials. In general, nanocrystallites with narrower size distributions, and a higher degree of crystallization can be obtained by solvothermal heat treatment compared to conventional oil-bath heating.

(viii) Electrochemical Synthesis

Electric discharge technique is one of the classical colloid preparation methods[86,87]. The electrochemical method of nanoparticle preparation induces chemical reactions in an electrolyte solution via the use of an applied voltage. This technique has the advantage of being compatible with a wide variety of materials. Electrochemical deposition is carried out by coating one face of the membrane with a metal film, which acts as a cathode for electroplating. Appropriate metal ions are then electrochemically reduced and deposited within the pores of the template membranes. The size and morphology of the nanoparticles can be controlled by varying the electrodeposition parameters, such as potential difference, electric charge passed in coulombs, temperature, deposition time, appropriate surfactants, or soluble polymers, etc., during the deposition process. Finally, the nanoparticles are released from the template by physicochemical means.

(ix) Photochemical Synthesis

Nanomaterials can be produced by photochemical reduction of the metal precursors. Here the metal ions are exposed to UV/vis radiation or laser, they directly or indirectly (in presence of an electron donating reagent) absorb the radiation energy and get reduced to atoms without requiring any chemical reducing agent, solvent or surface adsorbing species. It generates nanoparticles in a single step with high yield and purity. Shape-controlled synthesis of Ag, Au, and Pt nanoparticles by UV source, photo-catalyzed shape evolution of Ag nanoparticles using different laser wavelength are well investigated in the literature[88–91].

(x) Synthesis by Galvanic Replacement

Galvanic replacement is a solution phase redox process, where a metal of lower standard reduction potential is corroded by the ions of a second metal of higher standard reduction potential when both the metals are in contact. Two half reactions can be considered in this case: (i) the oxidation or corrosion of the first metal at the anode with loss of electrons and (ii) the reduction of the ions of the second metal gaining the electrons, and subsequent deposition of this metal at the cathode[92].The driving force for this reaction arises from the difference in their reduction potential[93]. This process is versatile and enables the production of nanostructure with hollow interior and bimetallic alloyed shell of thin to ultrathin walls in a single reaction step. But often the final morphologies are limited to shapes that represent the hollow analogues of the starting template nanocrystals.

1.7 Selected Applications Relevant to Current Study

1.7.1 Sensing

The principle behind designing a sensor is simply to alter a property of the sensor by the entity we want to sense. In case of nanoparticles, the LSPR frequency depends on the dielectric constant, i.e. the refractive index, RI of the medium surrounding the nanoparticle. With increase in the medium's RI, LSPR red shifts[65]. If this shift is reflected in the absorption or scattering spectroscopy, changes in the environment of the nanoparticles can be detected. The chemical or biological species which is the target analyte can affect the local RI in several ways, like – it can (i) bind to the nanoparticle surface directly, (ii) conjugate to recognition molecule(s) already attached to the nanoparticles, (iii) deform the structure of the nanoparticles (either by removing atoms from the surface or to cause aggregation), (iv) affect the binding of the nanoparticle-dye composite. In each case, the absorption or fluorescence or Raman spectrum exhibited by the nanoparticle itself or its modification has to show a measurable change to construct a usable optical sensing tool. Colloidal plasmonic and fluorescent nanoparticles are most useful probes as they give intense response to incident radiation[94]. Binding has to be specific to detect the target analyte in mixture. Often detection in a real matrix is asked for to validate the sensor applicability. Also, the change in spectra in response to RI should be regular and reproducible so that a standard plot can be obtained. This plot then can be used to trace the same target analyte in an unknown sample. To achieve sensitivities down to few molecules bound per nanoparticle, the plasmon band shift, or the change in intensity of fluorescence or Raman spectra is desired to be as high as possible in response to small RI changes. For this, nanostructural parameters are tuned to increase the plasmonic sensitivity

(Plasmon shift per refractive index unit (RIU) change). Shape of the nanomaterials is a factor easy to tune for attaining maximum sensitivity and that is why anisotropic nanomaterials are so important in this context. It is reported that nanostructure geometries that offer good plasmon resonance tunability also offer high plasmon sensitivity[95]. Thus silver nanoprisms (100 nm width, 50 nm height), with high sensitivity (200 nm/RIU), have been used for the detection of streptavidin, Alzheimer's disease markers and even in single-particle assays[65]. Other than prisms, i.e. triangular particles, structures having high surface curvature (high shape factor value) like nanorods, nano-bipyramids[13,96], tips and junctions like nanostars, nanoshells, particle dimers[97–99]also have been applied as useful sensors. Metal nanoshells show nearly exponential increase in the plasmon sensitivity with decreasing shell thickness relative to core size. When a nanodimer or any assembly of nanoparticles is formed, the LSPR of individual nanoparticle red-shifts due to favorable coupling between adjacent plasmon fields of the interacting particles. The red shift depends on the interparticle distances in the assembly. If the particles are appropriately functionalized, they form assembly in presence of the bioanalyte. It induces absorption shift or color change which have been applied in sensing DNA, antibody-antigen interactions, and disease biomarkers[100]. Some of them include the precision synthesis of nanoparticles in microfluidic systems, ultrasensitive detection of cancer biomarkers in human serum with time-gated QD fluorescence, multiplexed intracellular sensing of mRNA using superquenching AuNPs, multiplexed detection of analytes with simple technologies such as smartphones, *in vivo* sensing of reactive oxygen species and methyl mercury, and the integration of nanoparticle biosensors with advanced DNA/RNA target amplification protocols[94]. Functionalized nanomaterials have also been applied in different metal ion (especially heavy metals) sensing[101,102]. Another kind of sensing application of nanomaterials involves designing electrochemical sensors. Metal nanoparticles with high conductivity and catalytic properties, can act as "electronic wires" to enhance the electron transfer between redox centers and electrode surfaces, and increase the rate of electrochemical reactions as catalysts[19,103,104]. The specificity of the compound under investigation is characterized by position of peak potentials (measured by voltage) and the output current changes with the concentration which measures the sensitivity of the assay.

1.7.2 Diagnostics

Owing to the noble characteristics i.e. more biocompatibility and being an efficient scatterer of light (at the LSPR frequency), noble metal nanoparticles have been used in optical imaging and labeling of biological systems for long. Gold nanoparticles (AuNPs) have been used as radioactive labels *in vivo* since the 1950s[105]. Immuno-AuNPs conjugated to antibodies have been applied in electron microscopy for biological staining since the 1980s[106]. A number of imaging methods have been developed in recent years for better understanding of different biological processes occurring in living cells, tissues, organs, and to detect and quantify the disease in humans for coming up with better treatment methodology. Various methods ranging from conventional magnetic resonance (MR), positron emission tomography (PET), and ultrasound (US) to emerging optical approaches such as computed tomography (CT), single photon emission CT (SPECT), and near-infrared optical imaging (OI) have been used for medical and clinical research. In diagnostics, AuNPs offer several advantages over quantum dots and organic dyes.[107] AuNPs show low or no toxicity, their refractive index, distance from the surface, and also the surface features contribute to enhancement of spectroscopic properties, they are much better contrast agents for imaging compared to the organic dyes which are limited by rapid photobleaching. Size of the nanoparticle is very crucial for their uptake and retention by the cells and tissue[108]. Again, for *in vivo* imaging and therapeutic applications, the absorbance of the nanoparticles is strongly recommended to be in the near-infrared (NIR) region of the physiological window (650-1300 nm), to safely attain highest tissue transmittance[109]. Though the scattering from a 10 nm AuNP is negligible, a 40 nm AuNP shows an absorption cross-section 5 times higher than the conventional absorbing dyes, an 80 nm AuNP gives scattering 5 orders of magnitude larger than the typical emission from a strongly fluorescing dye[110]. Au nanocage has been reported as an attractive contrast agent with their strong, tunable SPR peaks with high absorption cross section in the near-infrared and comparatively smaller size. Such highly enhanced cross sections facilitate sensitive and highly contrasted imaging for dark-field microscopy and optical coherence tomography (OCT) imaging.[111,112] Baptista *et al.* has marked three distinct approaches involving AuNPs for biodiagnostics: (i) colorimetric sensing of specific DNA hybridization for the detection of specific nucleic acid sequences in biological samples based on inter-AuNP distance[113], (ii) surface-functionalized AuNPs providing highly selective nanoprobes, and (iii) signal enhancement by electrochemistry based approach.[114] Among the clinical diagnosis methods involving AuNPs immunoassays, there are standard enzyme-linked immunosorbent assays (ELISAs) for signal enhancement. Up to 1 $pg.mL^{-1}$ of the chorionic gonadotropin hormone has been detected using immunochromatographic test strips where both the primary and secondary antibodies are conjugated with the AuNPs[115]. Other sensors involving AuNP-functionalized fiber-optic evanescent wave[116]or AuNP-functionalized Cy5-antibody as the fluorescence probe are even better in sensitivity and they do not require a secondary antibody as in case of the standard ELISA assay[117]. AuNP probes have been used extensively as a marker of cancer, alzheimer, HIV, hepatitis B, tuberculosis, diabetes etc.[107]. Silver nanoparticles also have been applied in diagnosis, however, their use is somewhat limited by the cytotoxicity.[118] In general, noble metal nanoparticles are utilized in enhanced biomolecular diagnostics, including single-nucleotide polymorphism detection, gene expression profiles and different biomarker characterization[119,120].

1.7.3 Therapeutics - Photothermal Treatment

One major therapeutic application of noble metal nanoparticles is killing cancerous and infectious[121] cells by photothermal treatment[122]. Gold nanoparticles conjugated to cell specific antibodies can selectively bind to the membrane-proteins characteristic to the infected cells whereas extent of binding with the healthy cells remain insignificant[123,124]. Irradiation of these nanoparticle-labeled cells with suitable laser source of wavelength overlapping with the LSPR absorption maximum of the antibody coated nanoparticles results in selective heating and destruction of infected cells at much lower laser power than that required in case of healthy cells to which nanoparticles do not bind specifically. By principle, photothermal therapy is based on selective photothermolysis of a biological tissue containing a chromophore which can be a natural or artificial substance with a high coefficient of light absorption[5].As gold nanoparticles offer absorption coefficients 5 or more orders of magnitude larger compared to conventional dyes, much lower laser energy is sufficient to achieve cell destruction, making therapy minimally invasive[123,124]. Many plasmonic nanoparticles have absorption maxima in the visible and NIR region. In case of an anisotropic nanostructure, if the size and shape can be controlled, the absorption maxima vary accordingly and can be tuned as desired. While the use of visible light resonant gold nanospheres can be useful for exposed tumors or infected parts like external skin or surface cancer treatments, for tumors within bodily tissue, it becomes necessary to use NIR radiation in the biological window (650 nm-1350 nm). It has been demonstrated that the NIR absorbing capacity of several anisotropic nanomaterials such as nanorods [125], nanocages[126,127], nanoshells[128,129], nanopopcorns[60,130] can be used for the photothermal therapy. Also, due to the assembly of metal nanoparticle clusters on cells and resulting SPR coupling-induced red shift, absorption in NIR window can be achieved[131]. Even, NIR therapy with gold nanospheres is also possible by utilizing their two-photon absorption of 800 nm laser light[132]. Further, anisotropic metallic nanoparticles offer dual functions of therapy combined with darkfield imaging, which is a significant advantage over other non-metallic photothermal absorbers, such as quantum dots or carbon nanotubes, which are generally neither good scattering agent, nor possess phonon-based lattice vibration. Also, to exhibit fluorescence, they are needed to be excited in UV region which is formidable for in vivo application. As a result, their use has been restricted to only one of the two, imaging or therapy. During photothermal therapy, the light absorbed by the gold nanoparticles through Plasmon excitation is transferred to the nanocrystal lattice through electron-phonon coupling which creates the localized heating and can elevate the sight specific temperature very high. Thermalized nanoparticle will try to release the heat content by phonon-phonon relaxation and dissipates the energy to the surrounding antibody, aptamer, and cell environment. The mechanism of photothermal therapy is shown in **Figure 1.11**. It is well accepted in the literature that the plasomonic excitation which is a femto second (*fs*) phenomenon initiates the electron-phonon followed by phonon-phonon coupling in the picoseconds (*ps*) time scale ultimately raises the temperature suitable to decouple and break the bond between nanosurface and cargo molecule to release then from the surface in the nanosecond (*ns*) time scale.

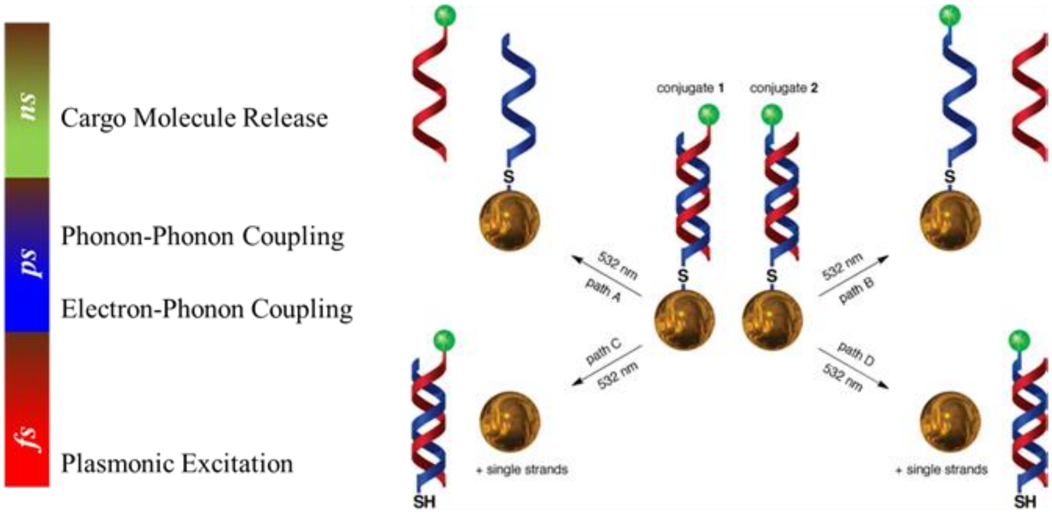

Figure 1.11: Illustration of mechanism of photothermal therapy. Right side figure shows the photothermal DNA/RNA melting for programmable drug release. Left side colour coded diagram explains the time scale for different electronic and plasmonic processes on nanoparticle surface.

Upon irradiating with a light source of same or closer wavelength, the nanomaterials can generate localized heat as high as few thousand Kelvin[133]. Due to the large absorption cross-sections of Au nanoparticles, the absorbed photons induce phonon vibrations of the crystal which finally dissipates as thermal energy to increase the temperature of the nanosystem. Hence by employing ultrafast laser (NIR)-induced heating process we can study the dynamic processes of drug release on the nanoparticle surface. By varying the power density, the duration of laser exposure, and the time response after irradiation, it is possible to optimize the treatment conditions to achieve effective destruction of the cancer. The percentage of dead cells increased with increasing exposure time. However, flat nanostructure like nanotriangle, with greater contact between the nanoparticle and cancer cells can reduce the required exposure times.[134] It is also reported that under same exposure conditions, ANP based PTT showed much better results than conventional Photo Dynamic Therapy, PDT[135]. In PDT based cancer therapy, singlet oxygen ($^1O_2$) formed by the influence of light on photosensitizer leads to cancer cell death by oxidative stress[136,137]. When the nanomaterials are attached to the target cell conjugating them with antibodies or other molecules like aptamers, they can transfer the generated huge heat locally inside or around the cell. ANPs can also be targeted passively to cancer cells through ‘enhanced permeability and retention’ (EPR) in cancerous cells. It leads to disruption of cell membrane permeability by punctating, controlled localized denaturation or cleavage of proteins and/or nucleic acids and eventually results to irreversible cell death. Thus metal nanoparticles serve as “light-activated nanoscopic heaters” for selective laser photothermolysis of cancer cells[98].

1.7.4 Superlattice

Nanoparticle superlattices are a kind of ordered assembly having periodic arrays of nanoscale inorganic building blocks including metal nanoparticles, quantum dots and magnetic nanoparticles. Such assemblies can exhibit exciting new collective properties different from those of individual nanoparticle or corresponding bulk materials and even disordered nanoparticle assemblies. For example, (i) coherent vibrational modes can only appear in highly ordered nanoparticle superlattices[138], (ii) synergistic effects in superlattices can lead to enhanced p-type electronic conductivity than the sum of the individual nanoparticle components[139], (iii) the direct-current conductivity of semiconductor films can be manipulated over at least six orders of magnitude by the addition of noble metal nanocrystals[140], (iv) 2D metal nanoparticle free-standing-sheets show unusual mechanical properties like Young's modulus of the order of several GPa, high flexibility and resilience, ability to withstand tensile stresses at even elevated temperature[141,142], (v) 2D superlattice sheets made of plasmonic nanomaterials, (termed as ‘Plasmene’, in analogy to graphene) exhibit novel plasmonic properties with unique structural features and plasmon propagation functionalities, well-pronounced dipolar, quadrupolar and octapolar localized surface plasmon resonance (LSPR) bands[143,144],(vi) spin-dependent tunneling influence magnetotransport properties in highly ordered magnetic-nanocrystal arrays[145], (vii) reversible metal-insulator transition is reported for silver quantum dot monolayers[146] etc. In addition, a variety of structures have been found to be formed by the superlattices e.g. face-centered cubic (*fcc*), body-centered cubic (*bcc*), hexagonal-closed packed (*hcp*), diamond-like lattice, and also lattice structures not existing in nature[147,148]. These properties depend on several factors different from case to case, like, the collective mechanical property is influenced by the ligands, rather than the metallic cores, whereas plasmonic properties depend mostly on the size, shape, composition and the packing order of the nanoparticles, again the electronic properties (being constrained by hopping of electrons among and beyond nearest neighbors) are highly affected by the presence and density of the dopants. However, the average potential energy and proximity among the particles are the two key parameters governing superlattice properties. The assembly of nanoparticles of two different materials is a special kind of superlattice materials (metamaterials) termed as binary nanoparticle superlattice that allows precisely controlled chemical composition and tight placement of the components. In theory hard spheres can lead to only a few stable binary superlattice structures, potentially limiting this approach. But additional contributions from entropic, van der Waals, steric and dipolar forces arising at the nanometer scale can stabilize a variety of binary nanoparticle structures. Shevchenko *et al.* has reported the synthesis of more than fifteen different novel structures from various combinations of metal, semiconductor, magnetic and dielectric nanoparticles[149].This demonstrates the potential of self-assembly in designing families of novel materials and metamaterials with programmable physical and chemical properties: (a) binary superlattices of semiconducting and magnetic nanoparticles can be applied for spintronic and magneto-optic data storage devices, (b) superlattices comprising two different semiconductors can be used for a new generation of thermoelectric devices and solar cells, (c) binary superlattices can be used to prepare multifunctional metamaterials, new effective catalysts with an accurate arrangement of catalytic centers[150]. In conclusion, superlattices have potential applications in future optoelectronic devices, biological diagnostics and energy-harvesting systems.

CHAPTER 2

EXPERIMENTAL METHODS, INSTRUMENTS, AND MATERIALS

OUTLINE: What does the chapter brief?

- Working principle of the characterization techniques involved
- Particulars about the instruments
- Specific methodologies that we apply
- List of materials used as a standard

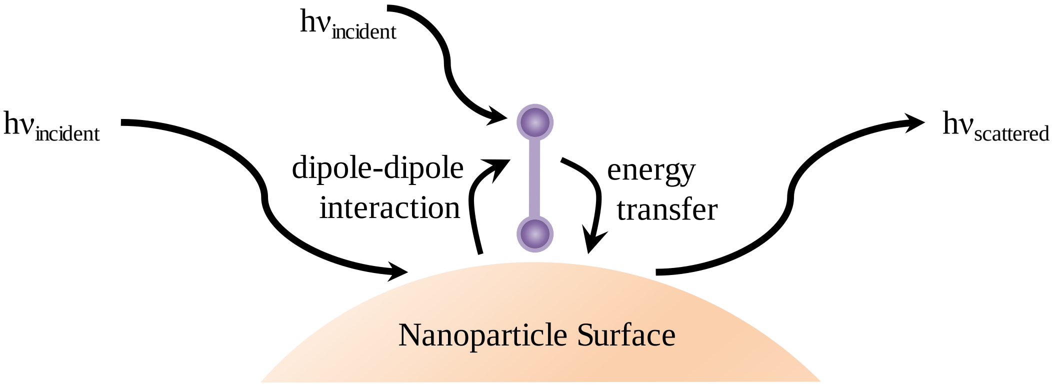

2.1 Characterization Techniques

A number of techniques are on hand for characterization of materials, which may be used to study nanoparticles also. The mostly used probes among them are electron, photon (light and X-ray), neutron etc. as they are complementary to the sensitivity at this nanoscale. These techniques can be broadly classified into (i) spectroscopic and (ii) microscopic techniques. Spectroscopy is widely used for the study of optical properties of different materials including nanoparticles. It includes measurement of absorption, emission as well as scattering of radiation depending on its interaction with the materials under investigation. On the other hand, microscopic techniques involve interaction of electron beams with the specimen, and the subsequent collection of transmitted or scattered electrons in order to develop an image. This process may be carried out by scanning of a fine beam over the sample surface (e.g. scanning electron microscopy) or by wide-field irradiation penetrating through the sample (e.g. transmission electron microscopy). The advantage of microscopic techniques is that it helps in the direct visualization of the nanoparticles.

2.1.1 UV-Vis-NIR Absorption Spectroscopy

2.1.1.1 Working Principle

Ultraviolet, visible and Near Infra-Red absorption spectroscopy measures the absorption, transmission and emission of radiation of corresponding wavelengths by matter in solution as well as in the solid and gaseous state[151,152]. When a radiation strikes atoms or molecules they may either bounce off or may cause the electrons to jump between well-defined electronic energy levels. Absorption of the electromagnetic radiation causes the electrons of the substance to move from lower energy levels to higher energy levels. This absorption wavelength strongly depends on the functional groups present in the molecule, the particle size, dielectric constant of the medium and chemical surroundings[153]. The intensity of absorption is directly proportional to the effective number of species (molecules or particles or ions) taking part in absorption. UV-visible spectroscopy enables the characterization of functional groups in a molecule as well as the determination of their concentration as per Beer-Lamberts law: $A = \varepsilon l c$, where A = Absorbance, ε = the molar extinction coefficient or molar absorptivity (or absorption coefficient), l = path length traversed by light through the sample and c = concentration of the sample.

The spectrophotometer comprises of a light source (generally hydrogen or deuterium arc lamp ranging 190-400 nm, light emitting diodes, Xenon arc lamp covering 160-2000 nm, tungsten filament with range 300-2500 nm etc.), a mirror, a collimator (lens) that converges the light, a filter, a monochromator (prism or grating) that can split the light into different wavelength constituting the light, a beam splitter, a wavelength selector (slit) that allow a range of wavelength or a particular wavelength, holders for placing cuvettes to take the sample as well as reference solution, a photoelectric detector (photomultiplier tube, photodiode array, charge-coupled device), and a digital display or a meter (**Figure 2.1**).

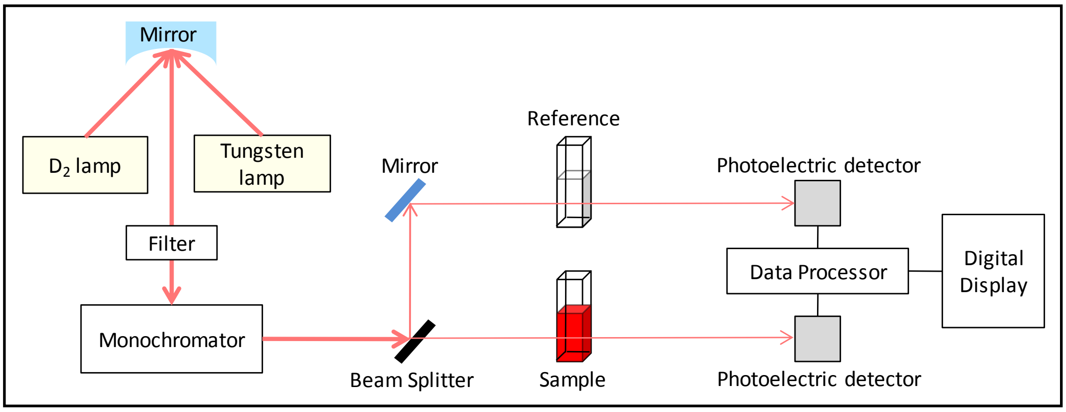

Figure 2.1: Schematic diagram showing different components present inside a spectrophotometer.

In case of nanomaterials, UV-vis-NIR spectra help to predict the following insights of a sample: (i) Size of the nanoparticles and its tunability, (ii) Shape - whether it is isotropic or anisotropic and what are the probable origin of different plasmonic modes, (iii) Possibility of aggregation which leads to broad tailing in higher wavelength region, (iv) kinetics of their growth (v) degree of monodispersity of the sample etc. Apart from these basic ideas, spectral data are also useful in purification step e.g. to confirm how effectively one nano-component in a mixture is separated from others after fractional centrifugation.

2.1.1.2 Instrument and Operating Parameters

In this thesis most of the UV-vis and vis-NIR absorption spectra were recorded on a Jasco V-650 and Jasco V-770 spectrophotometers respectively using a quartz cuvette with a 1 cm optical path at room temperature. In Jasco V-770 instrument, a photomultiplier tube detector is used for the UV to visible region and a peltier-cooled PbS detector is used for the NIR region. For silver nanowire characterization the vis-NIR absorption spectra were recorded in a PerkinElmer Alpha 750 spectrophotometer under similar conditions.

2.1.2 Scanning Electron Microscopy

2.1.2.1 Working Principle

Scanning electron microscopy (SEM) is a powerful and popular technique for imaging the surfaces of almost any material with a resolution down to about 1 nm[154]. The image resolution offered by SEM depends not only on the property of the electron probe, but also on the interaction of the electron probe with the specimen. When an electron beam impinges on a surface of the sample, it can penetrate the sample to a depth of a few microns, and scattered electron, photon and X-ray are produced in a volume called the ‘interaction volume’. This volume depends on the accelerating voltage of the electron beam, the mean atomic mass of the sample and the angle at which the beam hits the sample surface[155]. The interaction of an incident electron beam with the specimen produces secondary electrons (SE). The emission efficiency depends on the surface geometry, surface chemical characteristics and bulk chemical composition. SEM can thus provide information about the surface topology, morphology and chemical composition. Other than SE, interaction between the electron beam and the sample also generates back scattered electrons (BSE), X-ray, and Auger electrons in a bulk sample. These various electrons are detected in SEM and the signal detected contains information about the specimen under investigation. Specimen of higher atomic number produces BSE more because they are more likely to reflect back the electrons. The electron beam is applied in a raster scan approach, and the position scanned by the beam is correlated to the detected signal output to produce an image.

2.1.2.2 Instrument Details and Operating Parameters

The ZEISS SUPRA 40 scanning electron microscope fitted with a hot Schottky field emission gun (FEG) was used to obtain secondary electron images. For SEM measurements we used pieces of mirror polished p-type silicon wafers as sample support. We injected about 20-30µL of the concentrated nanomaterial sample on the tilted silicon wafer and the hydrophobicity of the wafer allows only a monolayer of the sample (mostly hydrophilic in nature as they are synthesized in water medium) to stick to the surface. It gets dried quickly to allow an immediate SEM measurement.

2.1.3 Transmission Electron Microscopy

2.1.3.1 Working Principle

Transmission electron microscopy (TEM) has played a key role in driving our scientific understanding of different physical, chemical and biological properties of a specimen under investigation, starting from material growth to cell dynamics, far beyond mere structural characterization. TEM is capable of imaging at a significantly higher resolution than the visible light microscope, owing to the small de Broglie wavelength of electrons. This enables the instrument's user to examine finer detail—even as small as a single column of atoms (up to a sub-angstrom level), which is tens of thousand times smaller than the smallest resolvable object in a light microscope.

In TEM, the specimen is prepared as a thin foil through which a parallel beam of electron is transmitted. Electrons interact with the specimen and produce different useful signals. The imaging lens or objective lens delivers a diffraction pattern in its back focal plane and an image which is then magnified on the fluorescent observation screen or detected by a sensor such as a CCD camera.[156] One major difference between SEM and TEM is that TEM detects transmitted electrons whereas SEM detects backscattered and or secondary electrons. The main parts of the microscope column are therefore the source of accelerated electrons, the ‘gun’, the illumination system with electron optics, the specimen manipulation system, the stage, the imaging system and the vacuum system.[157] **Figure 2.2** represents a simple schematic diagram of these parts in a visible light microscope (VLM) and those in a transmission electron microscope (TEM). The electron gun utilizes either thermionic emission or field emission depending on the requirement of brightness of the beam. Below the electron gun are condenser lenses that control the diameter of the beam that pass through the specimen. Deflection of electrons is caused by electromagnetic lenses, below which the specimen chamber lies where the specimen is held in the correct position with respect to the objective lens. Smooth manipulation of the horizontal position and angular tilt are permissible as necessary, however. The objective lens forms an intermediate magnified image and is also responsible for improving the contrast in the image.[155] The intermediate image is enlarged to the final magnification by a set of (two or three) projector lenses. Below the final projector lens, lies the fluorescent screen. The function of the vacuum system is very crucial in all TEM instrumentation. Owing to shorter wavelength, electrons can be very much more easily absorbed by many materials including oxygen than is light. To get rid of this unwanted absorption of electron energy by oxygen and to increase the penetration effect through sample specimen, all the electronic paths inside the microscope are evacuated to a pressure less than 10^{-4} Torr.[155]

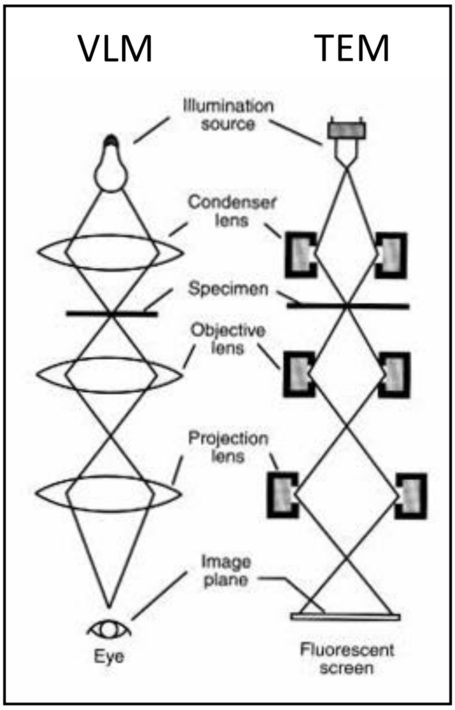

Figure 2.2: Schematic diagram of these parts in a visible light microscope (VLM) and those in a transmission electron microscope (TEM). (Adopted from Ref. 157).

2.1.3.2 Instrument and Operating Parameters

For both the normal and high resolution transmission electron microscopy (HRTEM) measurements we used a FEI, Tecnai G^{2}F30, S-Twin microscope operating at 120 and 300 kV, respectively. Compositional analysis was performed by energy dispersive X-ray spectroscopy (EDS, EDAX Inc.) attached to Tecnai F30. We used simple but modified techniques for close-to-clean monolayer sample preparation both for TEM and SEM. For the TEM measurements we used a 300-mesh copper formvar/carbon grid and followed either (i) drop casting or(ii) dip-and-dry technique to make the grid samples. For as–synthesized, relatively dilute nanomaterial solution we followed the drop casting method where a tiny volume of about 5-6 µL (just detachable from the tip) is dropped over the grid. For a concentrate nanomaterial solution like a centrifuged one, we used dip-and-dry technique where the TEM grid is immersed in the sample solution using a sharp and flexible tweezer. Hydrophobic formvar/carbon coating allows building up a monolayer sample stuck to copper mesh dried on a soft tissue paper. The grids were left undisturbed to get dried under ambient condition. After complete drying, the grid was used for TEM measurements.

2.1.4 Surface Enhanced Raman Scattering (SERS)

2.1.4.1 Working Principle

Raman spectroscopy has been established as an important analytical method for the specific identification of molecules. Experimentally this technique involves directing a tightly focused monochromatic light source (like laser) onto an unknown chemical sample. Most of the incident light will be scattered back at the same laser wavelength and results Rayleigh scattering. However, a small portion of it may be inelastically scattered at series of different wavelengths that are indicative of the vibrational transitions in the molecule. If there is a modulation of molecular polarizability (α) by the vibrations then only those vibrational modes of the molecule are Raman active[151]. In normal Raman we tune the excitation energy (by tuning the wavelength of the radiation) in such a way that the incident light is not capable to excite them to the first excited electronic level next. In that case molecule end up excited to a ‘virtual’ state (a state of unknown Eigen function) between the two states. The molecule, however, cannot stay long in the virtual state and will immediately come back to the ground state by radiating a single photon. If the molecule comes to the same vibrational level from where it was excited, the wavelength of the scattered light is the same as that of the incident light and the process is termed as Rayleigh scattering. It is also possible that the molecule may come back to a different vibrational level of the ground electronic state than from where it is excited either by radiating a photon with more or less energy that the incident radiation. This creates an energy difference between the emitted photon and the incident photons. If the emitted energy is smaller than the incident energy i.e., if the molecule absorbs some energy during the interaction then the process is called the Stokes scattering and if the emitted energy is greater than the incident energy i.e., if the molecule loses some energy during the interaction then the process is called the anti-Stokes scattering. As different molecules have different bonds and different combination of vibrational modes, the spectrum of inelastically scattered light can be thought of as analogous to a molecular fingerprint, uniquely identifying the molecule. But despite this high specificity, traditional Raman spectroscopy was considered limited because of very poor efficiency (cross section) of the inelastic scattering process and thus relatively weak signal. In fact we consider cross section, which is nothing but the probability of interaction of photon with the molecule, for Raman it is only 10^{-31}-10^{-26} cm^2/mol (whereas in case of fluorescence it is 10^{-15}-10^{-16} cm^2/mol). Emission intensity directly changes with cross section. So it is the biggest disadvantage of Raman Spectroscopy. However, with the advent of SERS, both the issues of specificity and sensitivity were overcome. Using this method, it is possible to probe even a single molecule adsorbed onto nanoparticle surface. Over 40 years ago, SERS was first observed in case of pyridine adsorbed on roughened Ag electrode.[158]But that time it was not recognized as an unusual new phenomenon. Later in 1977, it was simultaneously discovered by Jeanmaire, van Duyne and Albrecht and Creighton.[159,160]

In fact, a Raman spectrum serves as a “molecular fingerprint” of a Raman active sample, yielding information on molecular bonds, conformations, and intermolecular interactions. However, in spite of its advantages, its practical uses have been significantly limited as the Raman scattering signal is intrinsically weaker than most other fluorescence signals. Methods of enhancement have been developed to extend the detection limit. Among various methods, enhancement with noble metal nanostructures, a technique termed surface-enhanced Raman scattering (SERS), has been found to increase the output dramatically.

Though the SERS is approximately 40 years old,[159–163] most of the seminal research was carried out to understand the effect and it was largely understood that the SERS is primarily the result of electromagnetic enhancement associated with the excitation of intense and sharp localized surface plasmon.[164] Several research work in the last 20-30 years reveals that only the electromagnetic enhancement mechanism cannot explain the entire enhance factor rather need to consider other enhancement mechanism along with a deep knowledge of condensed matter physics and optical response of materials. Increase in intensity of Raman signal or Raman cross section has been regularly observed on the order of 10^4-10^6 and can be as high as 10^8-10^{14} for some systems. The total enhancement (TE) is attributed to two enhancement effects: Electromagnetic enhancement (EME) and Chemical enhancement (CE) which act multiplicatively i.e. TE = EME × CE.

2.1.4.1.1 Electromagnetic Enhancement Theory

If we consider a metal sphere with dimension much smaller than the wavelength of the interacting electromagnetic radiation, the metal sphere will sustain oscillating surface Plasmon multipoles of various order induced by the time-varying electric field vector of the incident light. This collective oscillation of the conduction electrons against the background of ionic metal core is defined by surface Plasmon and described in details in the introduction section. Though for smaller particle we need to consider only dipolar Plasmon but for bigger particles we have to consider higher modes too for proper estimation of the extent of light matter interaction. When the exciting light is in resonance with the dipolar Plasmon of the metal particle, it will radiate light with characteristics of dipolar radiation as a result of the coherent process with exciting field and is characterized by a spatial distribution of field magnitudes in which light intensity from a certain portion of space surrounding the particle is depleted while the intensity at certain portions near the metal particle is enhanced.[165,166] If we consider that the field enhancement factor (g) is averaged over the surface of the particle then the average magnitude of electric field (E_S) radiated by the metal particle can be mathematically defined as, $E_S = gE_0$ with E_0 as the magnitude of the incident field. Since E_S is the average local near field at the particle surface, molecules adsorbed at the surface of the metal particle will be excited by a field of magnitude E_S and the Raman scattered light produced by the molecule on the surface will have a field strength $E_R \propto \alpha_R E_S \propto \alpha_R g E_0$where α_R is the tensor component of polarizability. The Raman scattered fields can be enhanced further by the metal particle in exactly the same manner as the incident field was, i.e. the metal particle can scatter light at the *Raman-shifted* wavelength enhanced by a factor g'. As the cumulative affect the resultant SERS field intensity thus can be expressed as $E_{SERS} \propto \alpha_R g g' E_0$ and the average SERS intensity $I_{SERS} \propto |\alpha_R|^2 |gg'|^2 I_0$ where I_0 is the intensity of incident field. For low-wave number bands when$g = g'$, $I_{SERS} \propto |g|^4 \propto |E_S|^4 \propto \left|\frac{1}{\lambda}\right|^4$ and classically known to us for long time. For higher Raman modes the SERS intensity may not follow the same mechanism and we need to consider complicated Plasmon resonant properties of the metal nanoparticle in the form of Chemical Enhancement factor will be discussed the next section. In general, we can define the SERS enhancement due to Electromagnetic field enhancement, G, as the ratio of the Raman-scattered intensity in the presence of the metal particle to its value in the absence of the metal particle

$$G = {I_{SERS}}/{I_R} = {|\alpha_R|^2 |gg'|^2 I_0}\Big/{|\alpha_{R_0}|^2 I_0} = \left|\frac{\alpha_R}{\alpha_{R_0}}\right|^2 |gg'|^2 \qquad (2.1)$$

where, $\alpha_{R_0}$is the Raman polarizability of isolated molecule in absence of surface. Hence, to understand the electromagnetic enhancement of Raman scattering we need to consider the following four factors:

(1) Since $G \propto g^4$ and g is surface quantity, the major contribution in SERS comes from metal particle rather than by the surface adsorbed molecules.

(2) Though the $I_{SERS} \propto g^4 \propto E^4 \propto \left(1/_{\lambda}\right)^4$, the SERS effect is a linear optical effect that depends on the first power of I_o. To understand the extensive effect of g on SERS let us consider the Raman effect on silver nanoparticle. At 400 nm excitation near AgNP Plasmon the g has a measured value of ~30 which alone can contribute $30^4 = 8 \times 10^5 \sim 10^6$ factor to the Raman enhancement efficiency. By assuming even a considerable change in Raman polarizability, relative contribution cancels out each other to contribute a large enhancement.

(3) Though loosely we consider α_R as the Raman polarizability 'of the molecule', in fact it is the Raman polarizability of the scatterer that includes the molecule but, when the molecule is adsorbed on the metal particle's surface, will include contributions from the metal and may, as a result, be greatly altered in its magnitude, symmetry and resonant properties from the Raman polarizability of the isolated molecule.[164] Details of this factor will be discussed in the Chemical Enhancement mechanism.

(4) SERS excitation is a nearfield phenomenon. The near-field, especially near a metal surface, will have spatial components that decay more rapidly with distance than the spatial variation in the far-field (where the spatial 'structure' in the field is of the order of excitation wavelength).

2.1.4.1.2 Chemical Enhancement Theory

The Chemical Enhancement is generally the less contributing factor than the electromagnetic and less well understood. However, it accounts for enhancement of the order of 10-100 and requires that the molecule be adsorbed directly to the metal surface and there by interacts with it. This proximity may allow pathways of electronic coupling from which novel charge transfer intermediates emerge that have higher Raman scattering cross-section. This is very much like resonance Raman effect. There are two possibilities for the new excitations[167]: electrons can be excited from the filled adsorbate orbitals to the unfilled metal orbitals above the Fermi level (molecule to metal charge transfer) or metal electrons can be excited to the unfilled or partially filled adsorbate affinity level (metal to molecule charge transfer) which has been shown in **Figure 2.3A**. Both these transitions are low in energy than the allowed intrinsic transition. This introduces possibility of excitation at frequencies much lower than those of the intramolecular excitations of the free molecule. The most convincing experimental evidence for this picture comes from spectroelectrochemical experiments where metal to molecule charge transfer excitations red shift upon making the electrode potential more negative i.e. increasing the Fermi energy, and molecule to metal charge transfer excitations blue shift. The steps of the charge transfer are as follows (1) a photon is absorbed exciting an electron from the metal conduction band to the LUMO of the molecule, (2) if the LUMO is an antibonding or bonding MO, a change in bond order occur that leads to change in bond length and corresponding vibration, (3) charge or electron is transferred back to its original state and a Stoke-shifted photon is released.

2.1.4.1.3 Other Mechanisms

Beside these two prominent mechanisms of enhancement, there are few other mechanisms are reported in the literature which include:

(i) Coherent Capacitive Coupling Mechanism: In case of analyte induced aggregation, more than one nanoparticle comes close to each other to make nano junction to form Raman hot spot (**Figure 2.3B**). In this configuration the Raman active molecules remain localized at nanojunction and they induce coherent capacitive coupling between the particles. As a result of this the local incident near-field in the junction (between nanoparticles with spatial gap between them less than 1 nm) increases in a multiplicative way. In this spatial arrangement of nanoparticles and the proper placement of analyte molecules in the junction enhances SERS signal significantly compared to SERS on single nanoparticle. Though this effect was first observed by Aravind *et al.*,[168] later was standardized and validated by several research groups[169–171]. This mode of enhancement can account Raman cross sections as large as 10^{-13} cm^2.

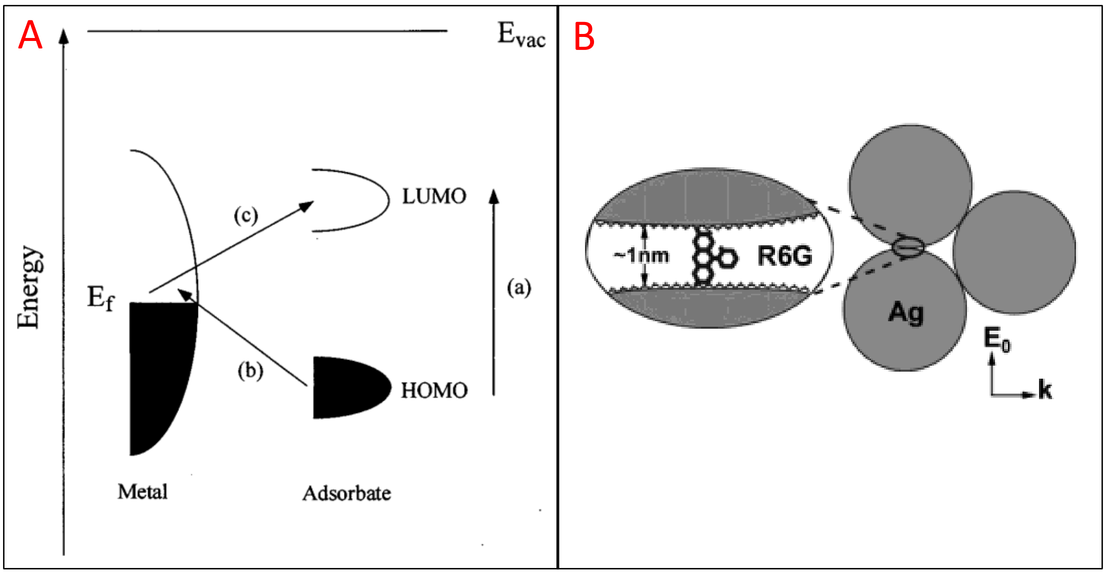

Figure 2.3: (A) Energy level diagram for a molecule adsorbed on a metal surface. There are two probable charge transfer excitations - from adsorbate's HOMO to unoccupied metallic orbital and from metal's occupied orbital to adsorbate's LUMO where orbital occupancy for the metal is determined with respect to Fermi energy level E_f. (adapted with permission from ref.167, Copyright 1998 Royal Society of Chemistry) and (B) Schematic representation of Raman hot spot produced at the junction of two nanoparticles as a result of analyte induced aggregation. (adapted with permission from ref. 171, Copyright 2003 American Chemical Society).

(ii) Polarizability Enhancement Mechanism: Another less explored mode of Raman enhancement is the polarizability enhancement mechanism.[172] This mode accounts the electronic mechanism of the SERS is due to the resonance transitions, in which the surface polarization and the surface–molecule interaction are very important. This mechanism explains the orientation- and distance-dependencies in the surface–adsorbate interacting systems. This mode of enhancement can account an enhancement factor as high as 10^{10}-10^{12}.

2.1.4.2 Instrument and Operating Parameters

SERS experiments were performed by using a homemade Raman setup and a ThermoScientific™ DXR™2 commercial Raman microscope for visible and NIR excitation light source respectively. For our home made setup we used a continuous wavelength diode-pumped solid state (DPSS) laser from Laserglow Technologies, Canada with model number LRS-0532-PFM-00300-03 for 532 nm laser source and LRS-0671-PFM-00300-03 for 671 nm laser source (at fixed excitation energy at 3mW, attenuated by neutral density filter throughout the experiment). For efficient focusing and filtering we used an InPhotonics made 532 nm and 670 nm fiber optics Raman probe with spectral range 200-3900 cm^{-1} (Stokes) for sample excitation and data collection. The Raman probe consists of two single fibers (105 μm excitation fiber and 200 μm collection fiber) with filtering and steering micro-optics, N.A. 0.22. Excitation fiber was connected to a fiber port to align the laser whereas the collection fiber was connected to the spectrometer. A miniaturized QE65000 scientific grade spectrometer from Ocean Optics has been used as the Raman detector with spectral response range 220–3600 cm^{-1}. The Raman spectrometer is equipped with TE cooled 2048 pixel CCD and interfaced to a computer through a USB port. At the end, the Raman spectrum was collected and analyzed by using Ocean Optics data acquisition SpectraSuite spectroscopy software. For Thermo Scientific™ DXR™2 commercial Raman microscope we used 780 nm laser line as the excitation light source with spectral range 50-3500 cm^{-1} (Stokes) for a single exposure of the CCD. Microscope optics is research-quality Olympus viewing optics. Experiments were repeated at least 5-6 times for each measurement and the average values have been reported. Our typical Raman set up is shown below in **Figure 2.4**.

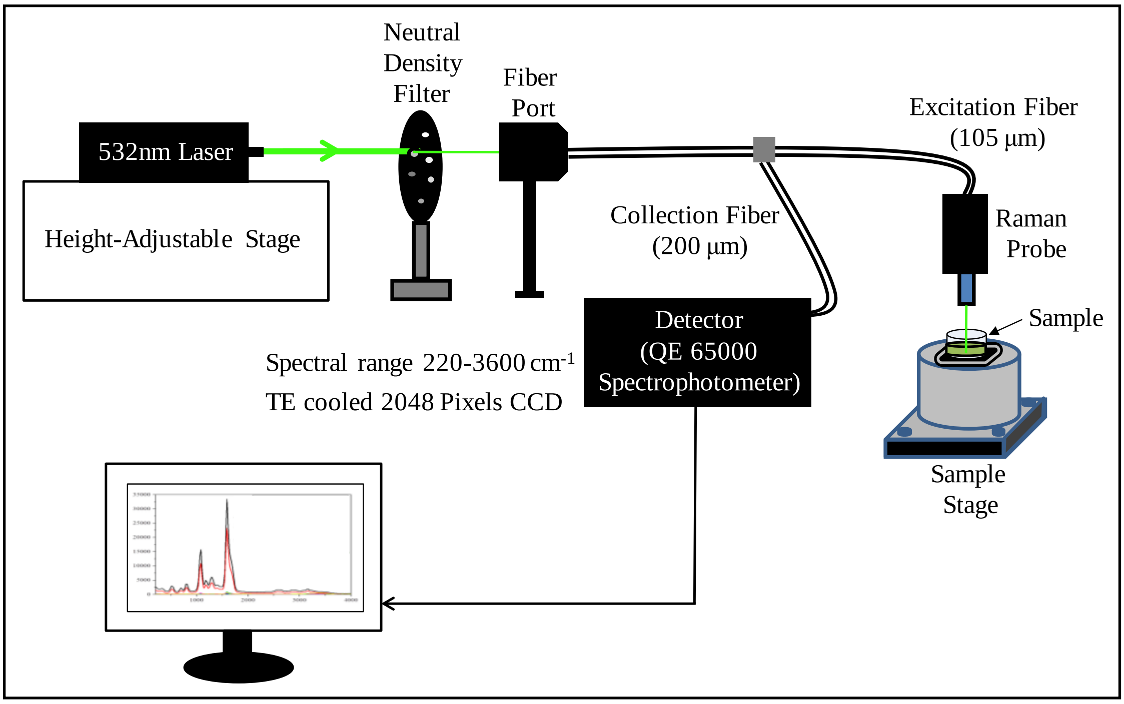

Figure 2.4: Schematic diagram of the home-made Raman setup used for performing SERS experiments.

2.1.5 Inductively Coupled Plasma-Optical Emission Spectrometry (ICP-OES)

2.1.5.1 Working Principle

It is an emission spectroscopy which uses inductively coupled plasma to produce excited atoms and ions that emit electromagnetic radiation at wavelengths characteristic of a particular element. Plasma is the ionized gas that can be formed simply by heating the gas or by subjecting it to a strong electromagnetic field. In case of ‘inductively coupled’ plasma, plasma is generated by the supply of electric current to the gas and this current is produced by placing the conductor in varying magnetic field i.e., current is produced by electromagnetic induction. Upon absorbing adequate energy, plasma can release electrons from atoms or molecules so that both the species i.e., ions and electrons can coexist. In the atomic emission spectrum, element type is determined from position of emitted photon and concentration of that element is obtained from the intensity of the emitted ray. Details of the ICP-OES is out of the scope of this thesis.

2.1.5.2 Instrument and Operating Parameters

We cross examined the quantity of Au-ions obtained from our turn-on colorimetric assay and optical ruler by ICP-OES (ICAP duo 6500 from Thermo-Scientific) to measure the actual Au-ion concentration. A 1000 *ppm* Au solution from NIST was used as standard for ICP-OES calibration. Details of the operating conditions employed are provided in **Table 2.1**.

Table 2.1: The operating parameters of the ICP-OES used for the measurement of Au-ion tracer

Method parameters	
RF power (W)	1150
Nebulizer flow (L/min)	0.5
Auxiliary flow (L/min)	1
Coolant gas flow (L/min)	12
Sample chamber	Cyclonic
Pump rate (rpm)	50
Replicates	3
Standard rinse time (s)	5
Plasma view	Radial

Element	Emission line (nm)
Au	201.2
	208.2
	242.5
	267.5

2.1.6 Dynamic light scattering (DLS) and Zeta potential measurement

2.1.6.1 Basic Principle for Dynamic Light Scattering

Dynamic Light Scattering (DLS, also known as **Photon Correlation Spectroscopy)** is a convenient tool commonly used to determine the hydrodynamic radius of micelles, polymers, proteins, emulsions, nanoparticles or colloids etc. It allows measurement of particle size across the range ~ 0.1 nm to ~ 10 µm. Its ability to measure the size of small particles (for particles of diameter 2 nm and above) is particularly valuable for producing accurate and reproducible data. DLS is based on the extraction of spectral information derived from time-dependent fluctuations of the light scattered from a spatially limited volume within the sample. When the sample (particle suspension or solution) is illuminated by a laser beam, generated scattered light waves spread out in all directions. The particles of the colloidal dispersion remain under Brownian motion. This results in fluctuations in the distances between the particles and hence also fluctuate the phase relations of the scattered light. Also, the number of particles within the scattering volume may vary with time. Scattered waves interference in the far field region generates a net scattered light intensity. The interference can be stochastically either constructive or destructive. Thus, a stochastic light intensity signal is produced due to the random motion of the suspended particles within the sample which is detected at a known scattering angle θ by a fast photon detector. Experimentally one obtains intensity fluctuations by computing the intensity correlation function, whose analysis provides the diffusion coefficient of the particles, D. D is then correlated to the hydrodynamic radius R of the particles by means of the Stokes-Einstein Equation:

$$D = \frac{k_B T}{6\pi\eta R} \tag{2.2}$$

Where k_B is the Boltzmann Constant, T the temperature and η is the viscosity of the dispersing medium.[173]

2.1.6.2 Basic Principle for Zeta Potential

In colloid chemistry, surface charge plays an important role as it contributes to the stability of the particles in solution. If a stable colloidal particle is considered (**Figure 2.5**), it should have a surface potential which make them stable in solution by repelling each other and preventing them to make aggregates. The immediate layer of counter ions of opposite charge surrounding the surface in a compact way is called the Stern layer. This layer is tightly bound to the particle (by electrostatic and moves with the particle in the dispersed medium. Then there lies a loosely attached layer of counter ions called the Slipping plane. Along with counter ions, this layer contains some ions from the solution which have similar charge as that of the particle. These are free ions that move in the fluid under the influence of electric attraction and thermal motion rather than being firmly anchored. It is thus kind of ‘diffuse’ layer. The potential difference between the Stern layer and Slipping plane in called the Stern potential and that between the slipping plane and the bulk fluid is called the Zeta (ζ) Potential[174]. In other words, zeta potential is the potential difference between the dispersion medium and the stationary layer of fluid attached to the dispersed particle. As distance from the particle surface increases the electric potential drops in the order surface potential > Stern potential > Zeta potential. Nevertheless, zeta potential is often the only available tool to get an idea of the surface charge of the dispersed particles and hence their stability in the medium. So, it is widely used for the determination of the type and magnitude of the charge.

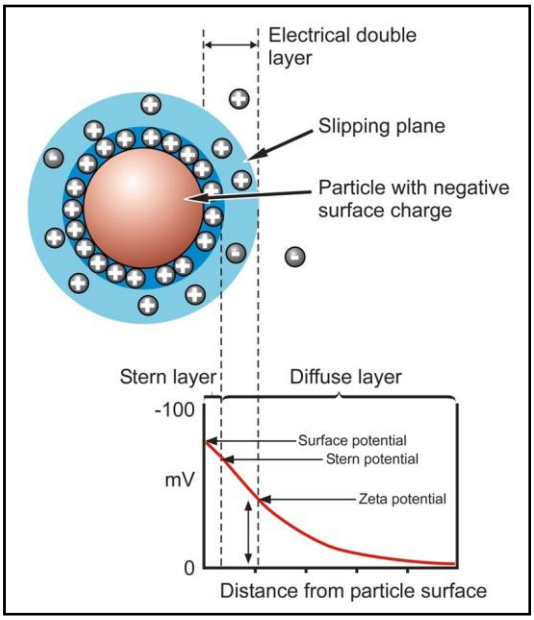

Figure 2.5: Illustration of Zeta potential with a schematic diagram that shows ionic distribution for a negative surface charged particle suspended in a dispersion medium

and the potential difference as a function of distance from the charged surface of the particle.

When an external electric field is applied, dispersed particles move towards one of the electrodes according to their charge along with the stationary layer of dispersing medium. The direction and velocity of the motion is regulated by the particle charge, the properties of the suspending medium, and the electric field strength. Particle velocity is then measured by observing the Doppler shift of the scattered light. The particle velocity is proportional to the electrical potential of the particle at the shear plane which is equal to the zeta potential. Particle motion under an applied electric field is known as electrophoresis. Thus, this optical method used to the determine zeta potential is known as laser Doppler electrophoresis too. Here, fine sample particles are suspended in a solvent of known refractive index, viscosity and dielectric constant. The sample is then placed in an electric field and irradiated with a laser light of wavelength. When the particles move under the applied electric field, the scattered light is measured at an angle and the particle mobility is determined from the frequency shift. The mobility is then related to the zeta potential at the interface using the Henry equation[175]or Smoluchowski equation[176].

Zeta potential is used as a key indicator to determine the stability of the nanoparticles. Nanoparticles also possess certain surface charge originating from their capping agent. If the surface charge is high, the extent of electrostatic repulsion between similarly charged nanoparticles in solution refrains them from approaching close and resists aggregation. When the surface charge is low, they may collide and not able to restore the dispersion any more. Thus they flocculate. So for nanoparticles, high value of zeta potential (negative or positive) contributes to stability whereas low value of it leads to aggregation or precipitation. Typically, nanoparticles with a zeta potential between −10 and +10 mV are approximately considered to be neutral and hence mostly unstable, while nanoparticles with zeta potentials of greater than +30 mV or less than −30 mV are considered to be strongly cationic and strongly anionic, respectively, and generally stable.[175]

2.1.6.3 Instrument and Operating Parameters

To determine the surface charge and to monitor its values with varying amounts of NaCl we measured zeta potential of nanomaterials using a ZetaSizer Nano-ZS dynamic light scattering (DLS) device (Malvern Instruments). The synthesized HHog gold nanoparticles showed a negative zeta potential (-34 mV to -15 mV) depending on the amount of NaCl (final Cl^- concentration in the mother solution varies between 250 µM - 40.25 mM) during the synthesis (the Zeta potentials for samples with PVP have not been measured). The value of zeta potential reduces gradually with the increase of the amount of NaCl, and vice versa.

2.1.7 Ultrasonic treatment or Sonication

2.1.7.1 Working Principle

In ultrasonic treatment, sound energy is used to agitate particles in solution. Sound is a mechanical wave that results from the back and forth (longitudinal) vibration of the particles of the medium through which it propagates and thus the wave exerts cycles of pressure on the medium molecules. These cycles of pressure form thousands of microscopic vacuum bubbles in the solution during sonication. Generally, ultrasonic wave of frequencies greater than 20 kHz are used for this purpose. The bubbles then collapse into the solution in a process called cavitation. This leads to release of enormous energy in the cavitation field. It is able to disrupt molecular interactions such as interactions between molecules of water, separates clumps of particles, helps in dissolution of solids in the medium and facilitates mixing. Also, the vibration by sound waves creates friction in the solution, which causes the heating effect. In nanoscience, sonication is used for synthesis of nanomaterials (Chapter 1, sonochemical synthesis), solubilizing chemicals like surfactants, purification by separation of desired nanomaterials from clumps and also for checking the mechanical stability of the material.

2.1.7.2 Instrument Details

A bath sonicator (Ultrasonic Cleaner, Model SK321OHP) with an operating frequency 53kHz was used to determine the robustness of polymer screened nanoparticles against mechanical force compared to the bare one mentioned (Chapter 6).

2.1.8 Grazing Incidence Small Angle X-ray Scattering

2.1.8.1 Working Principle

Small-angle X-ray scattering (SAXS) is an analytical technique that measures the intensities of X-rays scattered by a sample as a function of very small scattering angle typically in the range of 0.1° to 5°. Bragg's law ($2\text{d} \sin \theta = n\lambda$, where d = interplanar distance in a lattice, θ = scattering angle, n = a positive integer and λ = the wavelength of the incident wave) indicates that with decreasing the scattering angle θ, increasingly larger structural features (d) can be explored. SAXS signal is observed from a material containing structural features on the length scale of nanometers, typically in the range of 1-100 nm. By wide-angle X-ray scattering (WAXS), on the other hand, structural features on much smaller length scale, that of interatomic distances, can be probed. As the name says, it analyses the Bragg peaks scattered at a much wider range of angles (10° to 90°).

In last few years, Grazing Incidence Small Angle X-ray Scattering (GISAXS) has emerged as a useful tool to characterize micro- and nano-scale features, density correlations and shape analysis of objects at surfaces or at buried interfaces of the specimen. Though it operates in real space, GISAXS gives results in reciprocal space as an advanced feature. The experimental setup for SAXS measurements uses a transmission geometry where GISAXS setup is based on reflection geometry[177]. Therefore, SAXS data is more related to substrate scattering (can reveal information from deeper region from the surface) whereas GISAXS data is more related to surface scattering. GISAXS basically combines SAXS applying reflection geometry, a sort of diffuse reflectivity and an extended version of grazing incidence diffraction (GID)[178]. Only a minimal volume of sample is sufficient for GISAXS measurements. It does not demand much sophisticated sample preparation too like TEM. Moreover, being an ensemble technique, GISAXS can provide statistically richer data averaged out over a large sample volume than common microscopic techniques. The samples may be any solid objects - powders, amorphous, crystalline or semi-crystalline, it may be gels or even liquid dispersions. It practically covers a range of materials, such as thin films, polymers, biopolymers, soft matters as well as metals, semiconductors, nanoparticles etc. Also, *in situ* measurements are often feasible by GISAXS. These characteristics have made it advantageous over the more conventional nano-scale structural probes. However, applicability of GISAXS measurements performed at laboratory sources is very limited. It can be utilized with full potential using a synchrotron radiation source in combination with two-dimensional detectors.

SAXS method is one of the most versatile techniques for the structural characterization of nanomaterials. From the evaluation of the measured scattering profiles a wide range of information about the structure and properties of the materials can be obtained, such as: nanoparticle size distribution, particle shape, lattice details, particle structure (e.g. core-shell), specific surface area, aggregation behavior of nanoparticles, pore size distribution, liquid crystalline phases, etc.

2.1.8.2 Instrument Details and Operating Parameters

The experiment was performed at the Indian Beamline (BL-18B), Photon Factory, KEK using the GISAXS experimental setup. The energy of the X-ray beam used was 16 keV. The sample was kept at a fixed angle of 0.04°. The detector used was Pilatus 1M which was placed at 3850 mm distance apart from the sample. An evacuated beam path between the sample and the detector was used to reduce the background air scattering.

2.2 Methodologies

The protocols executed for synthesis and characterization of nanomaterials and that for MTT assay, cell culture and photothermal therapy have been presented in respective chapters in details.

2.2.1 Washing for Synthesis

All the glasswares used in the experiment are washed and cleaned thoroughly with the help of the liquid detergent extran. First, they are washed with copious amount of tap water and then washed thoroughly with double distilled water. Finally they are rinsed with Milli-Q water once or twice and dried in an oven before use.

2.3 Materials

Almost all the chemicals were purchased from Sigma Aldrich (listed in **Table 2.2**) and used without any further purification. Except the organic phase synthesis of superlattices (described in details in chapter 7), Milli-Q water with a resistivity of 18.2 MΩ.cm at 25 °C was used for all of the preparation steps.

Table 2.2: List of reagents with the specifications and company names.

Reagent Name	**Specification**	**Company**
Silver nitrate	$AgNO_3$; Bioxtra, 99%, (titration)	Sigma Aldrich
Ethylene glycol	EG, 99%	Sigma Aldrich
Poly(vinyl pyrrolidone)	PVP, $[C_6H_9NO]_{n,}$ average M_W~ 40,000	Sigma Aldrich
Poly(vinyl pyrrolidone)	PVP, $[C_6H_9NO]_n$, average Mw~55,000	Sigma Aldrich
Sodium fluoride	NaF, 99%	Sigma Aldrich
Sodium chloride	NaCl, AR, ≥99.9%	Sigma Aldrich
Sodium bromide	NaBr, 99%	Sigma Aldrich
Sodium iodide	NaI, 99%	Sigma Aldrich
Sodium sulfide	Na_2S, 99%	Sigma Aldrich
4-Mercaptobenzoic acid	$HS–C_6H_4–COOH$, 99%	Sigma Aldrich
DL-Dithiothreitol	$HS–CH_2–CH(OH)–CH(OH)–CH_2–SH$, 99%	Sigma Aldrich
Gold(III) chloride trihydrate	$HAuCl_4.3H_2O$; ≥99.9%, trace metals basis	Sigma Aldrich
Sodium citrate tribasic dihydrate	$C_6H_5Na_3O_7.2H_2O$; Bioultra, for molecular biology, ≥99.5% (NT)	Sigma Aldrich
L-Ascorbic acid	$C_6H_8O_6$, BioXtra, ≥99.0%, crystalline	Sigma Aldrich
Rhodamine 6G	$C_{28}H_{31}N_2O_3Cl$, Dye content 99%	Sigma Aldrich
Didodecyldimethyl-ammonium bromide	$C_{26}H_{56}BrN$, 98%	Sigma Aldrich
1-Dodecanethiol	$C_{12}H_{26}S$, ≥98%	Sigma Aldrich
Sodium hydroxide	NaOH, BioXtra, ≥98%	Sigma Aldrich
Hydrochloric acid	HCl, ACS reagent, 37%	Merck
Ethanol	C_2H_5OH, EMSURE,ACS,ISO, Reag. Ph Eur	Merck
Toluene	C_7H_8, extrapure AR	SRL
Water	Ultrapure, Milli-Q, resistivity 18.2 MΩ.cmat 25 °C	Merck Millipore

CHAPTER 3

ASPECT RATIO TUNABLE SILVER-NANOWIRES IN SERS-BASED *ppt* LEVEL Hg^{2+} SENSING

OUTLINE: What does the study offer?

- Plausible mechanism of silver nanowire formation based on real time direct experimental observation
- Synthesis of aspect ratio tunable silver nanowire, simply by varying the concentration of common salts
- SERS based detection of Hg^{2+} from ground water up to 50 *ppt* by silver nanowire-4MBA composite

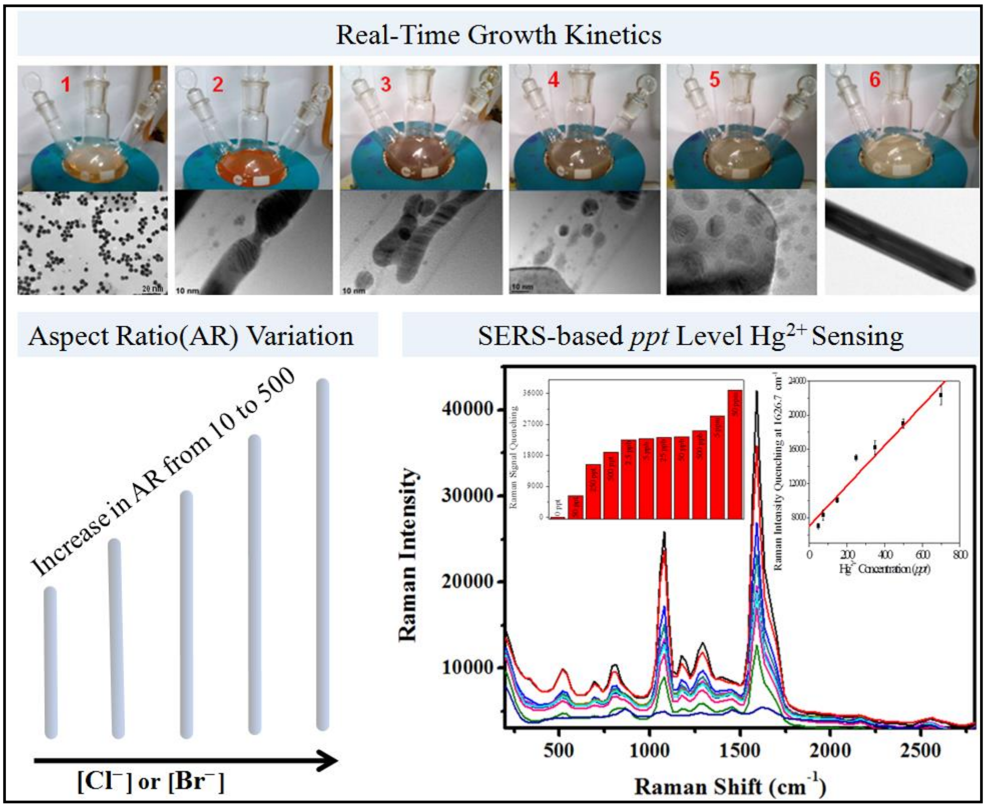

3.1 Introduction

One dimensional metallic nano-structure with variable aspect ratio[89,179] attract demanding interest of vast scientific community because of their potential applications in nanoscale electronic device fabrication[180–182], nano-optoelectronics[183], opto-mechanics and non-linear optics[184–186], light-harvesting[187–189], integrated circuits[2,190–192], and in ultra-sensitive molecular sensing devices[193,194]. To find their multidimensional applications, we need to know the exact mechanism of their real-time formation along with a simple but controlled synthetic methodology to tune their physicochemical and mechanical properties. The literature is rich with methods of synthesis of silver nanowires[14,180,186,193,195–198]and a number of chemical approaches have been actively explored to process silver into 1D nanostructures. For example, silver nanowires have been synthesized by reducing $AgNO_3$ with a developer in the presence of AgBr nanocrystallites[199], or by arc discharging between two silver electrodes immersed in an aqueous $NaNO_3$ solution[200]. Silver nanorods have also been produced by irradiating an aqueous $AgNO_3$ solution with ultraviolet light in the presence of poly-(vinyl alcohol)[201]. The final products of all these methods are, however, encountered by problems such as low yields, irregular morphologies, polycrystallinity, and low aspect ratios[199,200,202]. In contrast, the template-directed synthesis offers a better-controlled route to generate 1D silver nano-structure. A variety of templates have been successfully demonstrated by using this process, and typical examples include channels in macroporous membranes[203–205], mesoporous materials[206,207], or carbon nanotubes[208,209], block copolymers[210] DNA chains[211], rod-shaped micelles[212,213], arrays of calix[4]hydroquinone nanotubes[214] and steps or edges on solid substrates[215,216]. Previously, Xia *et al.*[14] reported a uniform silver nanowire synthesis by a seeded (Pt seed) growth technique and later[196] modified this method to synthesize nanowires without using any seed. In both these methods though the authors have tried to study their growth kinetics and explored their growth mechanism, but have not tried to vary their aspect ratio by controlling their epitaxial unidirectional growth and hence have not achieved any aspect ratio tunability. Synthesized silver nanowires by Xia *et al.*[14,197] show a mean diameter of ~38 nm with 6μm in length to give an aspect ratio of ~150. In a more recent paper, Gongxuan Lu and coworkers[195] have reported a NaCl induced silver nanowire synthesis without providing their actual dimensions. In this chapter we are reporting for the first time a simplified methodology for controlled aspect ratio tunable synthesis of silver nanowire just by varying the concentration of common salt. Moreover we used ethylene glycol as reducing agent compared to their higher glycols, which direct us to find an alternate route to synthesize them through a cost effective way as well as to make them more bio friendly. Besides that, as we use different salt samples (NaF, NaCl, NaBr, and NaI) for efficiently blocking different crystal facets, depending on their solubility product of the *in situ* generated sparingly soluble silver halides, we can vary their aspect ratio by allowing them to grow in a single direction. Generated nanowires are extremely stable for months and show different extent of surface properties depending on their aspect ratios. Though Xia *et al*.[14] have presented a plausible mechanism of silver nanowire formation by considering homogeneous and heterogeneous nucleation of the seeds based on TEM and SEM characterization, real-time observations lacks the explanation of how the *in situ* generated seeds attached to each other energetically to form the bigger nucleation center to queue up the seeds and *in situ* generated silver atoms to cover the space between nucleation centers in a stream line arrangement (**string with several knots**) which transfigure them into bigger nanowires. This study explains in details about the real-time direct observation (based on HRTEM) of nanowire growth starting from the formation of seed, inter seed interaction for the generation of bigger nucleation center, pentagonal nucleation site, stream line arrangement of pentagonal nucleation site-*in situ* generated seeds-silver atoms, and finally to transform this arrangement into bigger nanowires. We used a combined variable sonication cum fractional centrifugation technique to separate *in situ* generated unsymmetrical silver spheroids from silver nanowires. Besides their aspect ratio variated synthesis, we can effectively leach them by adopting galvanic replacement of silver by gold using $HAuCl_4$ to make them controlled hollow bimetallic nanotubes which is a completely different result obtained by Lu *et al.*[195] Once we synthesized and washed the nanowire, due to high specificity of mercury (compared to other metals)[217–220] we have successfully used them for ultrasensitive Hg(II) detection from ground water. Mercury has adverse effect on living system as it can damage DNA, causes malfunctioning of central nervous system, kidney, lungs, endocrine systems, etc. leading to fatal diseases. The types and extent of disruption varies with mercury present in zero oxidation state, as ions or as organomercuric compounds. The Environmental Protection Agency (EPA), United States, has prescribed a maximum uptake limit of 2 *ppb* for inorganic mercury in drinking water. Based on Localized Surface Plasmon Resonance (LSPR) effect, mercuric ion sensing in aqueous medium with silver nanowires produced in polyol method has been investigated with a detection limit in the mM (~1000 *ppm*) range[221]. With best of our knowledge, this is the only report to use silver nanowires successfully for highly specific (easy to distinguish between Au^{3+} and Hg^{2+}, in presence of other metal ions) and ultrasensitive (up to 50 *ppt*-level detection) mercury sensing by using a SERS-based technique.

3.2 Preparation of Silver Nanocubes

Silver nanocubes are synthesized by adopting a standard protocol reported before[127] by using $AgNO_3$ as building block, PVP (M_W ~ 40,000) as surfactant, Na_2S as facet blocking agent, and EG as solvent as well as reducing agent. After synthesis, the obtained aliquot was centrifuged at 6,000 *rpm* for 1 h to remove unreacted reagents from nanocubes.

3.3 Preparation of Silver Nanowires

Silver nanowire is synthesized in a three-neck flask. In the first step, 54 mL of EG was heated at 165 ˚C (below the boiling point of EG) for 1 h with continuous stirring to remove any dissolved oxygen. Then 13.5 mL of 0.18 M PVP (average $M_W \approx 40{,}000$) in EG solution (considering the molecular mass of vinylpyrrolidone monomer unit as 111.14 g), 1 mL of 2.7 mM NaCl in EG solution, and 4.5 mL of 0.28 M $AgNO_3$ in EG solution were added sequentially. Heating was continued for another 25 min. Colour of the solution changes from colourless to yellow initially and then it changes to orange, red, and then finally to muddy off-white when temperature reached again at near 165 ˚C. Same set of synthesis was repeated with 0 mL, 0.125 mL, 0.25 mL, 0.5 mL, 1 mL, 2 mL, 3 mL, 4 mL, 8 mL, 16 mL, 32 mL, 50 mL, and 64 mL NaCl solutions (stock solution of NaCl: 2.7 mM) to synthesize aspect ratio variated silver nano-wires. It's been observed that, below 1 mL NaCl there is no production of silver nanowire and forms only spherical nanoparticles. Our synthesized silver nanowires show moderate monodispersity (≥50%) which is a well known problem in the literature to achieve single sized nanowire. To quantify the aspect ratio of the synthesized nanowires by varying the concentration of added salt we have considered 10 or more image frames with each frame having more than 100 nanowires and measured not only the number averaged length distribution (X axis: length of silver nanowire and Y axis: number of nanowires at that particular length) but also estimated their average length (ensemble average) to report their mean length or aspect ratio in **Figure 3.1 and 3.2**. We have used simple but modified techniques for clean monolayer sample preparation both for TEM and SEM. For TEM measurement we used 300 mesh copper Formvar/carbon grid. We used dip-and-dry technique to make TEM samples. In this sample preparation technique we dip a TEM grid in the concentrated nanomaterial sample solution by using a tweezer and the hydrophobic carbon coating allow a monolayer of sample to stick on the copper mesh which we dry on a soft tissue paper. After complete drying we use this grid for TEM measurement. For SEM measurement we used a piece of mirror polished silicon wafer as sample support. We inject about 20 μL of the concentrated nanomaterial sample on the tilted silicon wafer and the hydrophobic nature of the wafer allows only a single layer of sample to stick on the surface which dries quickly to allow us for immediate SEM measurements.

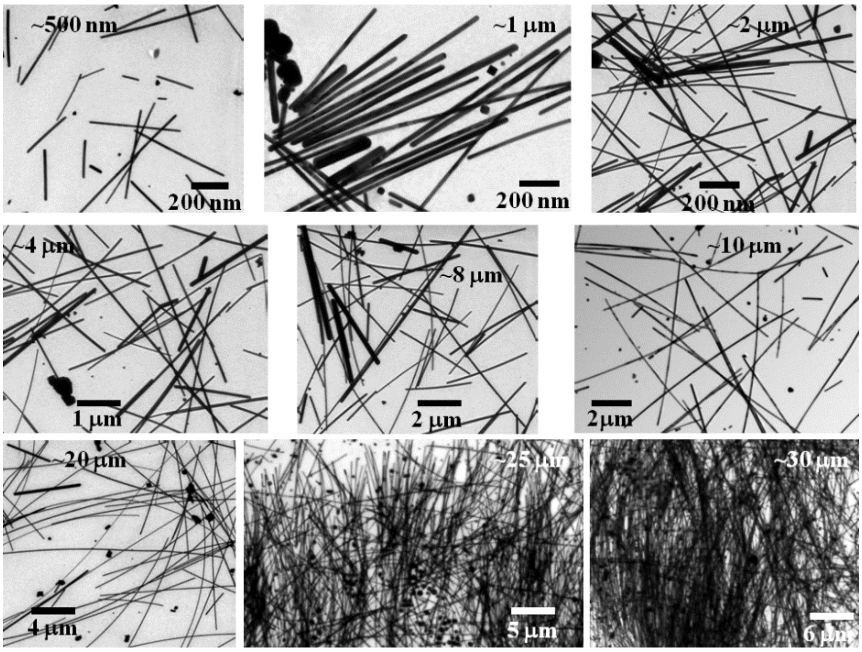

Figure 3.1: TEM-images of silver nanowires, synthesized by using different amount of NaCl. From left to right for first, second and third row we have added 1 mL, 2 mL, 3 mL, 4 mL, 8 mL, 16 mL, 32 mL, 50 mL, and 64 mL of 2.7 mM NaCl. Along with the measurement scale, an approximate length of the obtained silver nanowires has been mentioned on the top of each image.

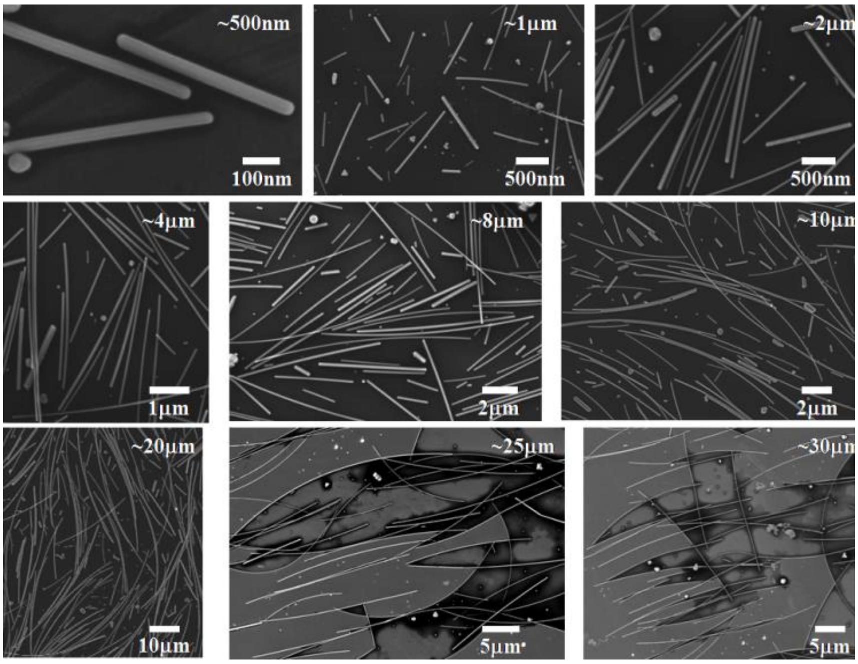

Figure 3.2: SEM-images of silver nanowires, synthesized by using different amount of 2.7 mM NaCl. From left to right for first, second and third row we have added 1

mL, 2 mL, 3 mL, 4 mL, 8 mL, 16 mL, 32 mL, 50 mL, and 64 mL of 2.7 mM NaCl. Along with the length scale marker at the lower right corner, approximate length of a randomly selected silver nanowire from each of the micrographs has also been mentioned at the upper right corner of the SEM images.

From the TEM and SEM measurements as shown in **Figure 3.1 and 3.2** respectively, it is evident that as we increase the concentration of NaCl, particles with bigger aspect ratio are originating. In fact both from the TEM and SEM images it was found that the aspect ratio of these nanowires changes from 10 to 500. Quantification of aspect ratio of synthesized nanowires has been shown in **Figure 3.3**.

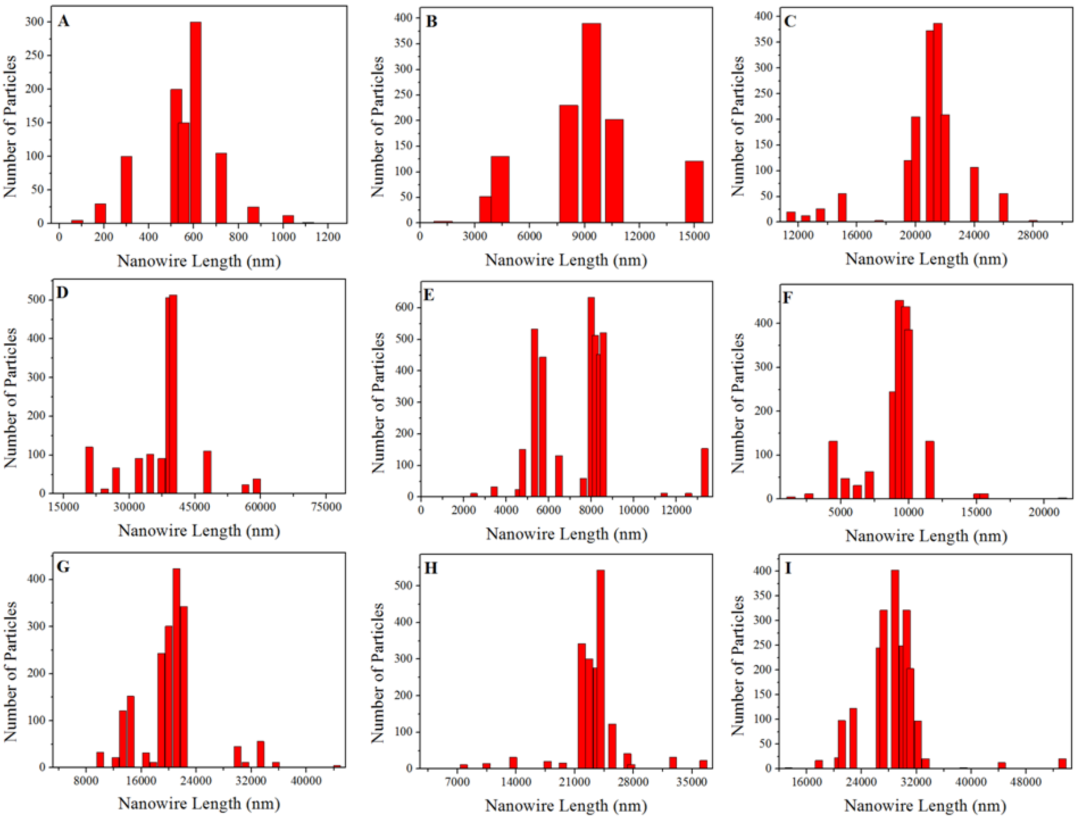

Figure 3.3: Quantification of aspect ratio of the synthesized nanowires by varying the concentration of added salt. We have considered 10 or more image frames with each frame having more than 100 nanoparticles for individual nanowires synthesized at different concentration of salt. Measurement shows the number averaged length distribution (X axis: length of silver nanowire and Y axis: number of nanowires at that

particular length) which corresponds to the estimated average length (ensemble average) as reported their mean length in Figure 3.1 & 3.2 of the main text. From A-I we have added 1 mL, 2 mL, 3 mL, 4 mL, 8 mL, 16 mL, 32 mL, 50 mL, and 64 mL of 2.7 mM NaCl.

By keeping the salt concentration same, we have synthesized silver nanowires by using different salts (NaF, NaBr, and NaI) to explore the effect of halogen atom in the salt. Detailed effect of halide variation and salt concentration have been discussed in the result and discussion section.

3.4 Preparation of Silver tubular nanocages

Once we synthesize aspect ratio variated silver nanowires, we made silver tubular nanocages by galvanic replacement reaction. We performed this reaction under two different conditions. In one method, we dissolved 1 mL of concentrated Ag nanowire in 50 mL milli-Q water and then increased the solution temperature up to the boiling point. After that we added different volumes of 10^{-3} M $HAuCl_4.3H_2O$ solution to prepare silver tubular nanocages. In another method, we took a dispersion of 200 μL of concentrated Ag nanowire in 10 mL ethylene glycol and added different volumes of 10^{-3} M $HAuCl_4.3H_2O$ solution under continuous stirring at room temperature. The structural difference of the nanostructures so produced has been discussed in details in the Results and Discussion section. Generated Silver tubular nanocages were purified by 3-times alternate centrifugation (at 2500 *rpm* for 1 h) followed by washing in water medium.

3.5 SERS

For the SERS measurement of the extent of mercury (II) present in the environmental samples, each Raman active analyte was made by mixing 5 μL of the concentrated silver nanowires with 5 μL pure water or 5 μL of different concentration of Hg(II) solution in a small micro centrifuge tube cap and then finally diluted with 190 μL of 4-mercaptobenzoic acid (4-MBA, 10^{-3} M) to make a total 200 μL aliquot for the control and mercury sensing measurements by exposing the sample at 532 nm laser light and the scattering signal was collected with 30 s acquisition time and 5 scan averaging. Each experiment has been performed 5–6 times and the average values are reported in this chapter. Laser power was kept at 3 mW for the entire experiment.

3.6 Result and Discussion

The central theme of this work is to establish a plausible mechanism of silver nanowire formation based on the real-time direct observation of each and every intermediate step either through colorimetrically or through electron imaging. This is the first experimental report where we could clearly see how the bigger nucleation centers, *in situ* generated seeds, and atomic silvers queue up in a stream line arrangement (**string with several knots**) to transfigure this assembly into bigger nanowires. Though there are few reports on real-time measurement to explain the mechanism of nanowire formation[14,180,196], due to the lack of finer intermediates in the imaging studies the picture of step-by-step nanowire growth was unclear and in that respect our study is unique to provide the complete picture of nanowire growth. Along with the microscopic full view of nanowire growth mechanism, a new synthetic strategy to fabricate silver nanowires with dimensional as well as plasmonic tunability has been explained in this chapter to find their enormous applications in tunable Plasmon spectroscopy. The plausible explanation based on the real-time direct experimental observation has been put forward to explain the formation of salt induced nanowires by considering the solubility product of the *in situ* generated silver halides, binding affinity of the added halides at the {111} facets on growing front, and the free energy associated with the crystallographic planes (obtained from HRTEM study) as the driving force. By virtue of their size tunability, our ultimate goal is to attune their physicochemical and mechanical properties for ultrasensitive chemical recognition. The originality of this work lies in its ability of tuning properties through a cost effective as well as green synthetic route and a supporting real-time direct experimental (HRTEM) observation–based growth mechanism has been illustrated in great details. Moreover, an easy technique has been prescribed to remove *in situ* generated silver spheroids from the high aspect ratio nanowires to make them highly mono-dispersed silver nanomaterials. As a whole; synthesis, purification, and preservation of high aspect ratio silver materials is such an easy venture that we can easily adopt our technique for industrial level of nanowire production. Moreover by adopting simple chemical treatment we can make improved nanowire networking for selective molecular trap or to transform them into controlled hollow bimetallic nanotubes. Following are the sections explained in details about the obtained results and a scientific discussion in support of the obtained results.

3.6.1 Role of common salt for the generation of silver nanowires

Though there are several reports[14,180,196] which explains the mechanism of salt-induced silver nanowire (SNW) formation, this is the lone report which describes the complete visualization of their microscopic growth and explain the aspect ratio dependent SNW formation depending on the variation of salt concentration as well as the halogen substituent in the salt. First reported production of SNW was achieved via reducing $AgNO_3$ with ethylene glycol (EG) in presence of platinum seeds and polyvinylpyrrolidone (PVP)[14,197] where EG serves as reducing agent while PVP serves as the surfactant. Later Slawinski *et al.*[222] reported another seeded growth technique by using gold nanoparticle as seed while cetyltrimethylammonium bromide (CTAB) as surfactant, silver nitrate as precursor, and ascorbic acid as reducing agent. Silver nanowires can also be prepared by a self-seeding process without external crystal seeds, in which initially generated silver particles serve as seeds for nanowire growth[223]. Scientists have reported several other self-seeded aqueous-phase methods to prepare SNW where EG has been replaced by N,N-dimethylformamide (DMF), potassium tartrate ($K_2C_4H_4O_6$), anionic surfactant dodecyl benzene sulfonic acid sodium (DBS) salt, and L-cysteine[224–227]. Gongxuan Lu[195] and coworkers have synthesized rectangular-SNW by using 1,2-propylene glycol as reducing agent followed by the same protocol as we have adopted in this work. So, it is clear from the above reported methods that we can easily control their morphology[186] by adjusting several parameters such as seeding condition, surfactant, surfactant to precursor ratio, reaction temperature, reaction time, etc. Silver nanowires synthesized in this study have the average diameter of ~50 nm (% average of SNWs with diameter ~50 nm is >90%) associated with variable length between 500 nm and 30μm and pentagonal cross section (as shown in **Figure 3.4**), with {100} facets on side surface and {111} facets on growing front as reported earlier[228].

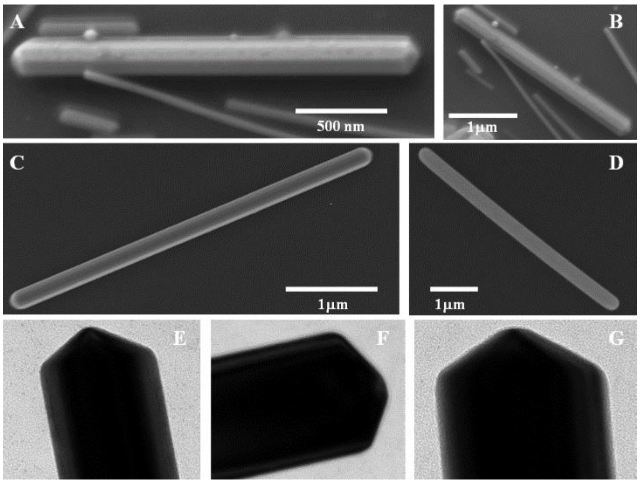

Figure 3.4: High and low magnification SEM images of the silver nanowires taken at *tilted* (A and B) and *non-tilted* (C and D) configuration of the sample mounting stage. E, F, and G are *tilted* TEM images. Comparison between *tilted* and *non-tilted* images clearly shows their pentagonally twinned face and pyramidal tipped structure.

In this study our aim is to investigate how these active crystal planes are affected by the increasing amount of added salt to produce aspect ratio variated SNWs and how the achieved aspect ratio affects their sensing ability. In case of silver nanocube synthesis (**Figure 3.5**), added Na_2S could act as facet blocking agent in two different way: (i) spontaneous dissolution of Na_2S can generate sulfide anions (S^{2-}) or atomic sulfur (S, by *in situ* oxidation) which has unbiased affinity to block all the facets equally to result nanocubes, or (ii) it could react with $AgNO_3$ to generate highly insoluble Ag_2S with solubility product, $K_{SP} = 6.3\times10^{-50}$ at 20 °C to block selective facets.

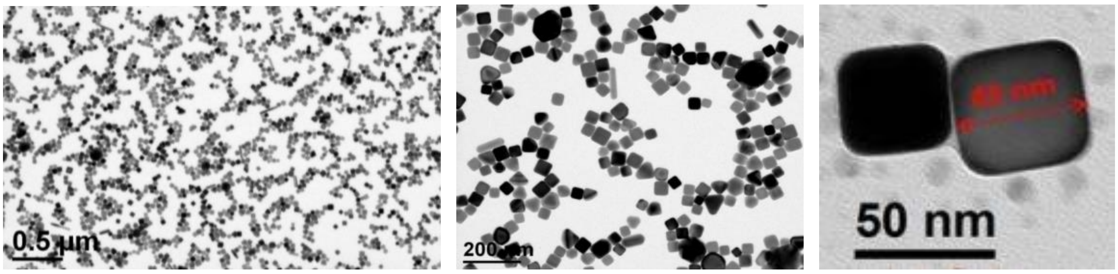

Figure 3.5: TEM images of the silver nanocubes at different magnifications

Obtained results indicate that the first path is much more favorable over the second one and hence the facet selective blocking is not possible by Na_2S. To avoid this situation and to allow the facet selective blocking for the production of one dimensional silver nanostructure, different halide salts have been used. The addition of NaCl to the $AgNO_3$ solution leads to immediate formation of AgCl, which can play an important role in the shape control mechanism. It has been suggested that underpotential deposition of silver halides occurs on the crystal facets of *in-situ* generated nano-seed, leading to symmetry-breaking nanoparticle formation[56,229–232].

It is clear from **Figure 3.1** and **3.2** that for a particular common salt (viz. NaCl), aspect ratio of the generated silver nanowires gradually increases as we increase the concentration of the added salt with respect to a fixed concentration of $AgNO_3$. Since the produced nanowires length varies between 500 nm-30 μm, recording the longitudinal plasmon mode is not possible by using our NIR spectrometer due to their out of range plasmons and only gives the information about their transverse plasmon mode which has been shown in **Figure 3.6**. NIR absorption spectra beyond 1750 nm was completely quenched due to strong absorption by EG and not presented in this figure.

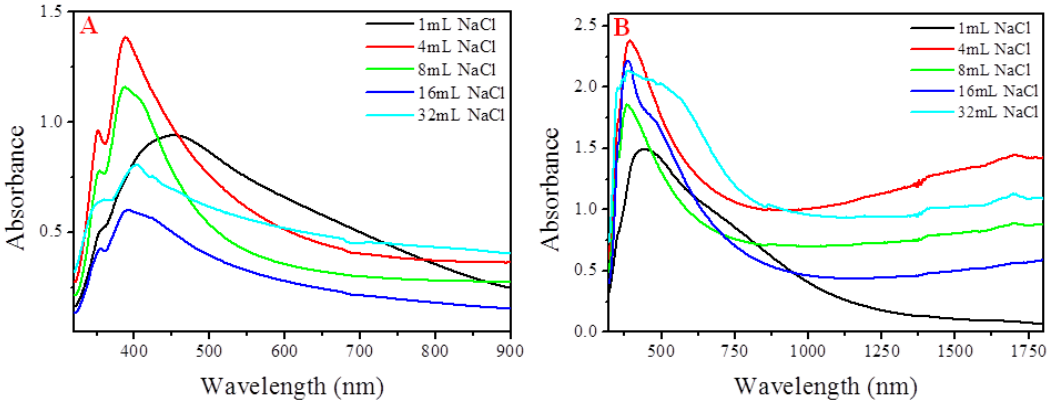

Figure 3.6: (A) UV-Vis and (B) Vis-NIR absorption spectra of NaCl induced nanowires. Amount of NaCl varies between 1 mL-32 mL.

To understand the nanowire growth phenomenon we studied the real-time HRTEM of the growth process which gives the microscopic mechanistic pathway of nanowire formation. As it is clearly visible from **Figure 3.7** that as the reaction proceeds the mother solution changes its colour from colourless to yellow initially and then it changes to orange, red, brown, gray, muddy off-white, and then finally to a silky off-white colour when temperature reaches again at 165 ˚C. We have taken ~100 μL aliquot from this mother reaction mixture during colour transitions and immersed into ice water to freeze the reaction and preserve the formed intermediate structure. In this technique we have collected several intermediate samples (100 μL each) over the time and made TEM grid from each sample to study their *real-time* growth process. NaCl-induced silver nanowire growth process is shown in **Figure 3.7** which explains their *real time* colour change as well as the *in-situ* growth as the reaction proceeds. It is clear from this *real-time* TEM, appearance of yellow color in the initial stage indicates the formation of *in situ* seeds.

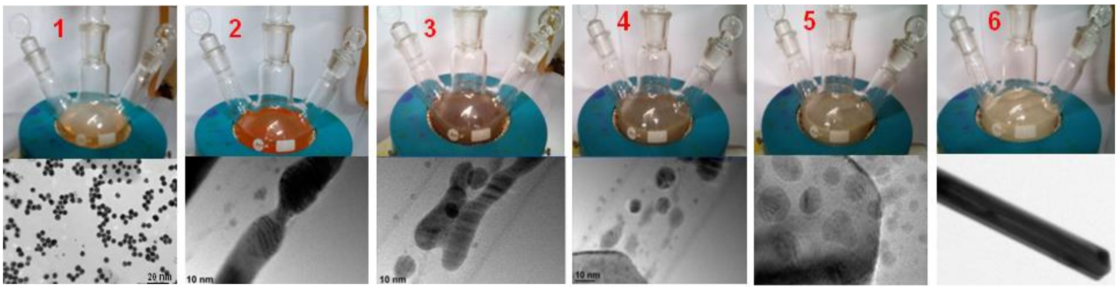

Figure 3.7: Real-time growth steps as anisotropic silver nanomaterials grow from seed to high aspect ratio nanowires. Attached TEM images explain their nanoscopic material development, attachments, and subsequent stream line arrangement to finally generate nanowires with high aspect ratio.

It is clear from the HRTEM study (**Figure 3.8**) that the *in situ* generated seeds are about 5 nm in diameter (Step 1, **Figure 3.7**) and pentagonally twinned single crystal (**Figure 3.8**) with all the active crystal facets grow up along {111} facial planes.

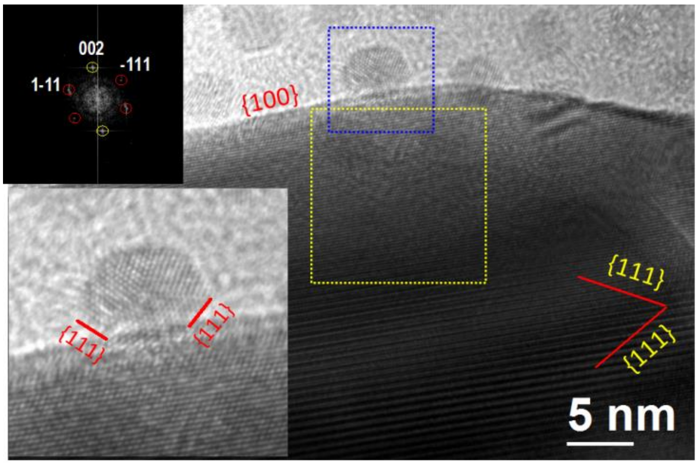

Figure 3.8: HRTEM images of the Pentagonally twinned seeds along with the finally developed silver nanowires. It is evident from the HRTEM study that all the five faces of the pentagonally twinned seeds are {111} facets. The growing front of the nanowire is also having low energy {111} facets and the side face is having {100} facets.

Immediately after the formation, seeds attached each other along {111} facial planes both axially as well as side wise (with respect to the final SNW axis) due to the lack of crystal selectivity to generate bigger nucleation site which has been shown in step 2 & 3 of **Figure 3.7** respectively. These intermediate steps we can term as attachment steps and initiate the formation of pentagonal-faced and pyramidal tipped rods by epitaxial deposition of silver atoms over {111} facial planes. Once a clear pentagonal nucleation site develops, the *in situ* generated seeds queue up and silver atoms cover the space in between them so that a stream line arrangement results as shown in step 4 & 5 of **Figure 3.7**. A structure resembling “string with several knots” is actually evident in the TEM pictures (**Figure 3.9**) and those later transfigure into bigger nanowires (Final step).

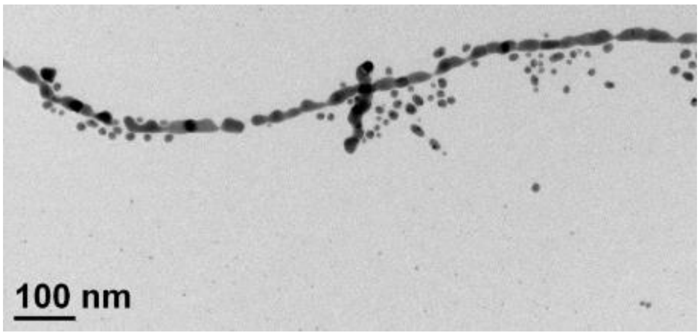

Figure 3.9: "String with several knots"– TEM image of ligation between seeds to form wire. Seeds queue up in a streamline arrangement and ligate face to face or side by side.

Formation of nanowire with greater surface area at the expense of these small nanospheres occurs following the principle of Ostwald ripening process[233]. A proof of this ligation process among seeds along with close views of the multiply twinned seeds themselves under the process of growth along {111} axis is also visible from the obtained HRTEM (**Figure 3.8**) image.

When the attachment and jacketing of seeds is completed, the newly generated {100} surface tends to smoothen up and be continuous. According to literature, the free energies associated with the crystallographic planes of an *fcc* metal increases in the order: $\gamma(111) < \gamma(100) < \gamma(110)$[234]. Due to high energetic nature of the {100} facets, produced silver halides in the medium have higher tendency to deposit and ultimately blocks the {100} facets to increase the stability of the generated nanorods. Blocking of {100} facets indirectly influence the axial growth by continuous deposition of atomic silver or *in-situ* generated silver nanoparticles on {111} facet in a stream line arrangement fashion[198,228]. Diffusion of atomic silver or *in-situ* generated silver nanoparticles is facilitated by elevated temperature of the reaction medium.

Nanowires of several micron (μm) lengths can be synthesized by this method. The silver halides have a definite role in termination process of the {100} facet growth leading to finite wire shape. With increasing concentration of silver halide (when we add greater amount of sodium halide in the reaction mixture), relative deposition of silver halides on {100} facets and stream lining of atomic silver on {111} facets results generating silver nanowires with very high aspect ratio. However, at very high silver halide concentration, the selectivity of generated silver halides on {100} facet over {111} reduces due to the lack of available atomic silver for axial deposition and eventually gives rise to spherical particles and the situation merges to the same when there was no blocking agent.

We attempted to illustrate the effect of solubility product of silver halides on the aspect ratio of the synthesized nanowires. To do so, we have taken fluoride, chloride, bromide and iodide salts of sodium to produce AgF, AgCl, AgBr and AgI respectively in course of the reaction and the nanostructures we ended up are presented in **Figure 3.10**.

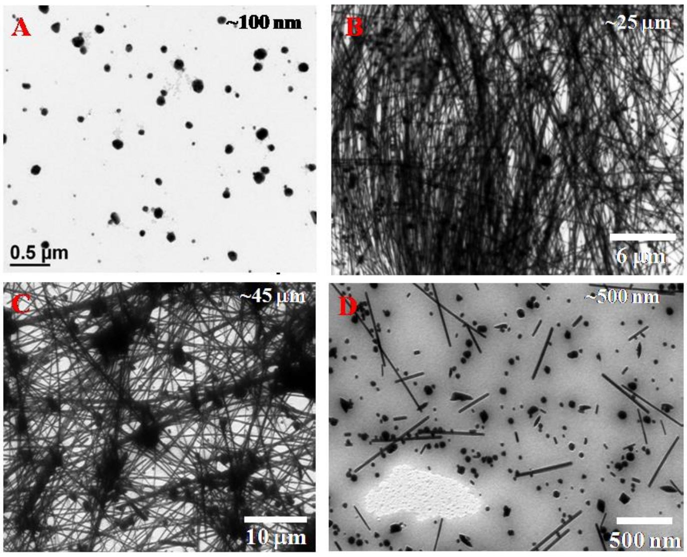

Figure 3.10: Efficiency of generating high quality (HQ) nano-wire based on the electronegativity of halides in the common salts. Where (A) NaF-based Ag-nano

sphere, (B) NaCl-based Ag-nano wire, (C) NaBr-based Ag-nano wire, and (D) NaI-based Ag-nano sphere/wire indicates their relative efficiency to generate high aspect ratio nanowires.

Ethylene glycol is freely miscible in water and it can be assumed that the trends in solubility in the latter will be similarly effective as that in the former. AgF is highly soluble in water and as a result it remains dissolved in the reaction medium and does not block any facet and results the formation of spherical particles only.

The solubility product of the other silver halides in water at 25 °C follows the order[235]:

$K_{SP}^{AgCl}(1.77\times10^{-10}) > K_{SP}^{AgBr}(5.35\times10^{-13}) > K_{SP}^{AgI}(8.52\times10^{-17})$

As the temperature rises, the solubility increases following the equation below[196]:

$$ln\left(\frac{K_{SP}^{2}}{K_{SP}^{1}}\right) = -\frac{\Delta H_0}{R}\left(\frac{1}{T_2} - \frac{1}{T_1}\right) \tag{3.1}$$

Where, ΔH_0 is the standard value for enthalpy of dissolution (Enthalpy of precipitation has same value but opposite sign) and R is the gas constant = 0.008314 kJ.mol^{-1}.K^{-1}. ΔH_0 for AgCl, AgBr, and AgI are 65.72, 84.83, and 111.13 kJ.mol^{-1}, respectively[236]. The increasing order of solubility product thus derived from the above equation at 165 °C is

$$K_{SP@165}^{AgCl}(8.5\times10^{-7}) > K_{SP@165}^{AgBr}(3.0\times10^{-8}) > K_{SP@165}^{AgI}(1.4\times10^{-10})$$

In the reaction mixture (considering the case for 8 mL 2.7×10^{-3} M halide salt solution in 54 mL EG), the product of the concentrations of silver ion (C_{Ag^+}) and the corresponding halide ion (C_{X^-}) in the final volume is $\sim4.3\times10^{-6}$. Therefore precipitation in the reaction medium is expected in case of all the silver halides (X= Cl, Br, and I). The extent of deposition will increase in the order AgCl <AgBr <AgI and enhances the AgX deposition as the reaction medium cools down to room temperature.

The preferred facial deposition will steer the anisotropic growth and this finally leads to extended nanowire moving from chloride to bromide as shown in **Figure 3.10** and in practice we could increase the aspect ratio of the generated nanowires by two times by adding NaBr instead of NaCl and the synthesized nanowires were as elongated as 50-60 μm in length. The presence of iodide ion is, however, observed to inhibit wire formation and a mixture of quasi-spherical particles and much smaller rods are the end products. The role of iodide ion is not totally comprehensible but it is suggested that I^- preferentially bind to {111} facets and thereby preventing further growth along that direction[76].

3.6.2 Purification, networking, leaching, and preservation of synthesized silver nanowires

Once we synthesize silver nanowires with variable aspect ratio; un-reacted NaCl, PVP, $AgNO_3$, and smaller silver spheroids formed in the course of reaction have been removed by repeated low speed centrifugation in EG as solvent. Depending on the dimension of the generated silver nanorods we applied variable centrifugation speed between 1000-3500 rpm for selective nanorod/wire precipitation and removal of the un-reacted chemicals along with smaller silver spheroids as top decant. Due to parallel arrangement as well as cross linking nature of the nanowires in the solution, bigger silver spheroids as side product got stuck in to the nanowire network and difficult to remove them by simple fractional centrifugation. To remove the bigger spheroids, we adopted a sonication cum fractional centrifugation technique where we sonicate the purified nanowires at 40% power of 53 kHz frequency at 20 °C for 1.0 min followed by centrifugation to remove the spheroids and collected the lower portion as pure nanowires. In sonication process, sound wave with high frequency (>20 kH_z) used here to shake off the nanowires to remove bigger silver spheroids in cleaning purpose for making ultrapure silver nanowires. Purity of the nanowires before and after centrifugation has been depicted in **Figure 3.11** which clearly shows that we could effectively remove almost all the silver spheroids by using this sonication cum fractional centrifugation method.

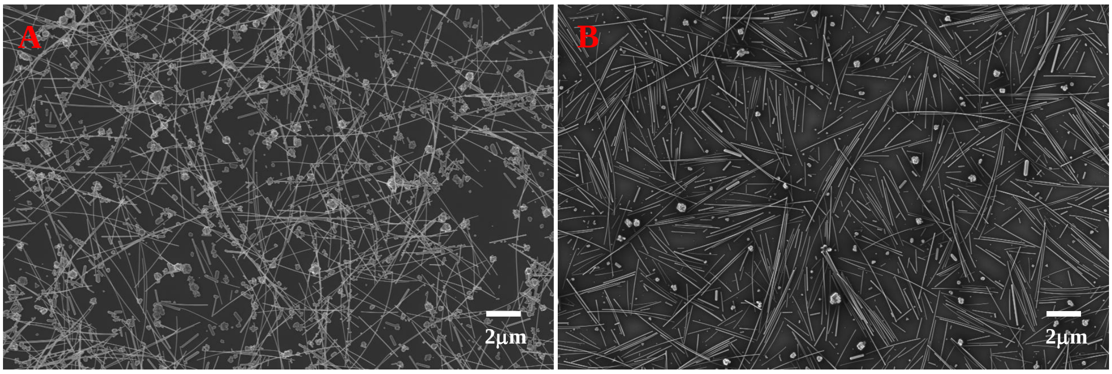

Figure 3.11: Improvement of wire quality (A) before and (B) after sonication cum fractional centrifugation to remove the spheroids and obtain purified silver nanowires.

After this purification step we followed the leaching technique as described in section 3.4 and simply by controlling the extent of gold ion (10^{-3} M) addition we could easily achieve fractional leaching to generate differently hollowed Au-Ag hybrid nanotubes. Details of this controlled generation of hollow nanotubes have been shown in **Figure 3.12**. It is noticeable that in boiling water, the nanotubes so produced have much even and smoother outer wall. Compared to water, nanotubes synthesized in EG have much rough surface as clearly observable from **Figure 3.12**.

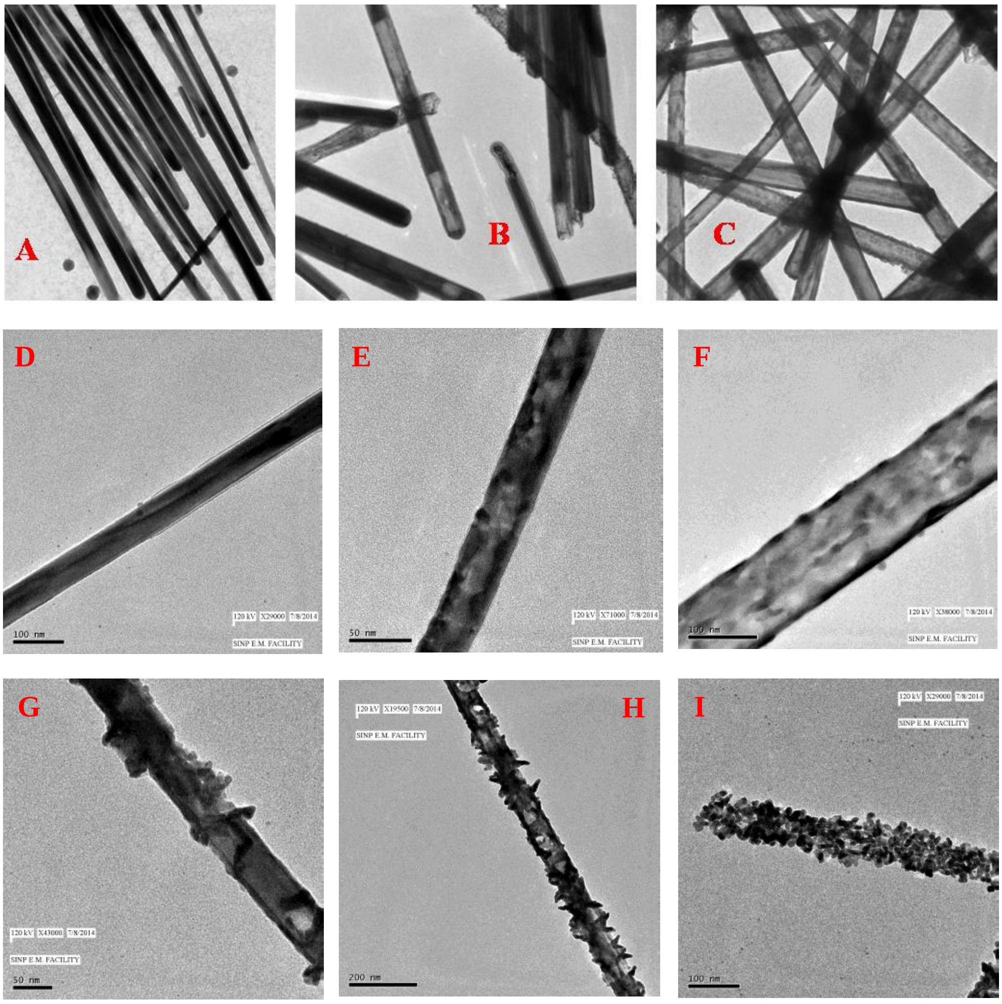

Figure 3.12: Controlled generation of hollow nanotubes: (A-C) stirring in boiling water, A: Without gold leaching, B: Less leaching, and C: More leaching and (D-I) stirring at room temperature in ethylene glycol, in presence of different amount of 10^{-3} M $HAuCl_4.3H_2O$ solution, D: 20 µL, E: 50 µL, F:100 µL, G: 200 µL, H:500 µL, I: 1000 µL.

To make interlinked nanowire networking, we have used dithiothreitol ($HS-CH_2-CH(OH)-CH(OH)-CH_2-SH$) as a linker in the reaction mixture. Keeping the reaction condition same, we have used different amount of 10^{-4} M dithiothreitol (DTT) solution in the reaction mixture. Though we have observed the nanowire formation at 165 $^{\circ}$C in absence of DTT, nanowire networking starts at 185 $^{\circ}$C in presence of DTT with a creamy yellowish colour appearance as the end product. The effect of dithiothreitol addition in the mixture is clearly shown in **Figure 3.13**.

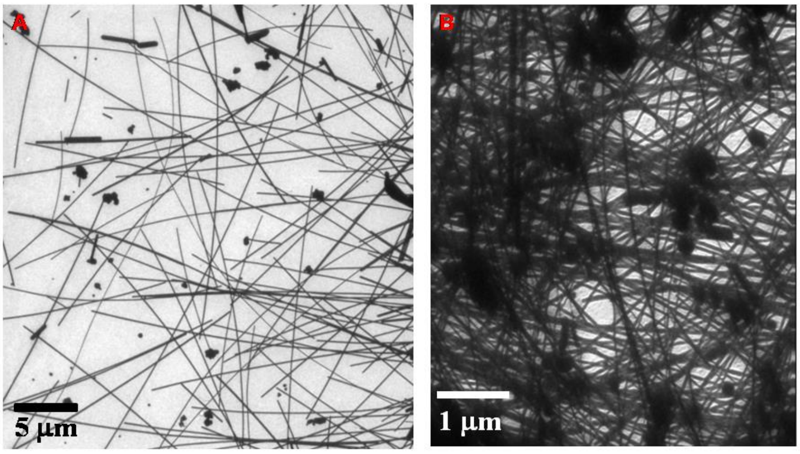

Figure 3.13: The effect of dithiothreitol addition in the reaction mixture when the synthesis was performed (A) without DTT, and (B) with DTT.

The corresponding UV-Vis spectra are shown in **Figure 3.14**. This not only gives us the ability to form the nanowire networking but also can be used as effective resources for atomic/molecular trapping material.

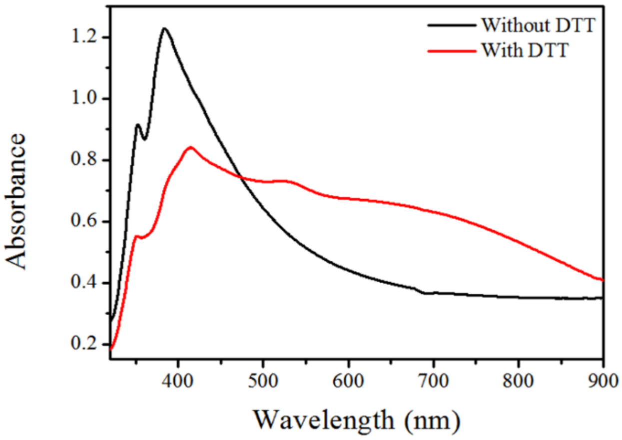

Figure 3.14: UV-Vis absorption spectral comparison of silver nanowires synthesized in absence (Black) and in presence (Red) of DTT (dithiothreitol).

3.6.3 Highly specific and ultrasensitive Hg (II) detection by silver nanowires

By looking toward the adverse effect of mercury on living systems and the Environmental Protection Agency (EPA) regulated maximum uptake limit of 2*ppb* for inorganic mercury in drinking water, present society seeks an efficient sensing assay for highly selective and ultrasensitive detection of mercury in ground water. Localized Surface Plasmon Resonance (LSPR)-based UV-Vis spectral detection technique[221] could measure soluble mercury concentration in the range of 10^{-4}-10^{-5} M (20-2 *ppm*) which is well above the EPA-limit. In a recent publication, Fan *et al.*[237] presented a colorimetric method for quantitative recognition of Hg^{2+} with excellent selectivity up to a detection limit of ~5 *ppb* which is close to the EPA-limit of Hg^{2+} in drinking water. In this work we have demonstrated a SERS based sensing of Hg^{2+} ion up to a detection limit of 50 *ppt* (10^{-10} M in solution), a value much lower than the granted upper limit fixed by EPA. SERS has been studied extensively in the last few decades[130,238–241] and promised to be one of the most useful analytical techniques for the future applications in diagnostics and sensing[242,243]. The usefulness of this technique lies in its ability to provide the chemical signature along with its signal amplification (10^{8}–10^{14} order) leads to state-of-the-art highly specific and sensitive assay for diagnosis, sensing and real-time monitoring[242,243]. Though bulk SERS enhancements have been understood as largely plasmon-based[163] since the first experimental demonstrations[158], resonance[244,245] and chemical contributions[246,247] can also be quite large under certain conditions. Noticeable Raman signal from 4-Mercaptobenzoic Acid (4-MBA) is achieved by surface adsorbing them on silver nanowires with high aspect ratio. The Raman enhancement factor, G, for this study is measured experimentally by direct comparison of Raman signal originating from ν(CC)$_{\text{Ring Stretching}}$ at 1589.7 cm^{-1} in presence of nanomaterials and in absence as described in details elsewhere[59]. All spectra are normalized for integration time. The enhancement factor estimated from the SERS signal is approximately 5×10^{5} which is about two orders less than the corresponding spherical silver nanoparticles obtained by adding 250 μL of 2.7 mM NaCl in the reaction mixture. This intrinsically low Raman cross section of silver nanomaterials is clearly observable in **Figure 3.15**. Variation of SERS intensity with aspect ratio (AR) for NaCl induced (synthesis protocol remains same but only the NaCl concentration changes) silver nanowires have been depicted in **Figure 3.15** with an inset which shows the effect of halogen containing common salt for maximum achievable Raman intensity.

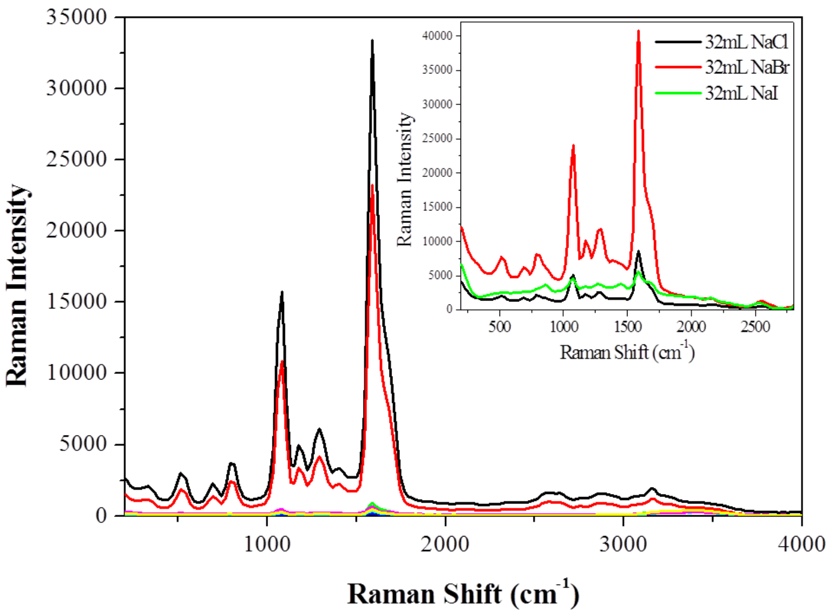

Figure 3.15: Variation of Raman intensity of the surface adsorbed 4-MBA on different aspect ratio SNW. Different spectra indicate the nanostructures obtained by using different amount of 2.7 mM NaCl in the reaction mixture. Black: 250 μL, Red: 750 μL, Green: 4 mL, Cyan: 16 mL, and Yellow: 64 mL NaCl. Halide effect of common salt on SERS enhancement factor is shown as inset.

It is evident from the figure that the SERS signal decreases gradually with AR and gives maximum Raman intensity for a sample which is mostly composed by spherical particles. Lower Raman cross section of silver nanowires compared to their spherical counterpart can easily be explained[21] by considering their relative surface-to-volume ratio (S/V). If we consider a spherical particle with radius R_{sp} then the $(S/V)_{sp}= 3/R_{sp}$ and $(S/V)_{wr}= 2/R_{wr}$ for a nano-wire with radius R_{wr} and length h. Since in the present set of experiment R_{sp} (~6 nm) $<R_{wr}$ (25 nm), (S/V) offered by the nano-wire is ~6 times less than the spherical particles obtained at lower concentration of NaCl (12 nm diameter Ag nanoparticles obtained in presence of 250 μL 2.7 mM NaCl).

Moreover, the relative Raman cross section due to S/V ratio is length independent, obtained Raman intensity from surface adsorbed molecules (4-MBA in this work) on different length nanowires remain more or less same if their diameter is approximately constant at 50 nm and this is clearly observable from **Figure 3.15**. It is logical to think that this independency of Raman cross section on the length of the nanowire is applicable only for same kind of nano-surface and Raman enhancement which is highly dependent on the surface composition should be different for nanowires synthesized by using different halogen containing common salts (NaCl, NaBr, and NaI). Dependence of Raman cross section on surface composition is clearly shown in the inset where we have observed maximum Raman cross section for NaBr-induced nanowires and minimum from NaI-induced one. This could be explained by the networking structure of the NaBr-induced nanowires which has enhanced adsorption ability compared to the NaCl-induced nanowires which mostly generates non-interacting individual nanowires. In case of NaI, generated nanoparticles are spherical in nature with average diameter of ~100 nm should produce 1.3 times less Raman cross section than a nanowire with average diameter of 50 nm as we have argued before and clearly observable from the inset of **Figure 3.15**. Though the offered SERS is more for a smaller spherical Ag nanoparticle, nanowires are suitable for Hg^{2+} sensing experiment due to the preferential binding of Hg^{2+} on the {111} facet as all the {100} facets are blocked by insoluble silver halides which prevent the direct access of analyte to the nanowire surface and initiate the leaching process through tips. Here preferential binding of any added metal on the {111} facet is stem from the unavailability of {100} facet and not due to their selective binding. It is worth to mention that the literature is rich to show the higher specificity of mercury to form silver amalgam compared to other metals[217–220]. As a result of this unavailability of {100} facet for binding, any of the added metals will be directed towards the {111} facet only but due to greater specificity to form silver amalgam other metals will show negligible binding to offer highly specific and selective detection through SERS quenching experiment. It is also well-known that most exciting optoelectronic activities of nanomaterials stem from their nanoscale sharp tips[248–250]. Expected more catalytic and plasmonic activity at sharp features (e.g., corners, crease edges, cracks, branches, tips, etc.) of the nanoparticles stem from their very low neighbouring atom density surrounding the corner atoms compared to edge atoms which offers little restoring force[52] and opens up the gate for easy access to Hg^{2+} ions for chemical reaction through tips. Though the obtained maximum Raman signal enhancement is offered by NaBr-induced silver nanowires, NaCl-induced nanowires gives the most consistent result with relatively high Raman signal strength and we have done all our sensing experiments by using NaCl-induced silver Nanowires. When Hg^{2+} is added in the solution it causes leaching of the nanowires and is expected to form silver-mercury alloy. Unlike the bulk silver which has comparable reduction potential as that of mercury (the standard electrode potential of Ag^+/Ag = 0.80 V vs. SHE and Hg^{2+}/Hg = 0.85 V vs. SHE), at nano level the reduction potential of silver is reduced with decrease in size[251] and Hg^{2+} is capable to oxidize Ag to Ag^+ efficiently. As a result, partial deformation of the nanowires takes place and there is a gradual decrement of the SERS signal produced as we move from lower concentration of mercury to a higher one. As a control experiment we have performed the same study of nanowire deformation by using Au^{3+} instead of Hg^{2+}. Due to large difference in reduction potential of the two metals (the standard electrode potential of Ag^+/Ag = 0.80 V vs. SHE and $AuCl_4^-/Au$ = 0.99 V vs. SHE)[252], gold ions can easily oxidize silver nanowires to form silver ions in a nano-galvanic cell reaction and our usual expectation to achieve more Raman intensity quenching as a result of the nanowire deformation. In reality, we have observed a much less nanowire etching in case of Au^{3+} addition compared to Hg^{2+} addition. This could be possibly because of the large lattice mismatch between Hg and Ag and not the case for Au and Ag (Au = 4.08 Å, Ag = 4.07 Å)[253]. As a result of this crystal lattice matching, gold crystallizes on {100} facets [$\gamma(111) < \gamma(100) < \gamma(110)$[234]] to produce hollow tubes with comparable surface for Raman activity but Hg^{2+} leaches silver nanowires through {111} facets to deform nanowires and results reduction in Raman intensity. The difference in SERS intensity due to the addition of Au^{3+} and Hg^{2+} is shown in **Figure 3.16**.

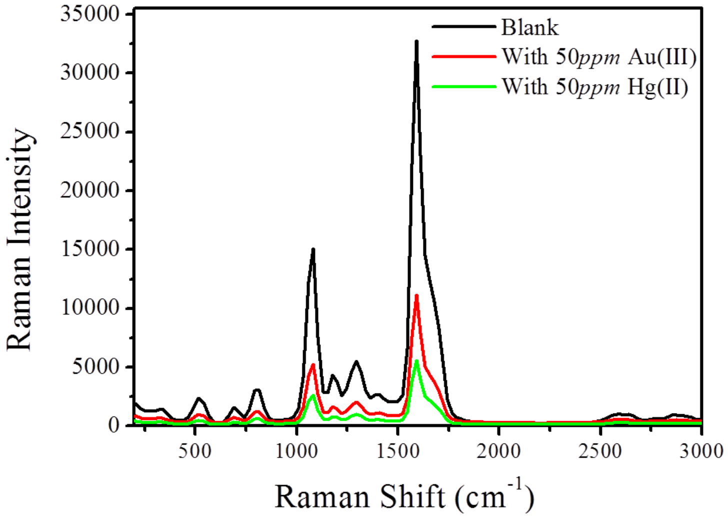

Figure 3.16: Relative ability of silver nanowire leaching by added gold and mercury ions (performed at 50 *ppm* concentration) and the resultant Raman signal (originated from surface adsorbed 4-MBA) quenching.

At lower concentration of Au^{3+} (below 10^{-4} M), apparently no change in Raman intensity offered by the surface adsorbed 4-MBA is due to not much effective surface area change. At 50 *ppm* concentration of Hg^{2+}, the deformation of silver nano-wire can be vividly observed in naked eye. At this level the signal is almost totally quenched. To verify the efficiency of silver nanowire-induced Raman signal of 4-MBA for ultra-sensitive quantification of Hg^{2+}, we have performed the SERS experiment at different concentration of Hg^{2+} prepared from one stock solution of 1M. The 4-MBA and Hg^{2+} solutions were made in a buffer of pH-4 throughout the experiment so that the metal ions stay stable in the medium and can effectively bind on the nanowire surface. Concentration dependent Hg^{2+} sensing by using NaCl-induced silver nanowire is shown in **Figure 3.17**. Left side inset of **Figure 3.17** indicates how the Raman intensity at 1589.7 cm^{-1} [$\nu(CC)_{\text{ring Stretching}}$: 1584 cm^{-1}][254] quenched as we increase the concentration of Hg^{2+}. It is clear from the plot that at lower concentration of Hg^{2+} the extent of Raman quenching at 1589.7 cm^{-1} varies linearly up to a certain limit (~1 *ppb*) but after that the variation is not linear anymore and remain almost constant before the concentration of Hg^{2+} is too high to completely dissolute the nanostructure and results maximum possible Raman quenching.

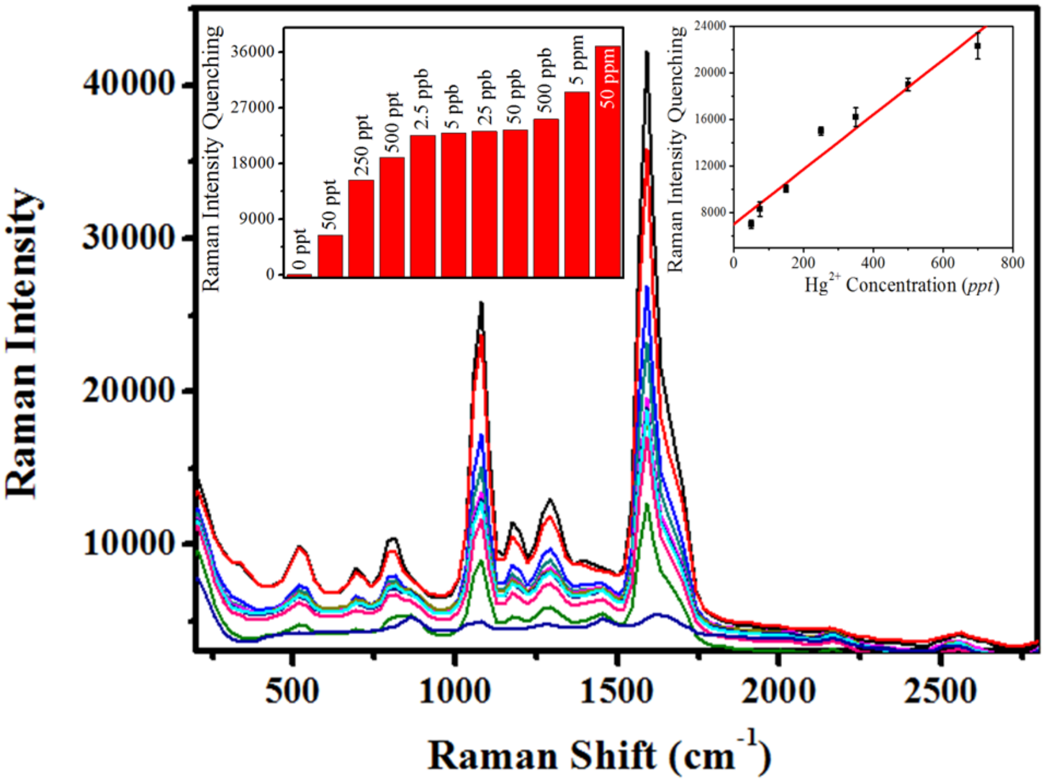

Figure 3.17: Concentration dependent Hg^{2+} sensing by using NaCl-induced silver nanowires. Concentration of Hg^{2+} has been varied between 50 *ppt* and 50 *ppm*. Left side inset indicates how the Raman intensity at 1589.7 cm^{-1} quenched as we increase the concentration of Hg^{2+}. It shows linear variation of Raman quenching at 1589.7cm^{-1} with Hg^{2+} concentration up to ~1 ppb limit which has been shown in the right side inset. The experimental data in right inset is represented by (■), and the line represents the linear fit with R=0.98.

At low concentration range (50-700 *ppt*) we have plotted SERS quenching at 1589.7 cm^{-1} against Hg^{2+} concentration which has been shown as the right side inset in **Figure 3.17**. It is clear from the plot that the SERS quenching signal intensity varies linearly (a prerequisite of a sensor) with the concentration of Hg^{2+} up to 700 *ppt*, which clearly demonstrates that it is possible to use our SERS assay as a sensor for the quantification of Hg^{2+} from water sample at low impurity level. The obtained Hg^{2+} detection limit of our study is 50 *ppt* which is of the order of 10^{-10} M in solution, a value much lower than the EPA granted upper limit of Hg^{2+} in drinking water. For real-life applications, e.g., in an environmental sample, there could be several different impurities due to other common metal ion. To check the selectivity of our assay for Hg^{2+} over other metal ions, we performed same SERS experiment with the chloride salts of Pb^{2+}, Fe^{3+}, Cu^{2+}, As^{3+}, Cr^{3+}, Cd^{2+}, Zn^{2+}, Co^{2+}, Ni^{2+}, Sr^{2+}, K^{+}, and Na^{+}. It is observed that at 50 *ppm* level (10^{-2} M concentration) of the salt solutions, many of these ions seem to interfere strongly whereas at 5*ppm* level (10^{-3} M concentration) only Pb^{2+}, Cu^{2+}, As^{3+}, and Cr^{3+} ions produce noticeable quenching interference. However, at 500 *ppb* (10^{-4} M concentration), the interferences of Pb^{2+}, Cu^{2+}, As^{3+}, and Cr^{3+} are evidently much weaker and at 50 *ppb* (10^{-5} M concentration) or below Hg^{2+} shows selective Raman quenching as shown in **Figure 3.18**. However, it can be stated that the extent of quenching caused by Hg^{2+} ion always remains sufficiently enough compared to others for the detection of this notoriously toxic element in a sample mixture.

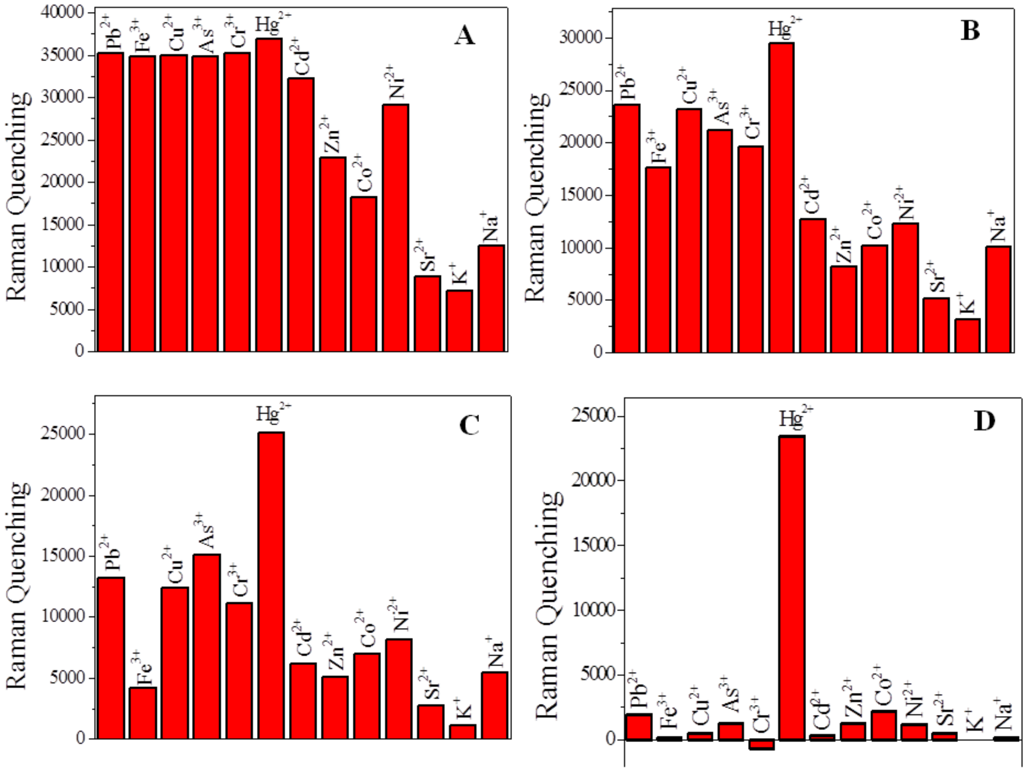

Figure 3.18: Raman quenching efficiency of Hg (II) at different concentrations (A: 50 *ppm*, B: 5 *ppm*, C: 500 *ppb*, and D: 50 *ppb*) which shows that the silver nanowire-4MBA composite can act as an excellent sensor for selective mercury ion detection in aqueous solution on or below 50 *ppb* concentration.

To demonstrate the potential and practical applications of our assay to measure the Hg^{2+} content in environmental samples, spiking experiments were performed and recovery values were determined. For this purpose, we have collected water samples from Calcutta Municipality Canal, Saha Institute of Nuclear Physics tap water, and bottled purified drinking water. We have filtered out the water samples by using a 0.2μm syringe filter to remove any bigger contaminants present in the water samples. Subsequently, different concentrations of Hg^{2+} were spiked and SERS was performed to determine the Hg^{2+} concentration. In **Table 3.1**, the supplied Hg^{2+} concentration and Hg^{2+} concentrations determined by our SERS probe are compared. Our data show that the recovery values are quite good within the experimental error. Our experimental data confirms the capability of our assay to detect a low concentration of Hg^{2+} ions (below 1 *ppb*) from environmental samples.

Table 3.1: Comparison of supplied and measured concentrations for Hg^{2+} from different source of water samples.

Water Sample	**Supplied Hg^{2+}**	**Determined Hg^{2+}**
Kolkata Canal Water	600 *ppt*	670±40 *ppt*
SINP Tap Water	500 *ppt*	480±60 *ppt*
Bottled Drinking Water	400 *ppt*	370±20 *ppt*

To check the structural effect of silver hollow wire on Hg^{2+} sensing, we have performed the same set of SERS experiments but the results were not encouraging as the initial Raman signal originating from adsorbed 4-MBA on hollow nanowires were intrinsically very low and is not suitable for high throughput sensing experiment.

3.7 Conclusions

In this work we have put forward a plausible explanation based on the real-time direct experimental observation (by HRTEM) of each and every intermediate state during growth for the common salt induced aspect ratio tunable Pentagonal Faceted Pyramidal Tipped (PFPT) silver-nanowire synthesis. Real-time direct experimental observation and the subsequent nanowire growth has been explained by considering the free energies associated with the crystallographic planes, solubility product of the *in situ* generated silver halides, and binding affinity of the added halides at the {111} facets on growing front. Reported results present the first controlled aspect ratio tunable nanowires synthesis technique simply by varying the salt concentration or by changing the halogen substituent in the common salt. This research work also prescribes an easy way to purify nanowires from spheroids, ligation technique for nanowire networking, and tubular silver nano-cages which may find several future applications. Driven by the needs, we have used these synthesized nanowires for higher specific (preferential binding of Hg^{2+} on {111} facets of silver nanowires over other metals) and ultra sensitive Hg^{2+} detection in the *ppt* level (50 *ppt*) which is 40 times lower in concentration than the EPA approved upper limit of Hg^{2+} in the drinking water. We strongly believe that this detailed study on silver nanowire will find enormous applications in future trace level sensing technology.

CHAPTER 4

ULTRA-TRACE GOLD (Au) DETECTION BY A COLORIMETRY BASED OPTICAL RULER

OUTLINE: What does the study offer?

- A highly selective and ultrasensitive colorimetric sensor to detect trace level gold i.e. up to 30 *ppt* in presence of common mining elements in natural gold ore
- An optical ruler based sensing that uses decoupling of *in-plane* dipole resonance modes
- Low cost, handy, precise and efficient way for analyzing gold quantity in environmental samples
- Plausible explanation for silver nanoparticles formation in presence of catalytic amount of gold-ion

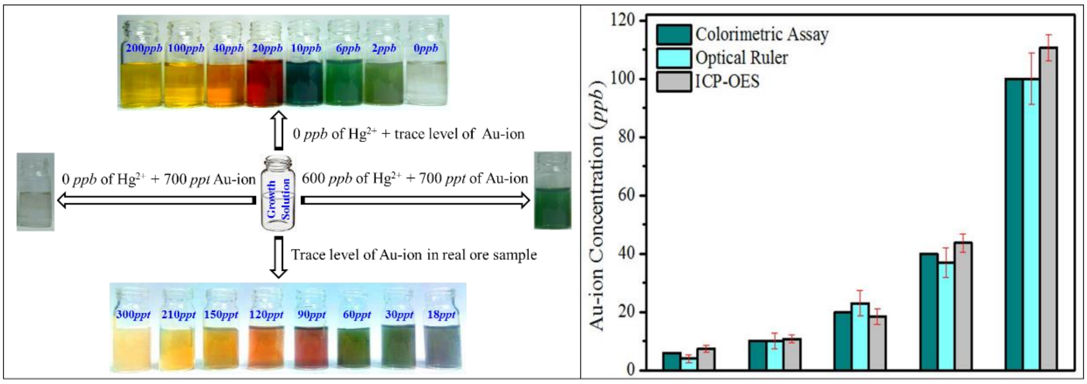

4.1 Introduction

Sensor technology always looks for a reliable and handy tool with greater specificity and ultra-sensitivity. The detection may be based on electrical or optical signal output. However, due to the easiness of understanding and performing optical sensors are more acceptable. Out of several optical sensors, colorimetric sensor is the simplest one due to the efficient readout by our own eyes undemanding an extra detector with additional cost of sensing. In the past, chemists and biologists have extensively used colorimetry for the detection of toxins,[184,255,256] biological components,[257–259] explosives,[260–262] pollutants,[263,264] and nutrients[265,266] both from commercial as well as environmental samples. These colorimetric sensors have been developed not only for their accurate identification through specific chemical interactions[260] but also for their ability to detect in trace level applicable for early stage detection of cellular components[259] in a biological process as well as for a chemical compound[263,264] as an active ingredient. Throughout the globe scientists have invested their time and effort to develop robust colorimetric sensors for heavy metals which include As(III and V), Pb(II), Hg(II), Cd(II) etc.[184,256,267] considering the severe health disorders they cause. Compared to these toxic heavy metals, efficient colorimetric sensors for precious metals like Au, Ag, Pt, Pd, Ru, etc. are very rare in the literature. Most of these colorimetric detections are based on change of the color or color intensity of the nanoparticle solution on exposure of the analyte to the mother solution. The deviated color or the degree of color intensity change measures the extent of analyte present. However, change in color based on decoupling of different plasmon modes offered by a nanoparticle upon exposure to a particular analyte (here gold-ion) at different concentrations to offer a color-coded sensing is probably the rarest report in the literature. Due to its attractive characteristics like, malleability, good conductivity of heat and electricity, strong reflectivity in infrared region, high density along with chemical resistivity, gold (Au) has widely been used as a precious metal in several fields such as jewellery, medicine, high-tech industries, electrical & electronic industries, catalysis, and corrosion-resistant coatings.[10,268–274] Driven by the needs, here we have reported a highly selective (over other metal ions) and ultrasensitive (up to *ppt* level) turn-on colorimetric assay-based optical ruler for accurate gold quantification. This assay is based on decoupled *in-plane* dipole resonance. In this study different silver nanodiscs (AgNDs) are generated *in situ* and as their disc diameter changes they show different extent of red shifting of the *in-plane* dipole resonance (longitudinal mode) based on their increased particle size as a result of decrease in the Au-ion concentration in the assay. In past, different instrumental techniques like, inductively coupled plasma mass spectrometry (ICP-MS), inductively coupled plasma optical emission spectrometry (ICP-OES), electrothermal atomic absorption spectrometry (ETAAS), energy-dispersive X-ray spectroscopy (EDX), flame atomic absorption spectrometry (FAAS), and spectrophotometry[275–283]have been employed to detect the extent of Au present in a sample. Among them, ICP-MS and ICP-OES are the most sensitive techniques to trace very low level of Au content. However, due to their high cost, intricate instrumentation and time-consuming nature have limited their use for routine applications.

Along with numerous sensitive detection techniques, several pre-concentration methods (e.g., ion exchange, membrane separation, co-precipitation, solvent extraction, cloud point extraction, and sorption on a solid phase) are also there to make enriched Au samples for easy detection through stable complex formation mechanism.[284–294] They are simple and effective techniques, but have disadvantages of high cost, time consuming nature, and the use of large volume of toxic solvents as extractants.[295–297] A rapid and selective Au-ion recognition and recovery was reported recently by a new type of mesoporous adsorbent,[298] where the solution acidity plays an important role to bind trace level of Au-ions. The specificity and fast complexation of the metal ions with ligand immobilized conjugate adsorbent was investigated for selective and sensitive detection and recovery of Au-ions from waste scrap.[299] Different functional-group ligands trapped on various solid matrices have also been used for sensitive determination of trace level Au-ions based on easy to use and cost effective adsorbents.[300]

The objective of this study was to develop a low cost turn-on colorimetric sensor for highly specific and ultrasensitive detection of trace level gold content simply by controlling the extent of decoupling of the *in-plane* dipole resonance (longitudinal mode) of the *in situ* generated AgNDs and tuning the same. In presence of different concentration of Au-ion (*ppm* to *ppt* level), a homogeneous mixture of sodium citrate tribasic dihydrate (TSC), silver nitrate ($AgNO_3$) and L-ascorbic acid (AA) in water which we termed as 'growth solution' forms different sized AgNDs (along with spherical silver nanoparticles, AgNPs). Controlling the decoupling of *in-plane* dipole resonance from *out-of-plane* dipole resonance and thereby tuning the *in-plane* dipole resonance of these *in situ* produced AgNDs generate different complementary colors. These colors indicate the extent of catalytic amount of gold present in the solution. This turn-on colorimetric assay-based optical ruler can be used as a potent tool for Au-ion detection as the appearance of color positively confirms the presence of gold as gold ion and the longitudinal plasmon (*in-plane* dipole resonance) tuning measures the extent of Au-ion present as tracer. A plausible mechanistic explanation, based on the relative oxidation/reduction potentials of active redox systems present in the sensor assay has been provided in great details. It elucidates the use of AA as a reducing agent catalyzed by Au-ion to reduce available soluble metal ions. Present study also investigates the extent of interference from foreign metal ions not only to measure the specificity of this sensor but also to understand the enhanced sensitivity and their stability with time. Finally, we have tested our assay to detect and measure gold concentration from real ore samples and to find out the possible interference of such real matrix. The interference actually helped to extend the detection limit without disturbing the overall specificity of the assay.

4.2 Growth Solution Preparation

Under continuous stirring condition 175 µL of 1% sodium citrate tribasic dihydrate (TSC), 250 µL of 10^{-2} M silver nitrate ($AgNO_3$) and 50 µL of 10^{-1} M of ascorbic acid (AA) were added one-after-another into 10 mL of Milli-Q water. This homogeneous solution was marked as the ‘growth solution’.

4.3 Synthesis of Silver Nanoparticles (AgNPs)

Under continuous stirring condition different concentration of Au-ion was added to the ‘growth solution’ and the whole solution turned colored within few minutes, indicating the formation of silver nanoparticles (AgNPs). The reaction was carried out at room temperature in a 15 mL Borosil glass bottle placed on a magnetic stirrer allowing continuous mixing of chemicals. The reaction was allowed to proceed for another ~2 min after the addition of all reagents. We also added different metal ions to the solution to check their influence in AgNP formation. The schematic representation of the stepwise synthetic procedure of the Au-ion catalyzed AgNP synthesis has been explained in **Figure 4.1(I)** and their corresponding plasmon peaks with variable shape and size have been presented in Figure **4.1(II)** with detail description in the later section. Associated control experiments to confirm the necessity of gold ion's presence has been tested in a systematic way. Influence of other heavy metals and alkali metals for the possible false positive sensing or for the improvement of the sensitivity of gold detection has also been discussed in details in the result and discussion section.

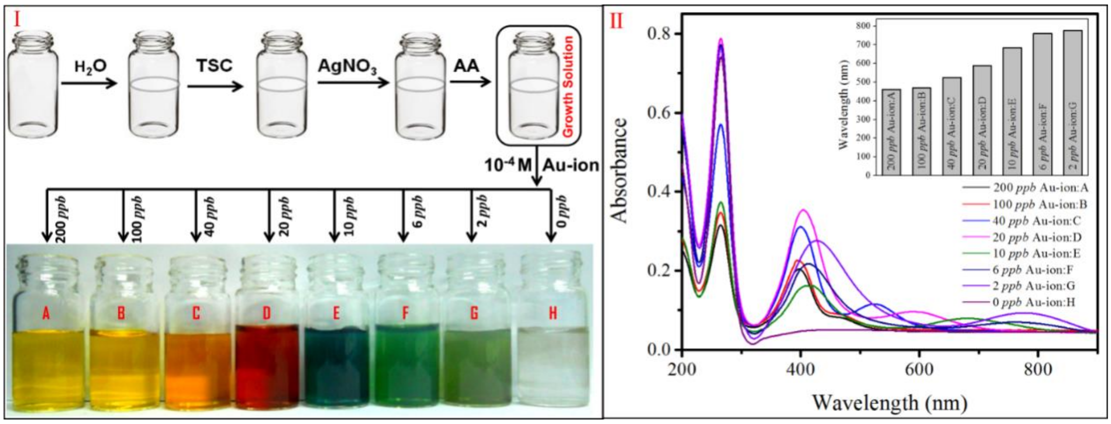

Figure 4.1: (I)A stepwise Au-ion catalyzed AgNDs synthesis process at room temperature in TSC medium by reducing $AgNO_3$ in presence of ascorbic acid and **(II)** UV-vis spectra of *in situ* generated AgNPs (mixture of nanospheres and nanodiscs) synthesized at different concentrations of Au-ion. The spectra show one strong peak at 265.5 nm and a small hump (Figure 4.2) near 335 nm due to the absorption of AA and *out-of-plane* quadrupole resonance of AgNDs respectively. The *out-of-plane* dipole resonance of AgNDs and both the *in-plane* and *out-of-plane* dipole resonances of AgNPs (nanospheres) give rise to a peak near 400 nm. Another tunable band between 500 and 800 nm originates from the *in-plane* dipole resonance of AgNDs. Tuning of *in-plane* dipole band maxima with gold ion concentration is shown as inset.

4.4 Extraction of Gold as Gold Ion from the Ore

Gold occurs in nature mainly in the metallic form, usually alloyed with silver as electrum, or with mercury as an amalgam and comparatively rarely with other elements in chemical composition. They may be either insoluble or highly soluble in water. For validating the optical ruler with real mining sample, gold ore was collected from Bugunda Gold Deposit in Tajikistan. To get Au in soluble form, extraction has been done by treating 0.01 g of oxidized ore with 100 µL of 10-times diluted aqua regia for 10min and then the extracted solution was centrifuged at 12000 rpm for 10 min to remove any insoluble materials. Top decanted solution after centrifugation was diluted 10 times further and used as stock solution for the entire sensing experiments.

4.5 Results and Discussion

Reagents which are commonly used to reduce Ag^+ to Ag^0 include N,N-dimethylformamide, hydrazine, ferric ions (Fe^{3+}), and sodium borohydride. Unfortunately, most of these reducing agents exhibit undesired toxicity, which limit their application in medical and packaging products. In this study, ascorbic acid, a non-toxic chemical, has been employed for the reduction of silver ions to form a mixture of spherical- and disc-shaped (AgND) silver nanoparticles. In the present set of demonstration, presence of trace level Au-ion is essential to generate these AgNPs. This observation is clearly illustrated in Figure **4.2(I)**, where right most bottle with 0*ppb* concentration of Au-ion did not produce any color and hence confirms the absence of any plasmonic nanoparticle formation. As the concentration of Au-ions increases gradually from 2 *ppb* to 200 *ppb*, the ‘growth solution’ tuned its color from light green to yellow. This has been explained by considering the formation of different sized AgNDs.

4.5.1 In-plane and Out-of-plane Surface Plasmon Modes and their Decoupling

The UV–vis absorption spectra corresponding to the turn-on colorimetric assay in presence of different concentration of Au-ion (sample A-G) and in absence of Au-ion (Sample H) at room temperature in aqueous medium was recorded and presented in **Figure 4.1(II)**. The absorption spectrum of the sample H doesn't show any surface plasmon band rather absorbs strongly at 265.5 nm due to the presence of AA. For samples A-G, in addition to this 265.5 nm peak they show a small hump near 335 nm and additional two surface plasmon absorption bands, one near 400 nm with smaller tunability between 397 nm and 427 nm and another tunable band between 500 nm and 800 nm. Due to the very low intensity and presence of several absorbance profiles, the *out-of-plane* quadrupole resonance near 335 nm is not clearly visible in Figure **4.1(II)** and plotted separately as **Figure 4.2**. This clearly shows a hump at 336 nm along with two intense plasmon band, one at 400 nm due to the *out-of-plane* dipole resonance (transverse plasmon band) and another one at 525 nm due to the *in-plane* dipole resonance (longitudinal plasmon band).

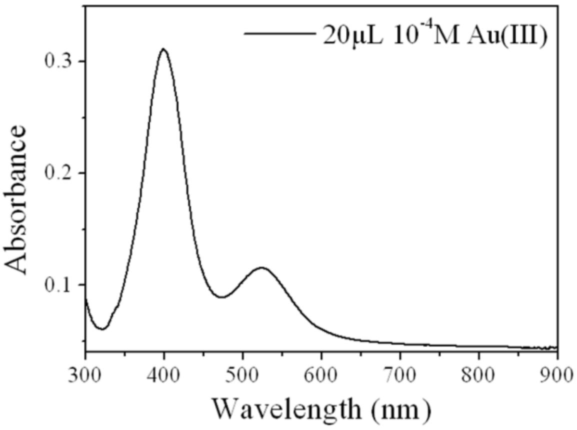

Figure 4.2: *Out-of-plane* quadrupole resonance at 336 nm observable from the ‘growth solution’ with 40 *ppb* Au-ion concentration.

Surface plasmon resonances are unevenly distributed around non-spherical metallic nanoparticles and this demonstrates their shape dependent localized surface plasmon resonance spectra[301,302]. For spherical silver nanoparticles both the *in-plane* and *out-of-plane* dipole plasmon resonances appear in the same energy and hence remain coupled in the extinction spectra to demonstrate a single intense sharp peak near 400 nm. When silver nanoparticles change their shape from spherical to two-dimensional disc, *in-plane* and *out-of-plane* resonances start appearing in different energy range of the electromagnetic spectrum and 'decouples' from each other. Despite forming spherical particles, decoupling of plasmons in the present study occurs mainly due to the formation of two dimensional AgNDs and depending on their dimension the *in-plane* dipole resonance tunes over a wide range (between 500 nm and 800 nm). According to the previous reports[90,303–305]the appearance of the hump near 335 nm is due to the *out-of-plane* quadrupole resonance, surface plasmon band near 400 nm originates from *out-of-plane* dipole resonance (transverse mode), and *in-plane* dipole resonance (longitudinal mode) band varies between 500 nm and 800 nm depending on the diameter and thickness of the *in situ* generated AgNDs. Expected *in-plane* quadrupole resonance band near 470 nm[303–305] does not appear as a clear band and could be enveloped inside the *out-of-plane* dipole resonance to make it difficult to decouple. Two times increment (from 60 nm to 130 nm) of full width at half maxima (FWHM) by moving the particle diameter from 5 nm to 50 nm indirectly proves our assumption. It is also noticeable from the absorption spectra that irrespective of the size and shape of the generated AgNPs, dipole resonances (*in-plane* and *out-of-plane*) are always more intense compared to their corresponding quadrupole resonances which is expected from their transition probabilities.[301] When the particle size is very small (below 5 nm), *in-plane* and *out-of-plane* dipole resonances appear close to each other and intend to merge into a single peak. Contrary to that as the particle size increases, the *in-plane* and *out-of-plane* dipole resonances start decoupling from each other depending on their diameter and thickness. As the diameter of the particle increases, both the *out-of-plane* and the *in-plane* dipole resonances red shifted with respect to their smaller particle counterparts. In case of *out-of-plane* dipole resonance the extent of red shifting is only 30 nm (between 397 nm and 427 nm) whereas for *in-plane* dipole resonance the extent of red shifting shows a much wider plasmon tuning of 313 nm (between 463 nm and 776 nm). The kinetics of the structural transition and the stability of the so-produced AgNDs was monitored by real-time UV-vis spectroscopy (**Figure 4.3**). It is clearly observable from Figure 4.3 that the *in-plane* dipole resonance peak or the longitudinal plasmon band (685.5 nm for Set-E and 770 nm for Set-F of **Figure 4.1(I)**) shifts gradually towards shorter wavelength. This gradual blue shifting of the coupled plasmon peak correlates to the formation of AgNDs of smaller particle size and hence the reduced aspect ratios as the particles get stabilized. Kinetics of morphology transition for two different sets (Set-E with 10 *ppb* Au-ion and Set-F with 6 *ppb* Au-ion) has been presented in **Figure 4.3**.

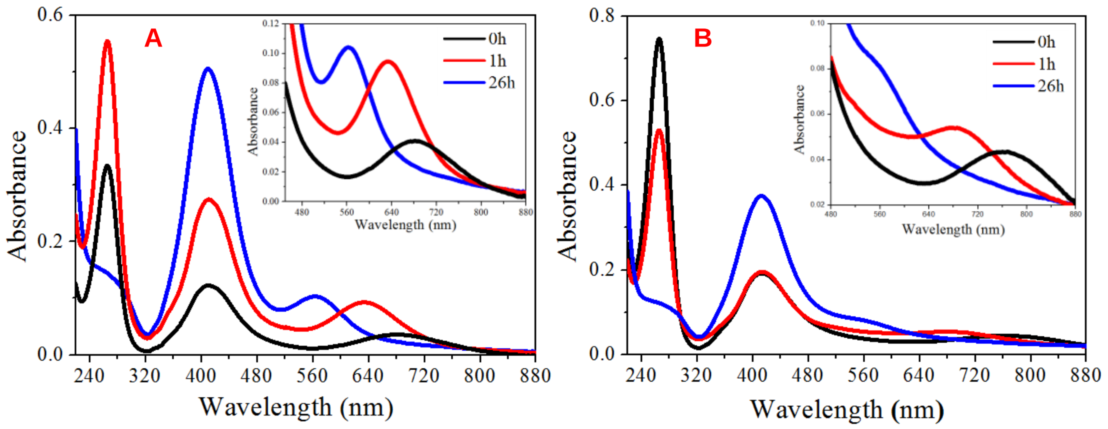

Figure 4.3: Kinetics of morphology transition for two different sets, (A) Set-E with 10 *ppb* Au-ion and (B) Set-F with 6 *ppb* Au-ion. Kinetics study has been performed over 26 h for both the samples, keeping all the other physical parameters constant except the concentration of Au-ion.

It is clear from the recent study of O'Brien *et al.*[305] that a very thin disc (below 10 nm thickness) does not generate any noticeable *out-of-plane* resonance band due to the lack of oscillating free electron in the perpendicular direction to support a plasmon. So the intensity of *out-of-plane* dipole resonance indirectly measures the thickness whereas the intensity of *in-plane* dipole resonance measures the diameter of the disc and aspect ratio of the disc controls the decoupling and hence tuning of their plasmons. Disc natures of the *in-situ* generated nanoparticles are clearly shown in **Figure 4.4(a-c)** by recording their energy filtered TEM images.[306]It is clear from our energy filtered TEM image for Sample-F (of **Figure 4.1(I)** with 6 *ppb* Au-ion) that the measured average thickness profile over the entire nanoparticle is showing flat-top morphology with an average thickness of ~9.75 nm which should not be able to support an *out-of-plane* dipole resonance. Hence the entire intensity of *out-of-plane* dipole resonance comes from *in situ* generated spherical AgNPs.

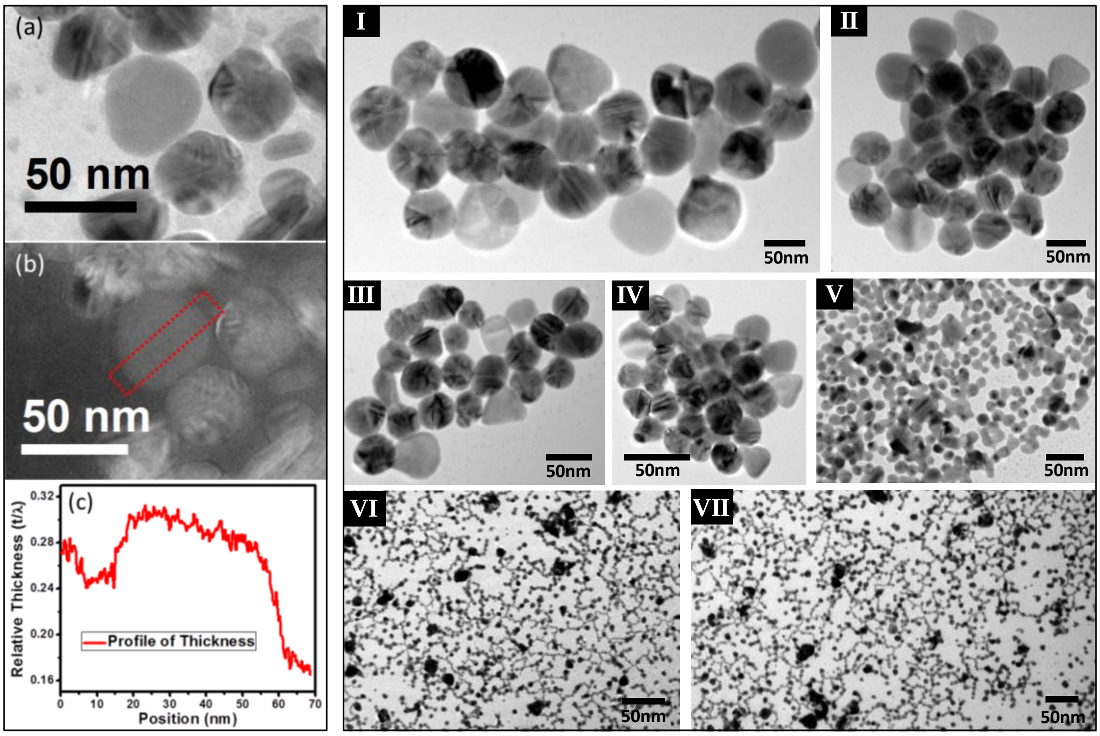

Figure 4.4: (a-c) Energy filtered TEM images: (a) Elastic image, (b) Relative thickness map, (c) Average thickness profile over dotted area marked in (b) showing flat-top morphology. From the figure (c) the relative thickness of nanodisc is about 0.065 which corresponds to about 9.75 nm (by considering λ at 150 nm), the average thickness of the nanodisc. (I)-(VII) present TEM images of size variable AgNDs with spherical AgNPs present in mixture using different concentration of catalytic gold (I: 2 *ppb*, II: 6 *ppb*, III; 10 *ppb*, IV: 40 *ppb*, V: 200 *ppb*, VI: 50 *ppm*, VII: 200 *ppm*).

4.5.2 Analytical Study illustrating Plasmon Shifting with Stress

The extent of plasmon shifting for a nanodisc to that of a nanosphere by applying same optical force has been calculated analytically. The aspect ratio for any sphere, AR_{sphere}, is always 1. However, that of a nanodisc of diameter d and of thickness h is d/h, so AR_{disc} increases as d increases for a fixed value of h. Let us consider five nanospherers: S1, S2, S3, S4, S5 and five nanodiscs: D1, D2, D3, D4, D5 (Figure 4.5A). By considering five spheres and five discs with diameters, d = 10 nm, 20 nm, 30 nm, 40 nm, 50 nm and a constant thickness of all the nanodiscs as 9.75 nm (relative thickness of nanodisc is about 0.065 which corresponds to about 9.75 nm (by considering λ at 150 nm), the average thickness of the nanodisc), calculated AR_{disc} are presented in **Table 4.5B**.

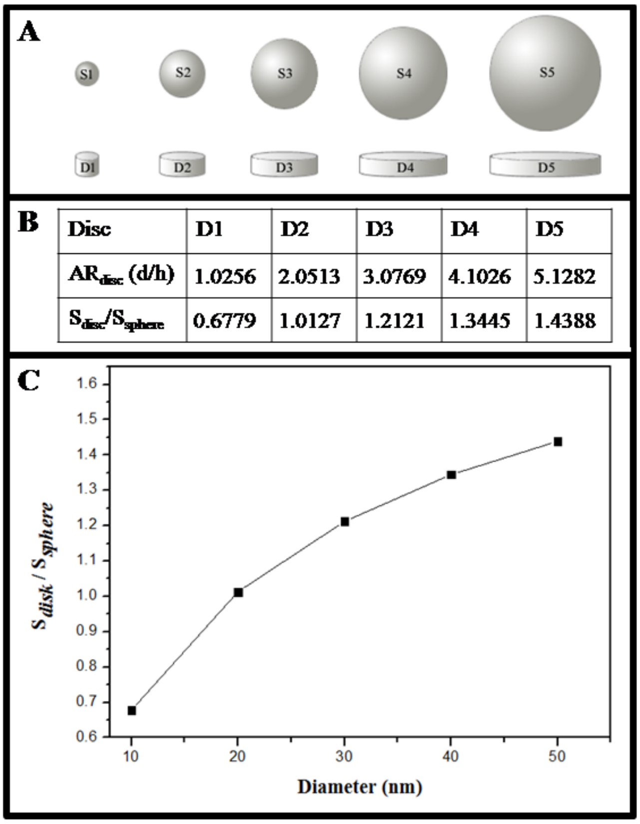

Disc	D1	D2	D3	D4	D5
AR_{disc} (d/h)	1.0256	2.0513	3.0769	4.1026	5.1282
S_{disc}/S_{sphere}	0.6779	1.0127	1.2121	1.3445	1.4388

Figure 4.5: (A) Variation of aspect ratio of nanodisc by varying their diameter (d) at a fixed thickness (h). Aspect ratio of a sphere with any diameter is always 1, (B) Gradual increment of the ratio of stress between disc and sphere at a particular optical force as the aspect ratio of nanodisc increases by varying their diameter (d) at a fixed thickness, h and (C) Variation of relative stress between disc and sphere with disc diameter at a constant disc thickness.

The extent of plasmon shift for a nanostructure towards higher wavelength may be correlated to the easiness with which the electron cloud over it can take part in collective oscillation. The more accessible and pliant the electron cloud is the less is the energy required to excite them. Gradual red shifting of plasmon is expected if the amount of required excitation energy also reduces gradually. Now, this pliancy is a measure of how easily the electron cloud can be disturbed or deformed.

Theoretically, we can have an idea of this by calculating the stress factor.

$$Stress(S) = \frac{Force(F)}{Area\ (A)}$$

If r = radius of the disc = radius of the sphere and h= thickness of the disc, then

Surface area for the disc, $A_{disc} = 2\pi r^2 + 2\pi \mathrm{rh} = 2\pi \mathrm{r(r+h)}$

and Surface area for the sphere, $A_{sphere} = 4\pi r^2$

The ratio of stress between disc and sphere at a particular optical force is then defined as

$$S_{disc}/S_{sphere} = A_{sphere}/A_{disc} = 4\pi r^2/2\pi \mathrm{r(r+h)} = 2r/(r+h)$$

$$= \left(2r/h\right)\Big/\left\{(2r+2h)/2h\right\} = AR_{disc}\Big/\left\{\left(AR_{disc}/2\right)+1\right\}$$

Where $\mathrm{AR_{disc}}$ = Aspect Ratio of the Disc = d/h = 2r/h

By applying the above formula, values of S_{disc}/S_{sphere} are obtained for the discs which have been provided in **Table 4.5B** and the corresponding plot of of $\mathrm{S_{disc}/S_{sphere}}$ vs. Diameter has been presented in **Figure 4.5C**. From **Figure 4.5C** it is clearly evident that $\mathrm{S_{disc}/S_{sphere}}$ increases with increasing the diameter which means stress is more effective in case of a nanodisc than a nanosphere but the extent of this increase of stress reduces gradually as higher value of diameter is approached. This increment of stress with diameter of nanodisc can be compensated by relaxing the electron cloud on nanosurface more easily and results surface plasmon shifting into red wing as we observed from the recorded tunable plasmon spectra (**Figure 4.1(II)**). Stress induced tuning of localized surface plasmon resonance wavelength for silver nanoparticle by mechanical force has been reported before by J. N. Aner *et al.*[307] In this work we have reported optical force induced large scale plasmon tuning simply by changing their aspect ratio where the induced stress directly depends on their aspect ratios.

4.5.3 Control Experiments

By any way we don't mean to establish this synthetic protocol as a methodology to generate AgNDs exclusively rather provides an easy colorimetric assay-based optical ruler technique for the trace-level quantitative gold detection simply by decoupling *in-plane* dipole resonance from their *out-of-plane* dipole resonance. As it is clear from the obtained TEM images that the gold-catalyzed silver nanomaterials synthesis generates both solid spherical particles as well as disc particles, it is expected to observe both *in-plane* and *out-of-plane* dipole resonances in their recorded UV-vis spectra where the *in-plane* dipole resonance contribution comes mainly from silver nanodiscs and *out-of-plane* contribution mostly comes from spherical silver nanoparticles. Relative intensity of *out-of-plane* and *in-plane* resonance measures their abundance and it is also clear from the UV-vis spectra that the extent of spherical particles formation is always much more compared to the nanodiscs.

The UV-vis peak at 265.5 nm indicates the presence of unreacted AA present in the solution and its intensity acts as a ruler to measure the catalytic efficiency of Au-ion to force AA to act as an efficient reducing agent. When we vary the final concentration of Au-ion in our assay between 200-2 *ppb*, an increment of the size of the generated AgNPs (between 5-50 nm) has been observed as evident from their UV-vis spectra (**Figure 4.1(II)**) as well as from TEM images in **Figure 4.4(I-VII)**. A dip-and-dry technique has been adopted to make TEM samples. After completion of the reaction, a TEM grid was immersed in the concentrated nanomaterial sample solution using tweezers, and the hydrophobic carbon coating allowed the formed monolayer of the sample to stick onto the copper mesh, which was dried on a soft tissue paper. After complete drying, the resulting grid was used for TEM. From **Figure 4.1(II)** it is also clear that the plasmon peak responsible for *out-of-plane* dipole resonance which indirectly measures the diameter of the generated spherical nanoparticles moves from 427 nm to 397 nm as we vary the added gold ion concentration between 2-200 *ppb*. Compared to the *out-of-plane* dipole resonance, the *in-plane* dipole resonance which measures the dimension of the AgNDs tuned between 800 nm and 500 nm by varying the Au-ion concentration in the same range.

To avoid any ambiguity of color coding, we have conducted several control experiments which include: (i) if we add variable amount of Au-ion solution in absence of TSC which acts as a surfactant in the composition (acts as a reducing agent only at elevated temperature) of 'growth solution', we have not observed any color appearance or color change, (ii) in absence of AA which acts a reducing agent (acts also as a stabilizing agent[57]), we could not achieve the reduction of Ag^+ and the subsequent formation of AgNDs to result color coding, (iii) in absence of both TSC and AA, formation of AgNDs is prohibited, and (iv) even in absence of TSC and $AgNO_3$ (to prove that the appearance of color is not due to the reduction of Au-ions by AA) there is no appearance of color. *In situ* generation of AgNDs are achieved only when all the essential components of the 'growth solution' with the optimal concentration (i.e. 5.3×10^{-4} M TSC, 2.5×10^{-4} M of $AgNO_3$, and 5×10^{-4} M of AA) reacts with an aqueous solution containing variable amount (200-2 *ppb*) of Au-ions and results different distinct colors. To confirm the fact further that the color of the growth solution is originating from AgNPs only, we performed another set of control experiments by varying the gold-ion concentration from 2 *ppb* to 1000 *ppb* in absence of silver nitrate solution while keeping other ingredients (TSC, AA) present in the above mentioned concentrations.

Several control experiments have been performed to make sure that we need the pre-formulated ‘growth solution’ to achieve the color-coded sensing of Au-ion. Figure **4.6(I)** and **(II)** clearly explain the necessity of the ‘growth solution’ composition to generate *in situ* AgNDs to generate different colors in presence of variable amount of soluble gold impurity. We have performed a number of control experiments to test the necessity of all of the four (4) components namely, TSC, Ag-ion, AA, and Au-ion in the ‘growth solution’, which are as follows:

(i) We performed the same experiment in absence of TSC, which known to be a stabilizing agent for spherical gold and silver nanoparticle synthesis, cannot generate any nanoparticle (gold or silver nanoparticle) and hence we have not observed any color appearance. This is clearly observable from the color of left most bottle of **Figure 4.6(I)**. This directly proves that the adequate amount of TSC is an essential component of the ‘growth solution’ to perform the color coded sensing of Au.

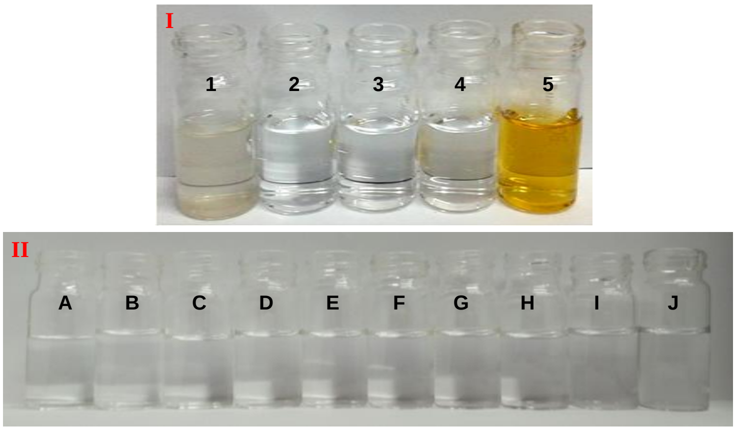

Figure 4.6: (I) 10 mL water solution containing (1) 250 μL 10^{-2} M $AgNO_3$ + 5 μL 10^{-4} M $HAuCl_4$ + 50 μL 100 mM AA, (2) 175 μL 1% TSC+ 250 μL 10^{-2} M $AgNO_3$ + 5 μL

10^{-4} M $HAuCl_4$, (3) 250 μL 10^{-2} M $AgNO_3$ + 5 μL 10^{-4} M $HAuCl_4$, (4) 5 μL 10^{-4} M $HAuCl_4$ + 50 μL 100 mM AA, (5) 175 μL 1% TSC + 250 μL 10^{-2} M $AgNO_3$ + 50 μL 100 mM AA + 2.5 μL 10^{-2} M (or 250 μL 10^{-4} M) $HAuCl_4$ or 500 *ppb* $HAuCl_4$. (II) 10 mL water solution containing 175 μL 1% TSC + 50 μL 100 mM AA + variable amount 10^{-4} M $HAuCl_4$ (A – 1 μL or 2 *ppb*, B – 3 μL or 6 *ppb*, C – 5 μL or 10 *ppb*, D – 10 μL or 20 *ppb*, E – 20 μL or 40 *ppb*, F – 50 μL or 100 *ppb*, G – 100 μL or 200 *ppb*, H – 200 μL or 400 *ppb*, I – 350 μL or 700 *ppb*, J – 500 μL or 1000 *ppb*).

(ii) Next we explored the role of AA by performing the colorimetric test in absence of AA while keeping all the other components present in the solution. In absence of Ascorbic acid, which generally acts as reducing agent (can act also as a stabilizing agent[308]), we could not achieve the reduction of Ag^+ and the subsequent formation of AgNDs and resultant color coding. The essential role of AA in the 'growth solution' is clearly visible from the color of the second bottle.

(iii) In the third bottle where we have added neither TSC nor AA and as we expect, addition of Au-ion does not produce any AgNDs and hence doesn't show any colorimetric change.

(iv) To make sure that the appearance of color in presence of soluble Au-ion is not due to the reduction of gold ions by AA, we performed the experiment in absence of TSC and $AgNO_3$. Generation of no color indicates that the added amount of Au-ion is not sufficient to show any visible color arising from gold nanoparticles which has been demonstrated in fourth bottle of **Figure 4.6(I)**.

(v) Bottle 5 represents the ideal case when all the essential components of the 'growth solution' are present in adequate amount and shows the yellow color from the generated AgNDs due to the addition of 500 *ppb* Au(III) in the 'growth solution'.

(vi) For further confirmation of the fact that the colours are originating from Ag nanoparticles and not interfered by any Au nanoparticle, we performed another set of control experiments by varying the gold solution concentration from 2 *ppb* to 1000 *ppb* (bottle A-J) in absence of silver nitrate solution which showed no noticeable colour arising in the visible region as reflected in Figure **4.6(II)**.

It is known in the literature[308] that AA can effectively act both as a stabilizing agent as well as reducing agent to generate gold nanoparticles. To cross check this, we have performed the same set of control experiments at higher concentration of Au-ion (>200 *ppb*) which generate nanoparticles predominated by gold nanoparticles and the subsequent color varies from yellow to red and finally to brown with a strong plasmon near 500 nm, a characteristic plasmon peak for gold nanoparticles. Effect of higher concentration of Au-ion to the ‘growth solution’ is described in **Figure 4.7**. This figure also explains that the presence of Hg^{2+} ($HgCl_2$) which enhances the detection sensitivity of Au by three times (×3), alone can't produce any color change; rather generates a grey color originating from insoluble AgCl.

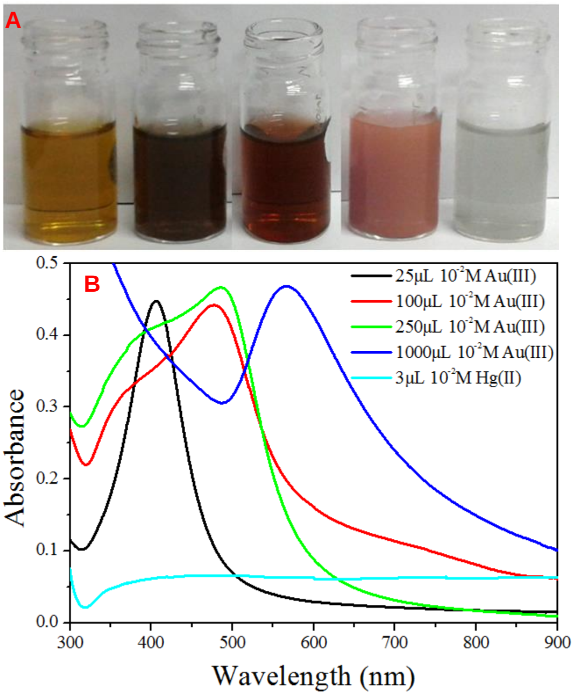

Figure 4.7: (A) (Left to right): 10 mL water with 175 µL 1% TSC, 250 µL 10^{-2} M $AgNO_3$, 50 µL 100 mM AA, and different amount of 10^{-2} M soluble gold (1) 25 µL, (2) 100 µL, (3) 250 µL, (4) 1000 µL, and (5) 3 µL of 10^{-2} M Hg^{2+} in absence of Au-ion. (B) Plasmonic response of 'growth solution' as we increase the concentration of Au-ion from ~1 µM to 1 mM.

4.5.4 Plausible Role of Au in Ag Nanoparticle Formation

Reported EDX data (**Figure 4.8**) show trace of Au only when the added Au-ion concentration is above 40 *ppb*. Elemental mapping of synthesized AgNDs have been performed by recording their EDX spectra. EDX spectra rely on the interaction between incident electrons and the materials inside the nanoparticles to provide unique set of X-ray emission[309] which gives the signature of the elemental composition[309]. Our measured EDX spectra in Figure 4.8 show trace of Au only when the added Au-ion concentration is above 40 *ppb*. Below 40 *ppb* of Au-ion, recorded EDX spectra does not show any signature of the Au-ion's presence but could easily be detectable by our colorimetric assay-based optical ruler which indirectly proves the sensitivity of our ‘growth solution’ based methodology for trace level of Au-ion detection.

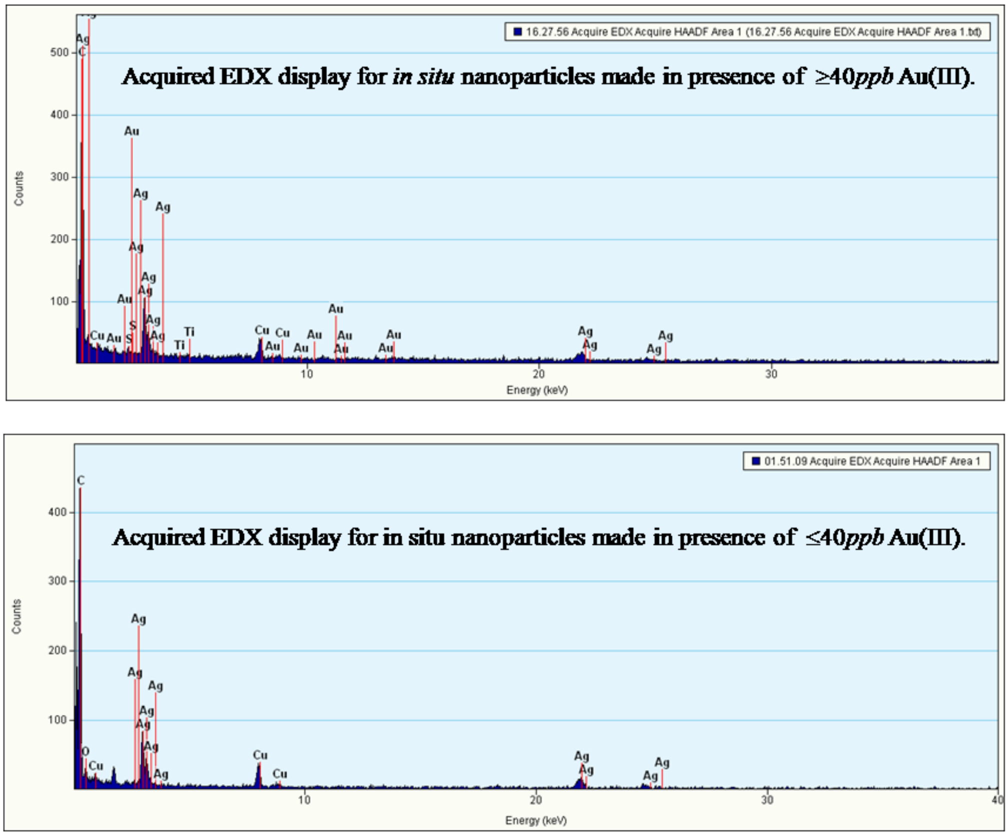

Figure 4.8: EDX spectra of the *in situ* generated AgNDs from the ‘growth solution’ in presence of Au-ion (top) ≥ 40 *ppb* and (bottom) ≤ 40 *ppb*.

Control experiments show the unusual and striking role of trace level Au-ions for the formation of AgNDs and offer a reliable methodology for highly specific sensing of different level of Au tracer. The role of trace level Au-ion can be explained by considering the reduction potentials of the component redox systems (a. Au^{3+}/Au^0, b. Ag^+/Ag^0 and c. AA^{2+}/AA) present in the ‘growth solution’. Reduction potentials for Au^{3+}/Au^0, Ag^+/Ag^0 and AA^{2+}/AA are 1.5, 0.81 and -0.066 V (at pH 7) respectively.[252,310–312] In absence of Au-ions, when the system is loaded by Ag^+ and AA, comparison of reduction potentials indicates that the available Ag^+ ions should be reduced by AA due to more +ve reduction potential of Ag^+/Ag^0 system and those electrons should be supplied by AA. Oxidation potential of AA is only +0.066 V and hence the differential reduction potential (between Ag^+/Ag^0 and AA^{2+}/AA) of ~0.8 V results a very low tendency to lose electrons to reduce Ag^+ for AgND formation and a large portion of AA (signifies the absorbance at 265.5 nm) remains un-reacted as evident from Figure 4.9. Though the differential reduction potential between Ag^+/Ag^0 and AA/AA^{2-} which is ~0.8 V results a very low tendency to reduce Ag^+ to Ag^0 for AgNP formation and a large portion of AA (absorbance at 265.5 nm) remain unreacted, presence of substantial amount of Au-ions changes the situation dramatically as the reduction potential of Au^{3+}/Au^0 is substantially higher than Ag^+/Ag^0 and the resultant differential reduction potential (between Au^{3+}/Au^0 and AA/AA^{2-} is 1.5 V) forces AA to acts as an efficient reducing agent. As a result, all the available AA is being used in the reduction process which corresponds to the disappearance of 265.5 nm peak from UV-vis spectra in Figure 4.9. Efficient use of AA as a reducing agent, catalyzed and regulated by Au-ion to reduce the available metal ions present in the 'growth solution' is clearly observable from Figure 4.9.

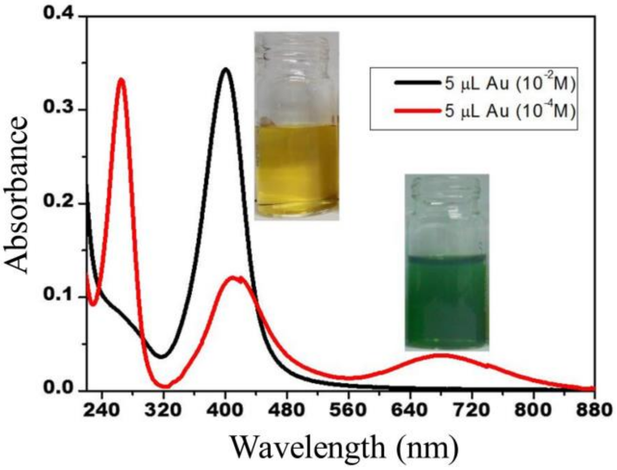

Figure 4.9: Au-ion regulated differential reduction potential to efficiently use AA as reducing agent. Disappearance of 265.5 nm absorbance originating from AA proves

the efficient use of AA as a component in the ‘growth solution’ to reduce Ag-ion in presence of substantial amount of Au-ion.

So, here Au-ions act as a catalyst to initiate the ascorbic acid oxidation process and the released electrons are mostly captured by silver ions due to 1000-fold more concentration of silver ions present in the solution compared to Au-ions. Observed EDX data (**Figure 4.8**) show that the generated nanoparticles are composed by silver only which alternatively proves our argument.

4.5.5 Selectivity of Sensing

Main challenge for any potential sensor is its selectivity towards the targeted one over competitive impurities present in the system. To show the specificity of this 'growth solution' towards Au-ions, we have tested this novel sensor in a multi elemental environmental sample. Preparation of the ‘growth solution’ remains same as we explained before and then added 600 *ppb* of different metal salts (Na^+, Pd^{4+}, Ru^{3+}, As^{3+}, Hg^{2+}, Mg^{2+}, Zn^{2+}, Cd^{2+}, Pb^{2+}, and Cr^{3+}) individually instead of Au salt to this ‘growth solution’ under constant stirring. We have not tested Pt as most of their salts are insoluble in water. As it is clear from **Figure 4.10A** that, in absence of Au-ions none of these samples (contaminated by different salts) are capable to generate AgNDs and thereby produce any visible change (Hg^{2+} gives gray color originating from insoluble AgCl) in the solution color for easy colorimetric detection. This proves the necessity of trace level of Au-ion for efficient formation of AgNDs.

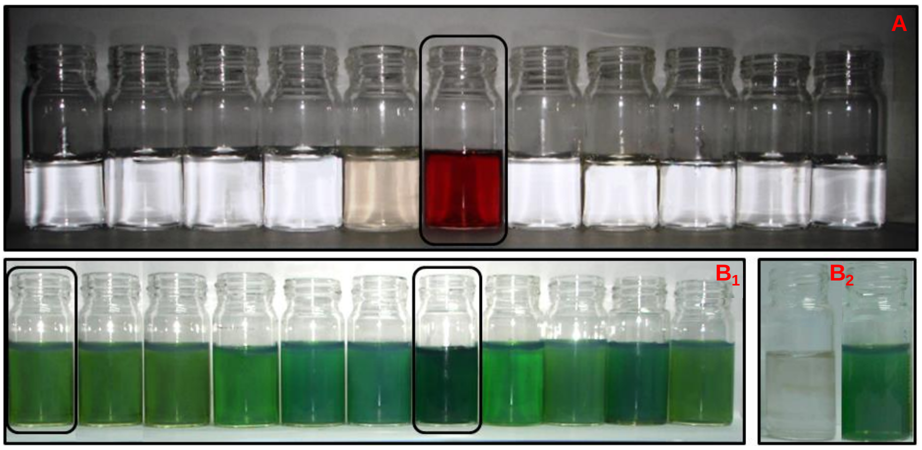

Figure 4.10: (A) Selective Au-ion sensing by the 'growth solution' in presence of different metal ions (600 *ppb*). From left to right: Na^+, Pd^{4+}, Ru^{3+}, As^{3+}, Hg^{2+}, Au^{3+} (20 *ppb*), Mg^{2+}, Zn^{2+}, Cd^{2+}, Pb^{2+}, and Cr^{3+}. (B_1) Effect of different interfering metals (600 *ppb*) in presence of 2 *ppb* Au(III). From left to right: Blank [2 *ppb* Au(III)], Na^+, Pd^{4+}, Ru^{3+}, As^{3+}, Mg^{2+}, Hg^{2+},Zn^{2+}, Cd^{2+}, Pb^{2+}, and Cr^{3+}, (B_2) Effect of Hg^{2+} to enhance the detection limit of Au tracer. From left to right: 'Growth solution' in presence of 700 *ppt* Au(III) without 600 *ppb* Hg^{2+} and with 600 *ppb* Hg^{2+}.

To find out the interfering aptitude of the other metals while gold present in the system, we have tested the sensing ability of our 'growth solution' by adding 2 *ppb* of Au(III) with 600 *ppb* of other metal salt solution individually or collectively. Except mercury, none of the other metal salts show much noticeable effect observable by simple colorimetric change. Worthwhile to mention that the presence of mercury (along with Au) doesn't change the color, plasmon resonance or the characteristics of the synthesized AgNDs rather it intensifies the color compared to the assay with equal amount of Au-ion without mercury impurity as clearly observable from **Figure 4.10B₁**. Presence of 600 *ppb* of Hg^{2+} enhances the Au-ion detection limit by three times and we could easily detect up to 700 *ppt* concentration. Effect of 700 *ppt* Au-ion in presence of 600 *ppb* of Hg^{2+} ions is shown in **Figure 4.10B2**. Maximum interference limit for other metal ions achieved from our experiment is 1 *ppm*.

4.5.6 Optical Ruler and its Sensitivity

4.5.6.1 Construction of Optical Ruler

Quantification of Au-ion can easily be achieved either from the observed color change or from the measured *in-plane* dipole resonance. Variation of *in-plane* dipole resonance with the concentration of added Au-ion has been plotted in **Figure 4.11** which shows an exponential fitting. We have repeated this detection several times (due to its low cost and one step detection nature) and gives absolutely reproducible result both spectroscopically as well as colorimetrically.

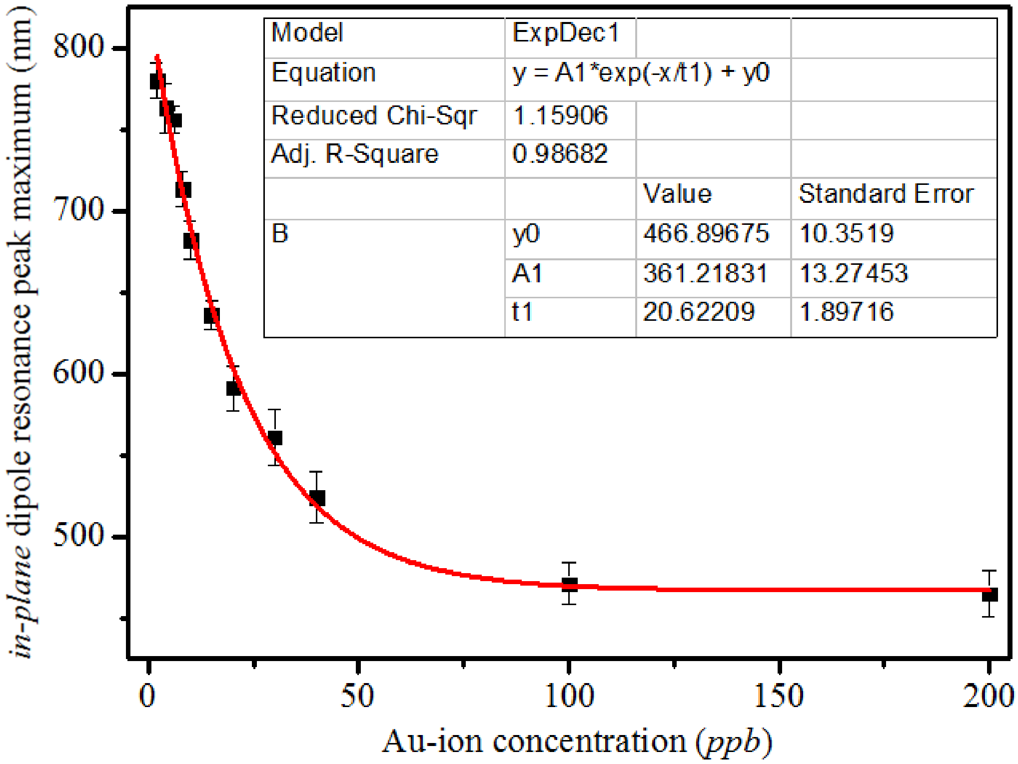

Model	ExpDec1		
Equation	y = A1*exp(-x/t1) + y0		
Reduced Chi-Sqr	1.15906		
Adj. R-Square	0.98682		
		Value	Standard Error
B	y0	466.89675	10.3519
	A1	361.21831	13.27453
	t1	20.62209	1.89716

Figure 4.11: Variation of *in-plane* dipole resonance with the concentration of added Au-ion where the plotted *in-plane* dipole resonance peak maxima are in nm and the gold ion concentrations are in *part-per-billion*.

To find the universal applicability of our turn-on colorimetric sensor, we have verified the detection and quantification ability of our assay by performing colorimetric test with cross examination by standard ICP-OES detection of available Au present in the assay. As an unknown gold sample we have taken trisodium citrate (TSC)-based gold nanoparticle solution with unknown concentration but doesn’t have contamination of other metals except gold. 10 μL of this gold nanoparticle solution first evaporated to dryness and then dissolved in 10 μL of a 5-time diluted aqua regia solution as Au-ions, which further diluted to 1mL to get the stock solution. From this stock solution we have taken 5, 10, 25, 50 and 90 μL of dissolved gold solution and mixed with our ‘growth solution’, which generates light green, deep green, deep red, orange and yellow color with tunable *in-plane* dipole resonance appearing at 759, 687, 583, 526 and 465 nm respectively. These specific colors correspond to the Au-ion concentration of 6, 10, 20, 40 and 100 *ppb* from our known colorimetric assay (**Figure 4.1(I)**) and 4, 10, 23, 37 and ~100 *ppb* from our optical assay as depicted in **Figure 4.11**.

We studied these aqueous phases obtained from our turn-on colorimetric assay by ICP-OES to measure the actual Au-ion concentration. For ICP-OES calibration, a 1000 *ppm* Au solution from NIST was used as known standard. Details of the employed operating conditions are listed in **Table 2.1** of **Chapter 2**.

Obtained gold concentration from the ICP-OES measurement for the above five solutions are 7.365, 10.8, 18.392, 43.7 and 110.61 *ppb* respectively that matches well with our expected values (average error: ~12% and obtained by calculating the % of error in Au-ion concentration measurement both from colorimetric and optical assay with respect to the standard ICP-OES method and then taking a final average of all detections from **Table 4.1**) and proves the robustness of our turn-on colorimetric assay for accurate Au-ion concentration measurement suitable for field applications both in mining industry as well as in forensic science.

4.5.6.2 Calculation of Average Error and Comparative Study for Sensitivity Analysis

We have taken 5, 10, 25, 50 and 90 μL from the stock solution of unknown Au-ion concentration and the measured values from different methods are recorded in **Table 4.1** against set-A, B, C, D and E respectively. The average error is obtained by calculating the % of error in Au-ion concentration measurement both from colorimetric and optical assay with respect to the standard ICP-OES method following equation (1) and (2) and then taking a final average of them.

$$\%\ \text{Error}_{\text{optical}} = \left| \frac{[Au]_{optical} - [Au]_{ICPOES}}{[Au]_{ICPOES}} \right| \times 100 \tag{4.1}$$

$$\%\ \text{Error}_{\text{colorimetric}} = \left| \frac{[Au]_{colorimetric} - [Au]_{ICPOES}}{[Au]_{ICPOES}} \right| \times 100 \tag{4.2}$$

Table 4.1: Au-ion concentration measurement from ICPOES, colorimetric and optical assay and the error calculated in colorimetric and optical assay with respect to the standard ICP-OES method.

Set	**A**	**B**	**C**	**D**	**E**
$[Au]_{ICPOES}$	7.365	10.8	18.392	43.7	110.61
$[Au]_{optical}$	4	10	23	37	100
$[Au]_{colorimetric}$	6	10	20	40	100
% $\text{Error}_{\text{optical}}$	45.689	7.407	25.054	15.331	9.592
% $\text{Error}_{\text{colorimetric}}$	18.533	7.407	8.742	8.466	9.592

As the optical error corresponding to Set A is $\approx$46% and justifiable to consider as an outlier data, it has been ignored in Average $\text{Error}_{\text{optical}}$ calculation. So,

Average $\text{Error}_{\text{optical}}$ = 14.346%

Average $\text{Error}_{\text{colorimetric}}$ = 10.548%

Average Error = ½ (Average $\text{Error}_{\text{optical}}$ + Average $\text{Error}_{\text{colorimetric}}$) = 12.447% $\approx$12%

A comparative sensitivity of Au-ion detection by our colorimetric assay-based optical ruler with respect to the ICP-OES as standard analytical sensing tool is shown in **Figure 4.12**.

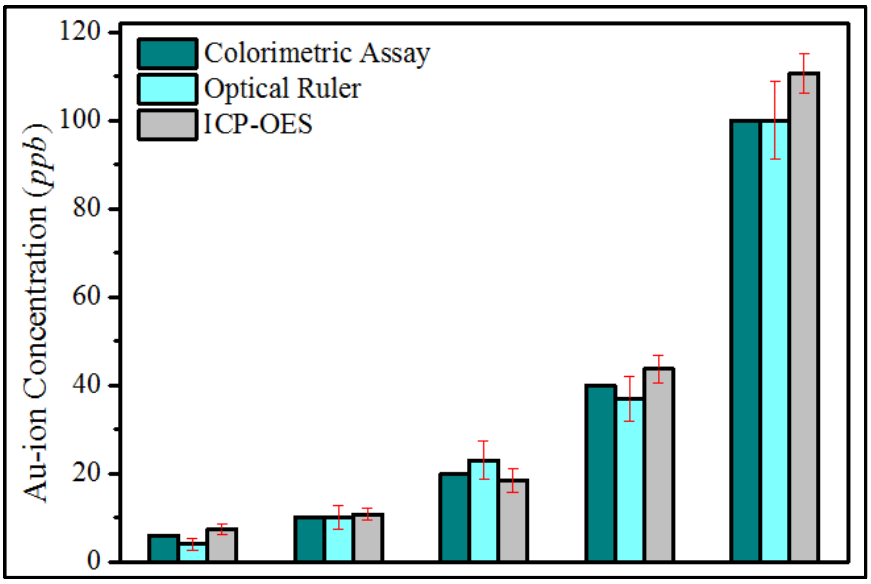

Figure 4.12: A Comparative sensitivity analysis of Au-ion detection by our colorimetric assay-based optical ruler with respect to the ICP-OES as standard analytical sensing tool is shown as bar plots. Average error both for colorimetric assay and optical ruler is estimated about ~12%.

4.5.6.3 Detection of Gold from Real Ore Sample

For any reliable sensor, the major concern is the possible interference of the matrix for real sample detection. To prove the reliability of our technique, we have verified our assay further by testing real environmental samples. We have received (from MISiS, Moscow, Russia) an oxidized gold ore and its tailing (Bugunda Gold Deposit, Tajikistan) with average gold content of 6 g/ton and 3 g/ton respectively. We have extracted gold from the oxidized ore by converting metallic gold (Au^0) into soluble gold (Au^{3+}) by dissolving the ore into aquaregia solution. To avoid the effect of pH on the detection efficiency we have pre-diluted the aquaregia which is sufficient to dissolve the deposited gold in the ore but the pH of the “growth solution” remains neutral after the addition of gold impurity. Due to the presence of several other heavy metals as co-minerals (silver, copper, iron, mercury, arsenic, etc.) in the ore, solubilization of gold ore also solubilizes other metals as ions and hence the resultant ore solution is a mixture of several different metal ions. As mentioned before that the detection efficiency highly depends on the concentration of mercury ion as impurity in the gold solution, contamination by several other metal tracer may influence the detection efficiency several orders compared to the ideal case as we have explained for pure gold ion detection. Details about the soluble gold extraction from oxidized ore and tailing has been described in the experimental section. We have taken 3, 5, 10, 15, 20, 25, 35 and 50 µL of the extracted stock solution from oxidized ore and added to the “growth solution” which generates gray, light green, deep green, red, orange and different shades of yellow color respectively after few minutes of treatment as has been shown in **Figure 4.13**.

Figure 4.13: Colorimetric response from oxidized ore samples as we vary the concentration of gold ion (L-R: 300, 210, 150, 120, 90, 60, 30 and 18 *ppt*).

By considering the initial gold content of 6g/ton (Confirmed by ICP-OES) for oxidized ore, the final concentration corresponding to different colors are 18 *ppt*: gray, 30 *ppt*: light green, 60 *ppt*: deep green, 90 *ppt*: red, 120 *ppt*: orange, 150 *ppt* and above: different shades of yellow. The detection limit (30 *ppt* concentration shows the first colorimetric signature) obtained from the oxidized gold ore sample is thus at least 10 times more sensitive compared to the pure gold or gold with mercury samples. Despite the more sensitivity of gold detection from ore sample, the pattern of color change with increasing concentration of gold content remains unchanged and this more sensitivity of gold detection could be due to the presence of innumerable different metals and nonmetals present in the ore samples which in general gives more sensitivity with unchanged specificity as has been described for Hg(II) impurity of gold sample.

4.6 Conclusion

In summary, present study reports the development of a turn-on colorimetric sensor assay for highly specific and ultrasensitive detection and quantification of gold (Au) content in a multi-elemental environmental sample (gold ore) with achievable sensitivity way down to 30 *ppt*. Detection and quantification of gold was achieved by a low cost green synthetic route mediated decoupled *in-plane* dipole resonance modulated colorimetric assay-based optical ruler of *in situ* generated variable sized AgNDs. We have put forward a plausible explanation of the role of Au-ion tracer to initiate the shape variable silver nanoparticle formation in the 'growth solution' by considering the reduction potentials of the component redox systems. By considering the cost, toxicity, and simplicity to perform a sensing experiment, our turn-on colorimetric sensor offers a robust analytical assay for accurate gold (Au) concentration measurement suitable for field applications both in mining industry as well as in forensic science.

CHAPTER 5

HEDGEHOG GOLD NANOPARTICLES SYNTHESIZED BY APPLYING LE CHATELIER’S PRINCIPLE OFFER TUNABLE PLASMONICS AND HIGH SERS SIGNAL

OUTLINE: What does the study offer?

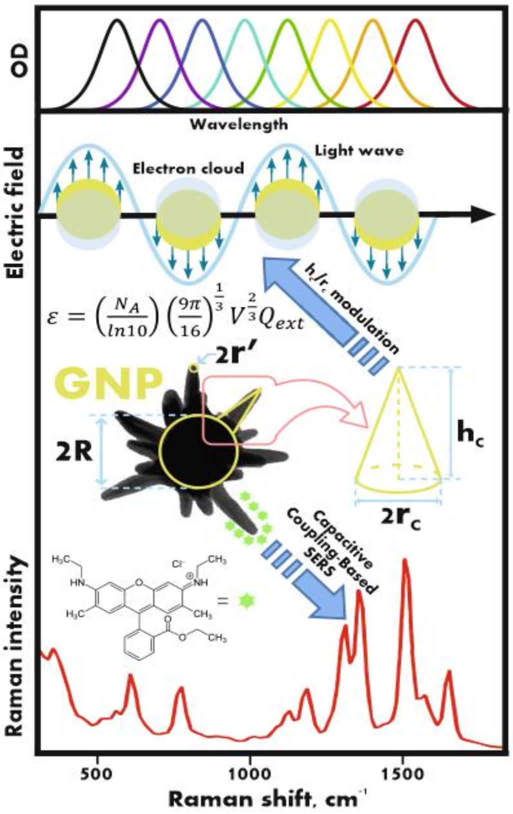

- A seed-less surfactant-less one pot synthetic strategy that produces highly anisotropic nanostructures resembling ‘Hegdehog’.
- Detailed mechanistic study of the growth of nanostructures in the light of Le Chatelier’s principle.
- Anisotropic noble metal nanostructures with tunable plasmonics and optical properties in physiological window.
- Tipped structure with sharp spikes, inter-spike space and highly exposed surface area exhibiting high SERS throughput signal.
- Discrete Dipole Scattering (DDSCAT) model for theoretical correlation of observed results.
- Nontoxic nanomaterials stable in high saline environment and optimum pH mimicking physiological condition - apt for theranostic application.

5.1 Introduction

Although the literature is rich with reports of anisotropic nanomaterial synthesis[9,246,313,314] by adopting a template-based reaction mechanism or multi-step seeding methodology, a simple seed-free and surfactant-free synthesis at room temperature by exploiting Le Chatelier's principle[315]-based 'common ion effect' is not only rare but also unique in the utilization of the chemical equilibrium conditions for controlling the degree of anisotropy of the synthesized nanoparticles. A new synthetic methodology with the ability to produce more benign nanostructures by avoiding toxic templates[10] while retaining plasmonic attributes, especially within the physiological window, is in high demand. The generation of highly anisotropic gold nanomaterials with the sharpest nanoscopic surface features able to support broad-band plasmon tunability and high throughput Raman scattering activity by a single-pot synthetic route could be advantageous both for cost-effective technological[1–4] and medicinal[5–7] applications due to their unusual optical, mechanical, electrical and magnetic properties,[316] along with their photo-chemical stability, negligible toxicity, easy synthesis, and standard protocols for surface modifications.[9,10]

Here we have demonstrated an anisotropic gold nanoparticle (GNP) synthetic strategy devoid of seed and shape-templating agents at room temperature simply by controlling the added salt (NaCl) concentration where trisodium citrate (TSC) and ascorbic acid (AA) were employed as a particle stabilizing agent and mild reducing agent, respectively. Effective deposition of the *in situ* generated 'common ion (Cl^-) effect'-induced solubility-tuned AgCl was investigated as the driving force for selective facet blocking to generate highly anisotropic sharper GNPs resembling 'hedgehog' (**Figure**

5.1). Because of structural similarities, we have named them hedgehog gold nanoparticles i.e. HHogGNPs.

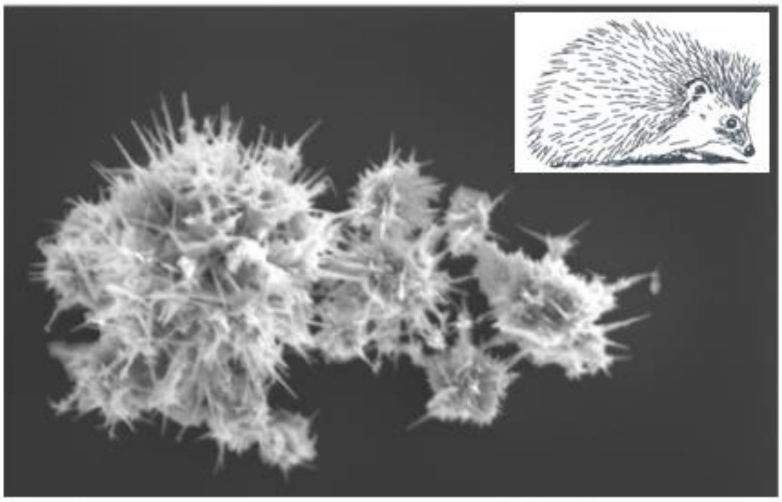

Figure 5.1: Synthesized Nanostructures with structural similarity of spines of a 'hedgehog' (inset picture taken from Ref.[317]) which we have named as – Hedgehog gold nanoparticles, HHogGNPs.

The synthesized HHogGNPs showed broad-band Plasmon tunability along with improved surface enhanced Raman scattering (SERS) efficiency as we incrementally tuned the NaCl concentration. A plausible explanation has been put forward in detail, to explain the highly anisotropic nature and superlative SERS activity as a function of the 'common ion' concentration in the mother solution.

Discrete dipole approximation for the scattering (DDSCAT) calculation has been used to understand the plasmonic and scattering properties of HHogGNPs as a function of their tip size. MTT-based dark toxicity test results prove their non-toxic nature in the absence of light. To the best of our knowledge, this is the first report where Le Chatelier's principle in the form of the 'common ion effect' is successfully used to generate highly anisotropic nanomaterials with regulated exposed surface areas, variable tip curvatures, and improved aspect ratios without employing any template ligand or seed to achieve the broad-band plasmon tunability with outstanding Raman activity.

5.2 Synthesis of HHogGNPs

There are reports where anisotropic gold nanostructures have been synthesized using TSC based spherical Au Nano seed which involves boiling gold chloride solution in presence of 1% TSC[314]. TSC works as reducing agent as well as stabilizing agent in these cases. We wanted to avoid any seed-mediated growth rather generating *in situ* seed simply by reducing the gold chloride solution in presence of ascorbic acid where variable amount of 1% TSC acts as a stabilizing agent and this is the logic behind the utilization of 1% TSC in the mother solution. The schematic representation of the comprehensive synthesis of seed-free and template-free gold nanostructure (nano stars and HHogGNPs) as a function of pH and the concentration of TSC, $AgNO_3$ and Cl^- is summarized in **Figure 5.2**. The role these parameters in controlling the growth and structure has been illustrated later in the **Results and Discussion** section.

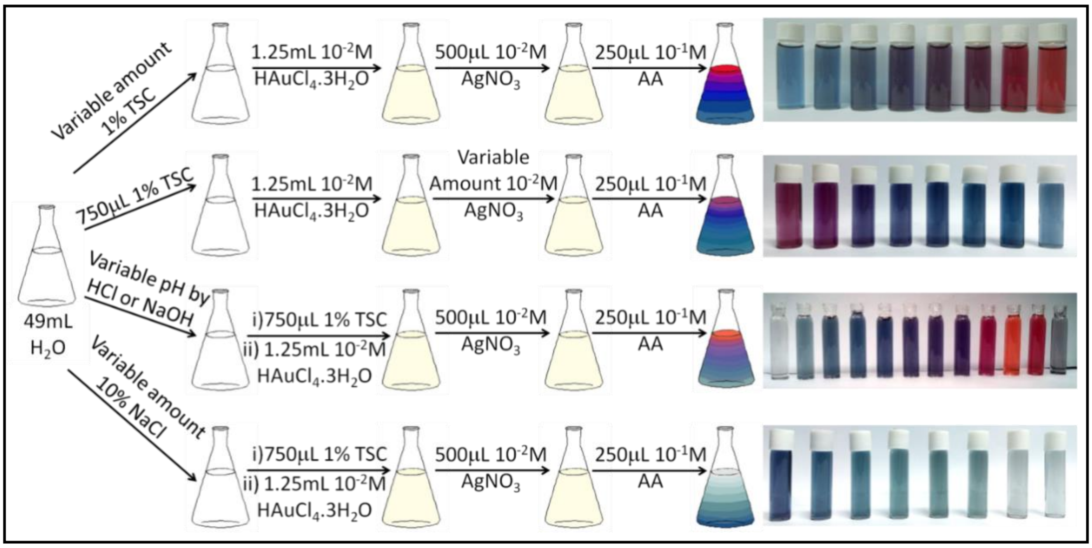

Figure 5.2: Schematic representation of seed-free and template-free gold nanomaterials synthesis by varying the concentration of TSC (top), $AgNO_3$ (second

from top), pH (second from bottom) and NaCl (bottom). The corresponding change of color of solutions with gradual increment of TSC, $AgNO_3$, pH and NaCl is represented beside each scheme.

In a typical synthetic protocol, 49 mL Milli-Q water was taken in a conical flask to which we added variable amount (0-2500 μL) of 1% TSC, 1.25 mL of 10 mM $HAuCl_4.3H_2O$ solution, 500 μL of 1.5 mM $AgNO_3$ and 250 μL of 10^{-1} M ascorbic acid solution (drop wise) in the mentioned sequence with continuous stirring (300 rpm) at room temperature (~25 °C). This protocol gives nanoflowers and nanostars (**Figure 5.3**) based on different amount of TSC.

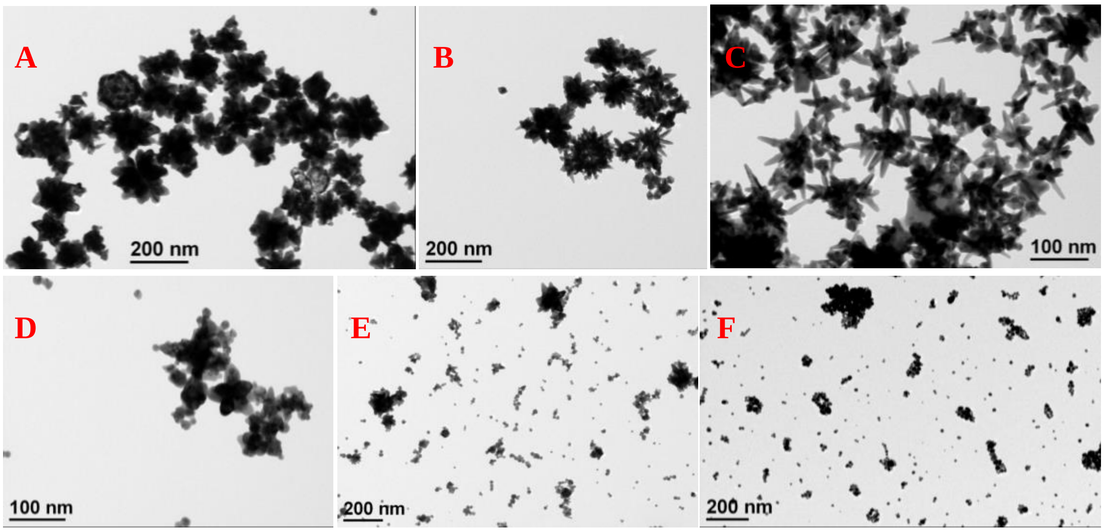

Figure 5.3: Structural evolution of gold nanomaterials as we increased the extent of TSC (A) 50 μL, (B) 250 μL, (C) 500 μL, (D) 875 μL, (E) 1000 μL and (F) 1250 μL.

It was noticed that though we could generate branched structures in absence or in presence of low concentration TSC, we cannot make them stable for longer period due to the lack of sufficient stabilizing agent to create enough electrostatic repulsion among them. In contrary, synthesized nanostructures tend to become spherical in shape with larger stability when we use higher concentration of TSC in the mother solution. **Figure 5.3** shows that the resultant nanomaterials evolved from flower shapes to spherical one as we increase the concentration of TSC. To avoid their instability while keeping their anisotropic nature intact, we have selected an optimum amount of 750 μL of 1% TSC in the mother solution and varied other reaction parameters. For example, to synthesize variable amount $AgNO_3$-based nanostars we took 750 μL of 1% TSC and the same reaction was carried out with 200-2500 μL of 1.5 mM $AgNO_3$. We prepared different pH solutions in the range of 1-12 either by adding controlled volume of HCl (for pH 1-4) or NaOH (for pH 5-12) in the mother solution. Keeping the molar ratios of TSC, $HAuCl_4.3H_2O$, $AgNO_3$ and ascorbic acid constant (750 μL of 1% TSC mixed with 1.25 mL of 10^{-2} M $HAuCl_4.3H_2O$, 500 μL of 1.5 mM $AgNO_3$ and 250 μL of 10^{-1} M ascorbic acid) we have generated highly anisotropic hedgehog gold nanoparticles (HHogGNPs) approaching lower pH (pH 1-4). Considering the role of HCl by decreasing the solubility of AgCl through 'common ion' effect, we have implemented NaCl (the salt also generates additional chloride ions, Cl^-, in the mother solution to offer same 'common ion' effect as offered by HCl) as a replacement of HCl to form HHogGNPs by keeping pH of the reaction mixture close to neutral. We took 0-1200 μL of 1.7 M NaCl solution to vary the Cl^- concentration between 250 μM to 40.25 mM ($HAuCl_4$ solution is the source of 250 μM Cl^- in the reaction mixture in absence of NaCl) into 49 mL water and added 750 μL of 1% TSC, 1.25 mL of 10^{-2} M $HAuCl_4.3H_2O$, 500 μL of 1.5 mM $AgNO_3$ and 250 μL of 10^{-1} M ascorbic acid in sequence with continuous stirring at 300 rpm at room temperature as mentioned above. In this case, hedgehog nanostructures are obtained particularly when NaCl concentration in the mother solution is 170 μM or higher.

After the synthesis of shape tunable HHogGNPs, aliquots were taken from the solutions to centrifuge at 2000-4000 rpm for 2 h depending on particle size to remove unbound reagents. These concentrated samples were the used for making TEM grids and for carrying out further SERS and toxicity experiments.

The synthesis with ascorbic acid only (in the absence of TSC, $AgNO_3$ and NaCl) has also been attempted. 1 mL of 10^{-2} M ice-cooled $HAuCl_4.3H_2O$ solution was rapidly added into 20 mL of ice-cooled solution of 10^{-1} M ascorbic acid with constant stirring (300 rpm); the mixture was then kept on ice. A deep blue colour appeared and the corresponding absorption spectra and TEM image has been shown in **Figure 5.4**. The solution remains stable for months if we kept them in refrigerator.

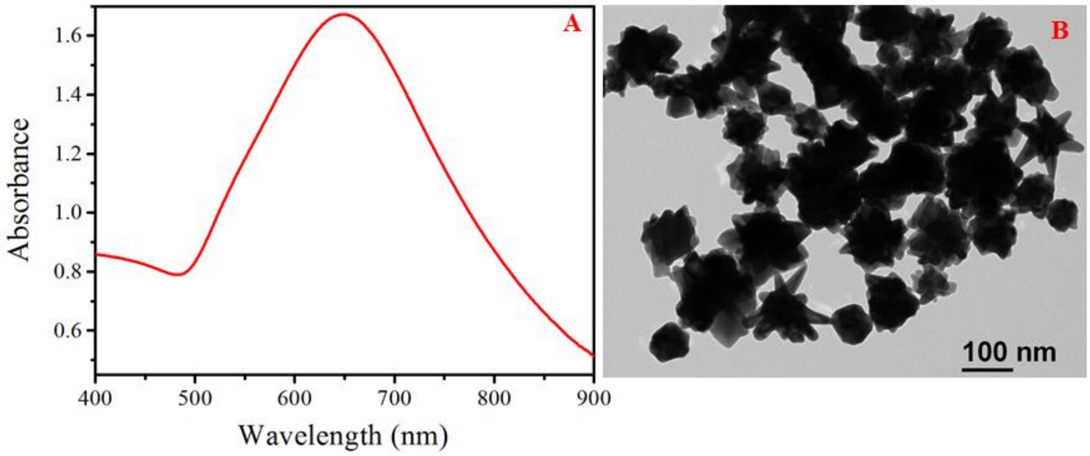

Figure 5.4: (A) Absorption spectra of gold nanostars synthesized by reducing Au(III) with ascorbic acid only in the absence of TSC, $AgNO_3$ and NaCl and (B) corresponding TEM image of the obtained gold nanostars.

5.3 Results and Discussion

5.3.1 Alteration of Structural Parameters with NaCl Variation

To understand how NaCl controls the growth and structure of the HHogGNPs, we synthesized them in the presence of variable (35 µM–20 mM) ‘common ion’ concentrations and recorded the corresponding TEM and SEM images of the HHogGNPs (represented in **Fig. 5.5**). Except at very low concentrations, the diameter of the synthesized HHogGNPs is independent of [Cl^-] and remains constant at 220 nm, although the numerical exposed surface area gradually increases and ultimately results in coreless particles.

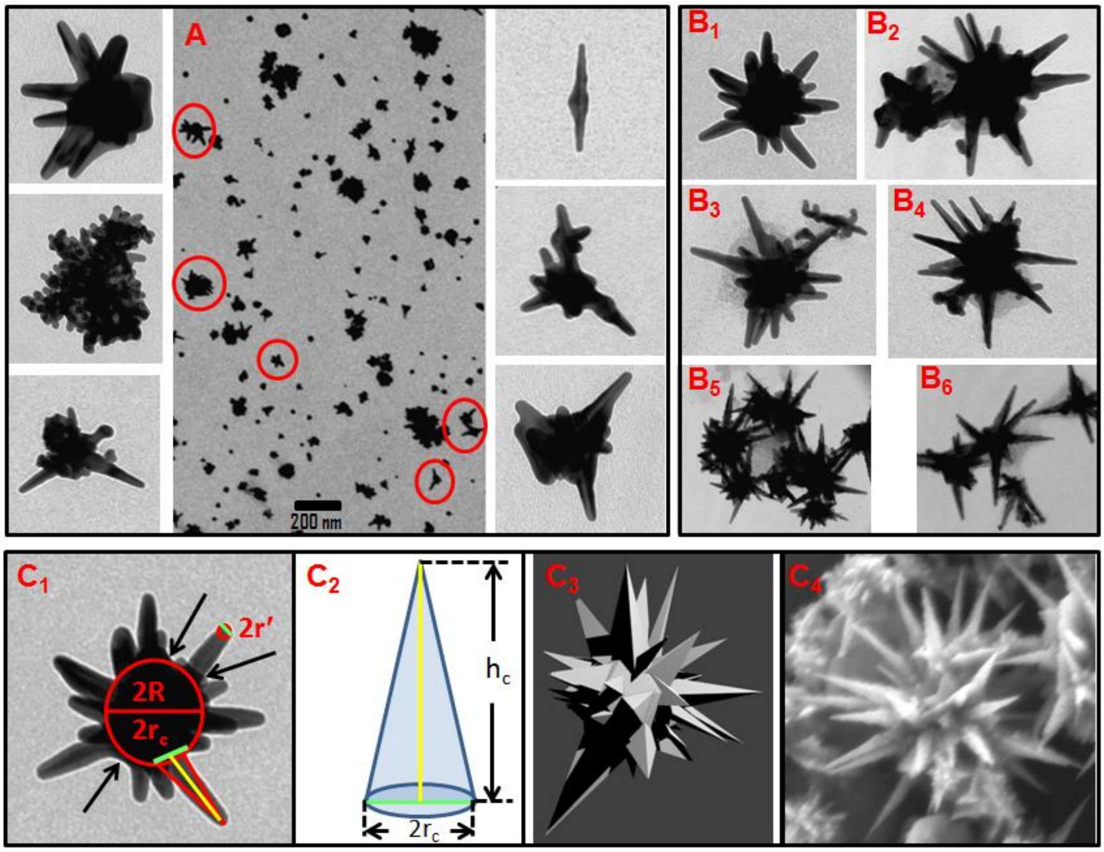

Figure 5.5: TEM images of the HHog nanomaterials synthesized using (A) low concentrations of NaCl (up to 136 µM) and (B_1–B_6) tunable high concentrations of NaCl (170 µM–20 mM). Schematic representations of (C_1) a 2D TEM image of an individual HHogGNP; (C_2) a cone-shaped individual sharp tip; (C_3) a model HHog structure for DDA and DDSCAT calculations created by Blender software; (C_4) a 3D SEM image of a discrete HHogGNP.

However, recording of large area TEM and SEM is very important to find out their monodispersive nature and to evaluate their aggregation behaviour. **Figure 5.6** represents the corresponding large area TEM and SEM recorded from 10 mM NaCl-based HHogGNPs. All HHogGNPs synthesized in the presence of 20 mM NaCl or less remains stable for months.

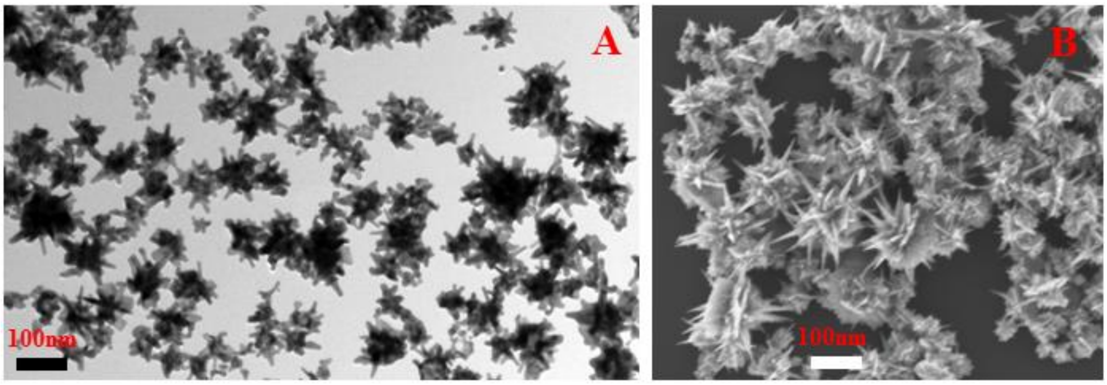

Figure 5.6: (A) Large area TEM and (B) SEM image of HHogGNPs synthesized by using 10 mM NaCl in the mother solution.

To find out the number of tips, N, we had first taken TEM images for ~30 different hedgehog structures synthesized at a particular NaCl concentration. Then we counted the total number of visible spikes for 2π solid angles to get an idea about the possible number of spikes for 4π solid angles (3D-space) for each of the structures. In the **Figure 5.7** the tips are marked based on which we have counted and obtained the average number of tips.

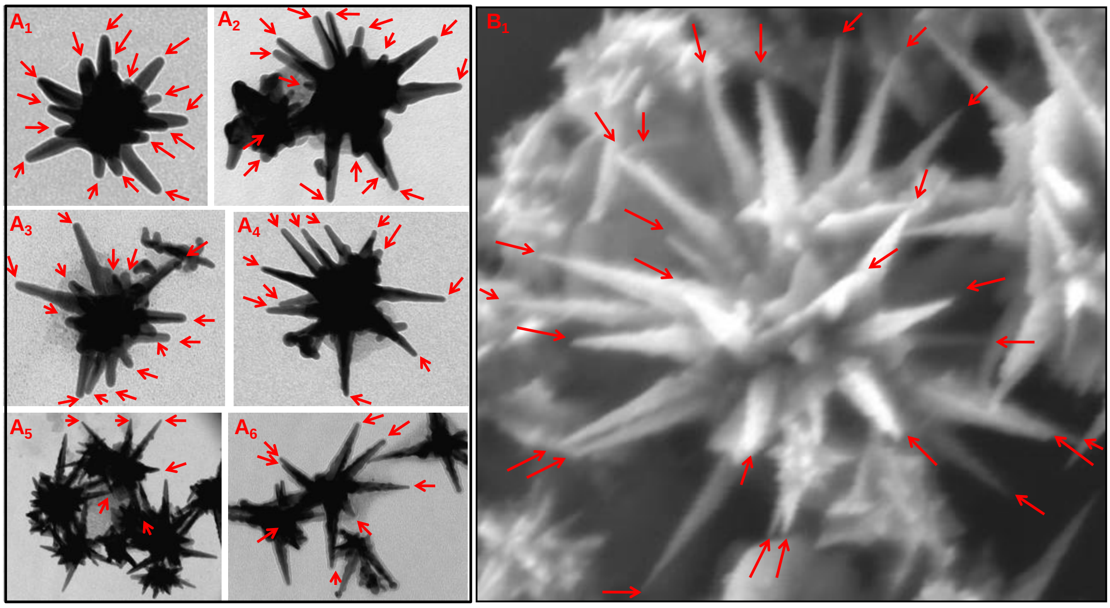

Figure 5.7: (A_1-A_6) are TEM images of HHogGNPs synthesized at different NaCl concentration: A_1 – 170 µM, A_2 – 340 µM, A_3 – 1.7 mM, A_4 – 3.4 mM, A_5 – 10 mM, A_6 – 20 mM and B1 is the SEM image of a HHogGNP synthesized in presence of 10 mM NaCl.

The SEM and TEM images show very sharp tips projected throughout the 4π solid angle of the tiny central core with gradual increments of tip curvature (κ) and average aspect ratio (AAR) and a steady reduction of the central spherical core diameter ($2R$), the number of tips (N) projecting out from the core, and the 2D-projected angle (degree) covered by tips as we increase the 'common ion' concentration. Detailed structural statistics of the synthesized HHogGNPs are listed in **Table 5.1**.

As discussed earlier,[52] by considering each sharp tip as a cone with 'r_c' as the average radius of the base, 'h_c' as the average length of the tips and 'R' as the average radius of the HHogGNP core, the relative surface area (RSA) offered by the collective face of the surface tips over the uncovered (by sharp tips) central spherical core can be formulated and calculated as:

$$RSA = \frac{N\pi r_c\left(\sqrt{{h_c}^2+{r_c}^2}\right)}{4\pi R^2 - N\pi {r_c}^2} \tag{5.1}$$

In **equation (5.1)**, numerator is the collective surface area of sharp tips and the denominator is the effective surface area of the central spherical core which is not covered by sharp tips. The mathematical term $N\pi r_c^2$ measures the extent of the surfacearea of the central core which is covered by sharp tips. Detailsof the mathematical formulation of **equation (5.1)** can be understood from **Fig. 5.5C$_1$ and 5.5C$_2$**. Due to the rapid reduction of the spherical core diameter compared to the base diameter of sharp tips, incremental modulation of common [Cl$^-$] results in a ~3 times increment of RSA which indirectly controls the SERS activity and is discussed in details in later sections.

Table 5.1: Detailed structural statistics of Le Chatelier's Principle based common Cl^- induced synthesized HHogGNPs.

NaCl concentration (M)	170×10^{-6}	340×10^{-6}	170×10^{-5}	340×10^{-5}	10×10^{-3}	20×10^{-3}
Average particle diameter (nm), $2R_0$	220±19	220±16	220±09	220±21	220±11	220±13
Average surface-tip length (nm), h_c	60±11	69±15	80±09	89±09	93±11	95±06
Average core diameter (nm), $2R$	100±17	94±17	73±05	68±11	50±07	30±04
Average number of tips, N	32±06	28±07	26±05	20±03	16±04	10±03
Average diameter at the tip (nm), $2r'$	5.0±0.9	3.6±1.1	3.2±0.6	2.6±0.7	2.4±0.2	2.0±1.0
Curvature at the tip (cm^{-1}), $\kappa = (r')^{-1}$	(4.2±0.7) ×10^6	(6.1±1.9) ×10^6	(6.5±1.2) ×10^6	(8.3±2.2) ×10^6	(8.4±0.7)× 10^6	(1.3±0.7) ×10^7
Tip base diameter (nm), $2r_c$	10±1.3	9±0.8	8±0.8	7.5±0.5	5.6±0.6	5±0.2
2D projected angle covered by the tip (degree)	12.8±1.3	10.3±1.8	7.6±0.4	7.1±0.7	5.6±0.3	4.7±0.1
Average Aspect Ratio (AAR) of surface tips	9±3.0	14.4±4.6	17.5±7.5	23.1±11.2	27.7±11.1	33.3±13.7
Zeta potential (mV)	-32	-29	-22	-20	-17	-16
RSA	1.04±0.1	1.05±0.2	1.74±0.6	1.5±0.2	1.75±0.5	2.8±0.7

5.3.2 Theoretical Correlation from Discrete Dipole Scattering (DDSCAT) approximation

Here we have used the DDSCAT[318] calculation by modeling the TEM images of the HHogGNPs to understand their experimentally observed scattering and absorption patterns. More than 15 spikes are modelled in each of the HHogGNPs where ImageJ software is used to model the three-dimensional HHog shape from the two-dimensional projection of TEM images. With the help of Blender software, we have considered more than 40 objects to make a HHog shape as shown in **Fig. 5.5C$_3$**. From the ImageJ analysis and experimental observations, we have considered the maximum tip-to-tip distance of 85±3 nm where ±3 represents the anisometric shape of the nanoparticles. To implement the idea of rapid growth of the tips compared to their core, the length of the individual tip to the spherical core is considered in the ratio of 2.5 : 1.5. Water is used as the surrounding medium (n = 1.33) for the surface Plasmon resonance (SPR) calculation. We have calculated the extinction constant factor (Q_{ext}), scattering constant factor (Q_{sca}), and absorption constant factor (Q_{abs}) (where $Q_{ext} = Q_{abs} + Q_{sca}$)[319] and have listed these values in **Table 5.2** in order to quantify the extinction coefficient (ε in $M^{-1}cm^{-1}$) for the HHogGNPs using the following formula:

$$\varepsilon = \left(\frac{N_A}{ln10}\right)\left(\frac{9\pi}{16}\right)^{\frac{1}{3}} V^{\frac{2}{3}} Q_{\_ext} \qquad (5.2)$$

Here, N_A is Avogadro's constant and V is the volume of the HHogGNPs. The variation of the calculated molar extinction coefficient (ε), extent of scattering, and SPR maxima (in μm) shows the same incremental trends as we observed experimentally with the growing tip-to-tip distance and the theoretically calculated result is depicted in **Fig. 5.8**.

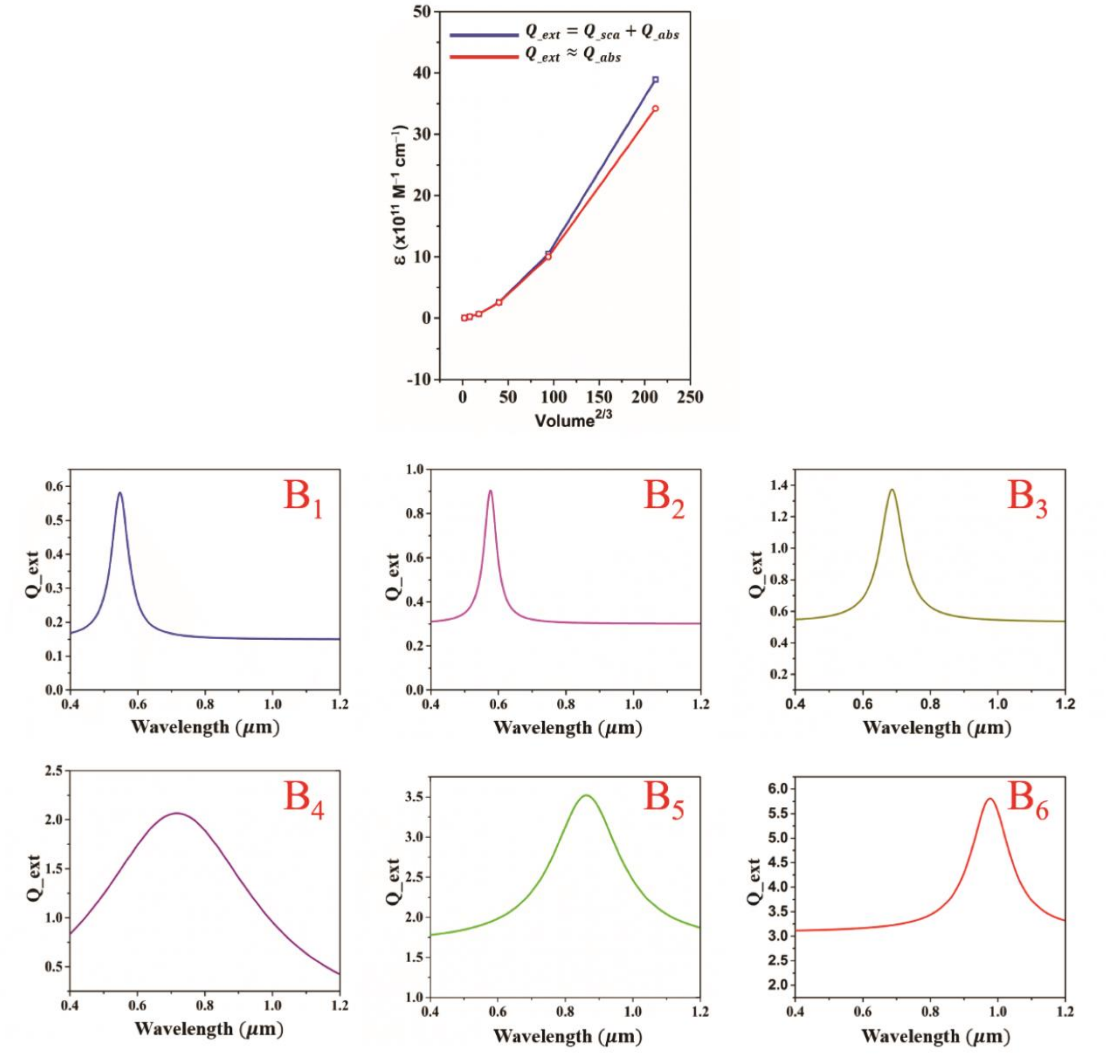

Figure 5.8: (A) Variation of molar extinction coefficient (ε) with the volume of the HHog nanoparticles and SPR maxima (in μm) for different tip-to-tip distances (B_1: 9 ± 1 nm, B_2: 15± 1 nm, B_3: 23±2 nm, B_4: 35±3 nm, B_5: 55±3 nm, B_6: 85±3 nm,) nanoparticles.

Our calculated SPR maxima and extinction coefficients show that the values increase with particle size. Similarly, the effect of scattering is also observable as we increase the particle size. Furthermore, our results show that surface plasmon resonance (SPR) depends on the size/area of the nanoparticle. In the case of a smaller tip-to-tip distance, the SPR value depends only on the dissipation of energy due to inelastic collisions

(Q_{abs}); whereas for particles with bigger tips, the RSA increases gradually which results in higher-order electron oscillations on the surface in order to enhance both the scattering cross section and extinction coefficient.[320] These trends are very much in agreement with previous reports.[321,322]

Table 5.2: The calculated geometrical properties (Tip-to-tip distance, volume, and surface area), SPR maxima, absorption constant factor (Q_{abs}), scattering constant factor (Q_{sca}) and extinction coefficient (ε) for modelled HHog nanoparticles.

Tip-to-tip distance (nm)	Volume ($\times 10^3$ nm^3)	Surface ($\times 10^3$ nm^2)	SPR maxima (µm)	Q_{abs}	Q_{sca}	ε ($M^{-1} cm^{-1}$)
9 ± 1	0.0027	0.037	0.548	0.551	0.000	3.37×10^{9}
15 ± 1	0.0222	0.150	0.597	0.904	0.002	22.63×10^{9}
23± 2	0.0750	0.339	0.658	1.180	0.010	6.69×10^{10}
35 ± 3	0.2534	0.762	0.731	2.025	0.035	2.60×10^{11}
55 ± 3	0.9136	1.793	0.852	3.360	0.161	1.04×10^{12}
85 ± 3	3.0834	4.035	0.960	5.108	0.703	3.89×10^{12}

5.3.3 Growth Governed by Le Chatelier's Principle

The role of NaCl in the crystal stabilization in absence of any seed or shape templating reagent has been explored by recording their high resolution TEM (HRTEM) data as depicted in **Figure 5.9**. It is well known in the literature[323] that most of the noble metal nanomaterials crystallize in the face-centered cubic (*fcc*) crystal structure and surface energy considerations are very crucial to explain their stability. It is clear from the diffraction pattern (strong diffraction ring in **Figure 5.9A$_2$**) and lattice spacing in **Figure 5.9** that the entire sharp tips projecting out of the central spherical core are oriented in {111} direction.

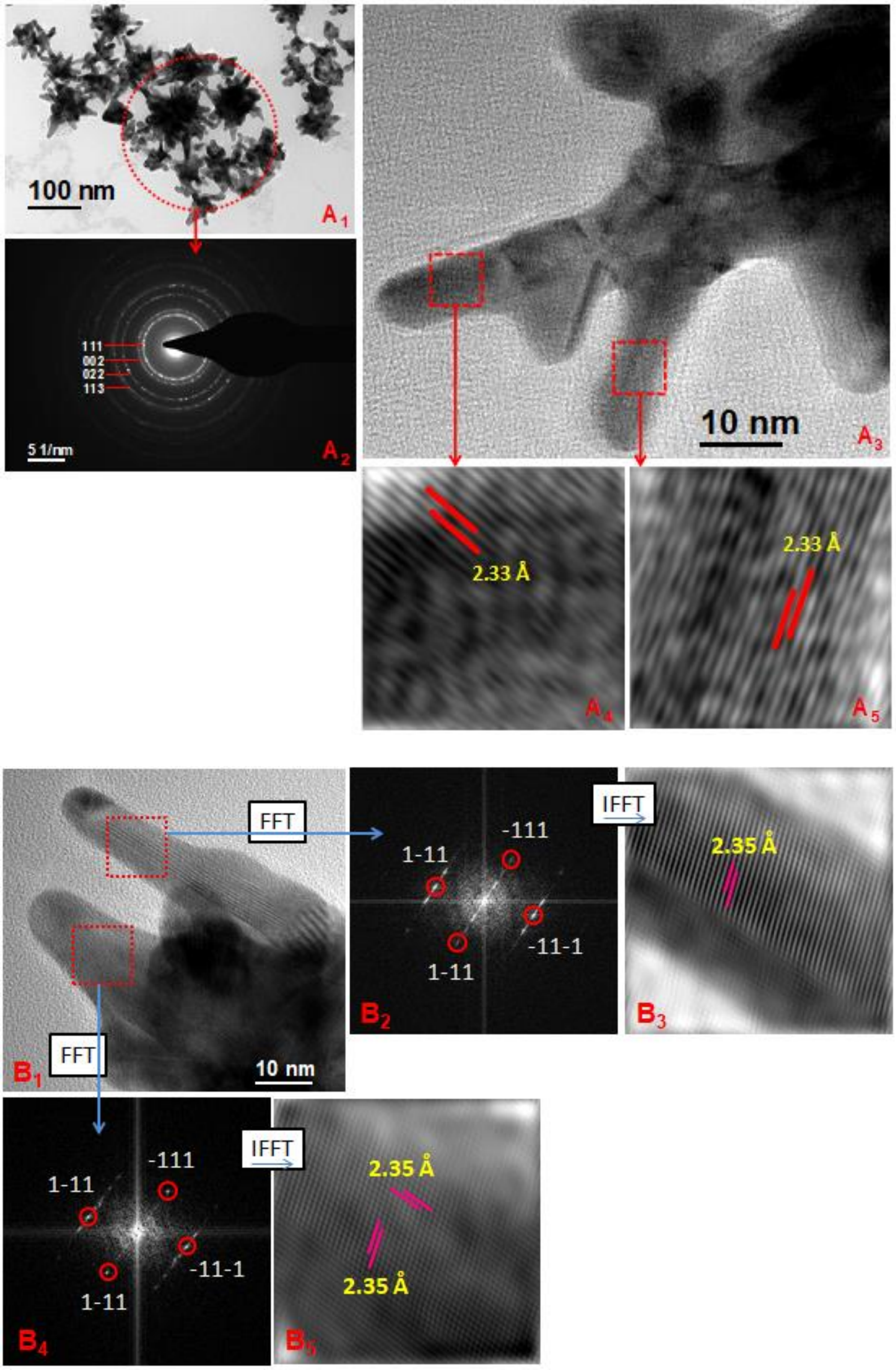

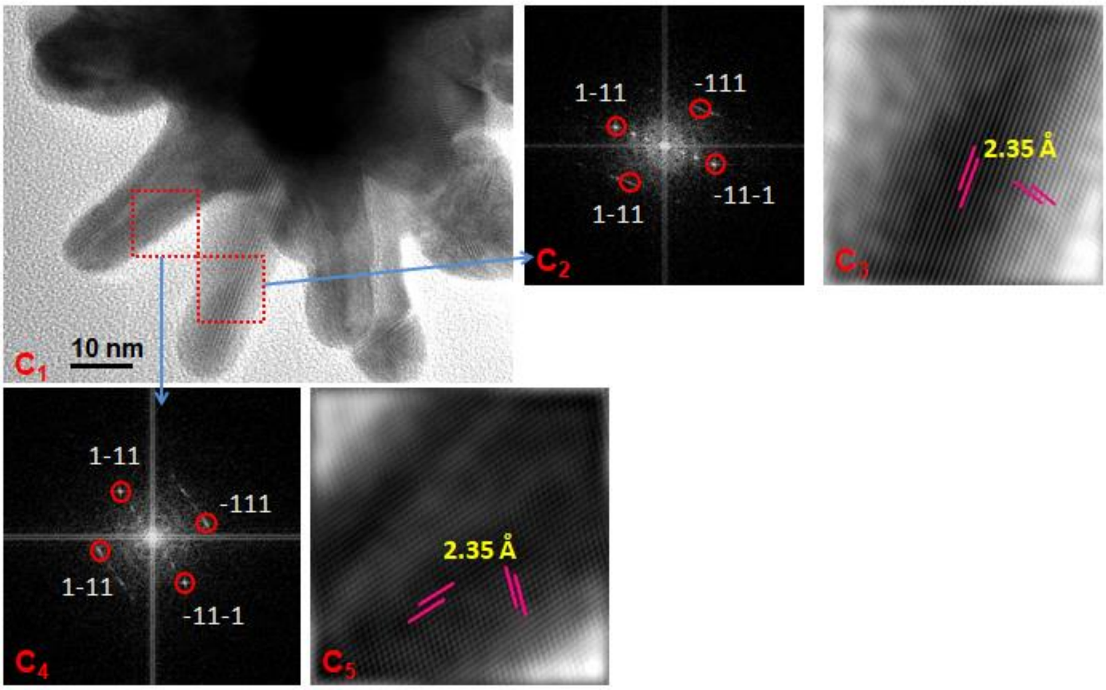

Figure 5.9: HRTEM of the seed-free, template-free salt-induced HHogGNPs synthesized in presence of 3.4 mM NaCl. (A_1-A_5), (B_1-B_5), (C_1-C_5) represent data for three different HHog gold nanostructures.

The free energies associated with the crystallographic planes of an *fcc* metal increases as the coordination number of the respective facets reduces (highest number of breaking bonds per unit cell) in the order: $\gamma(111) < \gamma(100) < \gamma(110)$.[234] Since these HHogGNPs form instantaneously, our result is consistent with the existing literatures to form energetically most stable structure with predominant crystal facets oriented in {111} plane. As argued before,[324] other facets like {110} and {100} of *fcc* unit cells also take part actively in the process of crystal growth to generate the final HHog nanostructures. Though we used variable amount of NaCl during the synthesis of HHogGNPs, the extent of insoluble AgCl (Origin: $\mathrm{Cl}^- + \mathrm{Ag}^+ = \mathrm{AgCl}\downarrow$; Source of Cl^-ion: both NaCl and $HAuCl_4$) production is independent of NaCl concentration as the concentration of Cl^-originates from $HAuCl_4$ (2.5×10^{-4} M) itself is enough to capture all the available Ag^+ (1.5×10^{-5} M) present in the mother solution. Considering the molar solubility (S) and solubility product (K_{sp}) of AgCl in water at 25 °C as 1.33×10^{-5} $\mathrm{molL^{-1}}$ and 1.76×10^{-10} respectively, addition of NaCl (between 250 µM to 20 mM) in the mother solution not only contributes additional Cl^- but also acts as a source of 'common ion' to repress the solubility of AgCl (as ions) according to the Le Chatelier's principle.[315] Ignoring the negligible contribution from solid AgCl and by considering the variation of $[Cl^-]$ between 250 µM to 20 mM, solubility of the *in situ* generated AgCl varies between 7×10^{-7} and 9×10^{-9} $\mathrm{molL^{-1}}$. This clearly shows that the presence of excess Cl^- reduces the molar solubility of the *in situ* generated AgCl between 2 to 4 orders by repressing the solubility of AgCl to control their facet dependent growth mechanism.[315] These *in situ* generated AgCl has higher propensity to deposit on highly energetic {110} and {100} facets by leaving all the reduced gold ions for selective nucleation of {111} facets to grow smaller number of sharper (smaller base) and longer tips (6-times increment of AAR) with higher tip-to-tip distance to result incremental plasmon tuning. Though the average particle size remains more or less constant at 220 nm, the core size decreases and the tip length increases gradually. This is clearly observable from our present TEM data in **Figure 5.5(B_1–B_6)** or previously reported results on silver nanowire[324] and supports the expected trend from the free energy point of view. **Figure 5.10** schematically illustrates how the extent of blocking by AgCl affects the number, length, sharpness of tips along with the core size of the nanostructures with increase in NaCl concentration.

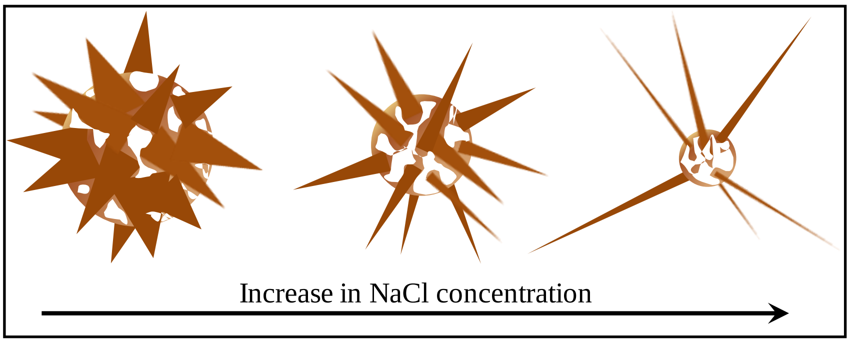

Figure 5.10: Schematic diagram illustrating the pattern of HHogGNPs produced with increase in NaCl concentration (indicated by the arrow) in support of Figure 5.5 (B_1–B_6). With increase in NaCl concentration, the extent of AgCl deposition also increases which is marked by the white colored random patches over the cores. It indirectly controls the number, length, sharpness of tips, intra-tip distance and the diameter of the core size of the nanostructures.

Thus the Le Chatelier's principle plays the pivotal role not only to generate the HHogGNPs but also to tune their tip curvature, AAR and RSA by exploiting the NaCl-based 'common ion' effect. A step-by-step view of the anisotropic growth leading to the formation of the final HHogGNP starting from seed has been presented in **Figure 5.11**.

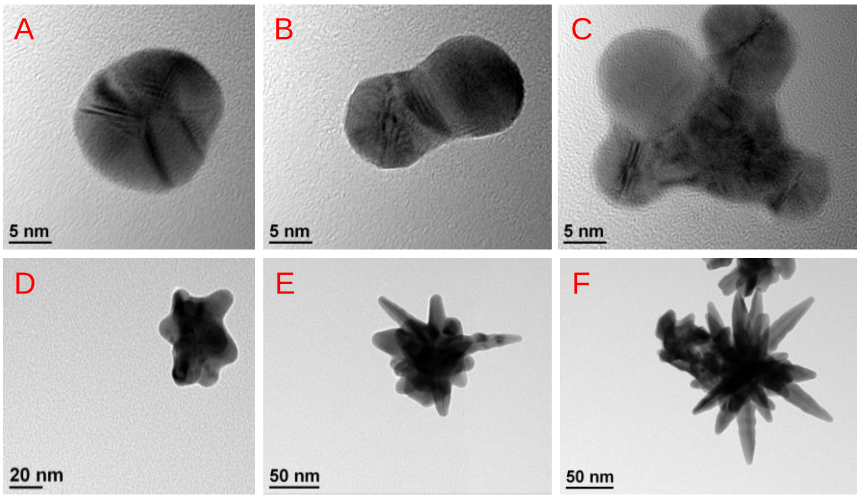

Figure 5.11: (A-F) Stepwise transition from seed to HHogGNP recorded by TEM imaging.

5.3.4 Tunable Plasmon Spectroscopy

Variable reaction condition dependent plasmon tuning has been summarized in **Fig. 5.12**, where along with the extent of NaCl, variation of TSC and $AgNO_3$ concentration or the alteration of pH are also used as growth regulating factors.

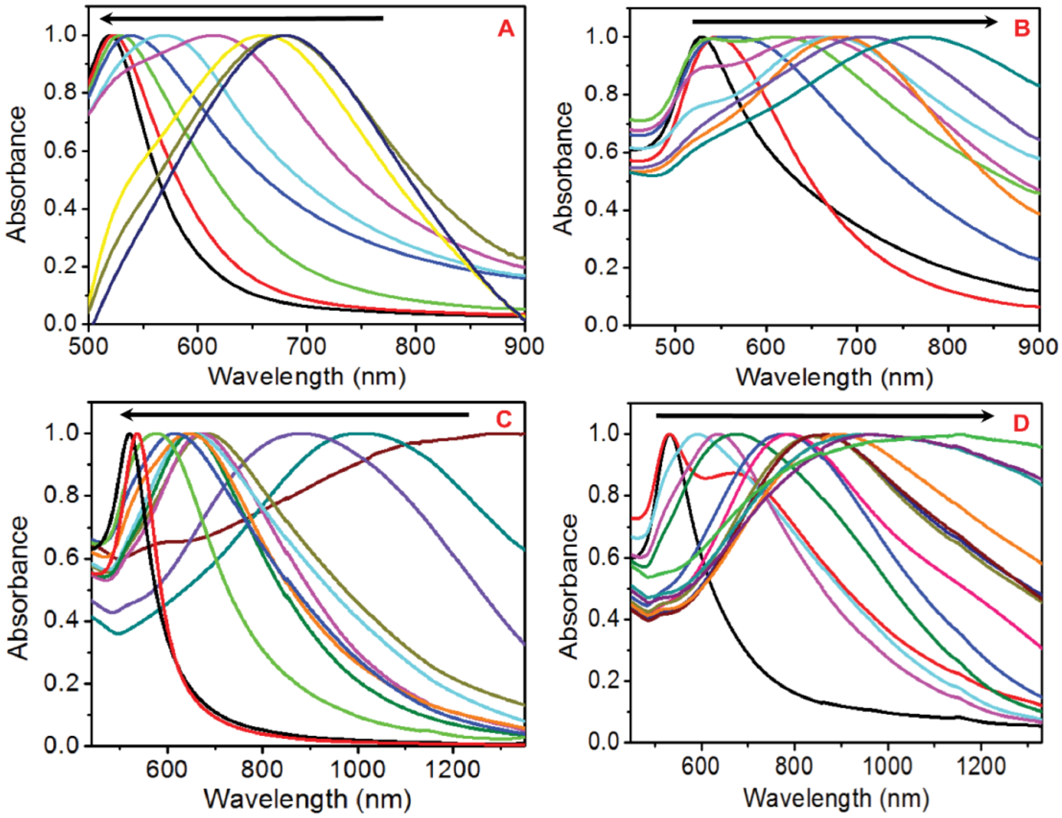

Figure 5.12: Details of UV-vis-NIR absorption spectra obtained by (A) 1% TSC variation (Navy: 50 μL, Dark yellow: 100 μL, Yellow: 250 μL, Magenta: 500 μL, Cyan: 875 μL, Blue: 1000 μL, green: 1125 μL, Red: 1250 μL, Black: 2500 μL); (B) 1.5 mM $AgNO_3$ variation (Black: 100 μL, Red: 200 μL, Blue: 350 μL, Green: 500 μL, Magenta: 875 μL, Cyan: 1000 μL, Orange: 1125 μL, Purple: 1250 μL, Dark cyan: 2500 μL); (C) pH variation (Wine: pH 1, Dark cyan: pH 2, Violet: pH 3, Dark yellow: pH 4, Magenta: pH 5, Cyan: pH 6, Olive: pH 7, Orange: pH 8, Blue: pH 9, Green: pH 10, Black: pH 11, Red: pH 12); (D) 1.7 M NaCl variation (Black: 1 μL, Red: 5 μL, Cyan: 10 μL, Magenta: 20 μL, Olive: 50 μL, Blue: 100 μL, Pink: 200 μL, Dark yellow: 300 μL, Navy: 400 μL, Wine: 500 μL, Orange: 600 μL, Dark cyan: 800 μL,

Purple: 1000 μL, Green: 1200 μL). In each plot, the arrow indicates the direction of shift of the wavelength with increments of the variables.

As already mentioned, upon increasing the TSC concentration, experimental observation shows the formation of more stabilized but less anisotropic (mostly spherical) nanoparticles whereas decrease of TSC concentration make them more anisotropic with less electrostatic stability. As a result of this we observed a blue shift in their absorption spectra as we increase the concentration of TSC during their synthesis. This has been clearly shown both in the **Figure 5.2** (colorimetry with TSC variation) as well as in **Figure 5.12A**. In case of $AgNO_3$ variation, *in situ* generation of $AgCl\downarrow$ varies incrementally with increasing $AgNO_3$ concentration. Insoluble AgCl blocks the high energy {110} and {100} facets and directs the growth along {111} plane to generate more anisotropic structures which has already been discussed in previous sections. As a result of this we have observed a red shift in the absorption spectra (**Figure 5.12B**) by tuning (100-2500 μL) the amount of $AgNO_3$. Regulation of $AgNO_3$ beyond 2500 μL has not been performed to avoid the formation of any silver nanoparticle in the system. To check the effect of pH variation we prepared different pH solutions in the range of 1-12 either by adding controlled volume of HCl (for pH 1-4) or NaOH (for pH 5-12) in the mother solution. At lower pH solutions, addition of HCl increases the concentration of Cl^- ion and due to common ion effect the insolubility of AgCl increases which results higher anisotropy and clearly observable from the corresponding absorption spectra (**Figure 5.12C**). On the other hand when NaOH is added to raise the pH of the solution, Ag_2O is formed by consuming available Ag^+ ions ($2AgNO_3 + 2NaOH \rightarrow Ag_2O + 2NaNO_3 + H_2O$) present in the reaction medium that reduces the anisotropy. The effect of pH driven common ion effect (blue shifting in the higher pH and red shifting in the lower pH) has been depicted in **Figure 5.12C**. However, maximum plasmon tunability (530–1100 nm) is observed for Figure **5.12D** as we vary the 'common Cl^-' concentration in the mother solution. Due to their salt induced synthetic modality, reported HHogGNPs obviously show much greater stability in saline compared to other common plasmonic nanomaterials.[9,52,325,326] to work as a suitable material for plasmon spectroscopy.

5.3.5 SERS Measurement

To measure the enhanced Raman cross section offered by the HHog surface, we have used Rh6G as a Raman tag in this study. Since most of the surface-induced optical phenomena (e.g., SERS, NSET, etc.) are the result of short-range forces between metal surface and surface-adsorbed analytes, surfactant-free naked HHogGNPs should act as a better transducer[327,328]. Details about the mechanism of SERS and the mathematical formulation of the Raman enhancement factor, G, has been described in details elsewhere.[163] It is derived by the following equation:

$$\mathrm{G} = \frac{I_{SERS}/N_{surf}}{I_{NRS}/N_{vol}} \tag{5.3}$$

where I_{SERS} is the surface enhanced Raman intensity, N_{surf} is the number of molecules bound to the nanometallic substrate, I_{NRS} is the norman Raman intensity and N_{vol} is the number of molecules in the excitation volume. Comparing the Raman intensity of the 1511 cm^{-1} normal mode[260] both in the bulk as well as in the HHogGNP surface, the obtained G factor for 670 nm excitation is approximately 8.9×10^{10} which is at least 15 times more compared to the 25 nm diameter TSC-stabilized spherical gold nanoparticle having similar plasmonic properties and has been represented in **Figure 5.13**.

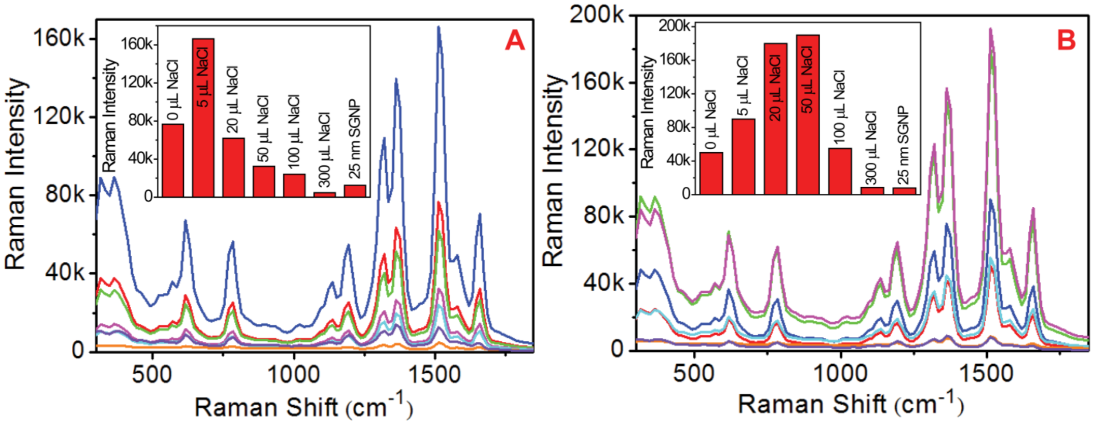

Figure 5.13: Recorded SERS signals and relative SERS strength of 1511 cm^{-1} Raman band (inset) from Rh6G with different samples (HHogGNPs induced by varying concentration of NaCl, Red: 0 μM, Blue: 170 μM, Green: 680 μM, Magenta: 1.7 mM, Cyan: 3.4 μM, Orange: 10.2 μM, and Violet: 25 nm diameter TSC-based spherical gold nanoparticle) for laser excitation at (A) 670 nm and (B) 780 nm.

Due to the resonance excitation of 670 and 780 nm plasmon bands, 170 μM and 1.7 mM NaCl-based HHogGNPs provide maximum Raman enhancement respectively. This observed gigantic Raman cross section could be due to several factors (as illustrated in **Figure 5.14**) including (a) template-free more widely exposed surface area (RSA) of HHogGNPs to hold more analytes on their surface, (b) enormous number of pointed sharper tips and edges on each HHogGNP surface for efficient focusing of electromagnetic field at their apexes to enhance the field strength, and (c) close-by spikes, inter-spike space, and finer teethes (as seen from HRTEM) on each spikes act either as active 'nano-pockets' to trap more Rh6G molecules or to form natural hotspots through capacitive coupling between nano surfaces[329] without aggregates to maximize the SERS signal.

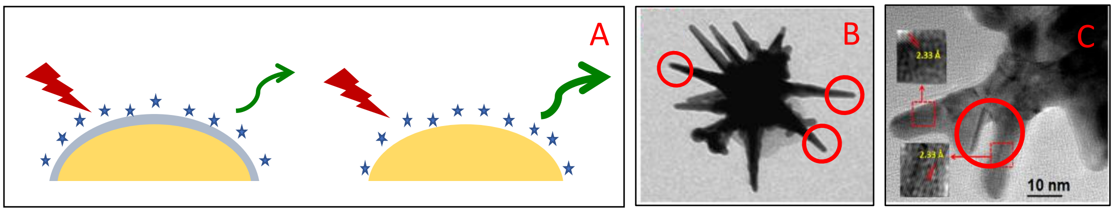

Figure 5.14: Figures illustrating the probable factors responsible for high Raman cross section: (A) more exposed surface are without a surfactant layer; (B) sharp, pointed spikes and (C) inter-spike space between adjacent spikes.

5.3.6 Toxicity test of HHogGNPs by MTT assay in dark

5.3.6.1 MTT Assay protocol

For dark-toxicity study we have selected RAW 264.7 mouse macrophage cell lines. RAW 264.7 cells were plated onto a 96-well plate (2×10^4 cells in 180 µL of DMEM culture medium supplemented with 10% heat inactivated FBS, 2 mM L-glutamine, 10 mM HEPES and 1 mM sodium pyruvate). After 24 h of incubation at 37 °C in 5% CO_2 environment, 20 µL of each of the NPs were added to each well. Plates were again incubated at 37 °C in 5% CO_2 environment for an additional 24 h. After the incubation, MTT solution was added to each well and incubated for another four hours maintaining the same conditions. The cells were washed twice with 1×PBS and the formazan crystals were dissolved with MTT dissolving solutions (11 g SDS in 50 mL 0.02 M HCl mixed with 50 mL isopropanol). The plate was incubated for 20 min in room temperature and absorbance was recorded at 570 nm. For each set we have performed three independent experiments keeping all the parameters same. The cell viability (% survival) was calculated as % related to the untreated control cells.

5.3.6.2 Result of MTT-based cell viability assay in dark

To check the nontoxicity of the HHogGNPs in the absence of light, we carried out the MTT-based dark-toxicity test by selecting RAW 264.7 mouse macrophage cell lines. Details about the samples used for the dark toxicity test and the corresponding '% Survival' of the HHogGNP treated cells for different doses are listed in **Table 5.3**, and their relative cell viabilities are shown in **Fig. 5.15**.

Table 5.3: Different samples used for the MTT-based dark toxicity test with variable NaCl concentrations and the average cell viability results for RAW 264.7 mouse macrophage cell lines.

Dose	**Type of Nanomaterial**	**Concentration of NaCl in the HHogGNPs**	**% Survival**	**Standard Deviation**
Control	Without Nanomaterials	Without Nanomaterials	100.0	0
1A	Mother Solution	1.7 mM	89.8	4.1
1B	Centrifuged	1.7 mM	110.9	6.8
2A	Mother Solution	3.4 mM	88.6	6.9
2B	Centrifuged	3.4 mM	120.8	8.2
3A	Mother Solution	10.2 mM	89.4	8.6
3B	Centrifuged	10.2 mM	101.7	4.7
4A	Mother Solution	17 mM	100.0	1.7

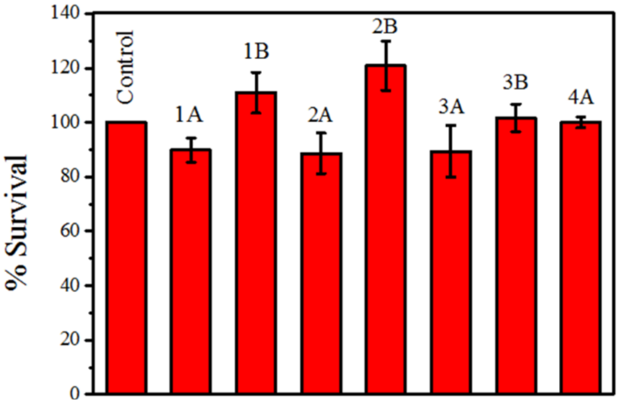

Figure 5.15: A comparative study (n=3) among the obtained cell viability results for samples mentioned in Table 5.3 applied on RAW 264.7 mouse macrophage cell lines.

It is clear from **Table 5.3** and **Figure 5.15** that the extent of survival remains unchanged after the addition of different doses of HHogGNPs in dark conditions, in other words the applied HHogGNPs are nontoxic in the absence of light.

5.4 Conclusion

In conclusion, here we have altered the chemical equilibrium condition of a reaction by exploiting Le Chatelier’s principle to generate up to 4-orders of magnitude more insoluble AgCl for the efficient blocking of highly energetic *fcc* facets and selective growth of {111} facets in a seed-free and template-free pathway to generate not only energetically more stable HHogGNPs in a cost effective way but also to regulate the AAR, tip curvature and RSA to tune their broad-band plasmonic and exceptional Raman enhancement properties. Due to the broad-band plasmon tunability throughout the biological window together with the large Raman activity and enhanced stability in the highly salted environment with non-toxicity, the synthesized HHogGNPs can find potential applications in medical imaging and photothermal therapy.

CHAPTER 6

DEPLETION STABILIZED HEDGEHOG GOLD NANOPARTICLES IN THERANOSTICS

OUTLINE: What does the study offer?

- A way to stabilize nanomaterials with benign polymer by applying depletion force
- Modified HHogGNPs withstanding wide range of physical and chemical condition
- Significant SERS output from depletion stabilized HHogGNPs for real time monitoring
- Theoretical calculation of temperature attainable at tips for photothermal therapy
- Application of HHogGNPs: *in vitro* photothermal treatment of cancerous cells

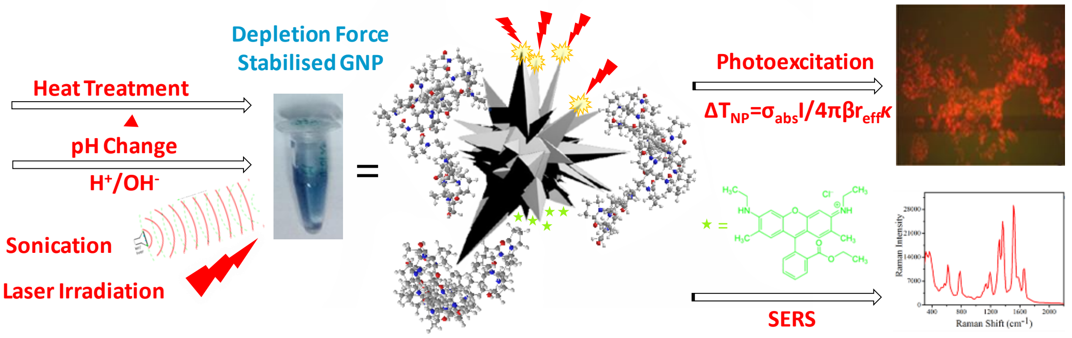

6.1 Introduction

Two classes of nanomaterials are represented either by Class I: the materials with novel optical,[59,324,326,330]mechanical,[331,332] electrical[332–334] and magnetic[335] properties without considering their toxicity for the applications in biomedicine and Class II: low-to non-toxic nanomaterials capable of a prolonged retention in the body without changing their size and shape yet structurally and plasmonically suitable for effective therapy. Although the literature is effluent by the Class-I materials, the suitable Class-II compounds remain much less common[15,336]; therefore, the need for nanomedicine is still unmet[337,338]. After an intense research on noble metal nanoparticles, evidences are accumulated in support of gold nanomaterials to be useful for both classes mentioned above[10]. Driven by the needs our recent invention of hedgehog gold nanoparticles (HHogGNPs) without adopting any seed-mediated and template-based synthetic modality at room temperature under a highly salted condition guaranteed the birth of new generation smart materials for theranostics application[60]. Intrinsically stable crystallization without toxic templating ligands[339]promotes these HHogGNPs to be an efficient nontoxic biocompatible material in nanomedicine. Due to their broad-band plasmon tunability with improved surface-to-volume (S/V) ratio and very high tip curvature, they emerge as promising materials for improved optical and spectroscopic sensitivity necessary for theranostics. Along with that, depletion stabilization of individual HHogGNPs by low-dose (0.01%) high molecular weight (Mw~55,000) polymer (polyvinyl pyrrolidone, PVP) improves their long-term stability in physiological salt condition. A plausible explanation has been provided to describe the depletion of London attractive force by introducing PVP. PVP acts here as a non-adsorbing floating polymer that increases the stability of individual nanoparticles by modulating their excluded volume. Combination of effective theranostics and long retention ability makes them appropriate for *in vivo* real-time therapeutic sensing. Transportation of nanoparticles with enhanced ability to kill cells photothermally without making any aggregation in the physiological saline condition is the most essential characteristics of our synthesized and surface screened materials. This challenge of prolonged retention in the body (better chance to reach and interact with tumor cells) to enhance therapeutic effect and to reduce their side effects[340]has been achieved for these HHogGNPs. Depending on the cellular environment (internalization vs. membrane binding), growth stages, degree of cell division (normal vs. tumor cells) and differential stress conditions the physiological pH may vary which demands a stable nanostructure to sustain this change for an effective theranostics[341–343]. Any photothermal therapy associated with hyperthermia raises the surrounding temperature beyond 38 °C due to failed thermoregulation of the body[344] during photothermal conversion and necessitates the plasmonic nanostructure with enhanced stability at elevated temperature. Along with these, for any photothermal therapeutic process the limiting condition for desired success is to design a material with maximum photostability and best electron-phonon coupling for efficient photothermal conversion. Designed and modified nanoparticles thus need to be stable throughout the biological optical window to reduce both the toxicity and to preserve their nanomedicinal properties. Optical imaging coupled with acoustic image based theranostics requires plasmonic nanoparticles with greater stability in presence of high frequency sound wave ($\geq$20,000 Hz) to guarantee its stability during therapy. Detailed experiment on HHogGNPs stability in different harsh conditions has been studied to ensure their theranostic applicability. Associated results of dark toxicity test in presence of these nanoparticles has been described in our previous study[60](chapter 5). Here the cell death studies after the completion of illumination using MTT conversion and propidium iodide (PI) staining have been performed to understand the cell death pattern caused due to effective photothermal therapy both in quantitative and qualitative manner respectively. By considering the role of nanoparticle's absorption cross section, laser intensity, size of the nanoparticle, number of heat releasing points and the thermal conductivities of both the plasmonic metal and surrounding medium (profile of temperature increase, ΔT, given by Coulomb potential outside the particle under uniform-temperature approximation)[345–349] we have calculated the approximate temperature at individual tips of a HHogGNPs when excited by a particular wavelength of light (red light with wavelength ~623 nm) which explains the observed cell death results when we consider the applied HHogGNPs as photothermal therapeutic agents for colon carcinoma cells.

6.2 Preparation of depletion force stabilized HHogGNPs

For screening the HHogGNPs produced *in situ*, aqueous solution of PVP (av. Mw ~ 55K) is used. The details of HHogGNPs synthesis is described in the previous chapter[60]. In a typical course of reaction, 0-4500 µL 1.7 M NaCl (equivalent to 0-0.9% NaCl in 50 mL of growth solution), 750 µL 1% TSC, 1.25 mL 10^{-2} M $HAuCl_4.3H_2O$, 500 µL 1.5 mM $AgNO_3$ and 250 µL 10^{-1} M ascorbic acid are added to 49 mL water in sequence and after 30 s, 50 µL of 10% PVP solution (0.01% PVP in 50 mL) is added to it under continuous stirring. For characterisation, checking the stability of so obtained HHogGNPs under different harsh conditions and for assessing the MTT assay-based photothermal lysis efficiency of them, 3.4 mM

NaCl-induced (taking 100 µL of 1.7 M NaCl) and 0.01% PVP-stabilised HHogGNP stock solution is used.

6.3 Results and Discussion

The major aim of this study is to formulate a methodology to achieve depletion stabilized HHogGNPs suitable for real-time theranostic application with long retention in the physiological condition to use them as *in vivo* nanomedicine. To the best of our knowledge this is the first experimental report where we have successfully used our recently synthesized salt-induced *in situ* generated non-toxic HHogGNPs after depletion screening by a low dose high molecular weight polymer exhibiting enhanced retention in the physiological condition and very high photothermal efficiency. Only a minimal laser exposure involving low power and very short time period is required for the photothermal treatment in our case and also, a low dose of as-synthesized nanoparticles is sufficient. These depletion stabilized HHogGNPs also show desirable stability in harsher therapeutic and physiological conditions. Following sections explain the obtained results in greater details and raised a scientific discussion in support of the results.

6.3.1 Depletion stabilization of HHogGNPs

Due to their salt-induced synthetic modality, HHogGNPs reported in this work show greater stability in saline condition compared to the other common plasmonic nanomaterials like, TSC-based spherical nanoparticle, cetyltrimethylammonium bromide-based nanorod or polyvinylpyrrolidone-based nanoprism[350,351]. However, despite their noticeable stability in highly salted environment, it is clear from their absorption spectra (**Figure 6.1A**) and TEM image (**Figure 6.1B**) that they show substantial aggregation beyond 20 mM NaCl concentration.

As we have already discussed in the introduction section, the main goal of this targeted research is to modify the anisotropic HHogGNPs with dual functionality of photothermal cell-killing and prolonged retention in the physiological condition, stabilization of nanoparticles in highly salted (0.6% to 0.9% salt solution) physiological condition is one of the biggest challenges to use them in medicinal application[350]. Hence, we need to formulate a methodology to modify the nanoparticle or the HHogGNP solution to achieve stable dispersion with intact physico-chemical properties beyond 20 mM salt concentration. In physiological condition, electrostatic repulsion between charged nanoparticles reduces due to the opposite ion (sourced from the salts present in the body fluid) induced charge screening and nanoparticles approach each other by experiencing London attractive force[352] to induce nanoparticle

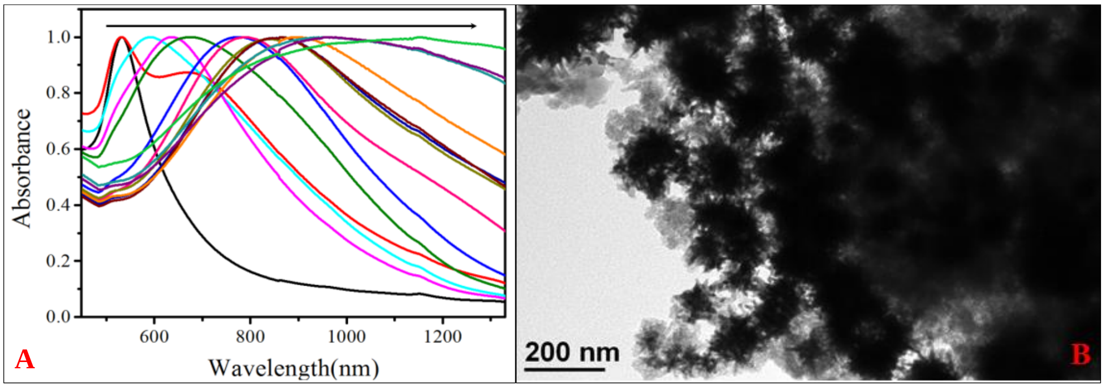

Figure 6.1: (A) Absorption spectra of synthesized HHogGNPs as a result of 1.7 M NaCl variation (1-1200 µL) during their synthesis. Arrow indicates the direction of shift of absorption peak with incremental variation of NaCl concentration. The spectrum in green colour with a broad peak is for 1200 µL NaCl (40 mM NaCl in the growth solution). (B) TEM image of HHogGNPs synthesized using 1200 µL NaCl. Dark part in Figure 6.1B shows the initiation of aggregation process.

aggregation. By using several thiolated ligand (e.g., thiolated DNA, thiolated PEG, etc) or high molecular weight PEG or micellar surfactant (e.g., CTAB, CTAC, etc) to coat the nanoparticle surface with a thickness greater than London interaction range[353–356], we can achieve dominating steric stabilization to counter the London interaction induced aggregation.

But, this steric stabilization prevents nanoparticle surface to interact with any foreign substrate to achieve the most striking surface induced effects (e.g. surface enhanced spectroscopy, nanoparticle bioconjugation, catalysis, heavy metal detection, drug delivery, etc.) originated from nanoparticles. However, in presence of low dose (0.01%) high molecular weight non-adsorbing and nontoxic polymer like polyvinyl pyrrolidone (PVP, M_w: 55,000, used as a binder in many pharmaceutical tablets, essential ingredient in personal care products and as old style adhesive used in postal system), these nanoparticles experience a depletion of attractive force originated from the excluded volume effect which is referred as depletion stabilization[357,358] and remain stable even in 100 mM (equivalent to 0.6%) external salt solution which is close to the physiological concentration of salt in the blood. The optimal dose of PVP is decided by taking the HHogGNPs solution in a series of different concentrations of PVP and treating them in 0.9% NaCl. Concentration dependent depletion stabilization offered by M_w: 55,000-PVP has been shown in **Figure 6.2 (I)**. The stability of these solutions is then examined by colorimetry i.e. noticing visible changes in colour in presence of 0.9% NaCl and confirmed further from their absorption spectra. **Figure 6.2 (II)** and **6.2 (III)** shows the effect of 0.9% NaCl on the absorption spectra of HHogGNPs before and after PVP screening respectively. A slight reduction in absorbance in presence of 0.9% is partly due to increased dilution.

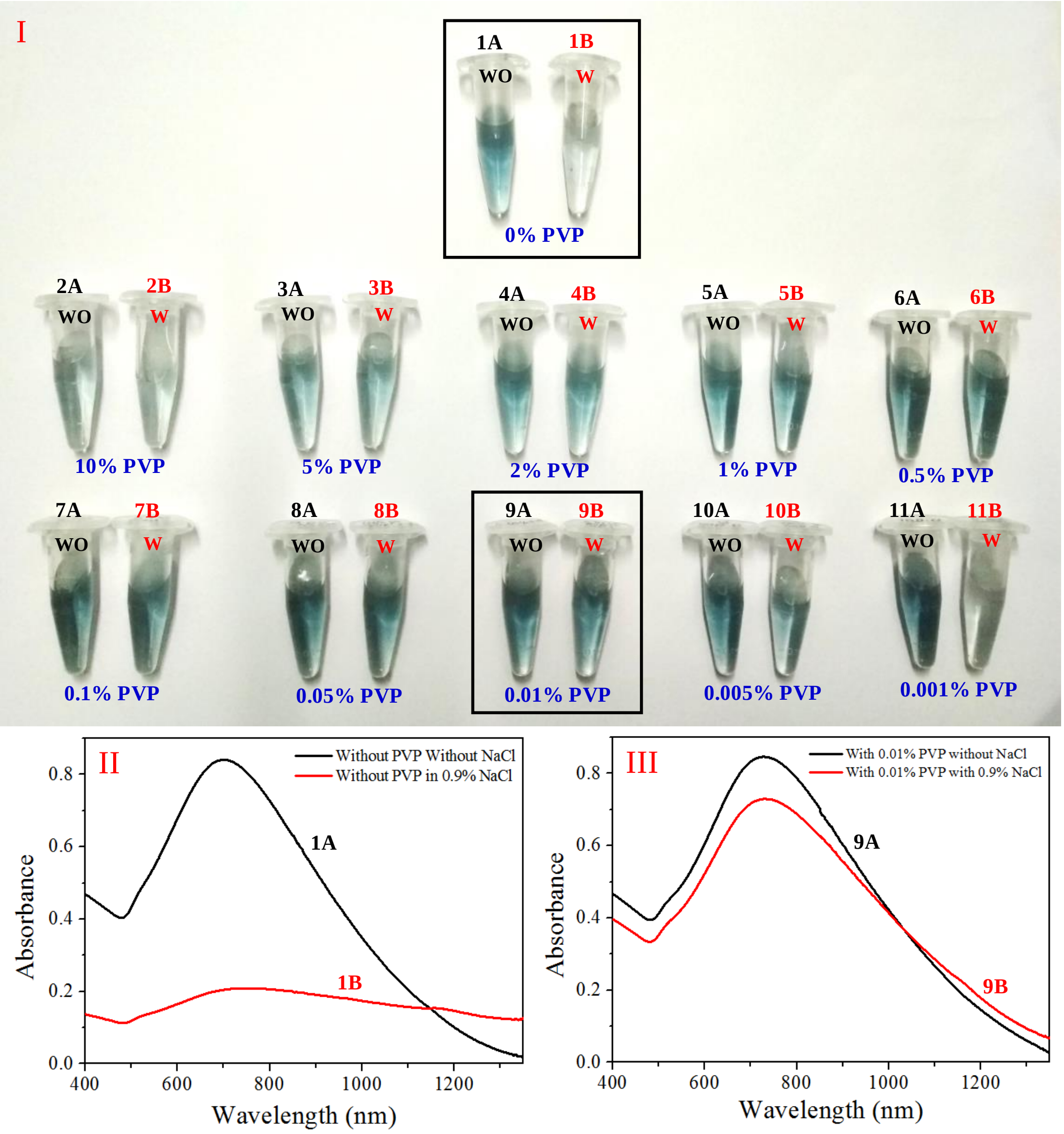

Figure 6.2: (I) Depletion stabilization of HHogGNPs offered by different concentration of 55K PVP in presence of 0.9% NaCl. In each set between A and B we have compared the extent of HHogGNP aggregation by examining their colorimetric and spectral change (all spectral data not shown here). Two centrifuge tubes labeled with WO and W represents the effect without and with 0.9% NaCl for PVP screened HHogGNPs respectively. For example, set 1A and 1B represents HHogGNPs without PVP without (WO) 0.9% NaCl and without PVP with (W) 0.9% NaCl respectively. Concentration of 55K PVP in depletion stabilized samples decreases gradually from set 2 to 11 (set 2: 10%, set 3: 5%, set 4: 2%, set 4: 1%, set 6: 0.5%, set 7: 0.1%, set 8: 0.05%, set 9: 0.01%, set 10: 0.005% and set 11: 0.001%). It is observed that at and

above 0.01%, PVP stabilizes the HHogGNPs for hours (faint colour of solutions of set 2 and set 3 are due to dilution of nanoparticle solution upon addition of 20% of mother PVP solution only) whereas below 0.01% evident color change proves destabilization due to aggregation; (II) Absorption spectra of sample 1A (without PVP without 0.9% NaCl) and 1B (without PVP with 0.9% NaCl); (III) Absorption spectra of sample 9A (with 0.01% PVP without 0.9% NaCl) and 9B (with 0.01% PVP with 0.9% NaCl).

Figure 6.3 shows the TEM picture (A and B) and absorption spectra (C and D) of HHogGNPs before and after PVP screening. The images clearly reveal that regularity in size and morphology is relatively higher in case of PVP stabilized HHogGNPs. This narrower size distribution is also reflected in their respective spectral data. Also, there occurs a red shift of ~20-40 nm in the peak position for the PVP screened sample and they remain stable for months. This slight red shifting of absorption spectra with narrower size distribution may be due to the change in refractive index of the suspending media.

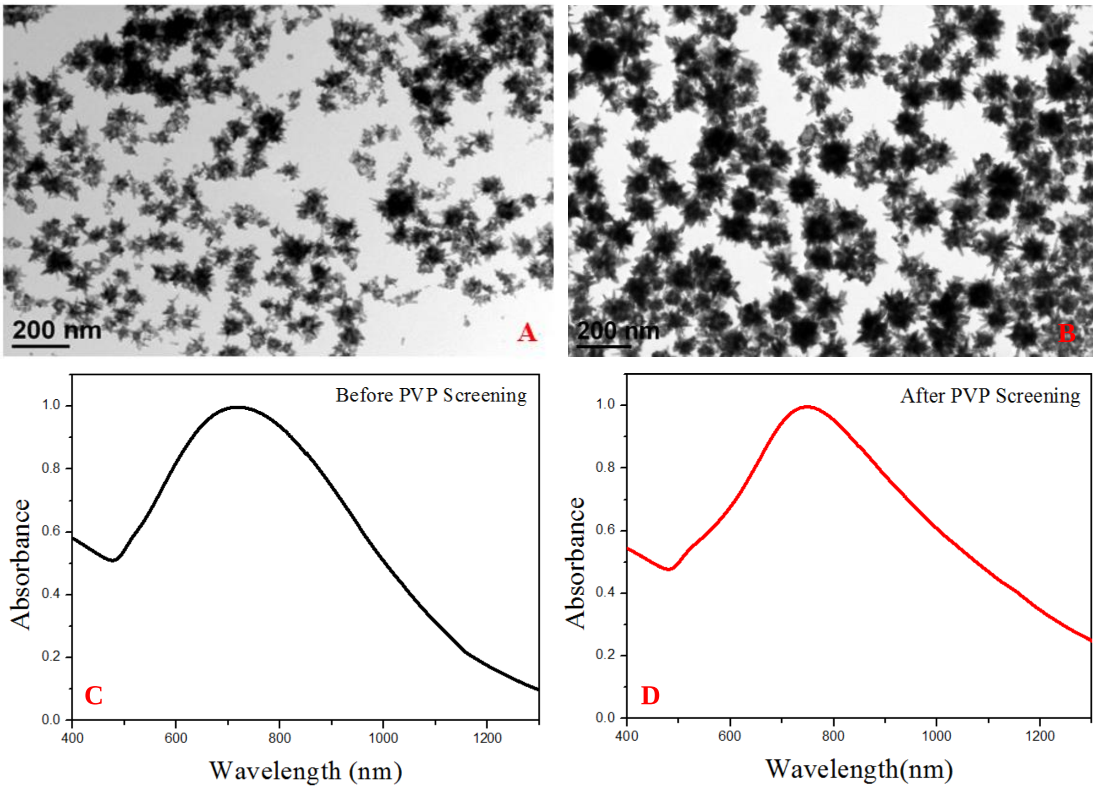

Figure 6.3: TEM pictures of HHogGNPs (A) before and (B) after PVP addition and (C and D) their respective absorption spectra.

To understand the role played by PVP, we tried to understand their distribution surrounding the nanoparticles in the sample solutions. By considering the molecular mass (M_W) of a monomer unit of PVP as 111.0 and the average molecular mass of individual polymer chain as 55,000, we have approximately 55000/111 ≈ 496 repeating units in a single polymer chain having effectively two C-C single bond length offered by each monomer unit along with a side chain of pyrrolidone group (**Figure 6.4A**). Therefore, if we assume a linear chain of PVP polymer the length should be around 2 X 0.154 nm X 496 ≈ 152.6 nm and it would practically get reduced for folding or any sort of intra-chain coiling which would further shorten the effective screening length of the polymer. By considering the average diameter of the HHogGNPs as 220 nm (average circumference,$2\pi r$ ≈ 690 nm), each PVP chain may block the surface only partially (~1/5th of the circumference of the HHog nanoparticle) without making any continuous shell on the surface (**Figure 6.4B**). So, the extent of blocking (or the excluded volume offered by the PVP chain for enhanced depletion of attraction) offered by 0.01% of M_w: 55,000-PVP is sufficient to avoid the London attractive force while keeping enough room for surface adsorption. The working principle of depletion stabilization is thus very simple to understand where the high molecular weight PVP molecules acts as floating random blocker to prevent nanoparticles to come close to each other (by Brownian motion) but does not make a continuous thick screen over the surface to prevent the interaction between nanoparticle and foreign substrate (**Figure 6.4C**). This controlled screening helped us to increase their colloidal stabilization along with the scope for necessary surface interaction.

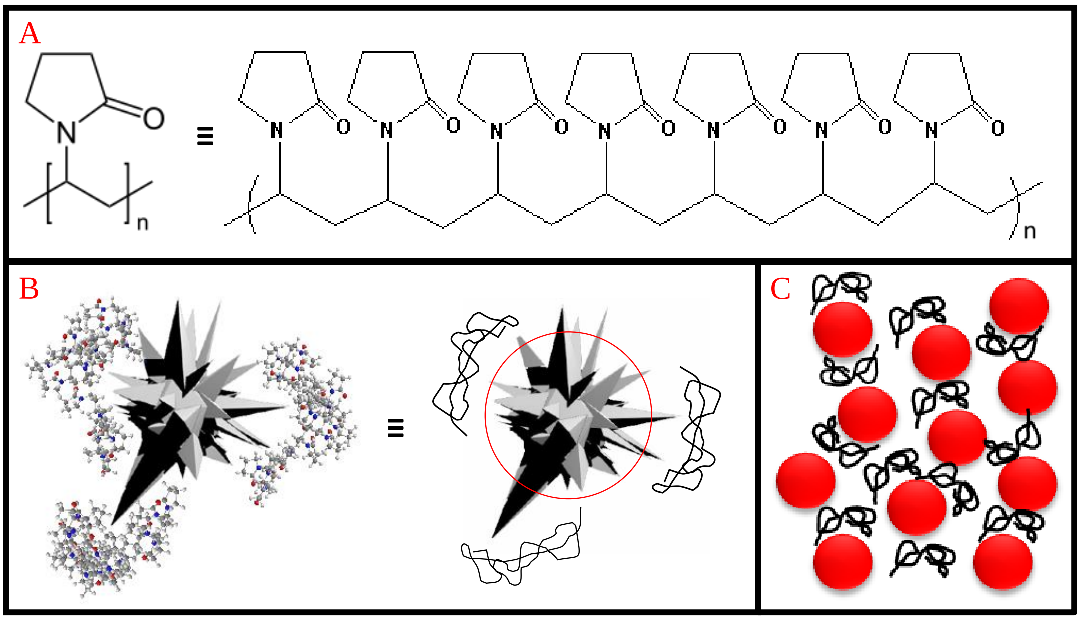

Figure 6.4: (A) Structural illustration of polyvinylpyrrolidone, PVP, monomer unit and its repetition; (B) schematic diagram of PVP coverage over a HHogGNP considering the average circumference of the nanoparticle (not to scale); (C) Depletion stabilization by partially coiled floating PVP polymer as random blocker.

To confirm the random blocking by PVP, we took the help of EDX spectra and elemental mapping (**figure 6.5**). Each PVP monomer unit has a nitrogen in its pyrrolidone ring. If PVP makes continuous layer over the HHogGNPs, enhanced localized density of N atoms over the nanoparticles is expected. But the observed mapping indicates random distribution of N atoms in the surrounding solution of the nanoparticles instead. It approves the fact that PVP does not make a mask over the nanoparticles and remains randomly floating in the solution.

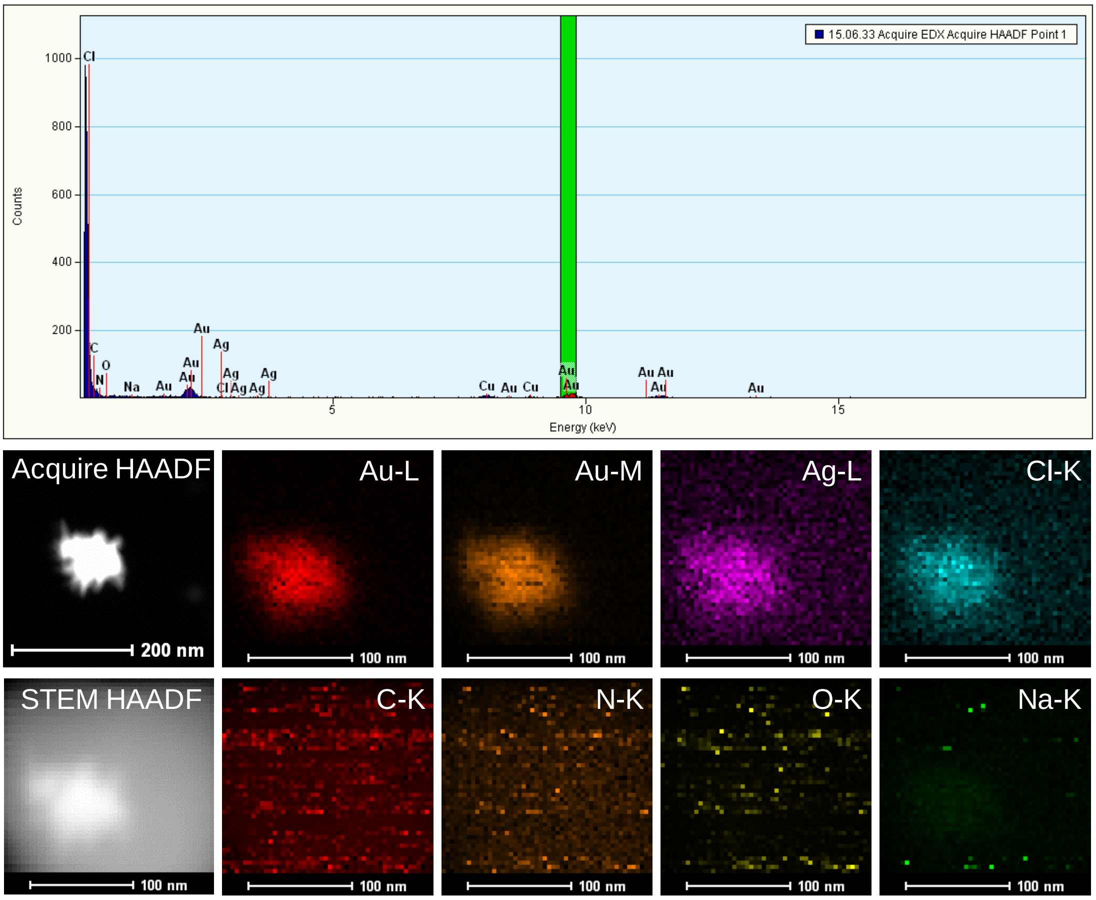

Figure 6.5: EDX spectra and elemental mapping of depletion stabilized HHogGNPs after addition of 0.01% 55K PVP.

We have also tested the stability of the 0.01% of M_w: 55,000-PVP screened HHogGNPs in physiological saline (0.9% NaCl solution in PBS buffer) and found that the dissolved salt has no effect on nanoparticle aggregation or plasmon even after prolonged (hours) incubation (data not shown). Therefore, it is highly probable that our depletion stabilized nanomaterials would be stable in the body fluid too. The depletion stabilized nanoparticles show no morphological or optical property change overall and rest of the studies we have performed by using these PVP screened HHogGNPs.

6.3.2 Depletion stabilized HHogGNPs under different external conditions

The stability and robustness of the PVP modified HHogGNPs are checked under different external environments - applying drastic change in pH, temperature, mechanical force and high intensity radiation and the results are described below.

6.3.2.1 pH response of Depletion stabilized HHogGNPs

To find out the structural integrity of the depletion stabilized HHogGNPs we have treated them in various pH solutions in the range of 1-12. Shifting of pH of a solution from neutrality either increases the concentration of H^+ for acidic solution (pH: <7) or OH^- for basic solution (pH: >7) compared to the neutral solution (pH:7) with equal concentration of H^+ and OH^-. By considering H^+ or OH^- simply as individual ions, depletion stabilized HHogGNPs follow the same working principle to block these ions to come within the excluded volume of the nanoparticles and thereby prevent the pH induced aggregation or degradation. **Figure 6.6** clearly signifies their improved stability under the influence of tunable pH in a considerable range (~pH 3-13), specially at high pH region they show extraordinary stability. Instability of both types of samples in very low pH solutions should not be an issue for implementing them in therapy because in human body only the pH of gastric acid in the stomach lumen is very low, but the nanoparticles are applied by intravenous treatment and hence do not come into its contact.

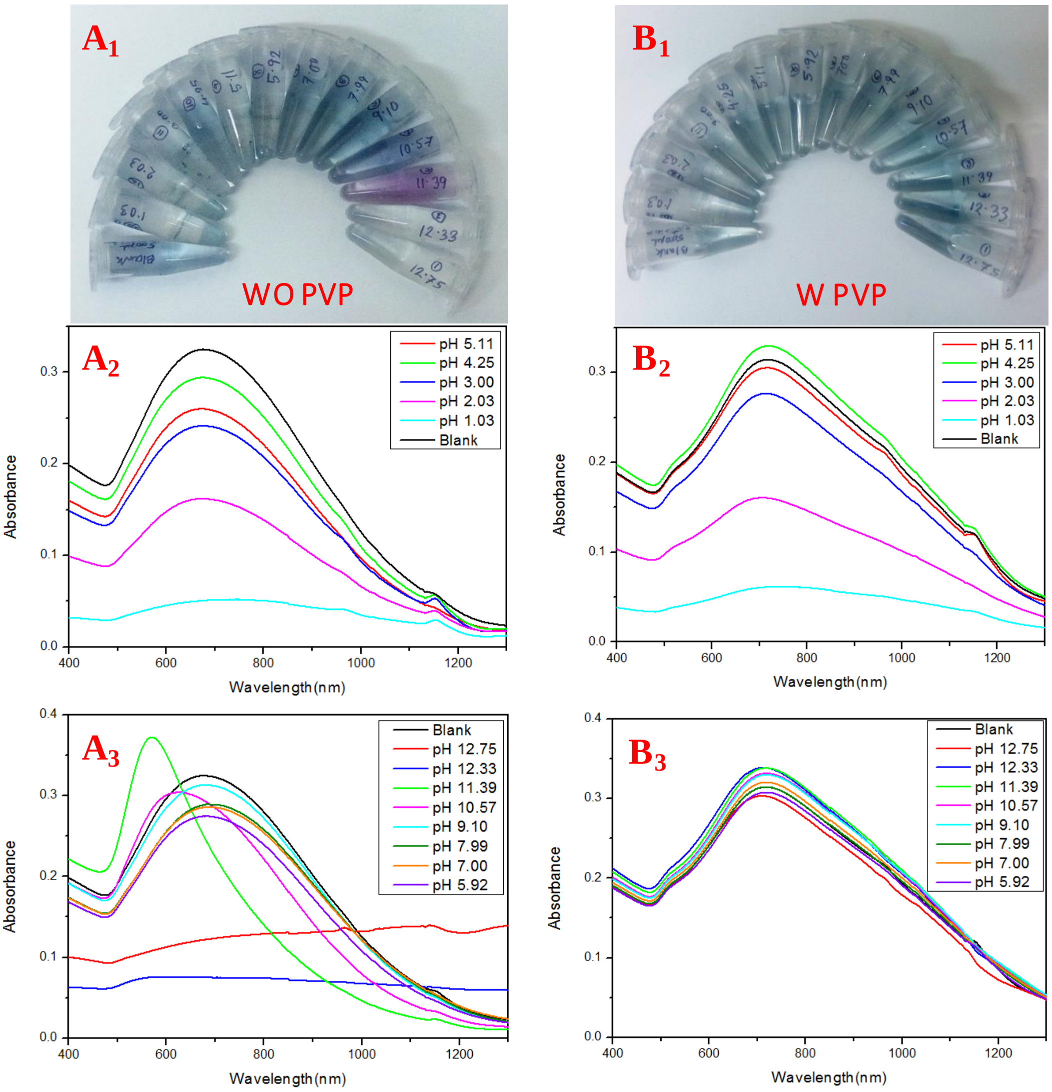

Figure 6.6: HHogGNP samples without PVP (A_1) and with 0.01% PVP (B_1) treated at different pH solution (starting from blank sample in water to pH ~1-13 from left to right). A_2 and A_3 represent the absorption profile of the samples without PVP at lower (1-5) and higher (6-12) pH region respectively whereas B_2 and B_3 show similar profiles by taking samples with PVP.

6.3.2.2 Thermal response of Depletion stabilized HHogGNPs

As mentioned before in the introduction section, any successful photothermal therapeutic reagent should sustain the temperature raise beyond 38 °C due to failed thermoregulation of the body. To justify the thermal stability of the formulated HHogGNPs beyond hyperthermic point we have studied their thermal response by recording their absorption spectra (i) at variable temperature well above the room temperature and (ii) at a constant temperature of 42 °C (=107.6 °F, an extremely elevated body temperature in case of hyperpyrexia) for 1 h. Obtained absorption spectra in **Figure 6.7** show their relative stability by reservation of spectral pattern upon thermal treatment.

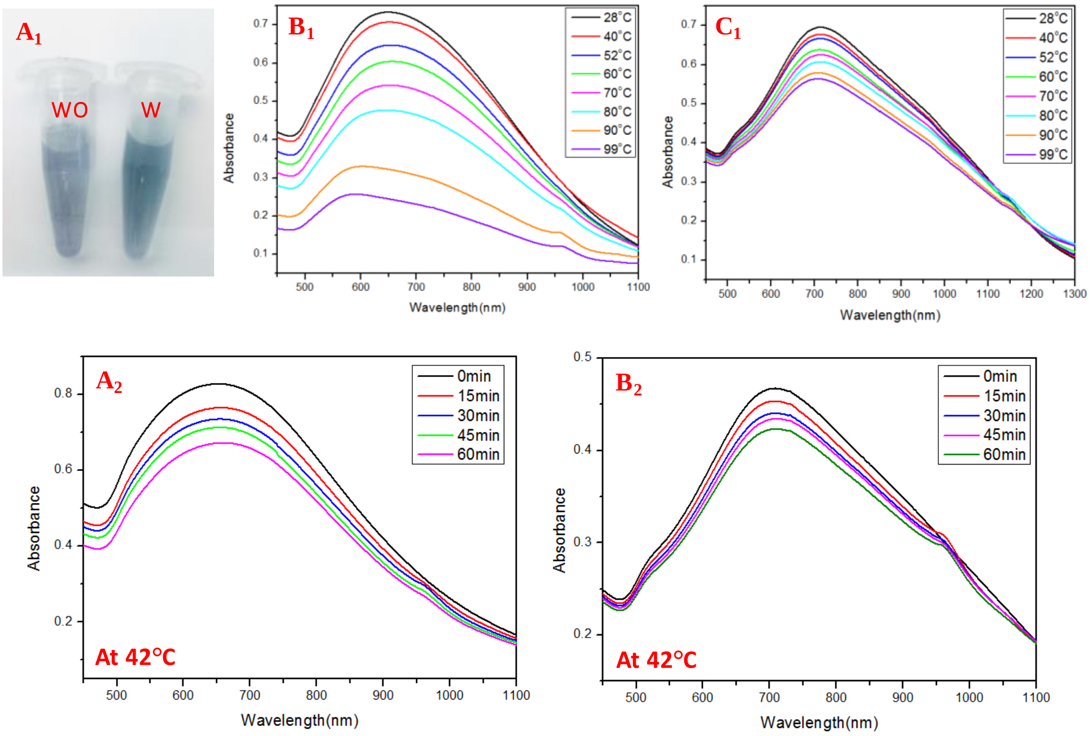

Figure 6.7: (A_1) HHogGNP samples without PVP (WO) and with 0.01% PVP (W) after treating at 99 °C starting from 28 °C. (B_1) and (C_1) represent the corresponding absorption profiles of these samples respectively at different temperature. (A_2) and (B_2)

show the effect of constant heat treatment for same HHogGNP samples without PVP (WO) and with 0.01% PVP (W) respectively at 42 °C (≈108 °F) for 1 h.

6.3.2.3 Photo-stability of Depletion stabilized HHogGNPs

Photostability of nanomaterials throughout the biological window (600-900 nm) is a must for a successful therapeutic material. Due to very high extinction coefficient of the HHogGNPs and enhanced photochemical process of the templating ligands we may expect an unprecedented photo-chemical reaction during their photo-physical (photothermalization) processes. Prevention of photochemical processes has been achieved by formulating depletion stabilized HHogGNPs and has been demonstrated in **Figure 6.8**. Here the HHogGNPs have been irradiated by 637 nm continuous laser source at different power before and after depletion stabilization and the spectral change has been recorded with time. It is clear that the depletion stabilized HHogGNPs show prolonged stability not only within broad-band biological window but also at variable photon energy which gives an indirect estimation of the limiting ‘photon-injection-input’ for non-degradative hyperthermia therapy.

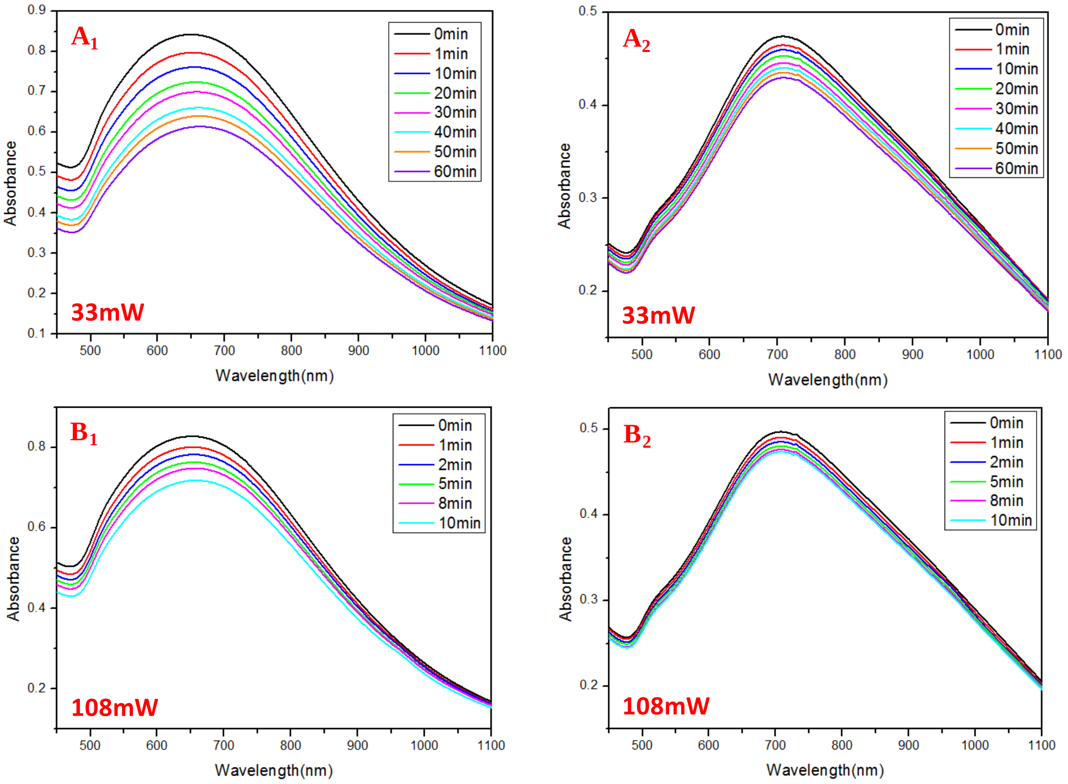

Figure 6.8: (A_1 and A_2) Time dependent absorption spectra of HHogGNP samples without PVP and with 0.01% PVP respectively, irradiated by 637 nm continuous laser source at 33 mW power. (B_1 and B_2) Time dependent absorption spectra of HHogGNP samples without PVP and with 0.01% PVP respectively, irradiated by 637 nm continuous laser source at 108 mW power.

6.3.2.4 Depletion Stabilized HHogGNPs under Ultrasonic Wave

To face the potentiality for several acoustic image based theranostics along with the traditional optical imaging, formulated depletion stabilized HHogGNPs should show greater stability in presence of high frequency sound wave (≥20,000 Hz). We have checked their stability by systematically studying under the influence of variable frequency ultrasonic exposure for variable time. Obtained results of structural integrity for PVP stabilized samples over samples without PVP has been included in **Figure 6.9**.

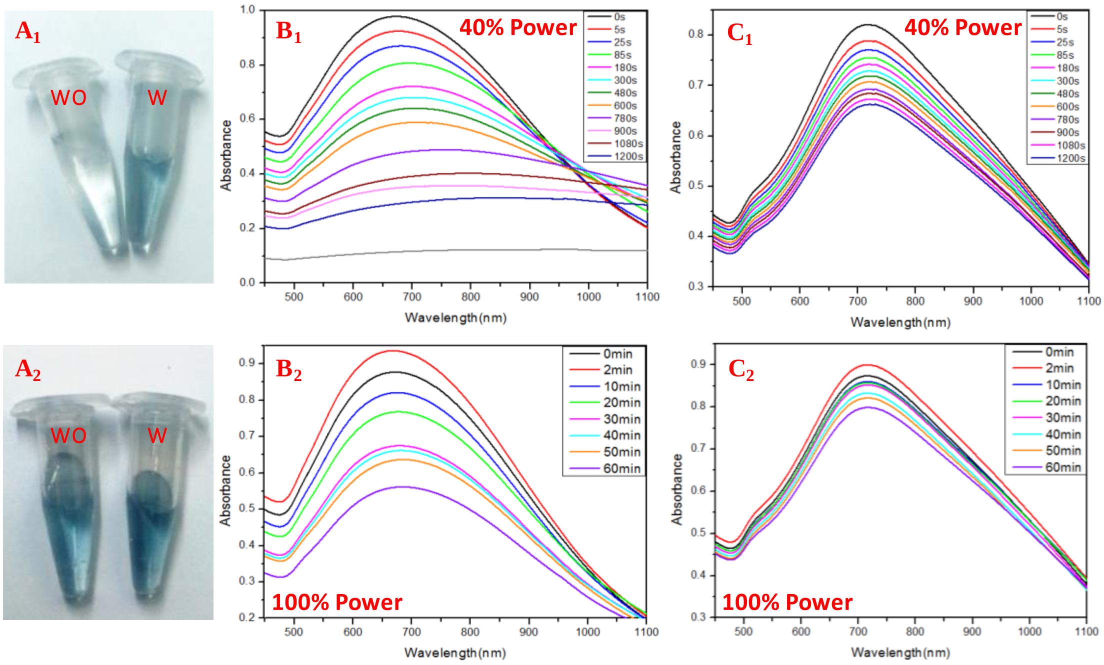

Figure 6.9: (A_1) HHogGNP samples without PVP (WO) and with 0.01% PVP (W) after treating them with ultrasonic wave operating at 53 kHz for 20 min at 40% power. (B_1) and (C_1) represent the corresponding absorption profiles of these samples respectively at different time interval. (A_2), (B_2) and (C_2) are similar records of sonication at 100% power for longer time (60 min).

6.3.3 Surface Properties retained by depletion stabilized HHogGNPs

The objective of this work is to generate a highly anisotropic nanoparticle with decent surface tagging by probe molecules, sufficient enough for sensing without altering their physical and chemical properties for high throughput theranostic applications. For this, the HHogGNPs must be able to retain their useful plasmonic and surface properties after depletion stabilization i.e. their tunable broad band absorption in the physiological window and gigantic SERS enhancement. The absorption spectra of the PVP modified HHogGNPs synthesized varying the NaCl concentration have been represented in **Figure 6.10** that shows desired tunability.

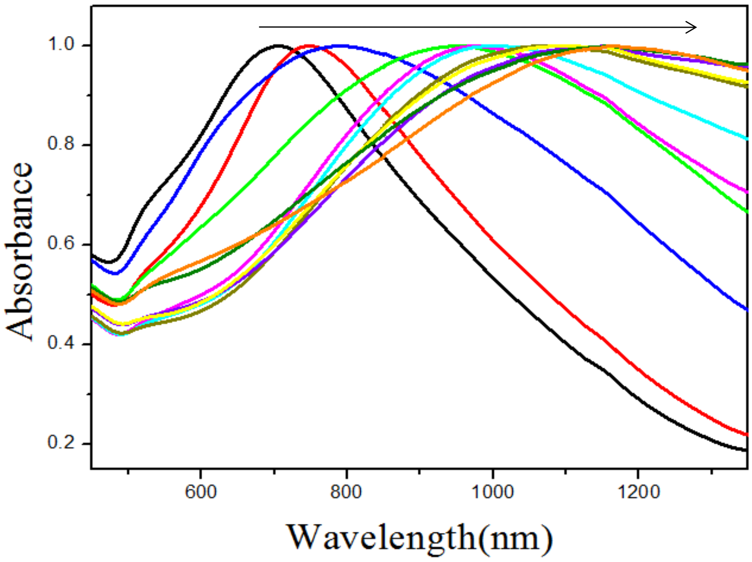

Figure 6.10: Plasmon tuning of depletion stabilized HHogGNPs synthesized by using 1.7 M NaCl variation (1-1200 µL). Arrow indicates the direction of shift of absorption peak with incremental variation of NaCl concentration.

To check the SERS activity, the as-synthesized HHogGNPs' bare surface was tagged by using low concentration (2.5×10^{-6} M) Rh6G which we used as a Raman probe to measure the enhanced Raman cross section offered by the HHog nanosurface. Due to the low concentration of Rh6G and the resultant incomplete surface coverage, dye tagged HHogGNPs can't make hotspot driven aggregation and remain stable in the solution. Immediately after the surface tagging by Rh6G, these dye tagged HHogGNPs were depletion stabilized by using a low-dose (0.01%) high molecular weight polyvinylpyrrolidone (PVP, M_w: 55,000) polymer and they remain stable for months without showing any significant aggregation at higher salt concentration (up to 0.6% NaCl which is close to the salt concentration in human blood) or in harsher physical and chemical environment. In contrary, at higher concentration of Rh6G ($\geq 5\times10^{-5}$ M) they aggregated precipitously almost instantaneously as shown in **Figure 6.11A$_1$** and we could not achieve to formulate dye tagged depletion stabilized individual HHogGNPs. Aggregation of nanoparticles in highly salted physiological condition is a longstanding issue that hampers their use in nanomedicine and in this respect our reported newly invented salt-induced synthesis of gold nanomaterial in the absence of any template[359] without employing a seeding method and subsequent low-dose polymer-based depletion stabilization provides a unique way to formulate nanomaterials suitable for long retention to act as an efficient nanomedicine. Most of the surface-induced optical detection techniques (e.g., SERS, NSET, etc.) are the result of a short-range force between metal surface and surface-adsorbed analytes (e.g., organic ligands, small chain peptides, etc.). The template which may form a finite double layer on the nanoparticle surface prevent the surface adsorbed molecules from accessing electromagnetic field generated by the metal core. Therefore, the naked nanoparticles synthesized by the above described protocol without using any template yet stable should acts as a better transducer[328]. Besides, very long (up to 95 nm) and sharp needle shaped spikes with tip diameter 2-5 nm on the central metal core offers very high SERS activity compared to the spherical gold nanoparticles having similar plasmonic properties. Details of the SERS activity and shape variable Raman signal enhancement for HHogGNPs has been described in **Chapter 5** and published before[60] which measures a huge Raman enhancement factor (G) of 8.9×10^{10} for surface adsorbed Rh6G and due to this huge Raman cross section we could observe substantial SERS signal even in this low concentration Rh6G (10^{-6} M). Due to their enhanced stability in the physiological condition under even harsher environment along with very high Raman intensity indeed these depletion stabilized HHogGNPs show potential application for high throughput theranostics. Moreover, due to the treatment of dye tagged HHogGNPs with low dose (0.01%) high molecular weight

(M_W ~55,000) PVP molecules, we have not observed any Raman spectral change (**Figure 6.11B**) which guarantees their application in finger printing.

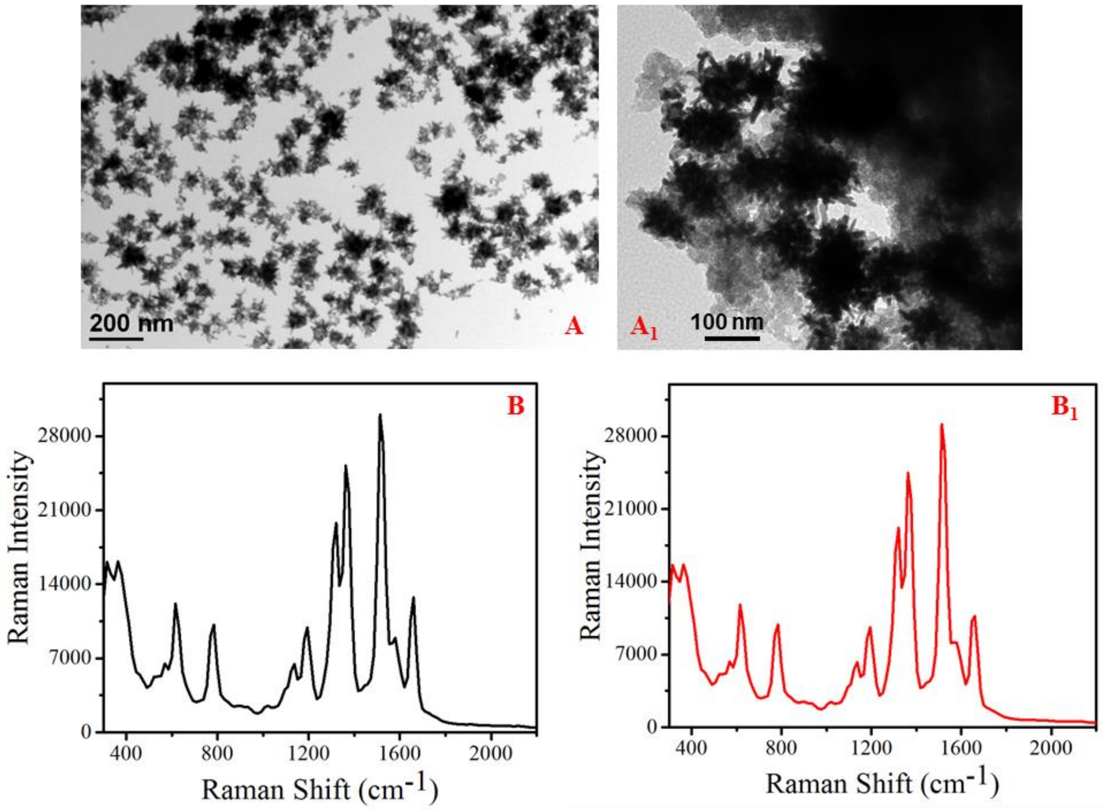

Figure 6.11: (A and A_1) TEM images of HHogGNPs with 2.5×10^{-6} M Rh6G for low coverage Raman tagging and with 10^{-5} M Rh6G for high coverage Raman tagging before depletion stabilization. Higher concentration of Rh6G triggers analyte-bridged aggregation as shown in Figure $5A_1$; (B and B_1) SERS spectra from Rh6G tagged HHogGNPs before and after depletion stabilization respectively (Figure B_1 should be replaced by less Raman intensity). Except substantial change in intensity of specific peaks, SERS spectra of Rh6G tagged HHogGNPs shows similar behavior (peak position) before and after depletion stabilization.

As discussed earlier, these dye tagged depletion stabilized HHogGNPs do not show any significant aggregation at higher salt concentration, we can potentially use them as active Raman tag in physiological condition and also can modify the surface by aptamer for specific targeting followed by photothermal therapy.

6.3.4 Photothermal Lysis Efficiency of Depletion Stabilized HHogGNPs

6.3.4.1 Protocols followed for Cell culture, Photothermal Therapy and MTT assay

Photothermal therapy (PTT) is emerging as a promising alternative towards next generation cancer treatment. Exposure of light to the cancerous cells are known to generate heat, which can elevate the temperature of tumor to an extent which is sufficient to induce necrosis or apoptosis leading to irreversible cellular damage and cell death. The cytotoxic activities of the nanomaterials were checked in both cancerous (HCT 116) as well as normal cells (RAW 264.7). For light independent toxicity study we have selected RAW 264.7 mouse macrophage cell lines (details have already been mentioned in chapter5). To find out the photothermal cell killing ability of the PVP stabilized HHogGNPs, we have performed systematic cell lysis experiments on HCT-116 colon carcinoma cells. At first we have tested the effect of red light (750 lumen, 8 W energy saving LED lamp equivalent to 75 W regular lamp with red filter to allow light with central wavelength at 623 nm) on the cell viability by using four different sized HHogGNPs and compared the obtained result with four different spherical nanoparticles. Then one of these suitable HHogGNPs have been chosen for further standardization with PVP screening in presence of 671 nm laser source at low power and short time. HCT-116 colon carcinoma cells were plated onto a 96-well plate (5×10^3 cells in 190 μL of DMEM culture medium supplemented with 10% heat inactivated FBS, 2 mM L-glutamine, 10 mM HEPES and 1 mM sodium pyruvate. After 24 h of incubation at 37 ˚C in 5% CO_2 environment, different amount (12, 25 and 50 μL of the equally concentrated) of each NPs were added to each well.

Plates were again incubated at 37 °C in 5% CO_2 environment for an additional 24 h and then illuminated by red light (red filtered white light) at the central wavelength of 623 nm for 50 min. No heating of the plate was registered as a result of the photo-exposure. Cell death was assessed immediately after the completion of illumination using MTT conversion and propidium iodide (PI) staining. PI was added only to the wells with the highest volume of NP (50 μL). We have not used any aptamer tagged HHogGNPs for antigen specific binding of HCT-116 colon carcinoma cells but simply studied their photothermal lysis ability to find out the applicability of these nanomaterials as hyperthermia agents and planning for cell specific targeting in the future experiments.

As already mentioned, we also checked the cell viability of HCT-116 cells with PVP screened HHogGNPs in presence and absence of light using MTT assay. HCT-116 cells were grown in DMEM medium as described earlier. Different volumes of PVP-HHogGNPs (20, 35, 50 and 75 μL) were treated to the cells for 4h at 37 °C, 5% CO_2. One set of NP-treated cells were exposed to red laser light of wavelength 671 nm (38 mW power) for 1min and the other set was kept unexposed to light. Cells without NP treatment and unexposed to light served as control.

6.3.4.2 Results of Photothermal treatment and MTT assay

Modulation of surface plasmon in the near infrared with very high absorption cross section for photon harvest and efficient photothermal conversion for the effective cell death leads to the fabrication of suitable nanomedicine. To achieve the controlled load dependent photothermal necrosis or apoptosis, applied nanomaterials must show nontoxicity in absence of light. The HHogGNPs indeed show nontoxic behavior in dark[60]. However, they are highly reactive to create substantial lysis in presence of light. This high throughput photolysis ability of the HHogGNPs can effectively be use for the application in therapy as therapeutic nanomedicine. Phototherapy could be either (i) photoradiation therapy where the photon source in the UV-vis wavelength range is directly used to degrade the toxic cell line and toxins or (ii) photothermal therapy where the adsorbed photon in the NIR-IR range (biological window) by the nanomaterials effectively converts photon energy into thermal energy by electron-phonon and phonon-phonon coupling. Photothermal conversion of energy by nanomaterials has been described in great details in **Chapter 1** and elsewhere.[130] Efficient photothermal conversion for photo excitation of HHogGNPs depends on few factors which include (a) extinction coefficient (electron-electron coupling) of the nanoparticle, (b) resonance condition between the surface Plasmon of that particular nanoparticle and excitation wavelength, (c) efficient electron-phonon and phonon-phonon coupling to initiate thermalization of nanoparticle through nanocrystal vibration, and (d) thermal conductivity and specific heat of the surrounding medium for heat transmission and preservation. Since the surrounding water medium for different doses remain same and all the different HHogGNPs are mainly made of by {111} facets, the extent of photothermal conversion efficiency depends heavily on their absorption cross section and resonance excitation. As we increase the concentration of NaCl in the mother solution during HHogGNPs synthesis, absorption cross section gradually increases due the enhancement of relative surface area, RSA (Listed in **Table 6.1**) and diameter but the probability of photo excitation (electronic transition) at a particular wavelength, 623 nm central wavelength, gradually reduces as the surface plasmon gradually moves towards 1100 nm to create a non-resonant condition.

Effective cell death not only depends on the extent of photothermal conversion but also depends on the effective temperature at the tip through which anisotropic nanomaterials attach with the cell membrane. More the nanoscopic temperature at the tip more is the probability of thermal cell damage. Nanoscopic temperature at the HHogGNPs tip depends on several factors which include (a) tip curvature, (b) 2D projected angle covered by the tip, (c) average Aspect Ratio (AR) of surface tips, and (d) relative surface area (RSA) offered by the tips. It is clear from **Table 5.1**of **Chapter 5** that as we increase the concentration of NaCl (from 170 µM-20 mM) in the mother solution during synthesis, all the four above factors favor to result better thermal lensing[52] at the tip to destroy the cell membrane more efficiently. We have used four different HHogGNPs ($NP_{5, 6, 7, 8}$) synthesized by using 170 µM, 10.2 mM, 3.4 mM and 20 mM NaCl respectively with *in plane* surface Plasmon maxima at 540, 800, 660 and 870 nm. Along with these we have synthesized four different spherical shaped nanoparticles ($NP_{1, 2, 3, 4}$) with diameters 8, 20, 40 and 100 nm by well-established TSC-based heating method with absorption maxima at 518, 524, 531 and 578 nm respectively to compare their ability as effective hyperthermia agents. **Figure 6.12** explains the details of the effect of HCT-116 colon carcinoma cells before and after the treatment with HHogGNPs in presence of photoexcitation.

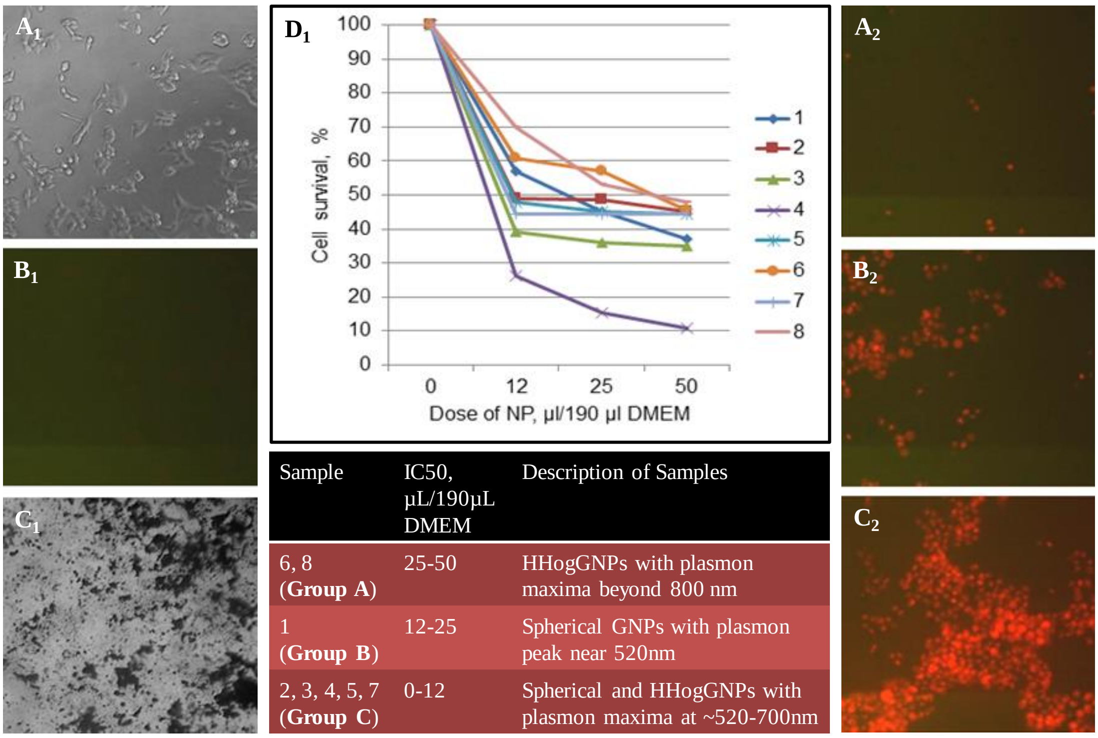

Sample	IC50, µL/190µL DMEM	Description of Samples
6, 8 (**Group A**)	25-50	HHogGNPs with plasmon maxima beyond 800 nm
1 (**Group B**)	12-25	Spherical GNPs with plasmon peak near 520nm
2, 3, 4, 5, 7 (**Group C**)	0-12	Spherical and HHogGNPs with plasmon maxima at ~520-700nm

Figure 6.12: (A_1) Phase contrast and (B_1) fluorescence optical images of the HCT-116 colon carcinoma cells in absence of NPs after photoexcitation by a red light (750 lumen, 8 W energy saving LED lamp equivalent to 75 W regular lamp with red filter to allow light of central wavelength 623 nm). C_1 is the phase contrast image of the HHogGNPs treated cells after photoexcitation. D_1 shows the cytotoxicity effect of different spherical shaped (NP$_{1, 2, 3, 4}$) and Hedgehog shaped (NP$_{5, 6, 7, 8}$) GNPs and the table shows that the GNPs are divided accordingly in three groups A, B, C and (A_2-C_2) show differential effects of NPs on permeability of the plasma membrane for PI where A_2 corresponds to group A, B_2 to group B and C_2 to group C.

Here **Figure 6.12A$_1$** and **6.12B$_1$** are the phase contrast and fluorescence optical images of the HCT-116 colon carcinoma cells after photoexcitation in absence of HHogGNPs which show well spread healthy cells. **Figure 6.12C$_1$** is the phase contrast image of the HHogGNPs treated cells after photoexcitation which shows that the morphology of the cell is not altered. To determine the apoptotic changes, cells were treated with an MTT reagent followed by colorimetric detection. As shown in **Figure 6.12 D_1**, NP_4 was the most cytotoxic whereas other 7 samples were also active but to a lesser extent than NP_4. The potency of NP_{1-8} was categorized into three groups as described in the Table given in **Figure 6.12**. The lowest IC_{50} (highest cytotoxicity) values were registered for $NP_{2,\ 3,\ 4,\ 5,\ 7}$ (group C) where as NP_1 (group B) and especially $NP_{6,\ 8}$ (group A) were less potent. Finally, **Figure 6.12 A_2-C_2** demonstrated differential effects of individual NP preparations on permeability of the plasma membrane for PI where **A_2** corresponds to group A, **B_2** to group B and **C_2** to group C. The increase of red fluorescence which indicates the photodamaging potency of NPs: group C compounds yielded the most pronounced necrosis/apoptosis, with ~100% cells damaged whereas for group A & B only a portion of cells included PI. Since the central wavelength of excitation at 623 nm has been used for the photothermal lysis is in close resonance with the surface Plasmon offered by $NP_{2,\ 3,\ 4,\ 5,\ 7}$ it is expected that these particles will offer better photon harvesting for their higher absorption cross section at 623 nm and in addition due to efficient thermal lensing by the sharp tips by $NP_{5,\ 7}$ the nanoscopic rise in temperature will be very high for these particles to initiate the nanoscopic photolysis process. In contrary for NP_1 and $NP_{6,\ 8}$ shows absorbance at 518, 800 and 870 nm respectively is in off resonance with the excitation wavelength at 623 nm to show very low photo harvest to offer minimum photothermalization. Observed results explains well of our hypothesis of photothermalization. This study also indirectly proves that the spherical as well as HHogGNPs without aptamers act as potent photothermal sensitizer and the extent of photodamage depend heavily on their shape and Plasmon nature. Moreover, rapid apoptosis or necrosis may co-exist and form the underlying mechanisms of cellular photodamage by HHogGNPs. To check the photothermal lysis efficiency of the depletion stabilized HHogGNPs, we took 3.4 mM NaCl mediated, PVP-stabilized HHogGNPs suitable for 671 nm laser excitation having plasmonic peak closer to it (**Figure 6.3D**). We checked for its photothermal cytotoxicity at 671 nm light in HCT-116 cells and compared the same with the light unexposed cells. The NP treated but light unexposed cells showed no toxic effect to HCT-116 cells whereas light exposure conditions showed significant cell death, decreasing the viability to approximately 50% with 75 µL of NP (**Figure 6.13**). Interestingly, cell without NP treatment but 1 min light exposure showed no observable cell death.

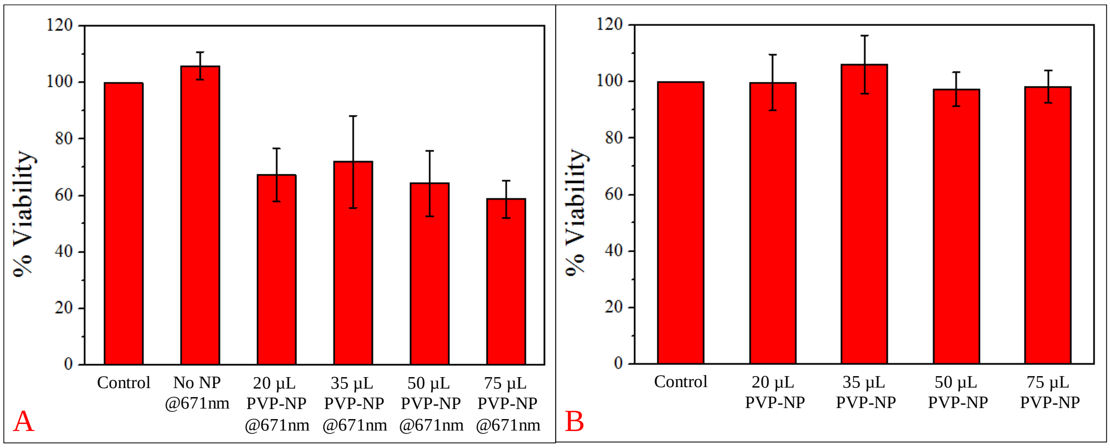

Figure 6.13: Cell viability results of HCT-116 cells with PVP screened HHogGNPs in (A) presence and (B) absence of light.

6.3.5 Analytical Calculation of the Local Temperature generated at tips of HHogGNPs

To understand and to estimate the extent of thermalization offered by the HHogGNPs we have adopted an analytical calculation by considering Coulomb potential outside the particle under uniform-temperature approximation[345–349]. The localized increase in temperature (ΔT) around a single nanoparticle depends upon the absorption cross section, laser intensity, size of the nanoparticle, and thermal conductivities of both the metal and the surrounding medium.[360] The temperature change on the surface of an individual nanoparticle in aqueous solution can be obtained following the equation below:

$$\varDelta T_{NP} = \frac{\sigma_{abs} I}{4\pi\beta r_{eff}\kappa} \tag{6.1}$$

Where σ_{abs} = absorption cross section (cm^2) of the HHogGNP, I = intensity of the incident light (Wcm^{-2}), r_{eff} = effective radius of a sphere with the same volume of one sharp tip, β = thermal capacitance coefficient of the nanoparticle and κ = thermal conductivity of water. By considering the absorption coefficient (σ_{abs})[321,360] of the HHogGNP as ~10^{-10} cm^2 and for an excitation source with 100 mW power and 2 mm diameter, we can calculate the intensity of the incident light as

$$I = \frac{100mW}{\pi(0.1cm)^2} = 3.183098\ Wcm^{-2} \tag{6.2}$$

We considered $\beta = 1$ by neglecting the dependence of β on nanoparticle aspect ratio. By considering a sharp tip as a cone (Chapter 5 describes the geometrical details of each sharp tip) with base radius r_c nm and height h_c nm, the calculated volume of the tip V_c can be mathematically defined as

$$V_c = \frac{\pi {r_c}^2 h_c}{3} \times 10^{-21}\ cm^3 \tag{6.3}$$

If we consider N number of such tips per HHogGNP, then r_{eff}, which is the equivalent radius of a sphere having same volume of the total number of cones, can be calculated as follows

$$V_{eff} = \frac{4}{3}\pi r_{eff}^3 = N \times V_c = N\frac{\pi {r_c}^2 h_c}{3} \times 10^{-21} cm^3\ OR\ r_{eff} = \sqrt[3]{\left(\frac{N {r_c}^2 h_c}{4} \times 10^{-21}\right)}\ cm \tag{6.4}$$

By considering $\kappa = 0.6\ Wm^2K^{-1}$ for water,

$$\varDelta T = \frac{10^{-10} cm^2 \times 3.183098 W cm^{-2}}{4\pi \times 1 \times \sqrt[3]{\left(\frac{N r_c{}^2 h_c}{4} \times 10^{-21}\right)} \times 10^{-2} m \times 0.6 W m^{-1} K^{-1}} \tag{6.5}$$

If we consider the release of thermal energy only through the tips (not through the surface, lensing effect) then we need to evaluate the tip volume out of the total hydrodynamic volume of the HHogGNP, i.e.

$Relative\ Vlume = \frac{\frac{4}{3}\pi R^3}{\frac{4}{3}\pi r_t^3}$ Where, R= hydrodynamic radius and r_t= radius at the tip

(6.6)

Hence, $\varDelta T\ per\ tip = \varDelta T \times Relative\ Volume = \frac{10^{-10} \times 3.183098 \times R^3}{4\pi \times 1 \times \sqrt[3]{\left(\frac{N r_c{}^2 h_c}{4} \times 10^{-21}\right)} \times 10^{-2} \times 0.6 \times r_t^3} K$

Details about the necessary parameters used to calculate average temperature change per tip is listed in **Table 6.1**.

Table 6.1: Calculated average temperature change per tip for variable HHogGNPs synthesized by varying NaCl concentration between 170 μM and 20 mM.

NaCl Concentration (M)	170×10^{-6}	340×10^{-6}	170×10^{-5}	340×10^{-5}	10×10^{-3}	20×10^{-3}
Average hydrodynamic radius R_0 (nm)	110	110	110	110	110	110
Tip base radius r_c (nm)	5.0	4.5	4.0	3.75	2.8	2.5
Average surface tip length h_c (nm)	60	69	80	89	93	95
Average number of tips N	32	28	26	20	16	10
Average radius at the tip r' (nm)	2.5	1.8	1.6	1.3	1.2	1.0
RSA	1.04	1.05	1.74	1.5	1.75	2.8
Average ΔT per tip (K)	157	451	677	1388	2276	4926

This calculation implies that the nanoscopic temperature generated at the tip varies between ~150-5000 K which is high enough to initiate the photothermal therapeutic process to lead the effective cell death. Similar effect of photothermalization of carbon nanotube in the range of 1000-5000 K followed by IR excitation has already been reported by A. H. Zewail[133] though has not described in details by considering the geometrical and optical parameters of nanomaterials. Obtained tip temperature by analytical calculation and observed photothrmal necrosis establishes our hypothesis to use the synthesized HHogGNPs as potential hyperthermic cell killing agent. Real life application of these synthesized HHogGNPs is under investigation on animal model (mice) and the obtained results will be communicated in the near future.

6.4 Conclusion

By considering their broad-band Plasmon tunability for effective photoexcitation in the biological window coupled with nontoxic behavior in absence of light along with gigantic Raman cross section made our synthesized HHogGNPs as a potential candidate for efficient nanotheranostics. In addition, depletion stabilization of these HHogGNPs by low-dose (0.01%) high molecular weight PVP (M_w: 55,000) make them absolutely stable in highly salted condition equivalent to physiological environment (0.6% NaCl in blood or 0.9% NaCl in PBS) for long retention along with their effective photothermal conversion by electron-phonon and phonon-phonon coupling to generate as high as 5000 K temperature at the tip. With their long retention in physiological condition, high throughput Raman cross section, and nanoscopic ultrahigh temperature generation at the tip has been testified by checking their cell killing ability on HCT-116 colon carcinoma cells. Reported results prove that the depletion stabilized HHogGNPs have enough potential both as Raman sensor to follow the real-time therapy as well as nontoxic highly efficient photothermal therapeutic material to reduce side effects.

CHAPTER 7

FUTURE DIRECTION AND CONCLUSION

OUTLINE: What does this chapter brief?

- Introduction to nanomaterial assembly
- Designing Superlattice with monometallic and bimetallic building blocks
- A general conclusion drawn from the overall study

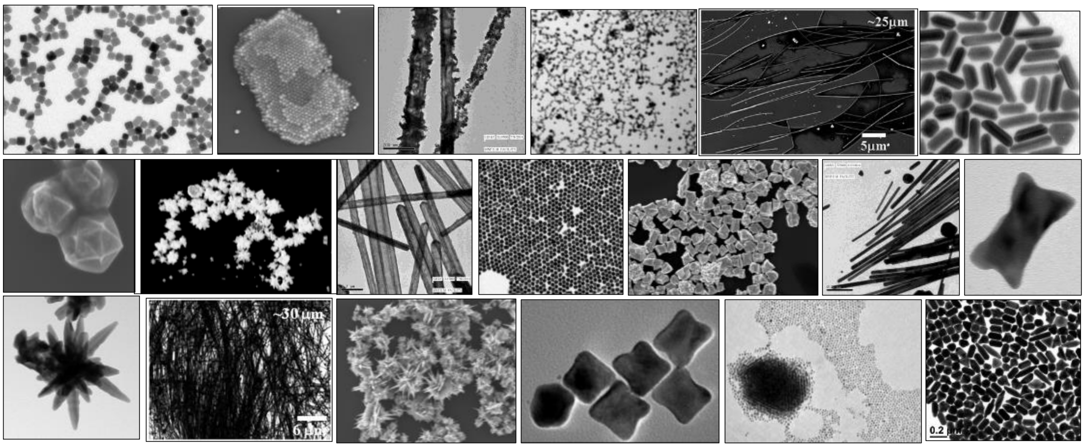

7.1 Introduction

In the previous four chapters, we mainly focused on the strategies of development of different anisotropic nanomaterials and their application in sensing and therapy. Basically, in all applications, we utilized the properties displayed by the nanomaterials as an ensemble effect. This ensemble effect can be enhanced further if an ordered assembly of nanomaterials is taken into consideration[313,361–363]. Collective effects are also exhibited by assemblies without order i.e. mere aggregates[364–366], but these effects are not manifested in a regular and precise way due to their (i) uncontrolled development, (ii) random and complex three-dimensional structure and (iii) instability with time. In comparison, properties exhibited by an ordered assembly are more consistent and controllable and predictable. Different strategies have been adopted for designing ordered assemblies of both isotropic and anisotropic nanoparticles[313,361,362,367]. For isotropic nanoparticles, properties vary uniformly along all the directions, so there is limited scope to make a directed assembly. But anisotropic nanomaterials have an inherent direction dependence. This allows the assemblies to grow in a specific direction or orientation utilizing preferred interaction among nanoparticles in that particular direction over others. This gives more scope to play with the resultant properties of the nano-assemblies too. For example, an end-to-end assembly of nanorods results in increase in the aspect ratio and a red shift is expected in the absorption spectrum whereas a side-by-side assembly may reduce the overall aspect ratio compared to the individual nanorods (depending on the aspect ratio of the individual nanorods and their average number forming side-by-side assembly) and there would be a blue shift then.[313]

Nanoparticle superlattices are a class of periodic assembly composed of nanoscale building blocks. They show novel chemical and physical properties arising out of the interactions between the constituent particles as discussed in the first chapter. For making this large-scale lattice, uniformity in shape and size of the constituent nanoparticles (NPs) is a prerequisite. In this respect, designing a superlattice of structurally anisotropic nanomaterials are even more challenging. Reports are there where supercrystals have been formed by morphologically anisotropic nanomaterials[362]. One established and well-practised way to design nanosuperlattices is to rationally arrange isotropic as well as anisotropic noble metal nanoparticles tethered by strands of thiolated DNA and a suitable linker DNA strand complimentary to them[368,369]. The main advantage of this assembly process is that it can be reversed by thermal denaturation. But for any DNA-mediated assembly, there are issues like, standardizing optimum salt concentration required for DNA annealing avoiding nanoparticle aggregation, optimum removal of positive surfactants (if used any as capping agent) over the nanoparticles to stop possible random interference of negative strands of DNA, cost of specified conjugate DNA strands etc. Muliti-component nanoparticle superlattices made of combinations of nanospheres and nano triangular plates of metal, semiconductor, magnetic and dielectric materials are also reported[149,370]. As we had mentioned in the very first chapter, anisotropy can arise from morphology as well as from chemical composition. We have opted to make superlattices by taking chemically anisotropic nano-building blocks. Our aim is to study some physico-chemical properties of 2D thin films and 3D superlattices made of multimetallic alloy nanoparticles. Though alloy nanoparticle superlattices are not new in literature[371,372], but the nano-alloys often show unexpected properties which is observed in neither of the pure components and alters with their composition[373]. Here, we have first made monometallic superlattices following a well-known procedure called 'digestive ripening'[374], checked their gradual development step by step with time, explored the lattice parameters from both TEM and GISAXS. We have then taken bimetallic precursors and followed similar protocol. In this last chapter, the data obtained for this till date have been included along with a general conclusion drawn from all the preceding studies.

7.2 Synthesis of Superlattice

7.2.1 Superlattice of monometallic nanoparticle units

As already mentioned, we have adopted a reported protocol[375] involving digestive ripening method for the synthesis of superlattices with slight modifications. Precisely, 0.1018 g of didodecyldimethylammonium bromide (DDAB) was dissolved in 10 mL toluene to make a 2.2×10^{-2} M DDAB solution.0.034 g of $HAuCl_4.3H_2O$ (0.0086 M) was then added to it. From a freshly prepared ice-cooled aqueous solution of 0.96 M $NaBH_4$ (0.1816 g $NaBH_4$ in 5 mL water) an amount of 500 µL was then added drop by drop with vigorous stirring for reduction of the gold salt and it was left under this stirring condition for another 1 h. After that, 200 µL 1-dodecanethiol was added to 2.5 mL of the as-prepared gold colloid. This was followed by nanoparticle precipitation with 7.5 mL of ethanol in order to purify the system from any byproducts. Once the particles are precipitated down, the upper layer of ethanol is discarded and it was allowed to get dried under ambient condition. It was then re-dispersed in 2.5 mL of toluene and 200 µL of 1-dodecanethiol was again added to it. This solution was taken in a round bottom flask and subjected to reflux at 110 ˚C with constant stirring for

90min under argon atmosphere. The refluxed solution is left undisturbed till it cools down to room temperature.

For GISAXS measurements, samples were prepared in two ways: (i) part of this refluxed solution was first taken in a watch glass where nanoparticles are allowed to form self-assembly with gradual evaporation of the solvent. The black precipitate so obtained was carefully placed on the center of properly washed (with extran, ethanol and milli-Q water) double frosted (ISO 8037) microscope glass slides (9100D01, Borosil) for a thicker sample and (ii) 50 µL of the solution was dropped directly on to the glass slides to form a thin layer of nanocrystals by solvent evaporation. For TEM measurement we used dip-and-dry technique (described in chapter 3) to make samples with 300 mesh copper Formvar/carbon grid.

7.2.2 Superlattice of bimetallic nanoparticle units

For preparing superlattices comprised of bimetallic nanoparticle units we took 1:1, 1:2, 1:3, 1:4 and 1:5 solutions of Au and Ag salts by molarity. To be specific, for each of the five sets, 0.017 g of $HAuCl_4.3H_2O$ (0.0043 M) was dissolved in $2.2x10^{-2}$ M DDAB solution. Then 0.0073 g (0.0043 M), 0.0146 g (2x0.0043 M), 0.0219 g (3x0.0043 M), 0.0292 g (4x0.0043 M) and 0.0365 g (5x0.0043 M) of $AgNO_3$ were added to make the 1:1, 1:2, 1:3, 1:4 and 1:5 AuAg samples respectively and they were reduced by 500 µL, 750 µL, 1000 µL, 1250 µL and 1500 µL of freshly prepared ice-cooled aqueous solution of 0.96 M $NaBH_4$. Rest of the process was exactly same as described above.

7.3 Results and Discussion

Absorption spectra of both types of samples, monometallic (only Au) and bimetallic (1:1 AuAg), have been provided in **Figure 7.1A** which shows that before and after reflux, the absorbance maxima practically remain unchanged (typically 511 nm for 1:1

AuAg sample and 523 nm for only Au sample). This is in accordance with the fact that assembly starts only with gradual evaporation of the solvent and before that though linked by sulfur atoms, they remain well separated in solution just as individual nanoparticles. **Figure 7.1B** shows the absorption of all the bimetallic samples before reflux with Au:Ag ratio varying from 1:1 to 1:5. There occurs a gradual blue shift of the plasmon maxima (towards the characteristic plasmonic peak position of Ag nanoparticles) as the proportion of Ag increases with respect to Au in the sample. We have taken two samples made of only Au and 1:1 Au:Ag for rest of the studies.

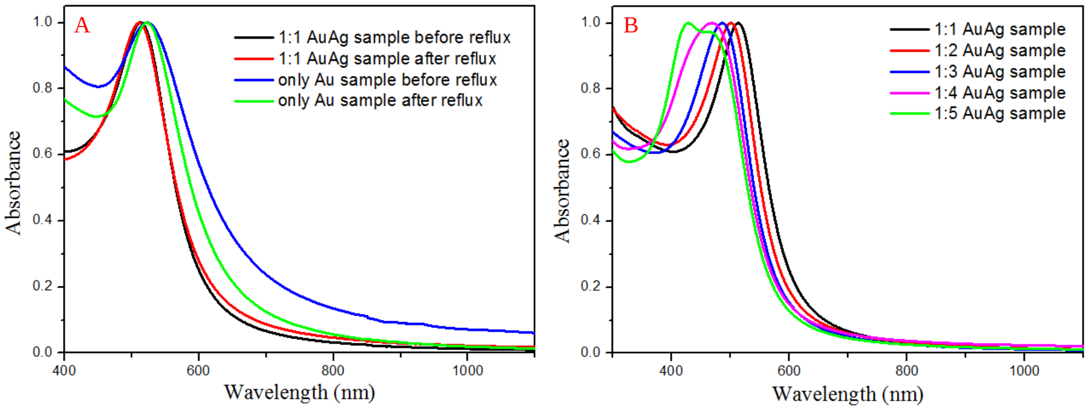

Figure 7.1: (A) Vis-NIR absorption spectra of 1:1 AuAg sample and only Au sample before and after reflux, (B) Vis-NIR absorption spectra of bimetallic AuAg samples with varying molar ratio between Au and Ag (1:1 to 1:5) before reflux.

Steps of the Au-nanosuperlattice formation have been interpreted in details elsewhere[374]. We attempted to capture it by taking TEM images for the monometallic Au-samples collected at different stages of the reaction (**Figure 7.2**). It shows that, initially, just after the reduction or purification by ethanol or even after addition of thiol before reflux, the particle-size-distribution remains broad (**7.2A-C** respectively), after which they tend to get leached in presence of excess thiol, a strongly interacting ligand, and under refluxing condition till they attain a size distribution close to uniformity. We stopped the reflux at different time intervals – 30, 60 and 90 min and collected samples for the images shown in figure **7.2D**, **E** and **F** respectively. **Figure 7.2 (G-J)** are images of the sample collected at different time intervals (2, 10, 24 and 48 h respectively) after the reflux. It is worth to mention that after reflux the pattern (shape, size), or distribution (2D or 3D structure) of the self-assembly of the nanoparticles is not observed to be dependent on time in our case.

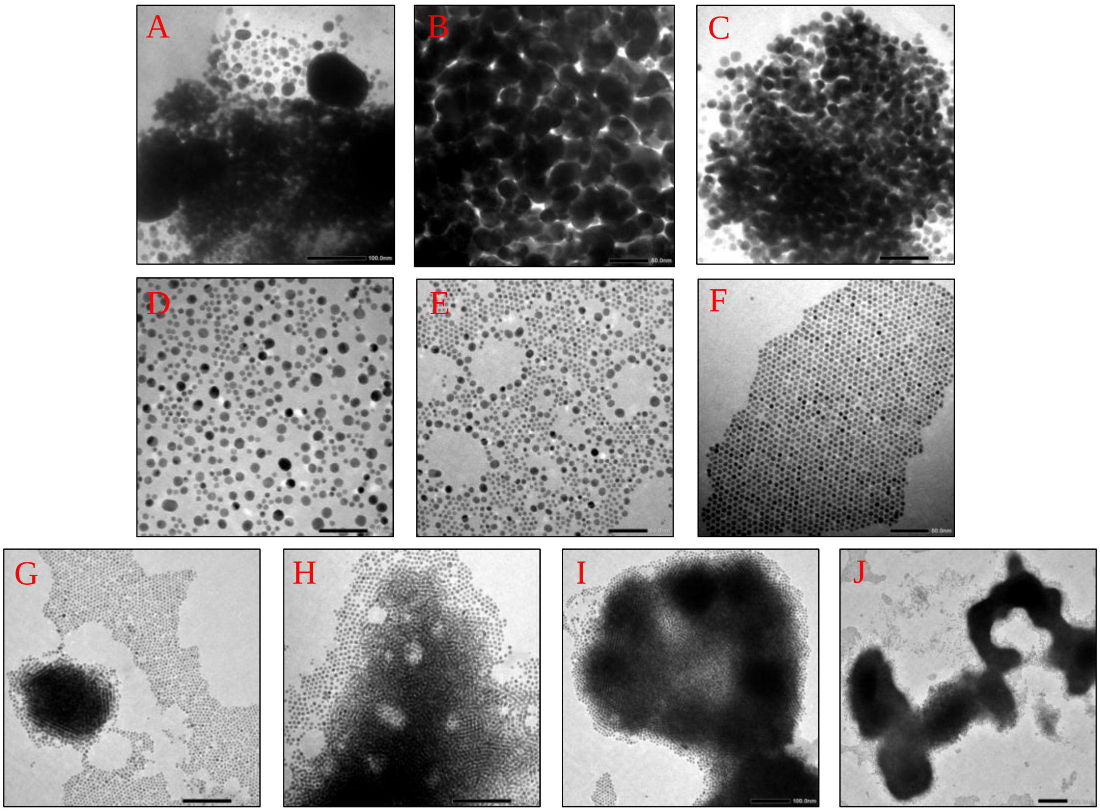

Figure 7.2: TEM images of only Au samples collected at different stages of the synthesis, (A) after reduction, (B) after purification by ethanol, (C) before reflux, (D-F) three different samples after 30 min (D), 60 min (E) and 90 min (F) reflux and subsequent cooling, (G-J) after complete 90min reflux when we cooled and allowed the sample for crystallization for different time range (2, 10, 24 and 48 h respectively).

The lattice structure of Au nano superlattice has been already studied for different synthesis methods[376] and from the illustration of TEM images, small and wide-angle electron diffraction pattern, XRD pattern etc. it has been observed that following digestive ripening method, where Au nanoparticles are synthesized by gold salt reduction in an inverse micelle system, arrangement in an *fcc* lattice is preferred under equilibrium control. In our case, this has been evaluated by measuring the scattering signals obtained from GISAXS experiments for the only Au sample, where the 2D detector image is integrated to yield I(q) vs. q_z in $Å^{-1}$ (details of the experimental parameters have been mentioned in chapter 2). Two peaks appear at $q_z = 0.242$ $Å^{-1}$ and 0.262 $Å^{-1}$ as shown in **Figure 7.3** which corresponds to two lattice parameters, $d_1 = 25.96$ Å and $d_2 = 23.98$ Å respectively following $q_z = 2\pi/d$. For an *fcc* lattice, $2d = a$ (where a is the unit length or inter-particle distance in the lattice as shown in **Figure 7.4A**), but presence of two peaks indicates a distortion in one direction. Considering that, a comes out to be 70.69 Å or ~7 nm as the inter-particle spacing (illustrated in Figure **7.4B**). This is in accordance with the spacing assessed from TEM images for these nanoparticles of ~5 nm diameter. However, there is a deviation in the degree of distortion as reflected by the spread of the second peak.

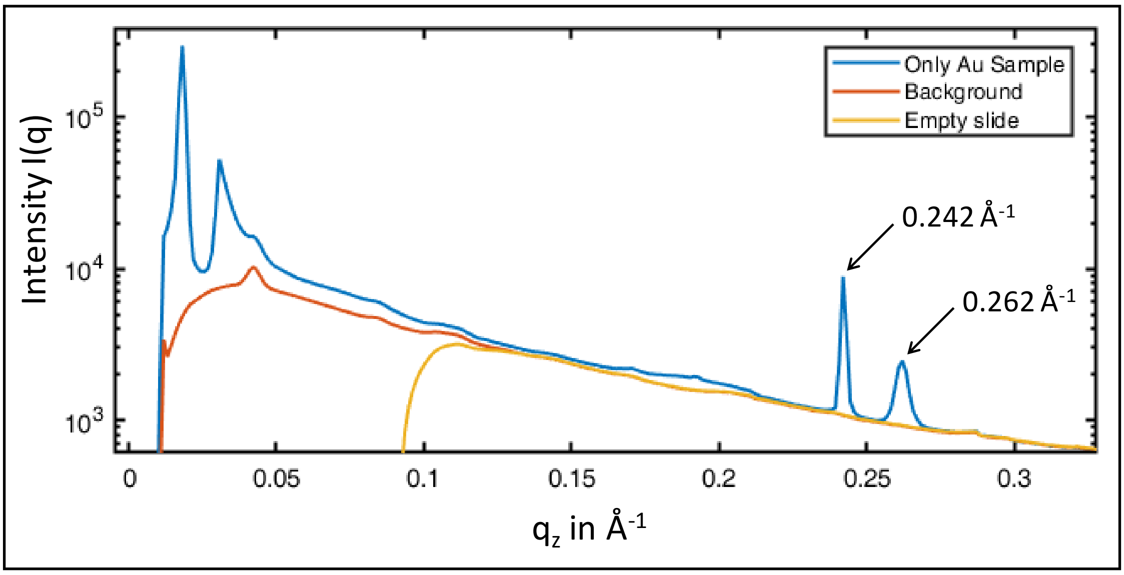

Figure 7.3: I(q) vs. q_z plot of the only Au sample two peaks at 0.242 Å^{-1} and 0.262 Å^{-1} (initial two peaks have appeared from the leakage of the beam stopper) with respect to the signals from the background and empty slide.

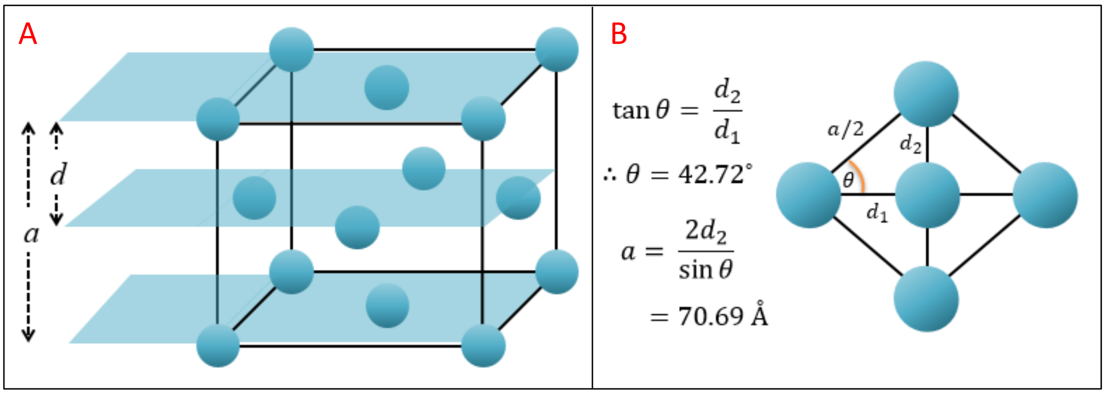

$$\tan\theta = \frac{d_2}{d_1}$$

$$\therefore \theta = 42.72^\circ$$

$$a = \frac{2d_2}{\sin\theta}$$

$$= 70.69\ \text{Å}$$

Figure 7.4: (A) Schematic diagram illustrating *a*, the unit length or inter-particle distance in an *fcc* lattice with respect to the lattice parameter *d* and (B) its derivation in our case considering two lattice parameters.

The TEM image (**Figure 7.5A**) of the Au-Ag samples just after the reduction step shows much better size distribution compared to the only-Au sample. The co-crystallization of Ag and Au has been assessed from their chemical mapping shown in Figure **7.5(B)** and **(C)**.

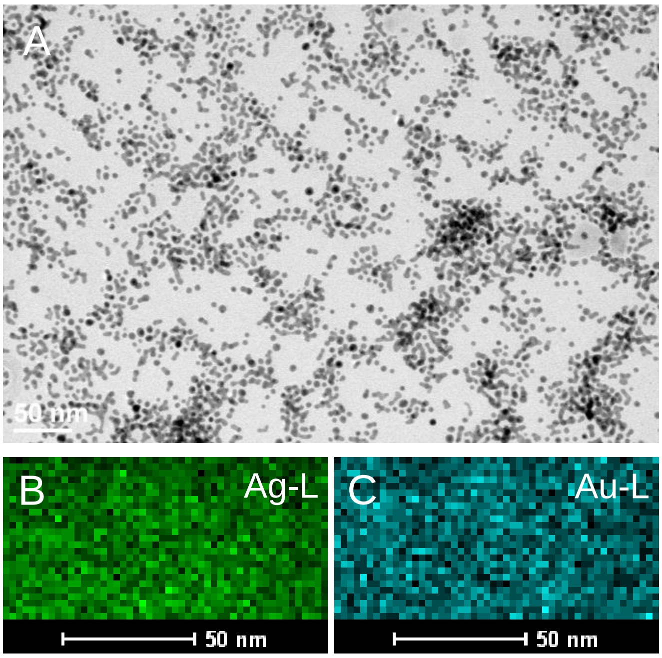

Figure 7.5: (A) TEM image of the Au-Ag sample after reduction before purification and reflux. (B) and (C) shows the chemical mapping for Ag and Au atoms in the sample.

After reflux, the samples show discrete Au-Ag nanoparticles of size ~5 nm distributed in 2D-plane (**Figure 7.6A**) as well as in 3D-structured assembly (**Figure 7.6B**). The presence of both the elements Au and Ag in the sample (after reflux) is further supported by the EDX spectra presented in **Figure 7.6C**.

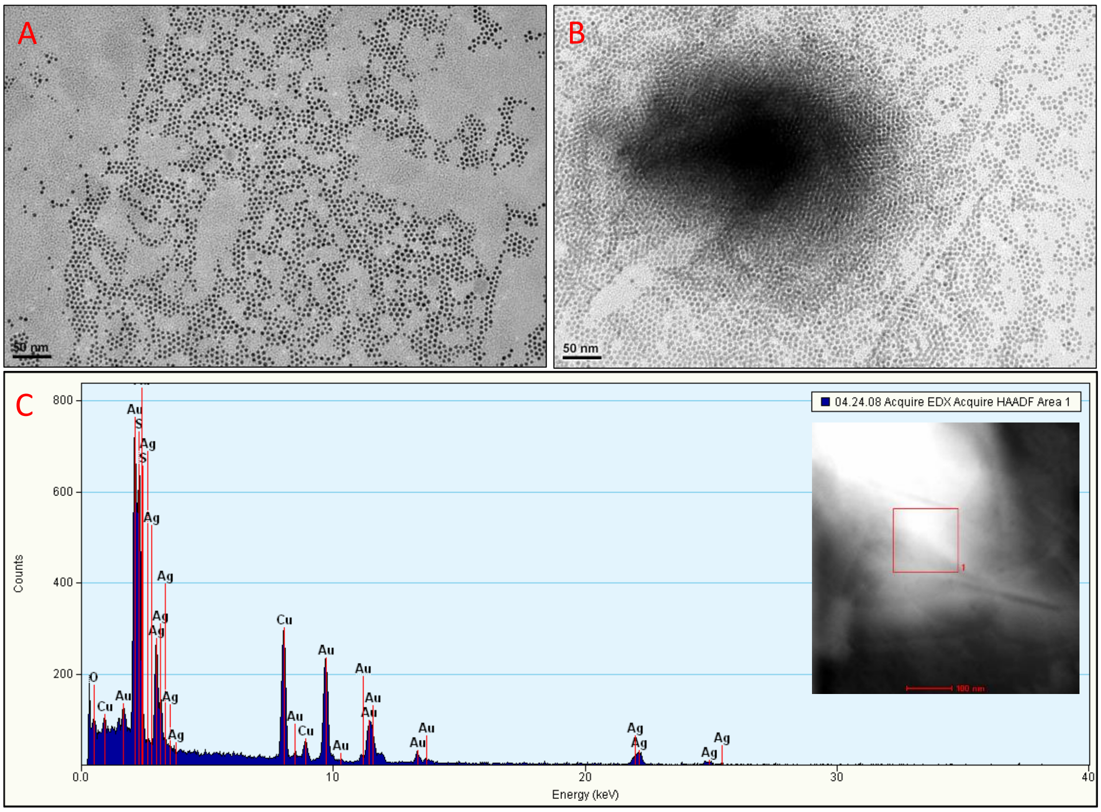

Figure 7.6: (A and B) TEM images of Au-Ag samples after reflux. (C) Acquired EDX spectra for the Au-Ag samples after reflux (inset shows the selected HAADF area highly illuminated due to the presence of Sulphur atoms in thiol).

To confirm the periodicity in our Au-Ag sample, and to find out its lattice parameters, we studied the small angle electron diffraction pattern for its different parts (**Figure 7.7**). From the ratio of the principal spot spacings and the angles between the principal plane normals, it is found that the diffraction pattern matches with the standard, indexed diffraction pattern for *fcc* crystals in the [011] beam directions[377].

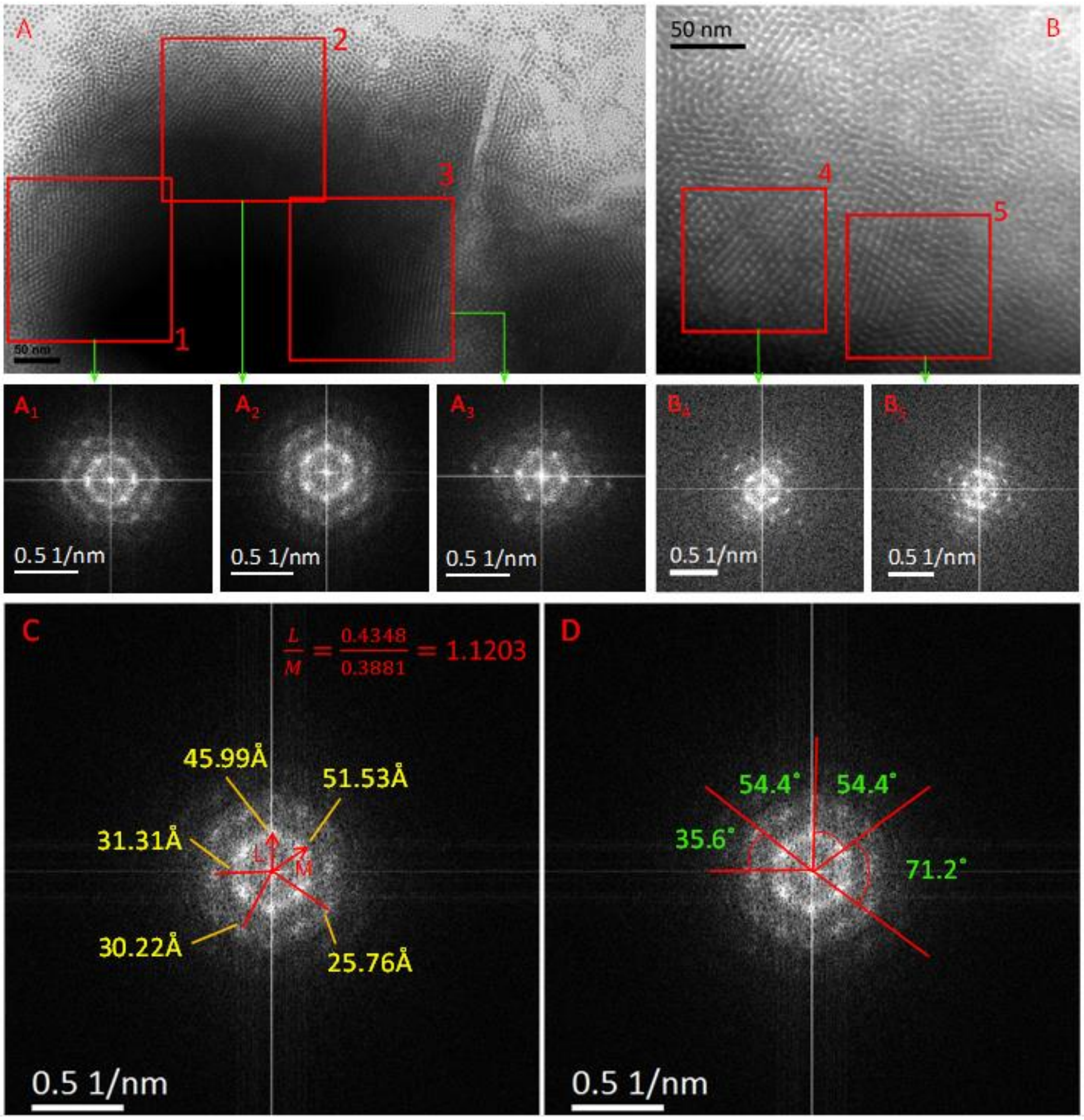

Figure 7.7: (A) and (B) TEM images of Au-Ag sample at different magnifications. (A_1- A_3) and (B_4, B_5) are the small angle electron diffraction patterns obtained for different parts (marked in frames 1, 2, 3, 4 and 5 respectively) of it. (C) represents the distances between the spots in real space mentioned in yellow calculated from the red lines indicating the same in reverse space. Ratio of the principal spot spacings, $\frac{L}{M}$ is ~1.12 here. The corresponding angles between the principal plane normals are marked in green in (D). All the spacings and angles have been averaged over several frames of different diffraction patterns and the average values have been shown here.

For unit length a of (*hkl*) lattice plane, the inter lattice spacing d_{hkl} can be obtained from,

$$d_{hkl} = \frac{a}{\sqrt{h^2+k^2+l^2}} \tag{7.1}$$

In our case, $d_{hkl} = d_{110} = 51.53$ Å

This implies that the inter lattice spacing, $a = 51.53 \times \sqrt{2} = 72.87$ Å $= 7.287\ nm$

Therefore, the inter-particle distance for AuAg nanoparticles (of diameter ~5 nm) in the assembly is ~7.2 nm. However, these results are based on the data obtained till now. It can be confirmed after some more experiments and further standardization which include structure and property analysis of these alloy-nanomaterial-assemblies as our future endeavor in this direction. We have already designed a GISAXS measurement mount (**Figure 7.8**) that can record the SAXS data with variable temperature. This would be helpful for understanding the crystal growth with temperature alteration and to determine the reversibility of superlattice or any periodic assembly formation.

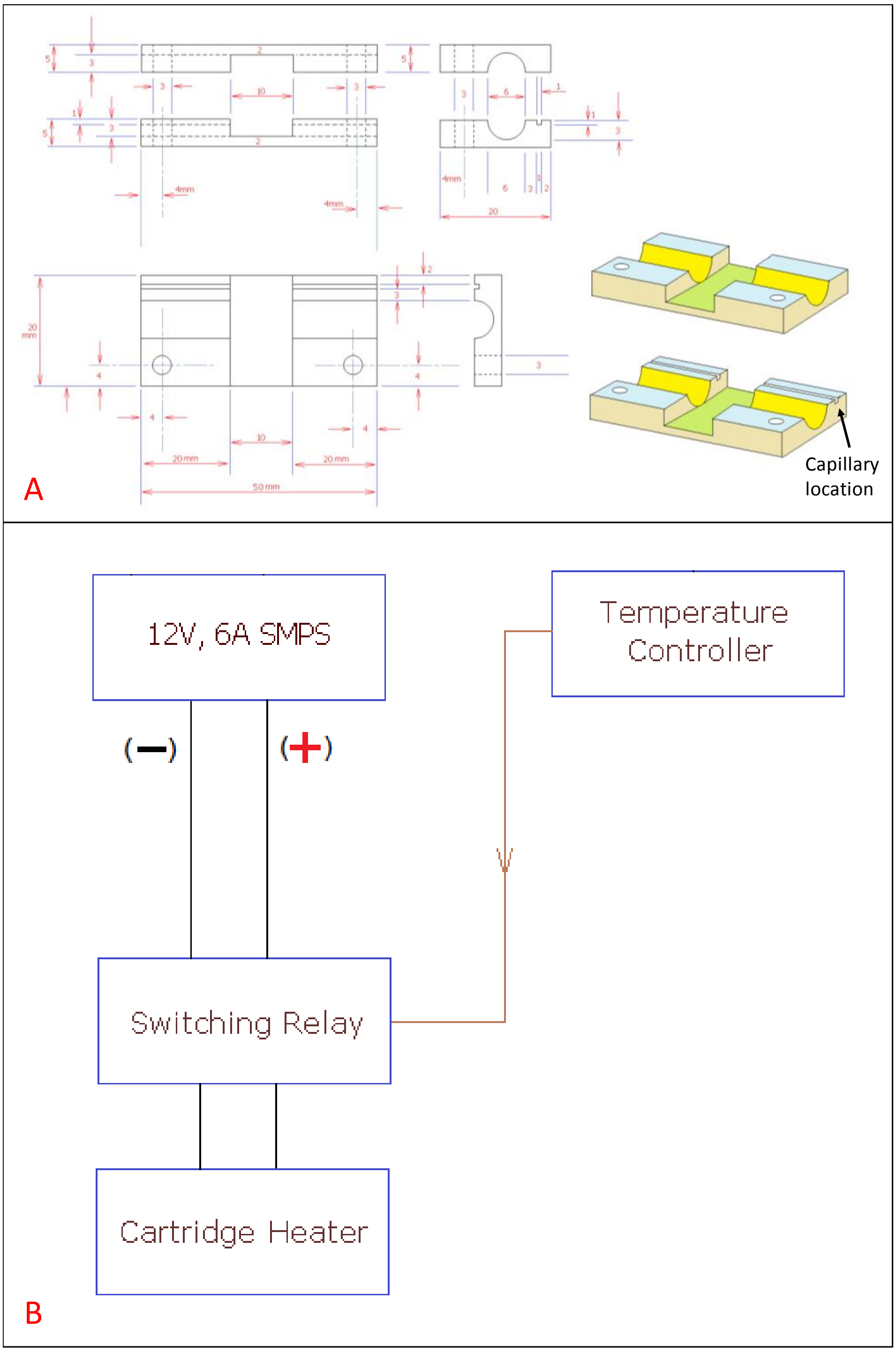

Figure 7.8: (A) Design of the temperature variable GISAXS measurement mount where the sample can be placed in a capillary and (B) schematic outline of its working principle.

7.4 A General Conclusion

In this thesis, an elaborate study has been recorded on the development strategies and application perspectives of different anisotropic nanomaterials. Literature is now extensively rich with plenty of such materials of various size, shape, composition and distribution (arrangement). Only the controlling factors are crucial to obtain the material of desired activity every time and modifying them for enhanced performance at user-end. In this respect, we chose anisotropic noble metal nanoparticles as our working system and focused on three aspects mainly - fabrication, detection and theranostics. A variety of such materials has been synthesized following bottom-up strategy, following modified or new protocols. Detail analysis has been done on the growth dynamics and developed nanostructure to find out the origin and controlling factors of their anisotropy. Then we attempted to assess their utility in sensing and biomedical applications using UV-vis-NIR Spectroscopy, electron microscopy and surface enhanced Raman scattering, optical and fluorescence microscopy and MTT assay. Application in sensing has been performed by taking silver nanowires and silver nanodiscs whereas hedgehog gold nanoparticles have been applied in theranostics. Then we have moved towards making ordered assemblies of the Au-Ag alloy nanoparticles to check their synergic effect. Depending on the reaction parameters, the physical and chemical properties of the end nano-products, either in individual or in assembly, varies. In near future may be any type of synthesis and assembly would be executed totally by machines[378–380]. But guidelines would be still required to get a nanomaterial with higher specificity, precision, reproducibility and yield for a particular function. This study is an addition of some such guidelines based on experimental based observations.

REFERENCES

(1) Hu, M.-S.; Chen, H.-L.; Shen, C.-H.; Hong, L.-S.; Huang, B.-R.; Chen, K.-H.; Chen, L.-C. Photosensitive Gold-Nanoparticle-Embedded Dielectric Nanowires. *Nat. Mater.* **2006**, *5* (2), 102–106.

(2) Gudiksen, M. S.; Lauhon, L. J.; Wang, J.; Smith, D. C.; Lieber, C. M. Growth of Nanowire Superlattice Structures for Nanoscale Photonics and Electronics. *Nature* **2002**, *415* (6872), 617–620.

(3) Barreto, J. A.; O'Malley, W.; Kubeil, M.; Graham, B.; Stephan, H.; Spiccia, L. Nanomaterials: Applications in Cancer Imaging and Therapy. *Adv. Mater.* **2011**, *23* (12), H18–H40.

(4) Saha, K.; Agasti, S. S.; Kim, C.; Li, X.; Rotello, V. M. Gold Nanoparticles in Chemical and Biological Sensing. *Chem. Rev.* **2012**, *112* (5), 2739–2779.

(5) Dykman, L.; Khlebtsov, N. Gold Nanoparticles in Biomedical Applications: Recent Advances and Perspectives. *Chem. Soc. Rev.* **2012**, *41* (6), 2256–2282.

(6) Qian, X.; Peng, X.-H.; Ansari, D. O.; Yin-Goen, Q.; Chen, G. Z.; Shin, D. M.; Yang, L.; Young, A. N.; Wang, M. D.; Nie, S. In Vivo Tumor Targeting and Spectroscopic Detection with Surface-Enhanced Raman Nanoparticle Tags. *Nat. Biotechnol.* **2008**, *26* (1), 83–90.

(7) Zhang, Q.; Iwakuma, N.; Sharma, P.; Moudgil, B. M.; Wu, C.; McNeill, J.; Jiang, H.; Grobmyer, S. R. Gold Nanoparticles as a Contrast Agent for *in Vivo* Tumor Imaging with Photoacoustic Tomography. *Nanotechnology* **2009**, *20* (39), 395102.

(8) Eustis, S.; El-Sayed, M. A. Why Gold Nanoparticles Are More Precious than Pretty Gold: Noble Metal Surface Plasmon Resonance and Its Enhancement of the Radiative and Nonradiative Properties of Nanocrystals of Different Shapes. *Chem. Soc. Rev*. **2006**, *35*, 209–217.

(9) Senapati, D.; Singh, A. K.; Ray, P. C. Real Time Monitoring of the Shape Evolution of Branched Gold Nanostructure. *Chem. Phys. Lett.* **2010**, *487* (1–3), 88–91.

(10) Murphy, C. J.; Gole, A. M.; Stone, J. W.; Sisco, P. N.; Alkilany, A. M.; Goldsmith, E. C.; Baxter, S. C. Gold Nanoparticles in Biology: Beyond Toxicity to Cellular Imaging. *Acc. Chem. Res.* **2008**, *41* (12), 1721–1730.

(11) Xia, Y.; Xiong, Y.; Lim, B.; Skrabalak, S. E. Shape-Controlled Synthesis of Metal Nanocrystals: Simple Chemistry Meets Complex Physics? *Angew. Chemie - Int. Ed.* **2009**, *48* (1), 60–103.

(12) Burrows, N. D.; Vartanian, A. M.; Abadeer, N. S.; Grzincic, E. M.; Jacob, L. M.; Lin, W.; Li, J.; Dennison, J. M.; Hinman, J. G.; Murphy, C. J. Anisotropic Nanoparticles and Anisotropic Surface Chemistry. *J. Phys. Chem. Lett.* **2016**, *7* (4), 632–641.

(13) Sajanlal, P. R.; Sreeprasad, T. S.; Samal, A. K.; Pradeep, T. Anisotropic Nanomaterials: Structure, Growth, Assembly, and Functions. *Nano Rev.* **2011**, *2*, 5883.

(14) Sun, Y.; Yin, Y.; Mayers, B. T.; Herricks, T.; Xia, Y. Uniform Silver Nanowires Synthesis by Reducing $AgNO_3$ with Ethylene Glycol in the Presence of Seeds and Poly(Vinyl Pyrrolidone).*Chem. Mater.* **2002**, *14*, 4736–4745.

(15) Ray, P. C.; Yu, H.; Fu, P. P. Toxicity and Environmental Risks of

Nanomaterials: Challenges and Future Needs. *J. Environ. Sci. Health. C. Environ. Carcinog. Ecotoxicol. Rev.* **2009**, *27* (1), 1–35.

(16) Klabunde, K. J. *Nanoscale Materials in Chemistry*,Wiley-Interscience: New York, 2001.

(17) Commission recommendation of 18 October 2011 *On the Definition of Nanomaterial (Text with EEA Relevance).*

(18) Koper, O.; Klabunde, K. J. Destructive Adsorption of Chlorinated Hydrocarbons on Ultrafine (Nanoscale) Particles of Calcium Oxide. 3. Chloroform, Trichloroethene, and Tetrachloroethene. *Chem. Mater.* **1997**, *9*, 2481–2485.

(19) De, S. K.; Mondal, S.; Sen, P.; Pal, U.; Pathak, B.; Rawat, K. S.; Bardhan, M.; Bhattacharya, M.; Satpati, B.; De, A.; Senapati, D. Crystal-Defect-Induced Facet-Dependent Electrocatalytic Activity of 3D Gold Nanoflowers for the Selective Nanomolar Detection of Ascorbic Acid. *Nanoscale* **2018**, *10* (23), 11091–11102.

(20) Bardhan, M.; Majumdar, A.; Jana, S.; Ghosh, T.; Pal, U.; Swarnakar, S.; Senapati, D. Mesoporous Silica for Drug Delivery: Interactions with Model Fluorescent Lipid Vesicles and Live Cells. *J. Photochem. Photobiol. B Biol.* **2018**, *178*, 19–26.

(21) Buffat, P.; Borel, J.-P. Size Effect on the Melting Temperature of Gold Particles. *Phys. Rev. A* **1976**, *13* (6), 2287–2298.

(22) Diehm, P. M.; Ágoston, P.; Albe, K. Size-Dependent Lattice Expansion in Nanoparticles: Reality or Anomaly? *ChemPhysChem* **2012**, *13* (10), 2443–2454.

(23) Mays, C. W.; Vermaak, J. S.; Kuhlmann-Wilsdorf, D. On Surface Stress and Surface Tension. *Surf. Sci.* **1968**, *12* (2), 134–140.

(24) Vermaak, J. S.; Mays, C. W.; Kuhlmann-Wilsdorf, D. On Surface Stress and Surface Tension. *Surf. Sci.* **1968**, *12* (2), 128–133.

(25) Qi, W. H.; Wang, M. P.; Su, Y. C. Size Effect on the Lattice Parameters of Nanoparticles. *J. Mater. Sci. Lett.* **2002**, *21* (11), 877–878.

(26) Qi, W. H.; Wang, M. P. Size and Shape Dependent Lattice Parameters of Metallic Nanoparticles. *J. Nanoparticle Res.* **2005**, *7* (1), 51–57.

(27) Daniel, M.-C.; Astruc, D. Gold Nanoparticles: Assembly, Supramolecular Chemistry, Quantum-Size-Related Properties, and Applications toward Biology, Catalysis, and Nanotechnology. *Chem. Rev.* **2004**,*104*, 293–346.

(28) Haruta, M.; Daté, M. Advances in the Catalysis of Au Nanoparticles. *Appl. Catal. A Gen.* **2001**, *222* (1–2), 427–437.

(29) Pingel, T.N; Jørgensen, M.; Yankovich, A. B.; Grönbeck, H.; Olsson, E. Influence of Atomic Site-Specific Strain on Catalytic Activity of Supported Nanoparticles. *Nat. Commun.* **2018**, *9* (1), 2722.

(30) Wu, J.; Li, P.; Pan, Y.-T. (Frank); Warren, S.; Yin, X.; Yang, H. Surface Lattice-Engineered Bimetallic Nanoparticles and Their Catalytic Properties. *Chem. Soc. Rev.* **2012**, *41* (24), 8066–8074.

(31) Kang, Y.; Snyder, J.; Chi, M.; Li, D.; More, K. L.; Markovic, N. M.; Stamenkovic, V. R. Multimetallic Core/Interlayer/Shell Nanostructures as Advanced Electrocatalysts. *Nano Lett.* **2014**, *14* (11), 6361–6367.

(32) Baddeley, C. J. Adsorbate Induced Segregation at Bimetallic Surfaces. *Chem. Phys. Solid Surfaces* **2002**, *10*, 495–526.

(33) Ross, M. B.; Mirkin, C. A.; Schatz, G. C. Optical Properties of One-, Two-, and

Three-Dimensional Arrays of Plasmonic Nanostructures. *J. Phys. Chem. C* **2016**, *120* (2), 816–830.

(34) Freestone, I.; Meeks, N.; Sax, M.; Higgitt, C. The Lycurgus Cup — A Roman Nanotechnology. *Gold Bull.* **2007**, *40* (4), 270–277.

(35) Sciau, P. Nanoparticles in Ancient Materials: The Metallic Lustre Decorations of Medieval Ceramics. *The Delivery of Nanoparticles*; InTech, 2012.

(36) Kelly, K. L.; Coronado, E.; Zhao, L. L.; Schatz, G. C. The Optical Properties of Metal Nanoparticles: The Influence of Size, Shape, and Dielectric Environment. *J. Phys. Chem. B* **2003**, *107* (3), 668–677.

(37) Kittel, C. *Introduction to Solid State Physics*; Wiley: New York, 1953.

(38) Cao, G.; Wang, Y. *Nanostructures and Nanomaterials : Synthesis, Properties, and Applications*; World Scientific, 2011.

(39) Suryanarayana, C. Structure and Properties of Nanocrystalline Materials. *Bull. Mater. Sci.* **1994**, *17*, 307-346.

(40) Hansen, N. Hall-Petch Relation and Boundary Strengthening. *Scr. Mater.* **2004**, *51*, 801–806.

(41) Yang, N.; Xu, X.; Zhang, G.; Li, B. Thermal Transport in Nanostructures. *AIP Adv.* **2012**, *2* (4), 041410.

(42) Likhachev, V. N.; Vinogradov, G. A.; Alymov, M. I. Anomalous Heat Capacity of Nanoparticles. *Phys. Lett. A* **2006**, *357* (3), 236–239.

(43) Cahill, D. G.; Ford, W. K.; Goodson, K. E.; Mahan, G. D.;Majumdar, A.; Maris, H. J.; Merlin, R.; Phillpot, S. R.Nanoscale Thermal Transport. *J. Appl. Phys.* **2003**, *93*, 793.

(44) Leslie-Pelecky, D. L.; Rieke, R. D. Magnetic Properties of Nanostructured Materials. *Chem. Mater.* **1996**, *8* (8), 1770–1783.

(45) Schubert, U. (Ulrich); Hüsing, N. *Synthesis of Inorganic Materials*; Wiley-VCH, 2012.

(46) Roduner, E. Size Matters: Why Nanomaterials Are Different. *Chem. Soc. Rev.* **2006**, *35*, 583-592.

(47) Jia, G.; Wang, H.; Yan, L.; Wang, X.; Pei, R.; Yan, T.; Zhao, Y.; Guo, X. Cytotoxicity of Carbon Nanomaterials:Single-Wall Nanotube, Multi-Wall Nanotube, and Fullerene. *Environ Sci Technol.* **2005**, *39* (5), 1378–1383.

(48) Derfus, A. M.; Chan, W. C. W.; Bhatia, S. N. Probing the Cytotoxicity of Semiconductor Quantum Dots. *Nano Lett.* **2004**, *4* (1),11–18.

(49) Asharani, P. V; Low, G.; Mun, K.; Hande, M. P.; Valiyaveettil, S. Cytotoxicity and Genotoxicity of Silver Nanoparticles in Human Cells. *ACS Nano* **2009**, *3* (2), 279–290.

(50) Deng, J.; Yao, M.; Gao, C. Cytotoxicity of Gold Nanoparticles with Different Structures and Surface-Anchored Chiral Polymers. *Acta Biomater.* **2017**, *53*, 610–618.

(51) Thanh, N. T. K.; Maclean, N.; Mahiddine, S. Mechanisms of Nucleation and Growth of Nanoparticles in Solution. *Chem Rev.* **2014**, *114* (15),7610–7630.

(52) Mandal, D.; Mondal, S.; Senapati, D.; Satpati, B.; Sangaranarayanan, M. V. Charge Density Modulated Shape-Dependent Electrocatalytic Activity of Gold Nanoparticles for the Oxidation of Ascorbic Acid. *J. Phys. Chem. C* **2015**, *119* (40), 23103–23112.

(53) Geddes, C. D.; Wiley InterScience (Online service). *Metal-Enhanced Fluorescence*; Wiley, 2010.

(54) da Silva, R. R.; Yang, M.; Choi, S.-I.; Chi, M.; Luo, M.; Zhang, C.; Li, Z.-Y.; Camargo, P. H. C.; Ribeiro, S. J. L.; Xia, Y. Facile Synthesis of Sub-20 Nm Silver Nanowires through a Bromide-Mediated Polyol Method. *ACS Nano* **2016**, *10* (8), 7892–7900.

(55) Liu, S.; Niu, W.; Firdoz, S.; Zhang, W. Iodide-Switched Deposition for the Synthesis of Segmented Pd–Au–Pd Nanorods: Crystal Facet Matters. *Langmuir* **2017**, *33* (43), 12254–12259.

(56) Grzelczak, M.; Pérez-Juste, J.; Mulvaney, P.; Liz-Marzán, L. M. Shape Control in Gold Nanoparticle Synthesis. *Chem. Soc. Rev.* **2008**, *37* (9), 1783–1791.

(57) Willets, K. A.; Van Duyne, R. P. Localized Surface Plasmon Resonance Spectroscopy and Sensing. *Annu. Rev. Phys. Chem.* **2007**, *58* (1), 267–297.

(58) Jain, P. K.; Huang, X.; El-Sayed, I. H.; El-Sayed, M. A. Review of Some Interesting Surface Plasmon Resonance-Enhanced Properties of Noble Metal Nanoparticles and Their Applications to Biosystems. *Plasmonics* **2007**, *2* (3), 107–118.

(59) Bardhan, M.; Satpati, B.; Ghosh, T.; Senapati, D. Synergistically Controlled Nano-Templated Growth of Tunable Gold Bud-to-Blossom Nanostructures: A Pragmatic Growth Mechanism. *J. Mater. Chem. C* **2014**, *2* (19), 3795–3804.

(60) Bhattacharya, M.; Mazov, V.; Satpati, B.; Jena, P.; Das Chakraborty, S.; Kumar, S.; Pathak, B.; Kuznetsov, D. V.; Senapati, D. Exploiting Le Chatelier's Principle for a One-Pot Synthesis of Nontoxic HHogGNPs with the Sharpest Nanoscopic Features Suitable for Tunable Plasmon Spectroscopy and High Throughput SERS Sensing. *Chem. Commun.* **2017**, *53* (75), 10402–10405.

(61) Arvizo, R. R.; Bhattacharyya, S.; Kudgus, R. A.; Giri, K.; Bhattacharya, R.; Mukherjee, P. Intrinsic Therapeutic Applications of Noble Metal Nanoparticles: Past, Present and Future. *Chem. Soc. Rev.* **2012**, *41* (7), 2943.

(62) Conde, J.; Doria, G.; Baptista, P. Noble Metal Nanoparticles Applications in Cancer. *J. Drug Deliv.* **2012**, *2012*, 751075.

(63) Thanh, N. T. K.; Green, L. A. W. Functionalisation of Nanoparticles for Biomedical Applications. *Nano Today* **2010**, *5* (3), 213–230.

(64) Mahouche-Chergui, S.; Guerrouache, M.; Carbonnier, B.; Chehimi, M. M. Polymer-Immobilized Nanoparticles. *Colloids Surfaces A Physicochem. Eng. Asp.* **2013**, *439*, 43–68.

(65) Jain, P. K.; Huang, X.; El-Sayed, I. H.; El-Sayed, M. A. Noble Metals on the Nanoscale: Optical and Photothermal Properties and Some Applications in Imaging, Sensing, Biology, and Medicine. *Acc. Chem. Res.* **2008**, *41* (12), 1578–1586.

(66) Rai, M.; Ingle, A. P.; Gupta, I.; Brandelli, A. Bioactivity of Noble Metal Nanoparticles Decorated with Biopolymers and Their Application in Drug Delivery. *Int. J. Pharm.* **2015**, *496* (2), 159–172.

(67) Liao, H.; Hafner, J. H. Gold Nanorod Bioconjugates. *Chem. Mater.* **2005**, *17*(18), 4636–4641.

(68) Paramasivam, G.; Kayambu, N.; Rabel, A. M.; Sundramoorthy, A. K.; Sundaramurthy, A. Anisotropic Noble Metal Nanoparticles: Synthesis, Surface Functionalization and Applications in Biosensing, Bioimaging, Drug Delivery and Theranostics. *Acta Biomater.* **2017**, *49*, 45–65.

(69) Murphy, C. J.; Sau, T. K.; Gole, A. M.; Orendorff, C. J.; Gao, J.; Gou, L.; Hunyadi, S. E.; Li, T. Anisotropic Metal Nanoparticles: Synthesis, Assembly,

and Optical Applications. *J. Phys. Chem. B* **2005**, *109* (29), 13857–13870.

(70) Huo, Z.; Tsung, C.; Huang, W.; Zhang, X.; Yang, P. Sub-Two Nanometer Single Crystal Au Nanowires. *Nano Lett.* **2008**, *8* (7), 2041–2044.

(71) Gao, C.; Zhang, Q.; Lu, Z.; Yin, Y. Templated Synthesis of Metal Nanorods in Silica Nanotubes. *J. Am. Chem. Soc.* **2011**, *133* (49), 19706–19709.

(72) Neugebauer, J. M. Detergents: An Overview. *Methods Enzymol.* **1990**, *182,* 239–253.

(73) Harris, E. L. V.; Angal, S. *Protein Purification Applications : A Practical Approach*; IRL Press at Oxford University Press, 1990.

(74) Phan, C. M.; Nguyen, H. M. Role of Capping Agent in Wet Synthesis of Nanoparticles. *J. Phys. Chem. A* **2017**, *121* (17), 3213–3219.

(75) Gao, J.; Bender, C. M.; Murphy, C. J. Dependence of the Gold Nanorod Aspect Ratio on the Nature of the Directing Surfactant in Aqueous Solution. *Langmuir*, **2003**, *19* (21), 9065–9070.

(76) Smith, D. K.; Miller, N. R.; Korgel, B. A. Iodide in CTAB Prevents Gold Nanorod Formation. *Langmuir* **2009**, *25* (16), 9518–9524.

(77) Millstone, J. E.; Wei, W.; Jones, M. R.; Yoo, H.; Mirkin, C. A. Iodide Ions Control Seed-Mediated Growth of Anisotropic Gold Nanoparticles. *Nano Lett.* **2008**, *8* (8), 2526–2529.

(78) Suzuki, K.; Ikari, K.; Imai, H.; Synthesis of Silica Nanoparticles Having a Well-Ordered Mesostructure Using a Double Surfactant System. *J. Am. Chem. Soc.* **2004**, *126*(2), 462-463.

(79) Sinha, T.; Ahmaruzzaman, M. High-Value Utilization of Egg Shell to Synthesize Silver and Gold–Silver Core Shell Nanoparticles and Their Application for the Degradation of Hazardous Dyes from Aqueous Phase-A Green Approach. *J. Colloid Interface Sci.* **2015**, *453*, 115–131.

(80) Liang, M.; Su, R.; Qi, W.; Yu, Y.; Wang, L.; He, Z. Synthesis of Well-Dispersed Ag Nanoparticles on Eggshell Membrane for Catalytic Reduction of 4-Nitrophenol. *J. Mater. Sci.* **2014**, *49* (4), 1639–1647.

(81) Flint, E. B.; Suslick, K. S. The Temperature of Cavitation.*Science* **1991**, *253* (5026), 1397-1399.

(82) Bang, J. H.; Suslick, K. S. Applications of Ultrasound to the Synthesis of Nanostructured Materials. *Adv. Mater.* **2010**, *22* (10), 1039–1059.

(83) Xu, H.; Zeiger, B. W.; Suslick, K. S. Sonochemical Synthesis of Nanomaterials. *Chem. Soc. Rev.* **2013**, *42* (7), 2555–2567.

(84) Gersten, B. Solvothermal Synthesis of Nanoparticles. *Chemfiles* **2005**, *5*, 11-12.

(85) solvothermal method - an overview. ScienceDirect Topics https://www.sciencedirect.com/topics/chemistry/solvothermal-method.

(86) Yu, Y.-Y.; Chang, S.-S.; Lee, C.-L. Wang, C. R. C. Gold Nanorods: Electrochemical Synthesis and Optical Properties. *J. Phys. Chem. B,* **1997**, *101* (34), 6661–6664.

(87) Rodríguez-Sánchez, L.; Blanco, M. C.; López-Quintela, M. A. Electrochemical Synthesis of Silver Nanoparticles. *J. Phys. Chem. B* **2000**, *104*, 9683-9688.

(88) Pietrobon, B.; Kitaev, V. Photochemical Synthesis of Monodisperse Size-Controlled Silver Decahedral Nanoparticles and Their Remarkable Optical Properties.*Chem. Mater.*, **2008**, *20* (16), 5186–5190.

(89) Kim, F.; Song, J. H.; Yang, P. Photochemical Synthesis of Gold Nanorods.*J. Am. Chem. Soc.*, **2002**, *124* (48), 14316–14317.

(90) Jin, R.; Cao, Y. C.; Hao, E.; Métraux, G. S.; Schatz, G. C.; Mirkin, C. A. Controlling Anisotropic Nanoparticle Growth through Plasmon Excitation. *Nature* **2003**, *425* (6957), 487–490.

(91) Abendroth, J. M. *The Photo-Mediated Synthesis of Silver Nanoprisms and Tuning of Their Plasmonic Properties*. University of Florida: Gainesville 2011.

(92) Xia, X.; Wang, Y.; Ruditskiy, A.; Xia, Y. 25th Anniversary Article: Galvanic Replacement: A Simple and Versatile Route to Hollow Nanostructures with Tunable and Well-Controlled Properties. *Adv. Mater.* **2013**, *25* (44), 6313–6333.

(93) https://en.wikipedia.org/wiki/Standard_electrode_potential_(data_page).

(94) Howes, P. D.; Chandrawati, R.; Stevens, M. M. Colloidal Nanoparticles as Advanced Biological Sensors.*Science*, **2014**, *346* (6205), 1247390.

(95) Jain, P. K.; El-Sayed, M. A. Surface Plasmon Resonance Sensitivity of Metal Nanostructures: Physical Basis and Universal Scaling in Metal Nanoshells.*J. Phys. Chem. C*, **2007**, *111* (47), 17451–17454.

(96) Taylor, A. B.; Zijlstra, P. Single-Molecule Plasmon Sensing: Current Status and Future Prospects. *ACS Sensors* **2017**, *2* (8), 1103–1122.

(97) Rodríguez-Lorenzo, L.; Álvarez-Puebla, R. A.; Pastoriza-Santos, I.; Mazzucco, S.; Stéphan, O.; Kociak, M.; Liz-Marzán, L. M.; García de Abajo, F. J. Zeptomol Detection Through Controlled Ultrasensitive Surface-Enhanced Raman Scattering. *J. Am. Chem. Soc.* **2009**, *131* (13), 4616–4618.

(98) Jain, P. K.; Huang, X.; El-Sayed, I. H.; El-Sayed, M. A. Noble Metals on the Nanoscale: Optical and Photothermal Properties and Some Applications in Imaging, Sensing, Biology, and Medicine. *Acc. Chem. Res.* **2008**, *41* (12), 1578–1586.

(99) Camden, J. P.; Dieringer, J. A.; Zhao, J.; Van Duyne, R. P. Controlled Plasmonic Nanostructures for Surface-Enhanced Spectroscopy and Sensing. *Acc. Chem. Res.* **2008**, *41* (12), 1653–1661.

(100) Rosi, N. L.; Mirkin, C. A. Nanostructures in Biodiagnostics. *Chem Rev.***2005**, *105*(4),1547–1562.

(101) Kim, Y.; Johnson, R. C.; Hupp, J. T. Gold Nanoparticle-Based Sensing of “Spectroscopically Silent” Heavy Metal Ions.*Nano Lett.*, **2001**, *1* (4), 165–167.

(102) Lee, S. J.; Lee, J.-E.; Seo, J.; Jeong, I. Y.; Lee, S. S.; Jung, J. H. Optical Sensor Based on Nanomaterial for the Selective Detection of Toxic Metal Ions. *Adv. Funct. Mater.* **2007**, *17* (17), 3441–3446.

(103) Luo, X.; Morrin, A.; Killard, A. J.; Smyth, M. R. Application of Nanoparticles in Electrochemical Sensors and Biosensors. *Electroanalysis* **2006**, *18* (4), 319–326.

(104) Marín, S.; Merkoçi, A. Nanomaterials Based Electrochemical Sensing Applications for Safety and Security. *Electroanalysis* **2012**, *24* (3), 459–469.

(105) Mieszawska, A. J.; Mulder, W. J. M.; Fayad, Z. A.; Cormode, D. P. Multifunctional Gold Nanoparticles for Diagnosis and Therapy of Disease. *Mol. Pharm.* **2013**, *10* (3), 831–847.

(106) Dykman, L. A.; Khlebtsov, N. G. Gold Nanoparticles in Biology and Medicine: Recent Advances and Prospects. *Acta Naturae.* **2011**, *3*(2), 34–55.

(107) Boisselier, E.; Astruc, D. Gold Nanoparticles in Nanomedicine: Preparations, Imaging, Diagnostics, Therapies and Toxicity. *Chem. Soc. Rev.* **2009**, *38* (6), 1759–1782.

(108) Zauner, W.; Farrow, N. A.; Haines, A. M. In Vitro Uptake of Polystyrene

Microspheres: Effect of Particle Size, Cell Line and Cell Density. *J. Control. Release* **2001**, *71* (1), 39–51.

(109) Weissleder, R. A Clearer Vision for in Vivo Imaging. *Nat. Biotechnol.* **2001**, *19* (4), 316–317.

(110) Jain, P. K.; Lee, K. S.; El-Sayed, I. H.; El-Sayed, M. A. Calculated Absorption and Scattering Properties of Gold Nanoparticles of Different Size, Shape, and Composition: Applications in Biological Imaging and Biomedicine.*J. Phys. Chem. B.* **2006**, *110*(14), 7238–7248.

(111) Wang, Y.; Xie, X.; Wang, X.; Ku, G; Gill, K. L.; O'Neal, D. P.; Stoica, G.; Wang, L. V. Photoacoustic Tomography of a Nanoshell Contrast Agent in the in Vivo Rat Brain.*Nano Lett.*, **2004**, *4* (9), 1689–1692.

(112) Chen, J.; Saeki, F.; Wiley, B. J.; Cang, H.; Cobb, M. J.; Li, Z.-Y.; Au, L.; Zhang, H.; Kimmey, M. B.; Xia, Y. Gold Nanocages: Bioconjugation and Their Potential Use as Optical Imaging Contrast Agents. *Nano Lett.* **2005**, *5* (3), 473–477.

(113) Kim, C. K.; Kalluru, R. R.; Singh, J. P.; Fortner, A.; Griffin, J.; Darbha, G. K.; Ray, P. C. Gold-Nanoparticle-Based Miniaturized Laser-Induced Fluorescence Probe for Specific DNA Hybridization Detection: Studies on Size-Dependent Optical Properties. *Nanotechnology* **2006**, *17* (13), 3085–3093.

(114) Baptista, P.; Pereira, E.; Eaton, P.; Doria, G.; Miranda, A.; Gomes, I.; Quaresma, P.; Franco, R. Gold Nanoparticles for the Development of Clinical Diagnosis Methods. *Anal. Bioanal. Chem.* **2008**, *391* (3), 943–950.

(115) Tanaka, R.; Yuhi, T.; Nagatani, N.; Endo, T.; Kerman, K.; Takamura, Y.; Tamiya, E. A Novel Enhancement Assay for Immunochromatographic Test Strips Using Gold Nanoparticles. *Anal. Bioanal. Chem.* **2006**, *385* (8), 1414–1420.

(116) Lai, N.-S.; Wang, C.-C.; Chiang, H.-L.; Chau, L.-K. Detection of Antinuclear Antibodies by a Colloidal Gold Modified Optical Fiber: Comparison with ELISA. *Anal. Bioanal. Chem.* **2007**, *388* (4), 901–907.

(117) Hsieh, B.-Y.; Chang, Y.-F.; Ng, M.-Y.; Liu, W.-C.; Lin, C.-H.; Wu, H.-T.; Chou, C. Localized Surface Plasmon Coupled Fluorescence Fiber-Optic Biosensor with Gold Nanoparticles. *Anal. Chem.*, **2007**,*79* (9), 3487–3493.

(118) Kim, J.-Y.; Lee, J.-S. Synthesis and Thermodynamically Controlled Anisotropic Assembly of DNA−Silver Nanoprism Conjugates for Diagnostic Applications. *Chem. Mater.* **2010**, *22* (24), 6684–6691.

(119) Pietro, P. Di; Strano, G.; Zuccarello, L.; Satriano, C. Gold and Silver Nanoparticles for Applications in Theranostics. *Curr. Top. Med. Chem.* **2016**, *16* (27), 3069–3102.

(120) Larguinho, M.; Baptista, P. V. Gold and Silver Nanoparticles for Clinical Diagnostics — From Genomics to Proteomics. *J. Proteomics* **2012**, *75* (10), 2811–2823.

(121) Zharov, V. P.; Mercer, K. E.; Galitovskaya, E. N.; Smeltzer, M. S. Photothermal Nanotherapeutics and Nanodiagnostics for Selective Killing of Bacteria Targeted with Gold Nanoparticles. *Biophys. J.* **2006**, *90* (2), 619–627.

(122) Kennedy, L. C.; Bickford, L. R.; Lewinski, N. A.; Coughlin, A. J.; Hu, Y.; Day, E. S.; West, J. L.; Drezek, R. A. A New Era for Cancer Treatment: Gold-Nanoparticle-Mediated Thermal Therapies. *Small* **2011**, *7* (2), 169–183.

(123) Elsayed, I.; Huang, X.; Elsayed, M. Selective Laser Photo-Thermal Therapy of

Epithelial Carcinoma Using Anti-EGFR Antibody Conjugated Gold Nanoparticles. *Cancer Lett.* **2006**, *239* (1), 129–135.

(124) Huang, X.; Jain, P. K.; El-Sayed, I. H.; El-Sayed, M. A. Determination of the Minimum Temperature Required for Selective Photothermal Destruction of Cancer Cells with the Use of Immunotargeted Gold Nanoparticles. *Photochem. Photobiol.* **2006**, *82* (2), 412–417.

(125) Huang, X.; El-Sayed, I. H.; Qian, W.; El-Sayed, M. A. Cancer Cell Imaging and Photothermal Therapy in the Near-Infrared Region by Using Gold Nanorods.*J. Am. Chem. Soc.*, **2006**, *128* (6), 2115–2120.

(126) Hu, M.; Chen, J.; Li, Z.-Y.; Au, L.; Hartland, G. V.; Li, X.; Marquez, M.; Xia, Y. Gold Nanostructures: Engineering Their Plasmonic Properties for Biomedical Applications. *Chem. Soc. Rev.* **2006**, *35* (11), 1084–1094.

(127) Khan, S. A.; Kanchanapally, R.; Fan, Z.; Beqa, L.; Singh, K.; Senapati, D.; Ray, P. C. A Gold Nanocage–CNT Hybrid for Targeted Imaging and Photothermal Destruction of Cancer Cells. *Chem. Commun* **2012**, *48*, 6711–6713.

(128) Hirsch, L. R.; Stafford, R. J.; Bankson, J. A.; Sershen, S. R.; Rivera, B.; Price, R. E.; Hazle, J. D.; Halas, N. J.; West, J. L. Nanoshell-Mediated near-Infrared Thermal Therapy of Tumors under Magnetic Resonance Guidance. *Proc. Natl. Acad. Sci.* **2003**, *100* (23), 13549–13554.

(129) Loo, C.; Lowery, A.; Halas, N.; West, J.; Drezek, R. Immunotargeted Nanoshells for Integrated Cancer Imaging and Therapy. *Nano Lett.* **2005**, *5* (4), 709–711.

(130) Lu, W.; Singh, A. K.; Khan, S. A.; Senapati, D.; Yu, H.; Ray, P. C. Gold Nano-Popcorn-Based Targeted Diagnosis, Nanotherapy Treatment, and In Situ Monitoring of Photothermal Therapy Response of Prostate Cancer Cells Using Surface-Enhanced Raman Spectroscopy. *J. Am. Chem. Soc.* **2010**, *132* (51), 18103–18114.

(131) Zharov, V. P.; Galitovskaya, E. N.; Johnson, C.; Kelly, T. Synergistic Enhancement of Selective Nanophotothermolysis with Gold Nanoclusters: Potential for Cancer Therapy. *Lasers Surg. Med.* **2005**, *37* (3), 219–226.

(132) Huang, X.; Qian, W.; El-Sayed, I. H.; El-Sayed, M. A. The Potential Use of the Enhanced Nonlinear Properties of Gold Nanospheres in Photothermal Cancer Therapy. *Lasers Surg. Med.* **2007**, *39* (9), 747–753.

(133) Mohammed, O. F.; Samartzis, P. C.; Zewail, A. H. Heating and Cooling Dynamics of Carbon Nanotubes Observed by Temperature-Jump Spectroscopy and Electron Microscopy. *J. Am. Chem. Soc.* **2009**, *131* (44), 16010–16011.

(134) Chen, Q.; Qi, H.; Ruan, L.; Ren, Y. Experimental Comparison of Photothermal Conversion Efficiency of Gold Nanotriangle and Nanorod in Laser Induced Thermal Therapy. *Nanomaterials* **2017**, *7* (12), 416.

(135) Celli, J. P.; Spring, B. Q.; Rizvi, I.; Evans, C. L.; Samkoe, K. S.; Verma, S.; Pogue, B. W.; Hasan, T. Imaging and Photodynamic Therapy: Mechanisms, Monitoring, and Optimization. *Chem. Rev.* **2010**, *110* (5), 2795–2838.

(136) Chen, H.; Di, Y.; Chen, D.; Madrid, K.; Zhang, M.; Tian, C.; Tang, L.; Gu, Y. Combined Chemo- and Photo-Thermal Therapy Delivered by Multifunctional Theranostic Gold Nanorod-Loaded Microcapsules. *Nanoscale* **2015**, *7* (19), 8884–8897.

(137) Huang, X.; El-Sayed, M. A. Plasmonic Photo-Thermal Therapy (PPTT). *Alexandria J. Med.* **2011**, *47* (1), 1–9.

(138) Courty, A.; Mermet, A.; Albouy, P. A.; Duval, E.; Pileni, M. P. Vibrational Coherence of Self-Organized Silver Nanocrystals in f.c.c. Supra-Crystals. *Nat. Mater.* **2005**, *4* (5), 395–398.

(139) Urban, J. J.; Talapin, D. V.; Shevchenko, E. V.; Kagan, C. R.; Murray, C. B. Synergism in Binary Nanocrystal Superlattices Leads to Enhanced P-Type Conductivity in Self-Assembled PbTe/Ag2Te Thin Films. *Nat. Mater.* **2007**, *6* (2), 115–121.

(140) Cargnello, M.; Johnston-Peck, A. C.; Diroll, B. T.; Wong, E.; Datta, B.; Damodhar, D.; Doan-Nguyen, V. V. T.; Herzing, A. A.; Kagan, C. R.; Murray, C. B. Substitutional Doping in Nanocrystal Superlattices. *Nature* **2015**, *524* (7566), 450–453.

(141) Cheng, W.; Campolongo, M. J.; Cha, J. J.; Tan, S. J.; Umbach, C. C.; Muller, D. A.; Luo, D. Free-Standing Nanoparticle Superlattice Sheets Controlled by DNA. *Nat. Mater.* **2009**, *8* (6), 519–525.

(142) Mueggenburg, K. E.; Lin, X.-M.; Goldsmith, R. H.; Jaeger, H. M. Elastic Membranes of Close-Packed Nanoparticle Arrays. *Nat. Mater.***2007**, *6* (9), 656–660.

(143) Ng, K. C.; Udagedara, I. B.; Rukhlenko, I. D.; Chen, Y.; Tang, Y.; Premaratne, M.; Cheng, W. Free-Standing Plasmonic-Nanorod Superlattice Sheets. *ACS Nano* **2012**, *6* (1), 925–934.

(144) Si, K. J.; Sikdar, D.; Chen, Y.; Eftekhari, F.; Xu, Z.; Tang, Y.; Xiong, W.; Guo, P.; Zhang, S.; Lu, Y.; *et al.* Giant Plasmene Nanosheets, Nanoribbons, and Origami. *ACS Nano* **2014**, *8* (11), 11086–11093.

(145) Black, C. T.; Murray, C. B.; Sandstrom, R. L.; Sun, S. Spin-Dependent Tunneling in Self-Assembled Cobalt-Nanocrystal Superlattices. *Science* **2000**, *290* (5494), 1131–1134.

(146) Collier, C. P.; Saykally, R. J.; Shiang, J. J.; Henrichs, S. E.; Heath, J. R. Reversible Tuning of Silver Quantum Dot Monolayers Through the Metal-Insulator Transition. *Science* **1997**, *277* (5334), 1978–1981.

(147) Auyeung, E.; Cutler, J. I.; Macfarlane, R. J.; Jones, M. R.; Wu, J.; Liu, G.; Zhang, K.; Osberg, K. D.; Mirkin, C. A. Synthetically Programmable Nanoparticle Superlattices Using a Hollow Three-Dimensional Spacer Approach. *Nat. Nanotechnol.* **2012**, *7* (1), 24–28.

(148) Zeng, C.; Chen, Y.; Kirschbaum, K.; Lambright, K. J.; Jin, R. Emergence of Hierarchical Structural Complexities in Nanoparticles and Their Assembly. *Science* **2016**, *354* (6319), 1580–1584.

(149) Shevchenko, E. V.; Talapin, D. V.; Kotov, N. A.; O'Brien, S.; Murray, C. B. Structural Diversity in Binary Nanoparticle Superlattices. *Nature* **2006**, *439* (7072), 55–59.

(150) Nanoparticle Superlattices: Properties and Applications https://www.azonano.com/article.aspx?ArticleID=3217.

(151) Banwell, C. N.; McCash, E. M.; others. *Fundamentals of Molecular Spectroscopy*; McGraw-Hill New York, 1994; Vol. 851.

(152) Pasquini, C. Near Infrared Spectroscopy: Fundamentals, Practical Aspects and Analytical Applications. *J. Braz. Chem. Soc.* **2003**, *14* (2), 198–219.

(153) Försterling, H.-D. JE Crooks: The Spectrum in Chemistry. Academic Press, London, New York, San Francisco 1978. 313 Seiten, *Berichte der Bunsengesellschaft für Phys. Chemie* **1979**, *83* (3), 287.

(154) Joy, D. C.; Pawley, J. B. High-Resolution Scanning Electron Microscopy. *Ultramicroscopy* **1992**, *47* (1–3), 80–100.

(155) Heydenreich, J. PJ Goodhew. Electron Microscopy and Analysis.(The Wykeham Science Series, Herausgegeben von Sir N. Mott Und GR Noakes) 191 Seiten, 118 Abbildungen, Preis£2, 50 Wykeham Publications Ltd., London/Winchester 1975. *Krist. und Tech.* **1976**, *11* (1), K13–K14.

(156) Williams, D. B.; Carter, C. B. Scattering and Diffraction. In *Transmission Electron Microscopy*; Springer, 2009; 23–38.

(157) Bozzola, J. J.; Russell, L. D. *Electron Microscopy: Principles and Techniques for Biologists*; Jones & Bartlett Learning, 1999.

(158) Fleischmann, M.; Hendra, P. J.; McQuillan, A. J. Raman Spectra of Pyridine Adsorbed at a Silver Electrode. *Chem. Phys. Lett.* **1974**, *26* (2), 163–166.

(159) Jeanmaire, D. L.; Van Duyne, R. P. Surface Raman Spectroelectrochemistry: Part I. Heterocyclic, Aromatic, and Aliphatic Amines Adsorbed on the Anodized Silver Electrode. *J. Electroanal. Chem. interfacial Electrochem.* **1977**, *84* (1), 1–20.

(160) Albrecht, M. G.; Creighton, J. A. Anomalously Intense Raman Spectra of Pyridine at a Silver Electrode. *J. Am. Chem. Soc.* **1977**, *99* (15), 5215–5217.

(161) Fleischman, M.; Hendra, P. J.; McQuillan, A. J. Surface-Enhanced Raman Scattering from Silver Particles on Polymer-Replica Substrates. *Chem. Phys. Lett.* **1974**, *26*, 123.

(162) Otto, A. Surface-Enhanced Raman Scattering:"Classical" and "Chemical" Origins. In *Light scattering in solids IV*; Springer, 1984; pp 289–418.

(163) Moskovits, M. Surface-Enhanced Spectroscopy. *Rev. Mod. Phys.* **1985**, *57* (3), 783–826.

(164) Moskovits, M. Surface-Enhanced Raman Spectroscopy: A Brief Retrospective. *J. Raman Spectrosc. An Int. J. Orig. Work all Asp. Raman Spectrosc. Incl. High. Order Process. also Brillouin Rayleigh Scatt.* **2005**, *36* (6–7), 485–496.

(165) Xu, H.; Käll, M. Polarization-Dependent Surface-Enhanced Raman Spectroscopy of Isolated Silver Nanoaggregates. *ChemPhysChem* **2003**, *4* (9), 1001–1005.

(166) Xu, H.; Aizpurua, J.; Käll, M.; Apell, P. Electromagnetic Contributions to Single-Molecule Sensitivity in Surface-Enhanced Raman Scattering. *Phys. Rev. E* **2000**, *62* (3), 4318.

(167) Campion, A.; Kambhampati, P. Surface-Enhanced Raman Scattering. *Chem. Soc. Rev.* **1998**, *27* (4), 241–250.

(168) Aravind, P. K.; Nitzan, A.; Metiu, H. The Interaction between Electromagnetic Resonances and Its Role in Spectroscopic Studies of Molecules Adsorbed on Colloidal Particles or Metal Spheres. *Surf. Sci.* **1981**, *110* (1), 189–204.

(169) Johnson, P. B.; Christy, R.-W. Optical Constants of the Noble Metals. *Phys. Rev. B* **1972**, *6* (12), 4370.

(170) Tanabe, K. Field Enhancement around Metal Nanoparticles and Nanoshells: A Systematic Investigation. *J. Phys. Chem. C* **2008**, *112* (40), 15721–15728.

(171) Jiang, J.; Bosnick, K.; Maillard, M.; Brus, L. Single Molecule Raman Spectroscopy at the Junctions of Large Ag Nanocrystals. *J. Phys. Chem. B* **2003**, *107* (37), 9964–9972.

(172) Nakai, H.; Nakatsuji, H. Electronic Mechanism of the Surface Enhanced Raman Scattering. *J. Chem. Phys.* **1995**, *103* (6), 2286–2294.

(173) Berne, B. J.; Pecora, R. Dynamic Light Scattering: With Applications to Chemistry, Biology, and Physics. 2000. *Mineola, NY Dover Publ.376*.

(174) Delgado, A. V; González-Caballero, F.; Hunter, R. J.; Koopal, L. K.; Lyklema, J. Measurement and Interpretation of Electrokinetic Phenomena (IUPAC Technical Report). *Pure Appl. Chem.* **2005**, *77* (10), 1753–1805.

(175) Clogston, J. D.; Patri, A. K. Zeta Potential Measurement. In *Characterization of nanoparticles intended for drug delivery*; Springer, *Methods Mol Biol.* **2011**, *697*, 63–70.

(176) Sze, A.; Erickson, D.; Ren, L.; Li, D. Zeta-Potential Measurement Using the Smoluchowski Equation and the Slope of the Current–Time Relationship in Electroosmotic Flow. *J. Colloid Interface Sci.* **2003**, *261* (2), 402–410.

(177) Müller-Buschbaum, P. A Basic Introduction to Grazing Incidence Small-Angle X-Ray Scattering. In *Applications of Synchrotron Light to Scattering and Diffraction in Materials and Life Sciences*; Springer, 2009; pp 61–89.

(178) Müller-Buschbaum, P. Structure Determination in Thin Film Geometry Using Grazing Incidence Small-Angle Scattering. In *Polymer Surfaces and Interfaces*; Springer, 2008; pp 17–46.

(179) Murphy, C. J.; Jana, N. R. Controlling the Aspect Ratio of Inorganic Nanorods and Nanowires. **2002**, *14*, 80–82.

(180) Xia, Y.; Yang, P.; Sun, Y.; Wu, Y.; Mayers, B.; Gates, B.; Yin, Y.; Kim, F.; Yan, H. One-Dimensional Nanostructures: Synthesis, Characterization, and Applications. *Adv. Mater.* **2003**, *15* (5), 353–389.

(181) Barnes, W. L.; Dereux, A.; Ebbesen, T. W. Surface Plasmon Subwavelength Optics. *Nature* **2003**, *424* (6950), 824–830.

(182) Anker, J. N.; Hall, W. P.; Lyandres, O.; Shah, N. C.; Zhao, J.; Van Duyne, R. P. Biosensing with Plasmonic Nanosensors. *Nat. Mater.* **2008**, *7* (6), 442–453.

(183) Beck, F. J.; Stavrinadis, A.; Diedenhofen, S. L.; Lasanta, T.; Konstantatos, G. Surface Plasmon Polariton Couplers for Light Trapping in Thin-Film Absorbers and Their Application to Colloidal Quantum Dot Optoelectronics. *ACS Photonics* **2014**, *1* (11), 1197–1205.

(184) Kalluri, J. R.; Arbneshi, T.; Afrin Khan, S.; Neely, A.; Varisli, B.; Washington, M.; McAfee, S.; Robinson, B.; Banerjee, S.; Singh, A. K.; *et al.* Use of Gold Nanoparticles in a Simple Colorimetric and Ultrasensitive Dynamic Light Scattering Assay: Selective Detection of Arsenic in Groundwater. *Angew. Chem.* **2009**, *121* (51), 9848–9851.

(185) Wang, Q.-Q.; Han, J.-B.; Gong, H.-M.; Chen, D.-J.; Zhao, X.-J.; Feng, J.-Y.; Ren, J.-J. Linear and Nonlinear Optical Properties of Ag Nanowire Polarizing Glass. *Adv. Funct. Mater.* **2006**, *16* (18), 2405–2408.

(186) Xiong, X.; Zou, C.-L.; Ren, X.-F.; Liu, A.-P.; Ye, Y.-X.; Sun, F.-W.; Guo, G.-C. Silver Nanowires for Photonics Applications. *Laser Photon. Rev.* **2013**, *7* (6), 901–919.

(187) Rath, A. K.; Pelayo Garcia de Arquer, F.; Stavrinadis, A.; Lasanta, T.; Bernechea, M.; Diedenhofen, S. L.; Konstantatos, G. Remote Trap Passivation in Colloidal Quantum Dot Bulk Nano-Heterojunctions and Its Effect in Solution-Processed Solar Cells. *Adv. Mater.* **2014**, *26* (27), 4741–4747.

(188) Beck, F. J.; Lasanta, T.; Konstantatos, G. Plasmonic Schottky Nanojunctions for Tailoring the Photogeneration Profile in Thin Film Solar Cells. *Adv. Opt. Mater.* **2014**, *2* (5), 493–500.

(189) Mihi, A.; Beck, F. J.; Lasanta, T.; Rath, A. K.; Konstantatos, G. Imprinted Electrodes for Enhanced Light Trapping in Solution Processed Solar Cells. *Adv. Mater.* **2014**, *26* (3), 443–448.

(190) Huang, Y.; Duan, X.; Wei, Q.; Lieber, C. M. Directed Assembly of One-Dimensional Nanostructures into Functional Networks. *Science* **2001**, *291* (5504), 630–633.

(191) Kovtyukhova, N. I.; Mallouk, T. E. Nanowires as Building Blocks for Self-Assembling Logic and Memory Circuits. *Chemistry* **2002**, *8* (19), 4354–4363.

(192) Melosh, N. A.; Boukai, A.; Diana, F.; Gerardot, B.; Badolato, A.; Petroff, P. M.; Heath, J. R. Ultrahigh-Density Nanowire Lattices and Circuits. *Science* **2003**, *300* (5616), 112–115.

(193) Tao, A.; Kim, F.; Hess, C.; Goldberger, J.; He, R.; Sun, Y.; Xia, Y.; Yang, P. Langmuir−Blodgett Silver Nanowire Monolayers for Molecular Sensing Using Surface-Enhanced Raman Spectroscopy.*Nano Lett.* **2003**, *3* (9), 1229–1233.

(194) Zhang, B.; Wang, H.; Lu, L.; Ai, K.; Zhang, G.; Cheng, X. Large-Area Silver-Coated Silicon Nanowire Arrays for Molecular Sensing Using Surface-Enhanced Raman Spectroscopy. *Adv. Funct. Mater.* **2008**, *18* (16), 2348–2355.

(195) Bi, Y.; Hu, H.; Lu, G. Highly Ordered Rectangular Silvernanowire Monolayers: Water-Assisted Synthesis and Galvanic Replacement Reaction with HAuCl4. *Chem. Commun.* **2010**, *46* (4), 598–600.

(196) Sun, Y.; Xia, Y. Mechanistic Study on the Replacement Reaction between Silver Nanostructures and Chloroauric Acid in Aqueous Medium.*J. Am. Chem. Soc.* **2004**, *126*(12), 3892-3901.

(197) Sun, Y.; Gates, B.; Mayers, B.; Xia, Y. Crystalline Silver Nanowires by Soft Solution Processing. *Nano Lett.* **2002**, *2*, 165–168.

(198) Wiley, B.; Sun, Y.; Xia, Y. Synthesis of Silver Nanostructures with Controlled Shapes and Properties. *Acc. Chem. Res.* **2007**, *40* (10), 1067–1076.

(199) Liu, S.; Yue, J.; Gedanken, A. Synthesis of Long Silver Nanowires from AgBr Nanocrystals. *Adv. Mater.* **2001**, *13* (9), 656–658.

(200) Zhou, Y.; Yu, S. H.; Cui, X. P.; Wang, C. Y.; Chen, Z. Y. Formation of Silver Nanowires by a Novel Solid−Liquid Phase Arc Discharge Method.*Chem. Mater.*, **1999**, *11* (3), 545–546.

(201) Zhou, Y.; Yu, S. H.; Wang, C. Y.; Li, X. G.; Zhu, Y. R.; Chen, Z. Y. A Novel Ultraviolet Irradiation Photoreduction Technique for the Preparation of Single-Crystal Ag Nanorods and Ag Dendrites. *Adv. Mater.* **1999**, *11* (10), 850–852.

(202) Yang, X.; He, W.; Wang, S.; Zhou, G.; Tang, Y. Synthesis and Characterization of Ag Nanorods Used for Formulating High-Performance Conducting Silver Ink. *J. Exp. Nanosci.* **2014**, *9* (6), 541–550.

(203) Martin, C. R. Nanomaterials: A Membrane-Based Synthetic Approach. *Science* **1994**, *266* (5193), 1961–1966.

(204) Martin, B. R.; Dermody, D. J.; Reiss, B. D.; Fang, M.; Lyon, L. A.; Natan, M. J.; Mallouk, T. E. Orthogonal Self-Assembly on Colloidal Gold-Platinum Nanorods. *Adv. Mater.* **1999**, *11* (12), 1021–1025.

(205) Zhang, Z.; Gekhtman, D.; Dresselhaus, M. S.; Ying, J. Y. Processing and Characterization of Single-Crystalline Ultrafine Bismuth Nanowires. *Chem. Mater.* **1999**, *11* (7), 1659–1665.

(206) Han, Y.-J.; Kim, J. M.; Stucky, G. D. Preparation of Noble Metal Nanowires Using Hexagonal Mesoporous Silica SBA-15. *Chem. Mater.*, **2000**, *12* (8),

2068–2069.

(207) Huang, M. H.; Choudrey, A.; Yang, P. Ag Nanowire Formation within Mesoporous Silica. *Chem. Commun.* **2000**, *0* (12), 1063–1064.

(208) Ajayan, P. M.; lijima, S. Capillarity-Induced Filling of Carbon Nanotubes. *Nature* **1993**, *361* (6410), 333–334.

(209) Ugarte; Chatelain; de Heer WA. Nanocapillarity and Chemistry in Carbon Nanotubes. *Science* **1996**, *274* (5294), 1897–1899.

(210) Zhang, D.; Qi, L.; Ma, J.; Cheng, H. Formation of Silver Nanowires in Aqueous Solutions of a Double-Hydrophilic Block Copolymer. *Chem. Mater.* **2001**, *13* (9), 2753–2755.

(211) Braun, E.; Eichen, Y.; Sivan, U.; Ben-Yoseph, G. DNA-Templated Assembly and Electrode Attachment of a Conducting Silver Wire. *Nature* **1998**, *391* (6669), 775–778.

(212) Jana, N. R.; Gearheart, L.; Murphy, C. J. Wet Chemical Synthesis of Silver Nanorods and Nanowires of Controllable Aspect Ratio. *Chem. Commun.* **2001**, *0* (7), 617–618.

(213) El-Sayed, M. A. Some Interesting Properties of Metals Confined in Time and Nanometer Space of Different Shapes. *Acc. Chem. Res.* **2001**, *34* (4), 257–264.

(214) Hong, B. H.; Bae, S. C.; Lee, C. W.; Jeong, S.; Kim, K. S. Ultrathin Single-Crystalline Silver Nanowire Arrays Formed in an Ambient Solution Phase. *Science* **2001**, *294* (5541), 348–351.

(215) Song, H. H.; Jones, K. M.; Baski, A. A. Growth of Ag Rows on Si(5 5 12). *J. Vac. Sci. Technol. A Vacuum, Surfaces, Film.* **1999**, *17* (4), 1696.

(216) Zach, M. P.; Ng, K. H.; Penner, R. M. Molybdenum Nanowires by Electrodeposition. *Science* **2000**, *290* (5499), 2120–2123.

(217) Deng, L.; Ouyang, X.; Jin, J.; Ma, C.; Jiang, Y.; Zheng, J.; Li, J.; Li, Y.; Tan, W.; Yang, R. Exploiting the Higher Specificity of Silver Amalgamation: Selective Detection of Mercury(II) by Forming Ag/Hg Amalgam. *Anal. Chem.* **2013**, *85* (18), 8594–8600.

(218) Ramesh, G. V.; Radhakrishnan, T. P. A Universal Sensor for Mercury (Hg, Hg ^{I} , Hg ^{II}) Based on Silver Nanoparticle-Embedded Polymer Thin Film. *ACS Appl. Mater. Interfaces* **2011**, *3* (4), 988–994.

(219) Chen, L.; Fu, X.; Lu, W.; Chen, L. Highly Sensitive and Selective Colorimetric Sensing of Hg^{2+} Based on the Morphology Transition of Silver Nanoprisms. *ACS Appl. Mater. Interfaces* **2013**, *5* (2), 284–290.

(220) Jelen, F.; Yosypchuk, B.;Kourilová, A.;Novotný, L.Paleček, E. Label-Free Determination of Picogram Quantities of DNA by Stripping Voltammetry with Solid Copper Amalgam or Mercury Electrodes in the Presence of Copper. *Anal. Chem.* **2002**, *74* (18), 4788–4793.

(221) Jiang, X. C.; Xiong, S. X.; Chen, C. Y.; Chen, W. M.; Yu, A. B. Polyol-Thermal Synthesis of Silver Nanowires for Hg2+ Sensing Detection. *J. Nanoparticle Res.* **2011**, *13* (10), 5087–5101.

(222) Sławin´ski, G. W. S.; Zamborini, F. P. Synthesis and Alignment of Silver Nanorods and Nanowires and the Formation of Pt, Pd, and Core/Shell Structures by Galvanic Exchange Directly on Surfaces. *Langmuir* **2007**, *23* (20), 10357–10365.

(223) Kan, C.-X.; Zhu, J.-J.; Zhu, X.-G. Silver Nanostructures with Well-Controlled Shapes: Synthesis, Characterization and Growth Mechanisms. *J. Phys. D. Appl.*

Phys. **2008**, *41* (15), 155304.

(224) Giersig, M.; Pastoriza-Santos, I.; Liz-Marzán, L. M. Evidence of an Aggregative Mechanism during the Formation of Silver Nanowires in N,N-Dimethylformamide. *J. Mater. Chem.* **2004**, *14* (4), 607–610.

(225) Gu, X.; Nie, C.; Lai, Y.; Lin, C. Synthesis of Silver Nanorods and Nanowires by Tartrate-Reduced Route in Aqueous Solutions. *Mater. Chem. Phys.* **2006**, *96* (2–3), 217–222.

(226) Zhou, G.; Lü, M.; Yang, Z.; Zhang, H.; Zhou, Y.; Wang, S.; Wang, S.; Zhang, A. Surfactant-Assisted Synthesis and Characterization of Silver Nanorods and Nanowires by an Aqueous Solution Approach. *J. Cryst. Growth* **2006**, *289* (1), 255–259.

(227) Sun, L.; Wang, L.; Song, Y.; Guo, C.; Sun, Y.; Peng, C.; Liu, Z.; Li, Z. Aggregation-Based Growth of Silver Nanowires at Room Temperature. *Appl. Surf. Sci.* **2008**, *254* (9), 2581–2587.

(228) Sun, Y.; Mayers, B.; Herricks, T.; Xia,Y. Polyol Synthesis of Uniform Silver Nanowires: A Plausible Growth Mechanism and the Supporting Evidence. *Nano Lett.* **2003**, *3*, 955–960.

(229) Sau, T. K.; Murphy, C. J. Room Temperature, High-Yield Synthesis of Multiple Shapes of Gold Nanoparticles in Aqueous Solution. *J. Am. Chem. Soc.* **2004**, *126* (28), 8648–8649.

(230) Liu, M.; Guyot-Sionnest, P. Mechanism of Silver(I)-Assisted Growth of Gold Nanorods and Bipyramids. *J. Phys. Chem. B* **2005**, *109* (47), 22192–22200.

(231) Li, Z.; Li, W.; Camargo, P. H. C.; Xia, Y. Facile Synthesis of Branched Au Nanostructures by Templating Against a Self-Destructive Lattice of Magnetic Fe Nanoparticles. *Angew. Chemie Int. Ed.* **2008**, *47* (50), 9653–9656.

(232) Zhang, H.; Wang, D. Controlling the Growth of Charged-Nanoparticle Chains through Interparticle Electrostatic Repulsion. *Angew. Chemie Int. Ed.* **2008**, *47* (21), 3984–3987.

(233) Sun, Y.; Xia, Y. Large-Scale Synthesis of Uniform Silver Nanowires Through a Soft, Self-Seeding, Polyol Process. *Adv. Mater.* **2002**, *14* (11), 833.

(234) Wang, Z. L. Transmission Electron Microscopy of Shape-Controlled Nanocrystals and Their Assemblies. *j. phys. chem. B* **2000**, *104*, 1153–1175.

(235) *CRC Handbook of Chemistry and Physics*, 90th Edition CD-ROM Version 2010

(236) Wagman. *Enthalpies of Precipitation of Silver Halides; Entropy of the Aqueous Silver Ion.Physics and Chemistry* **1973**, *77A*, 569-579.

(237) Fan, Y.; Liu, Z.; Wang, L.; Zhan, J. Synthesis of Starch-Stabilized Ag Nanoparticles and Hg Recognition in Aqueous Media. *Nanoscale Res. Lett.* **2009**, *4* (10), 1230–1235.

(238) Haynes, C. L.; Yonzon, C. R.; Zhang, X.; Van Duyne, R. P. Surface-Enhanced Raman Sensors: Early History and the Development of Sensors for Quantitative Biowarfare Agent and Glucose Detection. *J. Raman Spectrosc.* **2005**, *36* (6–7), 471–484.

(239) Quang, L. X.; Lim, C.; Seong, G. H.; Choo, J.; Do, K. J.; Yoo, S.-K. A Portable Surface-Enhanced Raman Scattering Sensor Integrated with a Lab-on-a-Chip for Field Analysis. *Lab Chip* **2008**, *8* (12), 2214.

(240) Vo-Dinh, T.; Yan, F.; Wabuyele, M. B. Surface-Enhanced Raman Scattering for Medical Diagnostics and Biological Imaging. *J. Raman Spectrosc.* **2005**, *36* (6–7), 640–647.

(241) Senapati, D.; Dasary, S. S. R.; Singh, A. K.; Senapati, T.; Yu, H.; Ray, P. C. A Label-Free Gold-Nanoparticle-Based SERS Assay for Direct Cyanide Detection at the Parts-per-Trillion Level. *Chem. Eur. J.* **2011**, *17* (30), 8445–8451.

(242) Alvarez-Puebla, R. A.; Liz-Marzán, L. M. SERS-Based Diagnosis and Biodetection. *Small* **2010**, *6* (5), 604–610.

(243) Vikesland, P. J.; Wigginton, K. R. Nanomaterial Enabled Biosensors for Pathogen Monitoring - A Review. *Environ. Sci. Technol.* **2010**, *44* (10), 3656–3669.

(244) Myers, A. B.; Mathies, R. A. *In Biological Applications of Raman Spectroscopy*; Spiro, T. G., Ed.; Wiley and Sons: New York, 1987.

(245) Myers, A. B. Resonance Raman Intensity Analysis of Excited-State Dynamics. *Acc. Chem. Res.* **1997**, *30* (12), 519–527.

(246) Senthil Kumar, P.; Pastoriza-Santos, I.; Rodríguez-González, B.; Javier García de Abajo, F.; Liz-Marzán, L. M. High-Yield Synthesis and Optical Response of Gold Nanostars. *Nanotechnology* **2008**, *19* (1), 015606.

(247) Persson, B. N. J. On the Theory of Surface-Enhanced Raman Scattering. *Chem. Phys. Lett.***1981**, *82* (3), 561–565.

(248) Boyd, G. T.; Yu, Z. H.; Shen, Y. R. Photoinduced Luminescence from the Noble Metals and Its Enhancement on Roughened Surfaces. *Phys. Rev. B* **1986**, *33* (12), 7923–7936.

(249) Chen, C. K.; Heinz, T. F.; Ricard, D.; Shen, Y. R. Surface-Enhanced Second-Harmonic Generation and Raman Scattering. *Phys. Rev. B* **1983**, *27* (4), 1965–1979.

(250) Boyd, G. T.; Rasing, T.; Leite, J. R. R.; Shen, Y. R. Local-Field Enhancement on Rough Surfaces of Metals, Semimetals, and Semiconductors with the Use of Optical Second-Harmonic Generation. *Phys. Rev. B* **1984**, *30* (2), 519–526.

(251) Pradhan, N.; Pal, A.; Pal, T. Silver Nanoparticle Catalyzed Reduction of Aromatic Nitro Compounds. *Colloids Surfaces A Physicochem. Eng. Asp.* **2002**, *196* (2–3), 247–257.

(252) Sun, Y.; Mayers, B. T.; Xia, Y. Template-Engaged Replacement Reaction: A One-Step Approach to the Large-Scale Synthesis of Metal Nanostructures with Hollow Interiors. *Nano Lett.* **2002**, *2* (5), 481–485.

(253) Davey, W. P. Precision Measurements of the Lattice Constants of Twelve Common Metals. *Phys. Rev.* **1925**, *25* (6), 753–761.

(254) He, D.; Hu, B.; Yao, Q.-F.; Wang, K.; Yu, S.-H. Large-Scale Synthesis of Flexible Free-Standing SERS Substrates with High Sensitivity: Electrospun PVA Nanofibers Embedded with Controlled Alignment of Silver Nanoparticles. *ACS Nano* **2009**, *3* (12), 3993–4002.

(255) Lim, S. H.; Feng, L.; Kemling, J. W.; Musto, C. J.; Suslick, K. S. An Optoelectronic Nose for the Detection of Toxic Gases. *Nat. Chem.* **2009**, *1* (7), 562.

(256) Beqa, L.; Singh, A. K.; Khan, S. A.; Senapati, D.; Arumugam, S. R.; Ray, P. C. Gold Nanoparticle-Based Simple Colorimetric and Ultrasensitive Dynamic Light Scattering Assay for the Selective Detection of Pb (II) from Paints, Plastics, and Water Samples. *ACS Appl. Mater. Interfaces* **2011**, *3* (3), 668–673.

(257) Lu, W.; Arumugam, S. R.; Senapati, D.; Singh, A. K.; Arbneshi, T.; Khan, S. A.; Yu, H.; Ray, P. C. Multifunctional Oval-Shaped Gold-Nanoparticle-Based

Selective Detection of Breast Cancer Cells Using Simple Colorimetric and Highly Sensitive Two-Photon Scattering Assay. *ACS Nano* **2010**, *4* (3), 1739–1749.

(258) Valentini, P.; Fiammengo, R.; Sabella, S.; Gariboldi, M.; Maiorano, G.; Cingolani, R.; Pompa, P. P. Gold-Nanoparticle-Based Colorimetric Discrimination of Cancer-Related Point Mutations with Picomolar Sensitivity. *ACS Nano* **2013**, *7* (6), 5530–5538.

(259) Wang, S.; Singh, A. K.; Senapati, D.; Neely, A.; Yu, H.; Ray, P. C. Rapid Colorimetric Identification and Targeted Photothermal Lysis of Salmonella Bacteria by Using Bioconjugated Oval-Shaped Gold Nanoparticles. *Chem. Eur. J.* **2010**, *16* (19), 5600–5606.

(260) Dasary, S. S. R.; Singh, A. K.; Senapati, D.; Yu, H.; Ray, P. C. Gold Nanoparticle Based Label-Free SERS Probe for Ultrasensitive and Selective Detection of Trinitrotoluene. *J. Am. Chem. Soc.* **2009**, *131* (38), 13806–13812.

(261) Üzer, A.; Can, Z.; Ak\in, I.; Erçağ, E.; Apak, R. 4-Aminothiophenol Functionalized Gold Nanoparticle-Based Colorimetric Sensor for the Determination of Nitramine Energetic Materials. *Anal. Chem.* **2013**, *86* (1), 351–356.

(262) Idros, N.; Ho, M. Y.; Pivnenko, M.; Qasim, M. M.; Xu, H.; Gu, Z.; Chu, D. Colorimetric-Based Detection of TNT Explosives Using Functionalized Silica Nanoparticles. *Sensors* **2015**, *15* (6), 12891–12905.

(263) Kim, Y.-R.; Mahajan, R. K.; Kim, J. S.; Kim, H. Highly Sensitive Gold Nanoparticle-Based Colorimetric Sensing of Mercury (II) through Simple Ligand Exchange Reaction in Aqueous Media. *ACS Appl. Mater. Interfaces* **2009**, *2* (1), 292–295.

(264) Bai, W.; Zhu, C.; Liu, J.; Yan, M.; Yang, S.; Chen, A. Gold Nanoparticle--Based Colorimetric Aptasensor for Rapid Detection of Six Organophosphorous Pesticides. *Environ. Toxicol. Chem.* **2015**, *34* (10), 2244–2249.

(265) He, P.; Shen, L.; Liu, R.; Luo, Z.; Li, Z. Direct Detection of $β$-Agonists by Use of Gold Nanoparticle-Based Colorimetric Assays. *Anal. Chem.* **2011**, *83* (18), 6988–6995.

(266) Chen, Y.-C.; Lee, I.-L.; Sung, Y.-M.; Wu, S.-P. Triazole Functionalized Gold Nanoparticles for Colorimetric Cr3+ Sensing. *Sensors Actuators B Chem.* **2013**, *188*, 354–359.

(267) Darbha, G. K.; Singh, A. K.; Rai, U. S.; Yu, E.; Yu, H.; Chandra Ray, P. Selective Detection of Mercury (II) Ion Using Nonlinear Optical Properties of Gold Nanoparticles. *J. Am. Chem. Soc.* **2008**, *130* (25), 8038–8043.

(268) Shaw, C. F. Gold-Based Therapeutic Agents. *Chem. Rev.* **1999**, *99* (9), 2589–2600.

(269) Rao, C. R. M.; Reddi, G. S. Platinum Group Metals (PGM); Occurrence, Use and Recent Trends in Their Determination. *TrAC Trends Anal. Chem.* **2000**, *19* (9), 565–586.

(270) Cui, J.; Zhang, L. Metallurgical Recovery of Metals from Electronic Waste: A Review. *J. Hazard. Mater.* **2008**, *158* (2–3), 228–256.

(271) Nakbanpote, W.; Thiravetyan, P.; Kalambaheti, C. Comparison of Gold Adsorption by Chlorella Vulgaris, Rice Husk and Activated Carbon. *Miner. Eng.* **2002**, *15* (7), 549–552.

(272) Laatikainen, M.; Paatero, E. Gold Recovery from Chloride Solutions with

XAD-7: Competitive Adsorption of Fe (III) and Te (IV). *Hydrometallurgy* **2005**, *79* (3–4), 154–171.

(273) Song, J.; Wang, L.; Zibart, A.; Koch, C. Corrosion Protection of Electrically Conductive Surfaces. *Metals (Basel).* **2012**, *2* (4), 450–477.

(274) Changmei, S.; Guanghua, Z.; Chunhua, W.; Rongjun, Q.; Ying, Z.; Quanyun, G. A Resin with High Adsorption Selectivity for Au (III): Preparation, Characterization and Adsorption Properties. *Chem. Eng. J.* **2011**, *172* (2–3), 713–720.

(275) Kumeria, T.; Santos, A.; Losic, D. Ultrasensitive Nanoporous Interferometric Sensor for Label-Free Detection of Gold (III) Ions. *ACS Appl. Mater. Interfaces* **2013**, *5* (22), 11783–11790.

(276) De La Calle, I.; Cabaleiro, N.; Costas, M.; Pena, F.; Gil, S.; Lavilla, I.; Bendicho, C. Ultrasound-Assisted Extraction of Gold and Silver from Environmental Samples Using Different Extractants Followed by Electrothermal-Atomic Absorption Spectrometry. *Microchem. J.* **2011**, *97* (2), 93–100.

(277) Liang, P.; Zhao, E.; Ding, Q.; Du, D. Multiwalled Carbon Nanotubes Microcolumn Preconcentration and Determination of Gold in Geological and Water Samples by Flame Atomic Absorption Spectrometry. *Spectrochim. Acta Part B At. Spectrosc.* **2008**, *63* (6), 714–717.

(278) Hassan, J.; Shamsipur, M.; Karbasi, M.-H. Single Granular Activated Carbon Microextraction and Graphite Furnace Atomic Absorption Spectrometry Determination for Trace Amount of Gold in Aqueous and Geological Samples. *Microchem. J.* **2011**, *99* (1), 93–96.

(279) Amin, A. S. Utility of Solid Phase Extraction for Spectrophotometric Determination of Gold in Water, Jewel and Ore Samples. *Spectrochim. Acta Part A Mol. Biomol. Spectrosc.* **2010**, *77* (5), 1054–1058.

(280) Jarvis, I.; Totland, M. M.; Jarvis, K. E. Assessment of Dowex 1-X8-Based Anion-Exchange Procedures for the Separation and Determination of Ruthenium, Rhodium, Palladium, Iridium, Platinum and Gold in Geological Samples by Inductively Coupled Plasma Mass Spectrometry. *Analyst* **1997**, *122* (1), 19–26.

(281) Elci, L.; Sahan, D.; Basaran, A.; Soylak, M. Solid Phase Extraction of Gold (III) on Amberlite XAD-2000 Prior to Its Flame Atomic Absorption Spectrometric Determination. *Environ. Monit. Assess.* **2007**, *132* (1–3), 331–338.

(282) Moawed, E. A.; El-Shahat, M. F. Synthesis, Characterization of Low Density Polyhydroxy Polyurethane Foam and Its Application for Separation and Determination of Gold in Water and Ores Samples. *Anal. Chim. Acta* **2013**, *788*, 200–207.

(283) Iglesias, M.; Antico, E.; Salvado, V. Recovery of Palladium (II) and Gold (III) from Diluted Liquors Using the Resin Duolite GT-73. *Anal. Chim. Acta* **1999**, *381* (1), 61–67.

(284) Chen, S.; Zhu, X. Simplified Cloud Point Extraction-Inductively Coupled Plasma Mass Spectrometry for the Preconcentration/Analysis of Ultra-Trace Gold. *Miner. Eng.* **2010**, *23* (14), 1152–1154.

(285) Sen, S.; Seyrankaya, A.; Cilingir, Y. Coal--Oil Assisted Flotation for the Gold Recovery. *Miner. Eng.* **2005**, *18* (11), 1086–1092.

(286) Sánchez, J. M.; Hidalgo, M.; Salvadó, V. Synthesised Phosphine Sulphide-

Type Macroporous Polymers for the Preconcentration and Separation of Gold (III) and Palladium (II) in a Column System. *React. Funct. Polym.* **2001**, *49* (3), 215–224.

(287) Kinoshita, T.; Ishigaki, Y.; Nakano, K.; Yamaguchi, K.; Akita, S.; Nii, S.; Kawaizumi, F. Application of Acrylate Gel Having Poly (Ethylene Glycol) Side Chains to Recovery of Gold from Hydrochloric Acid Solutions. *Sep. Purif. Technol.* **2006**, *49* (3), 253–257.

(288) Soleimani, M.; Kaghazchi, T. The Investigation of the Potential of Activated Hard Shell of Apricot Stones as Gold Adsorbents. *J. Ind. Eng. Chem.* **2008**, *14* (1), 28–37.

(289) Tuzen, M.; Saygi, K. O.; Soylak, M. Novel Solid Phase Extraction Procedure for Gold (III) on Dowex M 4195 Prior to Its Flame Atomic Absorption Spectrometric Determination. *J. Hazard. Mater.* **2008**, *156* (1–3), 591–595.

(290) Tavakoli, L.; Yamini, Y.; Ebrahimzadeh, H.; Nezhadali, A.; Shariati, S.; Nourmohammadian, F. Development of Cloud Point Extraction for Simultaneous Extraction and Determination of Gold and Palladium Using ICP-OES. *J. Hazard. Mater.* **2008**, *152* (2), 737–743.

(291) Qu, R.; Sun, C.; Wang, M.; Ji, C.; Xu, Q.; Zhang, Y.; Wang, C.; Chen, H.; Yin, P. Adsorption of Au (III) from Aqueous Solution Using Cotton Fiber/Chitosan Composite Adsorbents. *Hydrometallurgy* **2009**, *100* (1–2), 65–71.

(292) Ertan, E.; Gülfen, M. Separation of Gold (III) Ions from Copper (II) and Zinc (II) Ions Using Thiourea--Formaldehyde or Urea-Formaldehyde Chelating Resins. *J. Appl. Polym. Sci.* **2009**, *111* (6), 2798–2805.

(293) Koyanaka, H.; Takeuchi, K.; Loong, C.-K. Gold Recovery from Parts-per-Trillion-Level Aqueous Solutions by a Nanostructured Mn2O3 Adsorbent. *Sep. Purif. Technol.* **2005**, *43* (1), 9–15.

(294) Gomes, C. P.; Almeida, M. F.; Loureiro, J. M. Gold Recovery with Ion Exchange Used Resins. *Sep. Purif. Technol.* **2001**, *24* (1–2), 35–57.

(295) Akita, S.; Yang, L.; Takeuchi, H. Solvent Extraction of Gold (III) from Hydrochloric Acid Media by Nonionic Surfactants. *Hydrometallurgy* **1996**, *43* (1–3), 37–46.

(296) Kılıç, A. G.;Malcı, S.; Çelikbıçak, Ö.;Şahiner, N.;Salih, B. Gold Recovery onto Poly (Acrylamide-Allylthiourea) Hydrogels Synthesized by Treating with Gamma Radiation. *Anal. Chim. Acta* **2005**, *547* (1), 18–25.

(297) Fujiwara, K.; Ramesh, A.; Maki, T.; Hasegawa, H.; Ueda, K. Adsorption of Platinum (IV), Palladium (II) and Gold (III) from Aqueous Solutions onto l-Lysine Modified Crosslinked Chitosan Resin. *J. Hazard. Mater.* **2007**, *146* (1–2), 39–50.

(298) Awual, M. R.; Khaleque, M. A.; Ferdows, M.; Chowdhury, A. M. S.; Yaita, T. Rapid Recognition and Recovery of Gold (III) with Functional Ligand Immobilized Novel Mesoporous Adsorbent. *Microchem. J.* **2013**, *110*, 591–598.

(299) Awual, M. R.; Ismael, M. Efficient Gold (III) Detection, Separation and Recovery from Urban Mining Waste Using a Facial Conjugate Adsorbent. *Sensors Actuators B Chem.* **2014**, *196*, 457–466.

(300) Awual, M. R. Investigation of Potential Conjugate Adsorbent for Efficient Ultra-Trace Gold (III) Detection and Recovery. *J. Ind. Eng. Chem.* **2014**, *20* (5), 3493–3501.

(301) Hutter, E.; Fendler, J. H. Exploitation of Localized Surface Plasmon Resonance.

Adv. Mater. **2004**, *16* (19), 1685–1706.

(302) Sun, Y. G.; Xia, Y. N. Biological Applications of Localized Surface Plasmonic Phenomena. In *Proc. SPIE-Int. Soc. Opt. Eng*; 2003; Vol. 5221, pp 164–173.

(303) Jin, R.; Cao, Y.; Mirkin, C. A.; Kelly, K. L.; Schatz, G. C.; Zheng, J. G. Photoinduced Conversion of Silver Nanospheres to Nanoprisms. *Science* **2001**, *294* (5548), 1901–1903.

(304) Samanta, S.; Sarkar, P.; Pyne, S.; Sahoo, G. P.; Misra, A. Synthesis of Silver Nanodiscs and Triangular Nanoplates in PVP Matrix: Photophysical Study and Simulation of UV--Vis Extinction Spectra Using DDA Method. *J. Mol. Liq.* **2012**, *165*, 21–26.

(305) O'Brien, M. N.; Jones, M. R.; Kohlstedt, K. L.; Schatz, G. C.; Mirkin, C. A. Uniform Circular Disks with Synthetically Tailorable Diameters: Two-Dimensional Nanoparticles for Plasmonics. *Nano Lett.* **2015**, *15* (2), 1012–1017.

(306) Ghosh, T.; Bardhan, M.; Bhattacharya, M.; Satpati, B. Study of Inelastic Mean Free Path of Metal Nanostructures Using Energy Filtered Transmission Electron Microscopy Imaging. *J. Microsc.* **2015**, *258* (3), 253–258.

(307) Ameer, F. S.; Varahagiri, S.; Benza, D. W.; Willett, D. R.; Wen, Y.; Wang, F.; Chumanov, G.; Anker, J. N. Tuning Localized Surface Plasmon Resonance Wavelengths of Silver Nanoparticles by Mechanical Deformation. *J. Phys. Chem. C* **2016**, *120* (37), 20886–20895.

(308) Senapati, D.; Dasary, S. S. R.; Singh, A. K.; Senapati, T.; Yu, H.; Ray, P. C. A Label-Free Gold-Nanoparticle-Based SERS Assay for Direct Cyanide Detection at the Parts-per-Trillion Level. *Chem. - A Eur. J.* **2011**, *17* (30), 8445–8451.

(309) Goldstein, J. I.; Newbury, D. E.; Michael, J. R.; Ritchie, N. W. M.; Scott, J. H. J.; Joy, D. C. *Scanning Electron Microscopy and X-Ray Microanalysis*; Springer, 2017.

(310) Métraux, G. S.; Cao, Y. C.; Jin, R.; Mirkin, C. A. Triangular Nanoframes Made of Gold and Silver. *Nano Lett.* **2003**, *3* (4), 519–522.

(311) Ghosh, T.; Satpati, B.; Senapati, D. Characterization of Bimetallic Core--Shell Nanorings Synthesized via Ascorbic Acid-Controlled Galvanic Displacement Followed by Epitaxial Growth. *J. Mater. Chem. C* **2014**, *2* (13), 2439–2447.

(312) Borsook, H.; Keighley, G. Oxidation-Reduction Potential of Ascorbic Acid (Vitamin C). *Proc. Natl. Acad. Sci.* **1933**, *19* (9), 875–878.

(313) Sajanlal, P. R.; Sreeprasad, T. S.; Samal, A. K.; Pradeep, T. Anisotropic Nanomaterials: Structure, Growth, Assembly, and Functions. *Nano Rev.* **2011**, *2* (1), 5883.

(314) Yuan, H.; Khoury, C. G.; Wilson, C. M.; Grant, G. A.; Bennett, A. J.; Vo-Dinh, T. In Vivo Particle Tracking and Photothermal Ablation Using Plasmon-Resonant Gold Nanostars. *Nanomedicine Nanotechnology, Biol. Med.* **2012**, *8* (8), 1355–1363.

(315) Atkins, P.; De Paula, J.; Keeler, J. *Atkins' Physical Chemistry*; Oxford university press, 2018.

(316) Eustis, S.; El-Sayed, M. A. Why Gold Nanoparticles Are More Precious than Pretty Gold: Noble Metal Surface Plasmon Resonance and Its Enhancement of the Radiative and Nonradiative Properties of Nanocrystals of Different Shapes. *Chem. Soc. Rev.* **2006**, *35* (3), 209–217.

(317) Hedgehog drawing stock illustration. Illustration of hand - 48437051

https://www.dreamstime.com/stock-illustration-hedgehog-drawing-sketch-isolated-white-background-image48437051.

(318) Draine, B. T.; Flatau, P. J. Discrete-Dipole Approximation for Scattering Calculations. *JOSA A* **1994**, *11* (4), 1491–1499.

(319) Draine, B. T.; Flatau, P. J. User Guide for the Discrete Dipole Approximation Code DDSCAT 7.3. *arXiv Prepr. arXiv1305.6497* **2013**.

(320) Huang, X.; El-Sayed, M. A. Gold Nanoparticles: Optical Properties and Implementations in Cancer Diagnosis and Photothermal Therapy. *J. Adv. Res.* **2010**, *1* (1), 13–28.

(321) de Puig, H.; Tam, J. O.; Yen, C.-W.; Gehrke, L.; Hamad-Schifferli, K. Extinction Coefficient of Gold Nanostars. *J. Phys. Chem. C* **2015**, *119* (30), 17408–17415.

(322) Loumaigne, M.; Midelet, C.; Doussineau, T.; Dugourd, P.; Antoine, R.; Stamboul, M.; Débarre, A.; Werts, M. H. V. Optical Extinction and Scattering Cross Sections of Plasmonic Nanoparticle Dimers in Aqueous Suspension. *Nanoscale* **2016**, *8* (12), 6555–6570.

(323) Fujita, T.; Guan, P.; McKenna, K.; Lang, X.; Hirata, A.; Zhang, L.; Tokunaga, T.; Arai, S.; Yamamoto, Y.; Tanaka, N.; *et al.* Atomic Origins of the High Catalytic Activity of Nanoporous Gold. *Nat. Mater.* **2012**, *11* (9), 775.

(324) Bhattacharya, M.; Mandal, A. R.; Chakraborty, S. Das; Maiti, A.; Maity, A.; Kuznetsov, D. V; Mondal, P.; Senapati, D. Direct Experimental Observation of Salt Induced Aspect Ratio Tunable PFPT Silver-Nanowire Formation: SERS-Based *ppt* Level Hg^{2+} Sensing from Ground Water. *RSC Adv.* **2016**, *6* (51), 45279–45289.

(325) Griffin, J.; Singh, A. K.; Senapati, D.; Lee, E.; Gaylor, K.; Jones-Boone, J.; Ray, P. C. Sequence-Specific HCV RNA Quantification Using the Size-Dependent Nonlinear Optical Properties of Gold Nanoparticles. *Small* **2009**, *5* (7), 839–845.

(326) Senapati, D.; Senapati, T.; Wate, P. S.; Kanchanapally, R.; Fan, Z.; Singh, A. K.; Ray, P. C. Length Dependent NLO Properties of 2D Hollow Gold Nanoprisms Formed by Guided Assembly. *Chem. Commun.* **2012**, *48* (48), 6034–6036.

(327) Abadeer, N. S.; Murphy, C. J. Recent Progress in Cancer Thermal Therapy Using Gold Nanoparticles. *J. Phys. Chem. C***2016**, *120* (9), 4691–4716.

(328) Brouard, D.; Viger, M. L.; Bracamonte, A. G.; Boudreau, D. Label-Free Biosensing Based on Multilayer Fluorescent Nanocomposites and a Cationic Polymeric Transducer. *ACS Nano* **2011**, *5* (3), 1888–1896.

(329) Brus, L. Noble Metal Nanocrystals: Plasmon Electron Transfer Photochemistry and Single-Molecule Raman Spectroscopy. *Acc. Chem. Res.* **2008**, *41* (12), 1742–1749.

(330) Luo, M.; Huang, H.; Choi, S.-I.; Zhang, C.; Silva, R. R. da; Peng, H.-C.; Li, Z.-Y.; Liu, J.; He, Z.; Xia, Y. Facile Synthesis of Ag Nanorods with No Plasmon Resonance Peak in the Visible Region by Using Pd Decahedra of 16 Nm in Size as Seeds. *ACS Nano* **2015**, *9* (10), 10523–10532.

(331) Kobler, A.; Beuth, T.; Klöffel, T.; Prang, R.; Moosmann, M.; Scherer, T.; Walheim, S.; Hahn, H.; Kübel, C.; Meyer, B.; *et al.* Nanotwinned Silver Nanowires: Structure and Mechanical Properties. *Acta Mater.* **2015**, *92*, 299–308.

(332) Liu, C.-H.; Yu, X. Silver Nanowire-Based Transparent, Flexible, and Conductive Thin Film. *Nanoscale Res. Lett.* **2011**, *6* (1), 75.

(333) Su, H.; Li, Y.; Li, X.-Y.; Wong, K. S. Optical and Electrical Properties of Au Nanoparticles in Two-Dimensional Networks: An Effective Cluster Model. *Opt. Express* **2009**, *17* (24), 22223–22234.

(334) Nie, S.; Xing, Y.; Kim, G. J.; Simons, J. W. Nanotechnology Applications in Cancer. *Annu. Rev. Biomed. Eng.* **2007**, *9*, 257–288.

(335) Harisinghani, M. G.; Barentsz, J.; Hahn, P. F.; Deserno, W. M.; Tabatabaei, S.; van de Kaa, C. H.; de la Rosette, J.; Weissleder, R. Noninvasive Detection of Clinically Occult Lymph-Node Metastases in Prostate Cancer. *N. Engl. J. Med.* **2003**, *348* (25), 2491–2499.

(336) Fratoddi, I.; Venditti, I.; Cametti, C.; Russo, M. V. How Toxic Are Gold Nanoparticles? The State-of-the-Art. *Nano Res.* **2015**, *8* (6), 1771–1799.

(337) Sadikot, R. T.; Rubinstein, I. Long-Acting, Multi-Targeted Nanomedicine: Addressing Unmet Medical Need in Acute Lung Injury. *J. Biomed. Nanotechnol.* **2009**, *5* (6), 614–619.

(338) Schwartz Jr, S. *Unmet Needs in Developing Nanoparticles for Precision Medicine.* Future Medicine 2017.

(339) Zhang, Y.; Newton, B.; Lewis, E.; Fu, P. P.; Kafoury, R.; Ray, P. C.; Yu, H. Cytotoxicity of Organic Surface Coating Agents Used for Nanoparticles Synthesis and Stability. *Toxicol. Vitr.* **2015**, *29* (4), 762–768.

(340) Wang, Q.; Shen, M.; Zhao, T.; Xu, Y.; Lin, J.; Duan, Y.; Gu, H. Low Toxicity and Long Circulation Time of Polyampholyte-Coated Magnetic Nanoparticles for Blood Pool Contrast Agents. *Sci. Rep.* **2015**, *5*, 7774.

(341) Maouyo, D.; Chu, S.; Montrose, M. H. PH Heterogeneity at Intracellular and Extracellular Plasma Membrane Sites in HT29-C1 Cell Monolayers. *Am. J. Physiol. Physiol.* **2000**, *278* (5), C973--C981.

(342) Gerweck, L. E.; Seetharaman, K. Cellular PH Gradient in Tumor versus Normal Tissue: Potential Exploitation for the Treatment of Cancer. *Cancer Res.* **1996**, *56* (6), 1194–1198.

(343) Zager, R. A.; Schimpf, B. A.; Gmur, D. J. Physiological PH. Effects on Posthypoxic Proximal Tubular Injury. *Circ. Res.* **1993**, *72* (4), 837–846.

(344) Hutchison, J. S.; Ward, R. E.; Lacroix, J.; Hébert, P. C.; Barnes, M. A.; Bohn, D. J.; Dirks, P. B.; Doucette, S.; Fergusson, D.; Gottesman, R.; *et al.* Hypothermia Therapy after Traumatic Brain Injury in Children. *N. Engl. J. Med.* **2008**, *358* (23), 2447–2456.

(345) Baffou, G.; Quidant, R.; de Abajo, F. J. Nanoscale Control of Optical Heating in Complex Plasmonic Systems. *ACS Nano* **2010**, *4* (2), 709–716.

(346) Baffou, G.; Quidant, R.; Girard, C. Heat Generation in Plasmonic Nanostructures: Influence of Morphology. *Appl. Phys. Lett.* **2009**, *94* (15), 153109.

(347) Govorov, A. O.; Richardson, H. H. Generating Heat with Metal Nanoparticles. *Nano Today* **2007**. *2* (1): 30.

(348) Govorov, A. O.; Zhang, W.; Skeini, T.; Richardson, H.; Lee, J.; Kotov, N. A. Gold Nanoparticle Ensembles as Heaters and Actuators: Melting and Collective Plasmon Resonances. *Nanoscale Res. Lett.* **2006**, *1* (1), 84.

(349) Richardson, H. H.; Carlson, M. T.; Tandler, P. J.; Hernandez, P.; Govorov, A. O. Experimental and Theoretical Studies of Light-to-Heat Conversion and

Collective Heating Effects in Metal Nanoparticle Solutions. *Nano Lett.* **2009**, *9* (3), 1139–1146.

(350) Pamies, R.; Cifre, J. G. H.; Espín, V. F.; Collado-González, M.; Baños, F. G. D.; de la Torre, J. G. Aggregation Behaviour of Gold Nanoparticles in Saline Aqueous Media. *J. Nanoparticle Res.* **2014**, *16* (4), 2376.

(351) Chandra, M.; Dowgiallo, A.-M.; Knappenberger Jr, K. L. Controlled Plasmon Resonance Properties of Hollow Gold Nanosphere Aggregates. *J. Am. Chem. Soc.* **2010**, *132* (44), 15782–15789.

(352) Enustun, B. V; Turkevich, J. Coagulation of Colloidal Gold. *J. Am. Chem. Soc.* **1963**, *85* (21), 3317–3328.

(353) Wuelfing, W. P.; Gross, S. M.; Miles, D. T.; Murray, R. W. Nanometer Gold Clusters Protected by Surface-Bound Monolayers of Thiolated Poly (Ethylene Glycol) Polymer Electrolyte. *J. Am. Chem. Soc.* **1998**, *120* (48), 12696–12697.

(354) Zheng, M.; Davidson, F.; Huang, X. Ethylene Glycol Monolayer Protected Nanoparticles for Eliminating Nonspecific Binding with Biological Molecules. *J. Am. Chem. Soc.* **2003**, *125* (26), 7790–7791.

(355) Latham, A. H.; Williams, M. E. Versatile Routes toward Functional, Water-Soluble Nanoparticles via Trifluoroethylester- Peg- Thiol Ligands. *Langmuir* **2006**, *22* (9), 4319–4326.

(356) Jokerst, J. V; Lobovkina, T.; Zare, R. N.; Gambhir, S. S. Nanoparticle PEGylation for Imaging and Therapy. *Nanomedicine* **2011**, *6* (4), 715–728.

(357) Kim, S.; Hyun, K.; Moon, J. Y.; Clasen, C.; Ahn, K. H. Depletion Stabilization in Nanoparticle--Polymer Suspensions: Multi-Length-Scale Analysis of Microstructure. *Langmuir* **2015**, *31* (6), 1892–1900.

(358) Zhang, X.; Servos, M. R.; Liu, J. Ultrahigh Nanoparticle Stability against Salt, PH, and Solvent with Retained Surface Accessibility via Depletion Stabilization. *J. Am. Chem. Soc.* **2012**, *134* (24), 9910–9913.

(359) Yang, J.; Yan, D.; Jones, T. S. Molecular Template Growth and Its Applications in Organic Electronics and Optoelectronics. *Chem. Rev.* **2015**, *115* (11), 5570–5603.

(360) Huschka, R.; Zuloaga, J.; Knight, M. W.; Brown, L. V; Nordlander, P.; Halas, N. J. Light-Induced Release of DNA from Gold Nanoparticles: Nanoshells and Nanorods. *J. Am. Chem. Soc.* **2011**, *133* (31), 12247–12255.

(361) Self-Assemblies, N. Fabrication and Collective Properties Pileni. *J. Phys. Chem. B* **2001**, *105* (17), 3358–3371.

(362) Thorkelsson, K.; Bai, P.; Xu, T. Self-Assembly and Applications of Anisotropic Nanomaterials: A Review. *Nano Today* **2015**, *10* (1), 48–66.

(363) Nie, Z.; Petukhova, A.; Kumacheva, E. Properties and Emerging Applications of Self-Assembled Structures Made from Inorganic Nanoparticles. *Nat. Nanotechnol.* **2010**, *5* (1), 15.

(364) Schwartzberg, A. M.; Grant, C. D.; Wolcott, A.; Talley, C. E.; Huser, T. R.; Bogomolni, R.; Zhang, J. Z. Unique Gold Nanoparticle Aggregates as a Highly Active Surface-Enhanced Raman Scattering Substrate. *J. Phys. Chem. B* **2004**, *108* (50), 19191–19197.

(365) Ray, P. C. Size and Shape Dependent Second Order Nonlinear Optical Properties of Nanomaterials and Their Application in Biological and Chemical Sensing. *Chem. Rev.* **2010**, *110* (9), 5332–5365.

(366) Albanese, A.; Chan, W. C. W. Effect of Gold Nanoparticle Aggregation on Cell

Uptake and Toxicity. *ACS Nano* **2011**, *5* (7), 5478–5489.

(367) Grzelczak, M.; Vermant, J.; Furst, E. M.; Liz-Marzan, L. M. Directed Self-Assembly of Nanoparticles. *ACS Nano* **2010**, *4* (7), 3591–3605.

(368) Mirkin, C. A.; Letsinger, R. L.; Mucic, R. C.; Storhoff, J. J. A DNA-Based Method for Rationally Assembling Nanoparticles into Macroscopic Materials. *Nature* **1996**, *382* (6592), 607.

(369) Jones, M. R.; Macfarlane, R. J.; Lee, B.; Zhang, J.; Young, K. L.; Senesi, A. J.; Mirkin, C. A. DNA-Nanoparticle Superlattices Formed from Anisotropic Building Blocks. *Nat. Mater.* **2010**, *9* (11), 913.

(370) Murray, C. B.; Sun, S.; Doyle, H.; Betley, T. Monodisperse 3d Transition-Metal (Co, Ni, Fe) Nanoparticles and Their Assembly Intonanoparticle Superlattices. *Mrs Bull.* **2001**, *26* (12), 985–991.

(371) He, S. T.; Xie, S. S.; Yao, J. N.; Gao, H. J.; Pang, S. J. Self-Assembled Two-Dimensional Superlattice of Au--Ag Alloy Nanocrystals. *Appl. Phys. Lett.* **2002**, *81* (1), 150–152.

(372) Sun, S.; Murray, C. B.; Weller, D.; Folks, L.; Moser, A. Monodisperse FePt Nanoparticles and Ferromagnetic FePt Nanocrystal Superlattices. *Science* **2000**, *287* (5460), 1989–1992.

(373) Hashimoto, Y.; Seniutinas, G.; Balčytis, A.; Juodkazis, S.; Nishijima, Y. Au-Ag-Cu Nano-Alloys: Tailoring of Permittivity. *Sci. Rep.***2016**, *6*, 25010.

(374) Shimpi, J. R.; Sidhaye, D. S.; Prasad, B. L. V. Digestive Ripening: A Fine Chemical Machining Process on the Nanoscale. *Langmuir* **2017**, *33* (38), 9491–9507.

(375) Prasad, B. L. V; Stoeva, S. I.; Sorensen, C. M.; Klabunde, K. J. Digestive Ripening of Thiolated Gold Nanoparticles: The Effect of Alkyl Chain Length. *Langmuir* **2002**, *18* (20), 7515–7520.

(376) Stoeva, S. I.; Prasad, B. L. V; Uma, S.; Stoimenov, P. K.; Zaikovski, V.; Sorensen, C. M.; Klabunde, K. J. Face-Centered Cubic and Hexagonal Closed-Packed Nanocrystal Superlattices of Gold Nanoparticles Prepared by Different Methods. *J. Phys. Chem. B* **2003**, *107* (30), 7441–7448.

(377) Williams, D. B.; Carter, C. B. The Transmission Electron Microscope. In *Transmission electron microscopy*; Springer, 1996; pp 3–17.

(378) Chan, E. M.; Xu, C.; Mao, A. W.; Han, G.; Owen, J. S.; Cohen, B. E.; Milliron, D. J. Reproducible, High-Throughput Synthesis of Colloidal Nanocrystals for Optimization in Multidimensional Parameter Space. *Nano Lett.* **2010**, *10* (5), 1874–1885.

(379) Frisenda, R.; Castellanos-Gomez, A. Robotic Assembly of Artificial Nanomaterials. *Nat. Nanotechnol.* **2018**, 1.

(380) Peplow, M. The Robo-Chemist. *Nature* **2014**, *512* (7512), 20.